X-RAY AND OPTICAL STUDIES OF BINARY X-RAY PULSARS

BY

DAVID JOHN WATTS

Submitted in fulfilment of
the requirements for the degree of
Doctor of Philosophy

UNIVERSITY OF TASMANIA

HOBART

JUNE 1983

graduated 1984

Except as stated herein, this thesis contains no material which has been accepted for the award of any other degree or diploma in any university. To the best of my knowledge and belief, this thesis contains no copy or paraphrase of material previously published or written by another person, except when due reference is made in the text of the thesis.

David John Watts

June 1983.

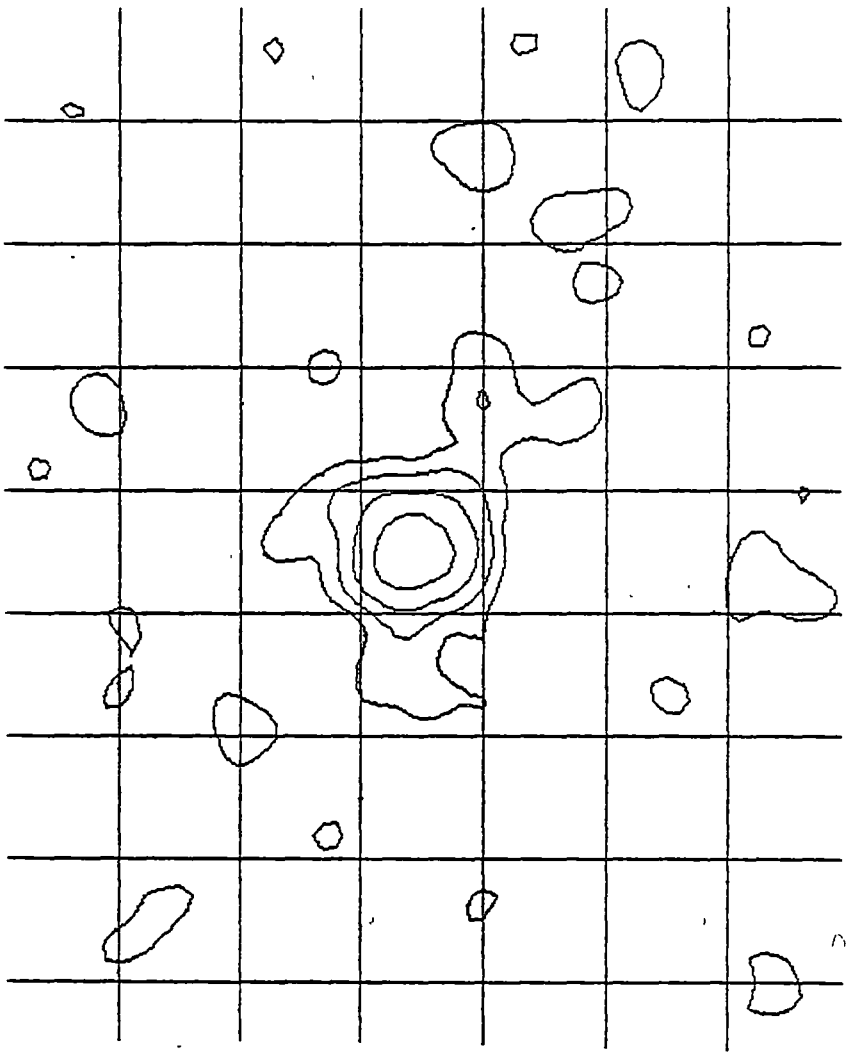

'Perhaps there are more than X-ray sources in space'

from Einstein IPC image of VY Sculptoris region.
Scale is 10 arcsec per mm.

SUMMARY

This dissertation is divided into two main areas. Part (i) in Chapters 2 to 4 deals with the University of Tasmania contribution to the University of Tasmania/Imperial College, London (UTIC) hard X-ray balloon-borne platform and the balloon flight of 1981 December 2. Part (ii) presented in Chapters 5 to 8 discusses the optical and soft X-ray observations of cataclysmic variables and miscellaneous X-ray sources. The introduction to both parts is in Chapter 1.

(i) The UTIC observatory consists of two large area detectors mounted in an alt-az configuration. The UT detector, with a sensitive area of 5200 cm^2, is a xenon-filled proportional counter sensitive in the energy range 20 to 100 keV. The IC instrument consists of 12 phoswich detectors with a combined area of 1680 cm^2 and an energy range of 20 to 200 keV. Both detectors use 2° FWHM collimators. The platform and UT detector are fully described in Chapter 2.

An onboard microprocessor continuously updates and drives to the altitude and azimuth of the object under observation. Both detectors are driven in altitude via a common shaft, and azimuth is controlled by reference to the earth's magnetic field with an accuracy of ~8 arcmin rms. A sunsensor is used to check the platform azimuth.

Data from each detector are independantly encoded into a PCM bit stream and telemetered on separate subcarriers. The data are treated separately at the ground station with independant UT and IC computers which provide output on VDU and teleprinter of housekeeping, aspect and quick-look X-ray data.

The platform was flown on 1981 December 2 for a duration at float of 6.5 hours. A mechanical fault of the altitude drive limited observations to two objects, the extreme Seyfert 1 galaxy IC4329A and the pulsar GX1+4. The upper limits on IC4329A are consistent with the soft X-ray flux measured by satellites. GX1+4 was in a hard low flux state. Due to this

low intensity, no periodic structure could be established. Comparison of the spectrum with previous observations shows GX1+4 exhibits spectral variability similar to other luminous galactic X-ray sources including Cyg X-1. The source of the hard X-ray photons is suggested to be soft photons that have been Compton scattered from a region or cloud of hot electrons. Changes in the size of this scattering region can explain the observed hardness and luminosity variations provided the total number of electrons in the scattering region are conserved.

(ii) The white dwarf equivalent of the binary neutron star pulsars are the recently discovered class of intermediate polars which are a subset of the cataclysmic variables. Optical observations of the intermediate polars 2A0526-328 and V1223 Sgr and soft X-ray observations of 2A0526-328 and the nova-like object VY Scl are presented in Chapters 5 and 6.

Spectroscopic observations of 2A0526-328 confirm that the emission line radial velocity period (5.48 hour) is significantly different from the photometric period (5.19 hour). Changes in the emission line velocity and profiles suggest that the accretion process is controlled by the white dwarf's magnetic field. Einstein X-ray observations show it is a hard source with a thermal spectrum of kT ~ 19 keV. There is no evidence of any strong soft X-ray component. Quasi-periodic variations on a timescale of ~700 sec are observed in the X-ray light curve. Similar fluctuations have been reported in optical photometry. A model for the object is proposed in which a rotating white dwarf revolves with a 4-day period in a retrograde orbit with a subluminous red giant. Predictions on the nature of the secondary are given and other observational tests are proposed.

Optical and IR light curves of V1223 Sgr confirm the photometric period of 0.14 day. The source of the 794 sec pulsations cannot be ascertained from the present data due to the failure to find a unique orbital beating period. The spectrum from UV to IR is consistent with

a disc model with no IR excess from the secondary being apparent. Spectroscopic observations over 2 hours showed a small radial velocity change accompanied by complex line profile changes. The low mass function derived from the radial velocity movement implies a low inclination angle for reasonable component masses. Upper limits to pulsed polarization at any of the expected white dwarf spin periods are ±3% at V, ±1% at R and ±10% at K.

A simple light curve model of the intermediate polars is developed and compared to the observed photometric data of 2A0526-328, V1223 Sgr and H2252-035.

Einstein observations of VY Scl indicate the spectrum is soft (kT = 1.2 keV) with little absorption (n_H = 4 x 10^{20} cm^{-2}). The low absorption may be a consequence of the system being pole-on with little obscuring material in the line of sight from the accretion disc.

Finally, summaries of observations of candidate stars in HEAO-1 and Einstein X-ray fields are presented in Chapter 8.

ACKNOWLEDGEMENTS

As a member of an experimental research group, I have appreciated the many contributions, both large and small, from the members who have or are still with the group. To my supervisor Dr. John Greenhill for his overall guidance of the group through its many traumatic and happy moments. His constructive comments on all aspects of my work including this thesis has been of great benefit. During my doctorate, the research fellows in our group, Dr. Richard Thomas in my first year and Dr. Barry Giles for the last two years have provided excellent sources of encouragement and contribution to the success of the UTIC project and the optical studies. Other members of the group who deserve special mention are Dr. K.B. Fenton, Dr. M.L. Duldig, Mr. M.W. Emery, Mr. D.M. Warren and Mr. S.C. Ashton. Finally the excellent help of the over-worked staff of the workshop, notably Mr. B. Wilson, for the construction of the platform.

The UTIC project has another half, the X-ray group at the Imperial College, London. I thank them for their contribution to the project. In particular to Mr. K. Harper for communicating the IC results from the 1981 balloon flight.

For their excellent balloon launching and support, the staff of the Australian Balloon Launching Service led by Mr. P. Oates deserve thanks. Similarly, the National Scientific Balloon Facility of the U.S.A. under Mr. R. Kubera are acknowledged for their help in the 1981 flight.

The optical observations have been conducted with the help of Drs. P.W. Hill and J. Bailey of the Anglo-Australian Observatory and N. Visvanathan of Mount Stromlo and Siding Springs Observatory. To Dr. Don Morton of the AAO for his assistance in the stellar classification of the stars in the X-ray fields. The granting of telescope time on the AAT by Australian Time Assignment Committee and the 1 metre of the MSSSO is acknowledged. The data from Mt. Canopus is courtesy and

assistance of Mr. K. Hill, C. Ashworth and Dr. M. Waterworth. The use of the Einstein Observatory would not have been possible without the generousity of the Harvard-Smithsonian Centre for Astrophysics through the Guest Investigator Program.

Financial support has been provided by a Commonwealth Postgraduate Award and is greatly appreciated since I would not have contemplated starting a Ph.D. without it. Australian Research Grants Council support for UTIC and the optical studies is acknowledged.

For typing the thesis, I thank my mother for the onerous task of the first draft and Miss Gullinar Gafar for the excellent nature and style of the final copy. The photos are courtesy of my father, as is the copying and binding. For the dull task of proof reading, I thank Dr. Marc Duldig. Finally to all other fellow students and staff who have provided the necessary lighter moments (and occasionally useful advice) that are needed to survive a doctorate.

CONTENTS

CHAPTER 1

INTRODUCTION

1.1 Introduction

From the turn of the century till the early sixties, the field of high energy astrophysics consisted only of the study of cosmic rays and radio emission of high energy electrons. Only with the development of rockets, was it possible to place X-ray detectors above the obscuring atmosphere. In 1962, in a rocket flight designed to search for X-ray emission from the moon, the first two extra solar X-ray sources were detected in the constellations Scorpius and Sagittarius. The first is now known as Sco X-1 and the second was the superposition of the many sources in the galactic centre region. In the last twenty years, observations using rockets, balloons and satellites have revealed the existence of a wide range of galactic and extra-galactic phenomena and X-ray astronomy has matured sufficiently to place it at the forefront of astronomy. From the previous attitude of astronomers conducting observations and analysis in restricted wavelength bands, the understanding of X-ray objects requires the use of data from radio through IR, optical and ultraviolet to soft (0.1 - 2 keV), medium (2 - 20 keV) and hard (20 - 200 keV) X-ray observations. The reason is vividly illustrated in the cataclysmic variables discussed in Section 1.8.3. Each energy window reaches a different physical regime. At IR wavelengths, the secondary is most prominent and in the optical and UV, the accretion process is the principal emitter. The inner disc emits in the EUV whilst hard X-rays are generated via shock, near the white dwarf. Reprocessed hard X-rays can emit as blackbody radiation from the surface of the white dwarf in the soft X-ray band.

The first eight years of X-ray observations were sporadic with the only vehicles available being rockets and balloons. By their nature, they only allowed short observations with a maximum timespan of ~3 days in the case of balloons. In 1970, with the launch of the first dedicated X-ray satellite Uhuru, the number and variety of X-ray objects increased

dramatically from ~30 to ~300. It was now possible to obtain sufficient data to begin to understand the physical processes necessary to release the large quantities of energy being observed. Other satellites with similar instruments that were launched in the 1970's were the Astronomical Netherlands Satellite (ANS), SAS-3, Ariel V, OSO-8 and Copernicus. The last of this type was HEAO-1 launched in 1977. Particular emphasis has been placed on the acquisition of data in the X-ray band 2 to 20 keV where source fluxes are higher. With high count rates, more precise source positions can be achieved. Ariel V, SAS-3 and HEAO-1 used a variety of rotating and scanning modulation collimators to derive source positions with an accuracy of ~30 arc sec making possible many optical identifications.

The Einstein X-ray Observatory (Giacconi et al., 1979) launched in 1978, in particular, has been responsible for a dramatic increase in our knowledge of the X-ray sky. By using Wolter I grazing incidence mirrors and various forms of position sensitive X-ray detectors, spatial resolutions of ~5 arc sec and very low background rates have enabled the detection of all major classes of astronomical objects except K or M supergiants. The maximum energy that these mirrors can function at is ~5 keV which excludes the many significant astrophysical processes that are seen above 20 keV in the hard X-ray region.

There have been relatively few observations in the hard X-ray band where, because of the small fluxes, large area high sensitivity detectors are required. Until the demise of HEAO-1 in January, 1979, the largest hard X-ray experiments were the HEAO A2 (Rothschild et al., 1979) and A4 instruments (Matteson, 1978) with respective total sensitive areas of 1600 cm^2 and 200 cm^2 covering the band 2-60 keV and 15-150 keV respectively. One currently operating X-ray satellite is Hakucho (Hayakawa, 1981) with a hard X-ray NaI(TI) detector of area only 45 cm^2. With the imminent launch of EXOSAT (Taylor et al., 1981), this situation will be changed

with the operation of the ME proportional counters with an area of 1800 cm^2, although the maximum energy is only 50 keV. The recently launched Japanese satellite ASTRO-B is also restricted to energies below 55 keV.

Many significant astrophysical problems require measurements over a wider energy range than any satellites likely to be launched within the next decade. They range from understanding the origin of the cosmic X-ray background to the elucidation of accretion processes onto neutron stars and white dwarfs in binary systems.

Currently the only vehicles for these detectors are balloons since sensitive high energy detectors are heavy and require large satellites. Contemporary platforms include the MPE/AIT instrument (Staubert et al., 1981) which first detected the Her X-1 cyclotron feature. The only satellite detector is on the proposed ESA X-80 mission. This is a 15-200 keV phoswich detector but will not be available until the end of the decade at the earliest.

In the following section, summaries of all the major classes of X-ray sources are given with the emphasis on galactic objects and the role hard X-ray observations can play in their understanding. Reviews of the individual sources observed are presented in their appropriate classes.

Extragalactic

1.2 The Cosmic X-ray Background

At all X-ray energies, from a few hundred eV to the MeV range, a more or less isotropic background is observed, referred to as the cosmic X-ray background (CXB). Its origin remains uncertain (Leiter and Boldt, 1982). It has been suggested that the CXB may be due to the superposition of the X-rays from unresolved extragalactic gas. The CXB is characterised in the hard X-ray range by a thermal spectrum with kT ~ 40 keV (Marshall et al., 1980).

If it originates in a hot intergalactic medium, problems arise concerning the source of the energy required for heating (Field and Perrenod, 1977). The flux and energy spectrum of Seyfert and other active galaxies seems incompatible with that of the CXB in the range from a few keV to several hundred keV (Mushotzky et al., 1980). The spectrum of only two quasars 3C273 and 0241+622 have been measured in the hard X-ray band (Worral et al., 1979, 1980). Their spectra are significantly different and that of 3C273 is compatible with the CXB. Further measurements of quasar and active galaxy spectra are required to ascertain typical spectra and their contributions to the CXB.

1.3 Clusters of Galaxies

The first detected X-ray emission from a cluster of galaxies was of the Coma cluster by Uhuru. The number of X-ray clusters is now in excess of 30. The spectra are soft ($kT \simeq 5$ keV) and thermal since iron line emission at 6.7 keV is seen. The accepted model is thermal emission from a hot intergalactic gas at a temperature of 10^8K, extending out to ~1 Mpc and densities $\sim 10^{-4} cm^{-3}$ (Jones, 1980). The mass of the optically thin gas is comparable to the mass of galaxies but not sufficient to close the universe. Einstein observations show a rich diversity of surface brightness distributions which are correlated with the cluster morphology and evolution. Hard X-ray observations are not particularly relevant due to the low temperatures.

1.4 Active Galaxies

X-ray emission has been detected from all classes of active galaxies ranging from the radio galaxies typified by Cen A to the more luminous members of Seyferts, BL Lac's and quasars. X-ray luminosities range from 10^{42} to 10^{46} erg sec^{-1} and there appears to be a continuous range of energetic behaviour from normal galaxies, through Seyferts and up to QSO's. The general consensus is that the source of radiation is gas accreting onto a massive black hole of mass $10^6 - 10^8 M_\odot$. Rapid

variability on time scales as short as 100 sec have been detected in the Seyfert galaxy NGC6814 (Tennant et al., 1981) and QSO 1525+227 (Matilsky et al., 1982) which place constraints on the dimensions of the 'power house' in these objects.

Seyfert galaxies are spiral galaxies with bright nuclei and are distinguished by broad optical emission lines ($\sim 10^4$ km sec^{-1}) generated in a small region (~0.1 pc) (Holt, 1981). Mushotzky et al. (1980) found that a sample of seven Seyfert 1 galaxies have very similar energy spectral indices of $\alpha = 0.7 \pm 0.1$ (from 5 to 50 keV) indicating a remarkable similarity in the X-ray power source at the nucleus.

The BL Lac sources on the other hand show a fairly diverse range of spectral indices from $\alpha = 0$ to 3, and are more variable than the Seyferts. This different behaviour and their radio loudness indicates that synchrotron emission is probably the source of the X-ray emission in BL Lac's but not in Seyfert's. In ~20% of all the observations of BL Lac's, a harder spectrum is seen above 5 keV possibly from self comptonization of the low energy spectral component (Holt, 1981). High energy observations are necessary to define the exact emission mechanism.

More than 100 quasars have been detected by the Einstein observatory out to a redshift of 3.5 but only two have been detected at hard X-ray energies. 3C273 is the brightest QSO and has an $\alpha \simeq 0.4$ (Worrall et al., 1979) whilst QSO 0241+622 is markedly different with $\alpha = 1.0$ (Worrall et al., 1980). One possibility is that radio loud quasars are BL Lac type objects at high redshift whilst the radio quiet quasars are similar to Seyferts (Holt, 1981). Correlating radio properties with the hard X-ray data from other quasars may answer this question. The brightest candidate at soft energies is the radio quiet QSO MR2252-178 (Ricker et al., 1978).

For a review of the many X-ray emission processes that may occur from galactic nuclei see Lightman (1982). Outlines of these models are presented in Chapter 4 in the discussion of the hard X-ray data from the extreme Sy 1 galaxy IC4329A. A summary of this galaxy is presented in the next section.

1.4.1 IC4329A

The Seyfert 1 galaxy IC4329A was first detected as an X-ray source by Ariel V and listed in the 2A catalogue as 2A1347-300 (Cooke et al., 1978). However, the error box also included the giant elliptical IC4329 and just excluded IC4327 (Elvis et al., 1978). No estimate of the relative contributions of each source could be made. The SAS-3 rotating modulation collimator observations of the region by Delvaille, Geller and Schnopper (1978) reduced the error box to an area of ~1 square arc min. They found extended emission compatible with either emission surrounding IC4329A or a 2nd point source with one third of the total flux at the position of IC4329. HEAO-1 scanning modulation collimator (MC) observations by Dower et al. (1980) in 1978 July 27 excluded both possibilities setting a 3σ upper limit of 15% emission from IC4329 compared to the SAS-3 observations. The flux of IC4329A had decreased to ~40% of the SAS-3 flux of $\sim 10^{-10}$ erg cm^{-2} sec^{-1}.

Further X-ray observations by Ariel V are described in the 3A catalogue (McHardy et al., 1981) and a light curve is shown in Figure 1 of Marshall, Warwick and Pounds (1981) showing variability on a timescale of months. Tennant and Mushotzky (1983) have studied the variability of active galaxies and concluded that IC4329A does not vary rapidly in keeping with the majority of the active galaxies they studied. IC4329A was detected during the two all sky survey scans of the HEAO-1 A2 experiment (Piccinotti et al., 1982). Einstein observations using the Solid State Spectrometer (SSS) show the source spectrum is well represented by a power law with photon spectral index 1.86 and 2.5 magnitudes of absorption

(Holt, 1981) as estimated from optical reddening. The spectral index is typical of Seyfert 1 galaxies.

An optical study of the nucleus of IC4329A by Wilson and Penston (1979) found it was heavily reddened. The Balmer decrement is steeper than found in any other Seyfert galaxy and the nuclear continuum is steep ($F_\nu \propto \nu^{-4.4\pm0.3}$). They have classified it as an extreme Seyfert galaxy. Since its redshift is 0.0138 and H_β luminosity is $\sim 10^{44}$erg sec^{-1}, they have dubbed it the nearest quasar. Studies of low redshift X-ray selected quasars by Grindlay et al. (1980) show a great overlap in luminosity of these quasars and Seyfert 1 galaxies indicating that quasars and Seyferts are essentially different manifestations of the same object.

Table 1.1 contains a list of X-ray observations of IC4329A. The HEAO-2 SSS spectrum has been integrated from 2 to 10 keV to provide a comparison with previous observations.

1.5 Normal Galaxies

Individual X-ray sources have been detected in M31 and from the LMC and SMC (Van Speybroeck and Bechfold, 1981) with fluxes up to 2.4×10^{38}erg sec^{-1} (0.5 - 4.5 keV). In M31, the 88 point sources can be divided into 16 globular clusters, 53 sources more than 2' from the nucleus and 19 within 2' of the centre. The latter two classes are the equivalent disc and bulge sources seen in our galaxy. All the sources in M31 are too weak and confused for current hard X-ray observations. On the other hand, the LMC and SMC are close enough to observe the brighter objects ($L_x \geq 10^{38}$erg sec^{-1}) at hard energies. They are similar to the high luminosity sources in our galaxy (section 1.8.1 and 1.8.2) and several are binary X-ray pulsars.

X-rays have been seen from ~30 other normal galaxies and represent $\sim 10^{-3}$ to 10^{-4} of the total luminosity. The nuclei of some of these objects have variable strong X-ray sources ($L_x \sim 10^{39}$erg sec^{-1}) and

TABLE 1.1

Journal of X-ray observations of IC4329A

Observer	Detector	Band (keV)	Flux x 10^{-11} erg sec^{-1} cm^{-2} mean	minimum	maximum	Log mean flux at source (erg sec^{-1})	Assumed H_0 km sec^{-1} Mpc^{-1}	Date
Cooke et al. (1978)	Ariel V	2 - 10	8.7±1.0			43.82	50	
McHardy et al. (1981)	Ariel V	2 - 10	8.97±0.86	1.50±0.7	28.76±0.62			
Delvaille, Geller and Schnopper (1978)	SAS-3 RMC	2 - 11	10			44	50	1976 June
Dower et al. (1980)	HEAO-1 MC	2 - 10	4.0			43.52	50	1978 July 27
Piccinotti et al. (1982)	HEAO-1 A2	2 - 10	8.0±0.45 7.46±0.80			43.82 43.79	50 50	
Tennant and Mushotzky (1982)	HEAO-1 HED 3	2 - 10	5.1			43.61	75	1978 July 27
Holt (1981)	HEAO-2 SSS	0.5-4.5	6.7					

represent small scale examples of active galactic nuclei (Van Speybroeck and Bechfold, 1981).

Galactic Sources

1.6 Nondegenerate Systems

Coronae Sources

Contrary to the expectation, from the extrapolation of the sun's X-ray flux, of little if any X-ray flux from ordinary stars the Einstein Observatory detected coronal X-rays from all classes of stars except the K-M supergiants (Linsky, 1981). Typical luminosities of dwarf stars range from $\sim 10^{27}$ to 10^{29} erg sec^{-1} and coronal temperatures are of the order of 10^7K. The emission region is generally considered to be magnetic loops similar to those seen in our sun.

RS Cvn binaries

These are detached binaries with periods between 1 and 14 days and generally consist of a K IV primary and G V secondary. Approximately 60 systems have been detected with luminosities between 3×10^{29} to 6×10^{31} erg sec^{-1} (Linsky, 1981). The emission region is considered to be magnetic loops similar to the corona emission region models except in this case there is the possibility of interactions between loops from both stars.

Flare Stars

UV Ceti and YZ CMi have been detected during outburst (Garmire, 1979) and the fluxes are comparable to large flare activity on the sun, suggesting a similar origin.

OB Stars

These are the brightest nondegenerate sources with a mean luminosity of $L_x \sim 6 \times 10^{33}$ erg sec^{-1} and typical $L_x/L_{bol} \approx 10^{-7}$. It is suggested that strong stellar winds are responsible for the X-ray emission since $L_x/L_{wind} \approx 10^{-4}$. The radiation line driven wind will produce regions of enhanced densities which will radiate soft X-rays from their bow shock

as they propagate out from the star (Linsky, 1981).

Algol systems

Algol is a 2 - 6 keV X-ray source (Garmire, 1979) with a temperature between 3 x 10^6K and 3 x 10^7K. Stellar winds, from the K IV subgiant onto the B dwarf have been proposed as the source of the X-ray flux with luminosities up to 10^{33}erg sec^{-1}.

Supernova Remnants

Over 50 supernova remnants (SNR) have been imaged by Einstein (Helfand, 1981). As the expanding shock moves through the interstellar medium , it generates X-rays via the compression of the interstellar medium and provides a valuable tool for the diagnosis of the initial explosion, its collapsed remnant and the surrounding interstellar medium. The Crab SNR has been imaged at hard energies (Makishima et al., 1980) with a resolution of 0.2 arc min, but it is not foreseeable that other SNR's will be imaged due to the low fluxes and their soft emission.

Several neutron stars in the centres of the SNR have been detected by their thermal emission (Helfand, 1981). The neutron stars in RCW103, Crab and Vela have temperatures of ~2 x 10^6K with similar upper limits to eight others.

Degenerate Systems

1.7 Non Binary

Hot Degenerates

Very soft X-rays have been detected from the degenerate dwarfs Sirius B and HZ43 and extreme UV from Feige 24 (Lamb, 1981). The energy distribution from optical to X-ray is consistent with photospheric emission from a hot (T ≃ 30,000 - 60,000 K) hydrogen-rich atmosphere. None have been detected at hard energies.

Radio Pulsars

Prior to the observations of the Einstein Observatory, only one example of an X-ray emitting radio pulsar was known, the Crab pulsar. With a period of 33 m sec, it is one of the youngest and fastest of the ~300 known radio pulsars. The radio to gamma ray emission all occur at the same phase of the rotation period.

Since it is one of the brightest X-ray sources and its spectrum is extremely constant, it is the ideal standard for calibrating X-ray detectors.

The Einstein Observatory increased the sample to two when it detected a 0.15 sec X-ray pulsar within the SNR MSH 15-52 (Seward and Harnden, 1982). Subsequent radio observations have revealed a radio counterpart and confirmed the high spin down rate of ~47 μsec yr^{-1} (McCulloch, Hamilton and Ables, 1982, Manchester et al., 1982). The other fast radio pulsar associated with a SNR is Vela X. Pulsations have been seen at gamma ray energies, but not in the X-ray band (Helfand, 1981). Hard X-ray observations of the pulsar in MSH 15-52 are required to understand the diverse spectral differences between the Crab and Vela pulsars.

1.8 Compact Binary Systems

The most spectacular advances that X-ray astronomy has contributed to the field of astrophysics is in the area of compact X-ray sources in which X-ray emission is powered by the accretion of gas onto a collapsed object, i.e. white dwarf, neutron star or in the case of Cyg X-1, the possibility of a black hole. The source of the accreting gas is the nondegenerate companion star and the various mass transfer mechanisms are (i) Roche Lobe overflow via evolution of the secondary or for short orbit systems ($<0.5^{d}$) decay of the orbit via gravitational radiation, and (ii) strong stellar winds with mass loss rates up to $10^{-6} M_{\odot} yr^{-1}$.

The X-ray luminosity of matter accreting onto a compact object with radius R_x and mass M_x can be estimated from the potential energy released when matter from infinity accretes at a rate of $\dot{M}$. The flux is

$$L_x = GM_x\dot{M}/R_x \quad . \tag{1.1}$$

In the case of the degenerate being a white dwarf ($R_x \simeq 10^4$km), the energy released is 1 MeV/nucleon whilst for neutron stars ($R_x \simeq 10$ km), it is 100 MeV/nucleon. The temperature of the material is of the order

$$T \sim \alpha\, m_p GM_x/k\, R_x$$
$$\sim 10^7 \alpha (M_x/M_\odot)/(R_x/R_\odot)\ K$$

where m_p is the proton mass, k the Boltzmann constant and α an efficiency factor for heating the gas. For adiabatic heating in a strong shock, $\alpha \sim 0.1$. For slow heating and where radiation losses dominate, like in a viscous disc, $\alpha \sim 10^{-5}$ (Pringle and Rees, 1972). To obtain $T \sim 10^8$K requires $(M_x/M_\odot)/(R_x/R_\odot) > 100$ which is only satisfied for degenerate objects.

From equation (1.1) extremely high X-ray fluxes can be generated. For white dwarfs, $\dot{M} \simeq 10^{-7} M_\odot yr^{-1}$ will produce luminosities of $\sim 10^{36}$ erg sec^{-1} and for neutron stars or black holes, $\dot{M} \simeq 10^{-8} M_\odot yr^{-1}$ will produce $L_x \simeq 10^{38}$erg sec^{-1}. However the limit is reached when the radiation pressure of the accreting material exceeds the gravitational force and prevents further matter accreting. This is the Eddington Limit and, for spherically symmetric accretion is given by

$$L_x \simeq 10^{38}(M_x/M_\odot) \text{erg sec}^{-1} \quad .$$

This may be exceeded if the accretion is not spherically symmetric but the factor is not more than 10. By their very nature, the compactness of neutron stars does not allow for direct observation of the intrinsic source spectrum due to electron scattering. On the other hand, in cataclysmic variables where the compact object is considered to be a white dwarf, the X-ray flux is $\sim 10^{-4}$ of the Eddington Limit. Therefore,

electron scattering is not as significant as in the massive binaries and the underlying optically thin bremsstrahlung spectrum is generally visible at infinity.

The mass of the components of a binary system can be estimated from the mass function. If M_c is the mass of the companion, M_x the mass of the X-ray source, i the inclination angle of the system, e the eccentricity of the orbit, G is the gravitational constant, a sini is the projected semi-major axis of the orbit of the star whose radial velocity has been measured (in this case M_x) and P is the orbital period then the mass function is

$$F = \frac{4\pi^2}{G} \frac{(a \sin i)^3 (1-e^2)^{3/2}}{P^2} = \frac{(M_c \sin i)^3}{(M_c+M_x)^2} \qquad (1.2)$$

where

$$a \sin i = \frac{P}{2\pi} V \sin i$$

and Vsini is the observed radial velocity amplitude. Although equation (1.2) is not sufficient to determine the component masses it does place useful constraints on M_c, M_x and i. If the radial velocity estimates are from absorption or emission lines from the companion, as in the OB stars, M_c and M_x need to be interchanged in equation (1.2).

If we place an infinitessimal body in the gravitational field of two point masses orbiting in circular orbits, then there exist 5 points designated the Lagrangian points L1 to L5 where the body will maintain a position fixed relative to the point masses. The contours on Figure 1.1 are called zero relative-velocity surfaces and represent equipotential surfaces where material can be moved without any change in their potential. The Roche Lobe is defined as the surface which intersects L1. If a secondary fills this lobe then matter can flow to the other star via L1. If we neglect radiation pressure and assume synchronization of the secondary between axial rotation and orbital revolution, then the Roche Lobe radius R_L is approximated by

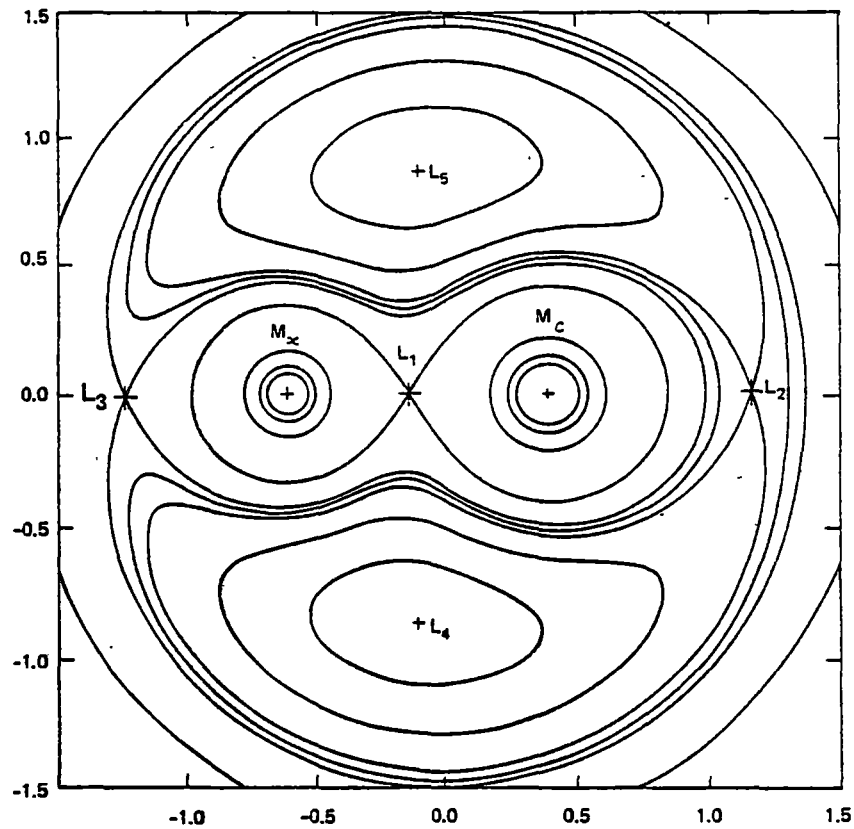

Figure 1.1 The equipotential surfaces surrounding the stars denoted by M_x and M_c. The Roche Lobe intersects the point L_1.

$$\begin{aligned} R_L &= a(0.38 + 0.20 \log q) \quad 0.8 < q < 20 \\ &= a(0.46(q/(1+q))^{1/3}) \quad 0 < q < 0.8 \end{aligned} \tag{1.3}$$

where the mass ratio $q = M_c/M_x$. If the secondary underfills its Roche Lobe, then mass transfer can occur via stellar winds.

1.8.1 Massive binaries

This class consists of the massive X-ray binary pulsars (for review see Rappaport and Joss, 1981) and the nonpulsing systems like 4U1700-37 and Cyg X-1. They are generally composed of a luminous massive early type companion and a neutron star (or in the case of Cyg X-1 and LMC X-3 possibly a black hole). One exception is the pulsar GX1+4 with an M6 giant companion (Davidsen et al., 1977). Their X-ray to optical luminosities L_x/L_{opt} range from 10^{-4} to 1 and are optically

bright (M_V ~ -6). The secondaries are usually O or B supergiants or giants with masses between 15 and 30 $M_\odot$. Orbital periods range from 2 to 20 days in the Roche Lobe systems to 560 days in the stellar wind powered Be system X Per (Worrall et al., 1981). The X-ray spectra are generally flat out to ~20 keV but steepen considerably thereafter.

Twenty one X-ray pulsars are known with pulse periods ranging from 0.069 msec in the Be system A0538-66 (Skinner et al., 1982) to 835 sec in X Per. Duty cycles are large (>50%) and the pulse profiles range from symmetric to highly assymetric shapes with no obvious correlations between pulse period or luminosity. Some sources show highly energy dependent pulse shapes (e.g. 4U0900-40) whilst others retain the basic profile over a range of energies (e.g. Cen X-3).

In the general model the neutron star has an intense magnetic field (B ~ 10^{12}G) whose axis is at some angle to the rotation axis. Matter, from the companion accretes down the field lines, generating X-rays close to the surface of the neutron star from the release of potential energy. The X-ray beam is viewed at different angles as it rotates to provide the observed pulse profiles. It is complicated by the presence of absorbing material above the X-ray emission region and the actual emission pattern of the X-ray source. Only recently have models emerged to explain the energy-dependent pulse profiles (Wang and Welter, 1981). High quality pulse profiles at high energies should determine the intrinsic beaming pattern since absorption effects are expected to be small.

The time dependent spin period of the pulsars have yielded unique information about the angular momentum torques from material accreting onto the neutron star. The pulse period behaviour is well known in eight pulsars with six showing spin up behaviour (Rappaport and Joss, 1981).

From the review of Rappaport and Joss (1977), the spin-up rate due to accretion torques is

$$\dot{P}/P \approx -3 \times 10^{-5} f (P/1\text{sec}) (L/10^{37}\text{erg sec}^{-1})^{6/7} \text{yr}^{-1} \qquad (1.4)$$

where L is the X-ray luminosity of the system and f is ~0.003 for a white dwarf star and ~1 for a neutron star with mass = $1M_{\odot}$, radius = 10 km and magnetic moment = 10^{30}G cm^2 corresponding to a magnetic field $B \approx 10^{12}$G. The observed spin up rates range from 0.03 yr^{-1} to 3×10^{-6}yr^{-1} (Bhatt, 1982) and are consistent with f = 1, i.e. the degenerate is a neutron star.

By measuring light time delays of the pulsations, the orbital parameters for seven pulsars have been determined (see Rappaport and Joss, 1981 and references therein). Some show negligible orbital eccentricity (e.g. Her X-1 and SMC X-1) whilst 4U0115+63 and GX301-2 have respective eccentricities of 0.34 and 0.44. This is only exceeded by the highly variable object Cir X-1 where the 16.6 day X-ray flares are probably due to periastron passage in a highly eccentric orbit (e ~ 0.7) (Murdin et al., 1980). Derived neutron star masses range from 0.5 to 3 $M_{\odot}$ (some with large errors) but all are consistent with the theoretically determined masses of 1.2 to 1.6 $M_{\odot}$ (Rappaport and Joss, 1981).

Seven of the twelve known Be X-ray binaries are pulsars (Rappaport and van den Heuvel, 1981). The X-ray luminosity of the Be objects tend to have more highly variable X-ray luminosities than the other massive binaries, to have smaller companion masses and longer orbital periods (>15 days). The companion underfills its Roche Lobe so to achieve accretion onto the compact object, a strong stellar wind is required. A0538-66 flares optically and in X-rays every 16.6 d. During these events, X-ray pulsations of 69 msec are seen. The model, which is applicable to the other members of the class, is a neutron star in an eccentric orbit about a Be star. When the neutron star approaches periastron, accretion via stellar wind is increased leading to the

observed flares. In the case of A0538-66, the eccentricity is sufficiently high for the neutron star to enter the envelope of the secondary (Skinner et al., 1982).

Rappaport and van den Heuvel (1981) estimate the space density of Be binaries to be ~100 within 2-5 kpc of the sun, which may be compared to the three Roche Lobe powered systems within the same distance. Total galactic populations are estimated to be 1500 for Be stars and 50 for Roche Lobe systems. The large difference is due to the evolution time-scale expected. In the Roche Lobe systems, X-ray emission is expected for $\sim 10^6$ years whilst in the Be stars, this is much longer since the stellar wind loss rates ($\leq 10^{-7}$ $M_\odot yr^{-1}$) hardly affect the evolution.

Spectra of the pulsars, time averaged or as a function of the phase of the pulsar period, can be used as a diagnostic of the structure of the magnetic field. Cyclotron features, either in absorption or emission yield direct estimates of the local field strength. In Her X-1, the cyclotron feature at ~60 keV shifts as a function of the phase of the 1.24 sec pulsations, giving possibilities of determining the local geometry (Voges et al., 1982). The steepening of spectra above 20 keV is a consequence of the interaction of cyclotron and scattering processes and can be used to estimate the local environment. (Pravdo and Bussard, 1981).

1.8.1.1 GX1+4

Of the many X-ray sources near the galactic centre, the X-ray pulsar GX1+4 is one of the strongest at hard energies (>10 keV). It was first detected in a balloon flight from Australia in 1970 October 16 by Lewin et al. (1971). Their error box was 2.24 square degrees. The light curve suggested that the source was modulated with a period of 2.3 minutes. Subsequent observations by the Copernicus satellite between 0.6 and 7.5 keV, confirmed the existence of the pulsating source (White et al., 1976) at a period of 4.3 minutes. The true period observed by

Copernicus was likely to be 2.2 minutes since the Nyquist frequency of the sampling time of the data was 2.9 minutes. Doty et al. (1981) have chosen the alias period of 2.17 minutes to ensure compatability with other observations.

Early observations of GX1+4 were by Ricker et al. (1976) on 1972 April 5 when no pulsations were seen and low energy OSO-8 observations during 1975 September 16-17 (Becker et al., 1976). Observations by OSO-8 (Dennis et al., 1980a) and Ariel V (Coe et al., 1981) of the galactic centre region show other sources dominate above 50 keV. Both require sources near the centre to fit the data.

Reanalysis of 1968 balloon data by Thomas et al. (1975) supported the contention that GX1+4 is the strongest hard source in the galactic centre region. However source confusion is quite possible since their error boxes are large due to the large field of view of their detector (5° x 30°), and the galactic centre is only 5 degrees from GX1+4. Observations by Johnson, Harriden and Haymes (1972) in 1971 November 20 of the galactic centre showed a strong source with a photon spectral index $\alpha = 2.37 \pm 0.05$ consistent with it being GX1+4. Source confusion was a significant problem since the detector field of view was 24° FWHM.

Excluding the source confused observations, the hard X-ray spectrum of GX1+4 is generally specified by a power law with photon spectral index of $\alpha = 2.4$ or thermal bremsstrahlung with $kT \simeq 30$-40 keV. Kendizorra et al. (1980) could not differentiate between the two but suggested thermal bremsstrahlung so as to be consistent with the low energy observations of Becker et al. (1976). Concurrent wide band observations would be needed to test this since GX1+4 is variable. The two observations that are markedly different from this result are the high energy data from OSO-8 (Dennis et al., 1980a) with $\alpha = 4.1$ and the low energy data (Parsignault and Grindlay, 1978, Becker et al., 1976) with $\alpha \simeq 1.2$ to 1.6. Combining HEAO-1 and HEAO-2 data, White et al.

(1983) find the best fit spectrum is a power law (α = 1) with a high energy cutoff factor of $\exp(\frac{E_c - E}{E_f})$ where E_f is the folding energy and E_c the cutoff energy. For the time averaged spectrum, E_f = 45 keV and E_c = 10 keV. The spectrum is shown in Figure 1.2 from Figure 2 of White et al. (1983). The spectral feature at 6 keV is the iron emission line with an equivalent width of 510±80 eV. It has a width of 2±1 keV, possibly indicating several emission features.

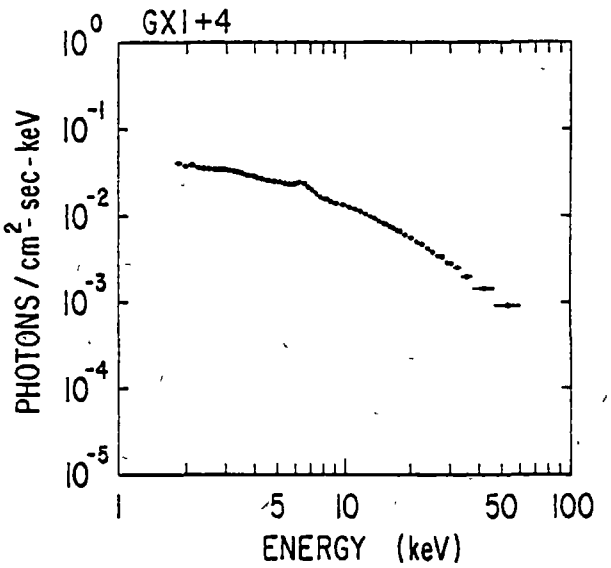

Figure 1.2 Time average spectrum of GX1+4 from HEAO-1. Note iron emission at 6 keV.

Variability of GX1+4 has been detected on all timescales. Uhuru observations showed the presence of a low energy source 4U1728-24 located within the hard X-ray error box which was variable by a factor of 2 on a timescale of months (Forman et al., 1978). The Astronomical Netherlands Satellite (ANS) observed GX1+4 in 1975 March 14-16 and 1975 September 16-18 (Parisgnault and Grindlay, 1978) during a study of all strong galactic sources. GX1+4 had the largest variability with an r.m.s. fluctuation of 81±20% of the mean intensity. Its long term behaviour over six months was also higher than average with an intensity change between the two observations of 2.77. A light curve of GX1+4 from 1 to 40 keV by OSO-7 is shown in Figure 7 of Markert et al. (1979). It shows intensity variations of ~3 and spectral variability with changes in α between 1.5 and 2.2.

GX1+4 was observed by SAS-3 on 1975 October 7-10, December 22-28, 1976 February 1-6 and July 4 (Doty et al., 1981). It was found to pulsate at an average period of 122.6 sec. In 1975 December, the long term spin-up rate of $\dot{P}/P \sim 0.02\ yr^{-1}$ changed dramatically to $\sim 0.055\ yr^{-1}$ and then by 1976 June it had decreased to $\sim 0.01\ yr^{-1}$. The spin-up episode is consistent with increased accretion torques onto a neutron star from an increase in the accretion rate (as inferred from the increase in luminosity).

The luminosity of GX1+4 during the SAS-3 observations was $\sim 5 \times 10^{37}$ erg sec^{-1} for an assumed distance of 10 kpc. The value of f for GX1+4 from equation 1.4 is ~2 implying that the degenerate object is a neutron star and not a white dwarf.

The true period of GX1+4 is open to some doubt. Either a single pole dominates yielding a rotation period of ~120 sec or both poles of the assumed dipole field have equal strength and are 180 degrees apart and hence the rotation period is ~240 sec. Koo and Haymes (1980) could not find any period between 121.0 and 129.0 sec but found a single pulsed peak at a period of 256.2±0.06 sec. Doty et al. (1981) could not find any difference between odd and even pulses from SAS-3 low energy data. Strickman et al. (1980) found that the pulse profile was significantly different for odd and even pulses in both 1976 and 1977 observations. The difference was principally in pulse shape and not amplitude. During 1977 April 11.5 to 15.5, Ariel V observed the galactic centre sources using the collimated proportional counter (CPC) and the scintillation telescope (ST). (Coe et al., 1981). Due to source confusion problems, no reliable spectra of GX1+4 could be obtained. However the pulsations from GX1+4 were quite distinct at a period of 118.72±0.005 sec. They were only detected by the CPC (1.6 - 16.2 keV). No modulation was evident from the ST (70 - 250 keV) with a 3σ upper limit of 3.6×10^{-3} photon $sec^{-1} cm^{-2} keV^{-1}$. Coe et al. (1981) tested for any variation in

pulse profile between odd and even pulses and could not find any statistically significant differences. Kendizorra et al. (1980) analysed 2 scans of GX1+4 from a balloon flight on 1978 November 22 and noted differences between odd and even pulses. The formal statistical error of this difference assuming Poissonian fluctuations, was 3.5σ. To further test the hypothesis that the true rotation period of the degenerate is twice the pulsation period, Kendizorra et al. performed 5000 Monte Carlo simulations of pulse profiles and found that the probability of the observed data fitting a single pulse model was 2×10^{-4} and 9×10^{-3} for the two observations. They conclude that the model of a single pulsation is not correct. Their data also had the largest modulation seen at the pulse period. They defined the degree of modulation by the fractional pulsed flux (fpf) i.e. fpf = (max-mean)/mean and obtained for GX1+4 a fpf ~ 0.52±0.08. For 100% modulation, fpf = 1.

White et al. (1983) did not find any evidence of differences between odd and even pulses. Pulse profiles at various energy bands from the HEAO-1 A2 experiment are shown in Figure 1.3 (from Figure 4 of White et al. (1983)). Of particular note is the absorption feature in the 2 to 7 keV light curve at phase 0.75. This probably represents the passage of the magnetic axis through the line of sight and absorption of the low energy X-rays by material in the accretion column. Also shown are the spectral changes as a function of pulse phase. The equivalent width of iron emission reaches a maximum at the minimum of the hard pulse whilst the variation of folding energy E_f and photon spectral index α show large changes in the spectrum.

Ariel VI observations during 1979 July and 1980 April showed that GX1+4 had increased its spin up rate from ~0.024 yr^{-1} to ~0.026 yr^{-1} during this period (Ricketts et al., 1982). The spectrum, from 1 to 50 keV, could not be acceptably fitted by single temperature bremsstrahlung

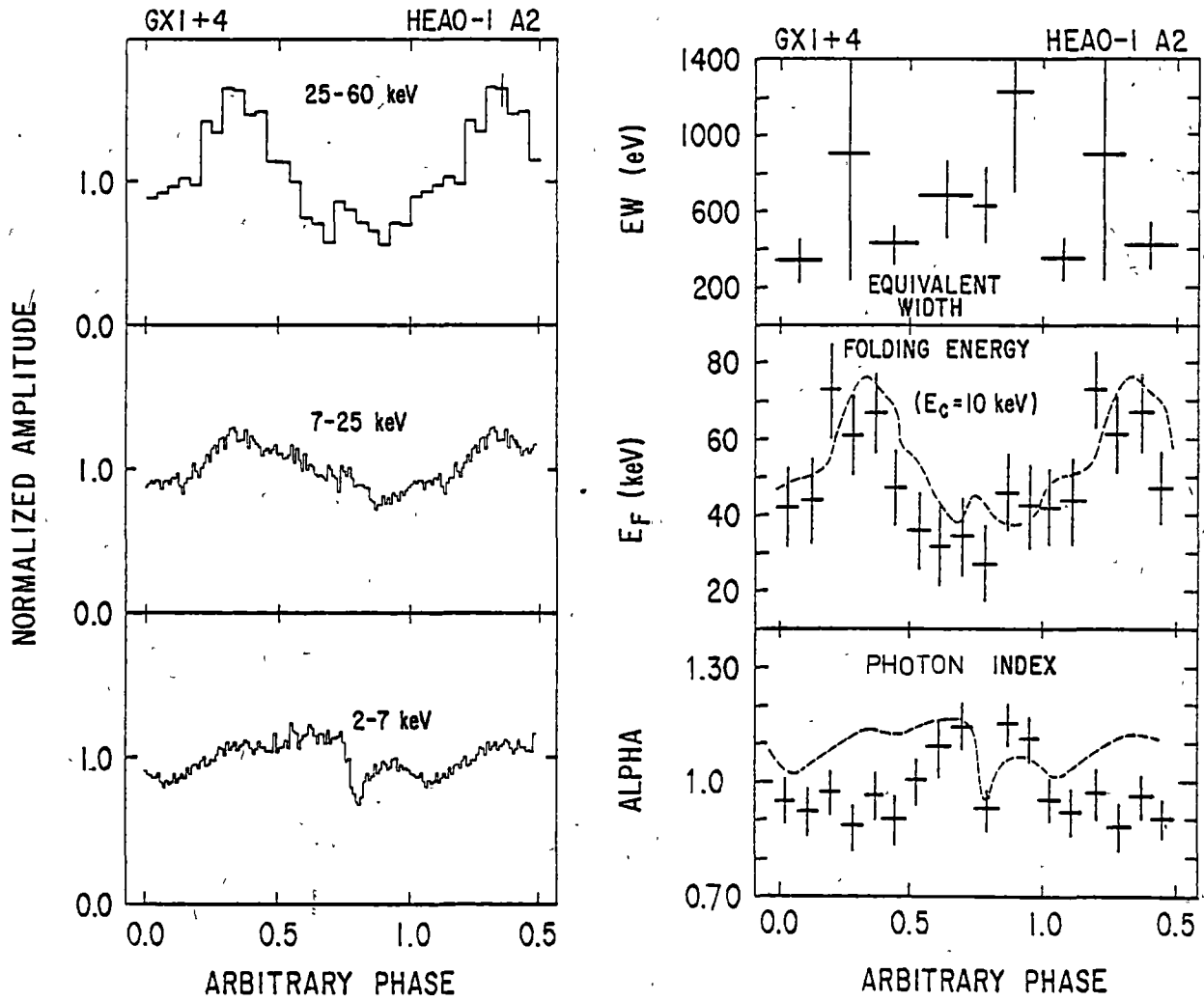

Figure 1.3 Left Side. Normalised pulse profiles of GX1+4 at three energy bands. Note the notch at phase 0.8 in the 2-7 keV light curve.
Right Side Spectral parameters as a function of pulse phase. EW is equivalent width of the iron line emission. E_f the folding energy whilst E_c is set constant at 10 keV. Dashed lines are superimposed pulse profiles.
Note the pulse period is 115 sec.

or blackbody spectra, but either by a power law ($\alpha \simeq 1.0$) with a high energy cutoff of ~30 keV or a multitemperature blackbody with maximum kT ~ 7 keV. Alternate pulses were indistinguishable but the data have lower precision than the high energy data of Kendizorra et al. (1980). The pulse profile from 3 to 20 keV was different than the 8 - 19 keV pulse profile from the SAS-3 observations of Doty et al. (1980) suggesting secular changes. Since the spin up rate is smaller than the $-0.032\ yr^{-1}$ measured by Doty et al. (1980), Ricketts et al. (1982) suggest the broader pulse profile of the Ariel VI observations may be related to the lower accretion rate inferred from the spin up data.

Iron line emission at 6.5 keV was found to be amplitude modulated at the pulse period by a factor of 2. From the line strengths, the large fraction of the solid angle subtended by the fluorescing source suggests the iron line source is the disc or Alfvén surface and not the companion. The variation in amplitude may arise from obscuration of the source by material in the accretion column.

Table 1.2 is a list of all published observations in order of observation date giving pulsation period, fractional pulsed flux and best fit power law or thermal bremsstrahlung spectral parameters. All previous spectral observations apart from the spectrum from White et al. (1983) have been converted to a uniform system using the equations listed below Table 1.2. Figure 1.4 is a plot of pulsation period versus epoch assuming a double peak pulse. It is adopted from Figure 6 of Kendizorra et al. (1980) and includes data published since 1980 except for the Ariel 6 observations (Ricketts et al., 1982). The line represents the best fit spin-up rate of $\sim 0.024\ yr^{-1}$. GX1+4 has the second fastest spin-up rate of any pulsar (Bahtt, 1982).

Detection of the optical counterpart of GX1+4 was first tentatively claimed by Glass and Feast (1973) by infrared scanning of the 2 arc min diameter X-ray error box of Hawkins et al. (1973) from Copernicus

Table 1.2 X-ray observations of GX1+4

Observer	Instrument	Date	Pulsation period (sec)	Modulation (fpf)	Spectrum* A	α	B	kT	Energy band (keV)	Comments on other sources in field of view
Thomas et al. (1975)	Adelaide balloon	1968 Feb 29	none reported		18.6	2.4±0.3			30-140	source confusion
Lewin et al. (1971) Ricker et al. (1973)	MIT balloon	1970 Oct 15	135±4		6.0±0.6	2.4±0.7	7.6±0.2	28±12	18-150	
Johnson et al. (1972)	Rice balloon	1971 Nov 20			14.7±3.0	2.42±0.05			30-2.3 MeV	source confusion
Ricker et al. (1976)	MIT balloon	1972 Apr 5	none seen	0.25	34.6±2.7	2.6±0.2	16.0	18±2	15-60	
White et al. (1975)	Copernicus	1972 Sep 11 1972 Sep 18 1973 Mar 25	259.9±0.24 257.2±1.2 263.4±8.4	0.11					3-8 3-8 3-8	
Koo & Haymes (1980) Haymes et al. (1975)	Rice balloon	1974 Apr 2	256.2±0.6	0.26±0.03	38	2.78±0.06			20-2 MeV	source confusion
Parsignault and Grindlay (1978)	ANS	1975 Mar 14-16 Sep 16-18			0.058 0.067	1.2±0.7 1.6±0.7		>30 12±8	1-28	
Becker et al. (1976)	OSO-8	1975 Sep 16 Sep 17	122.46±0.03	0.09 to 0.14	0.21 0.17	1.3 1.27		35 35	2-20	
Doty et al. (1981)	SAS-3	1975 Oct 7-10 1975 Dec 22-28 1976 Feb 1-6 1976 Jul 4	122.34±0.06 121.367±0.004 120.6589±0.0003 120.19±0.05	0.36±0.03 (19-55keV)				27±6	1.5-55	
Coe et al. (1981)	Ariel V	1977 Apr 11-15	118.725±0.005						2-16	
Maurer et al (1982)	NRL balloon	1977 Nov 24			46.1±0.2	2.9±0.1	0.22±0.008	32±3	20-250	1976 data was possibly source confused
Strickman et al. (1980)		1976 May 11 1977 Nov 24	241.0±1.0 234.9±0.4	0.36±0.07 0.29±0.05						
Doty et al. (1978)	HEAO-A4	1978 Apr 11	116.51							
Dennis et al. (1980a) Dennis et al. (1980b)	OSO-8	1978 Sep 2-25	114.26±0.01		3980±400	4.1±0.04	2.13±0.17	19±4	21-197	
Kendziorra et al. (1980)	AIT/MPI balloon	1978 Nov 22-23	227.5±0.5	0.52±0.08	7.6	2.6±0.2		41±8	18-130	
Ricketts et al. (1982)	Ariel VI	1979 July	112.076±0.003 109.668±0.003	0-0.75	-0.2	-1.0±0.15		<7	1-50	
White et al. (1983)	HEAO-1 HEAO-2	dates not specified	~115	2-7 keV 0.15 7-25 keV 0.23 25-60 keV 0.57	0.15	1.0	and E_c=10±2 E_f=45	**	2-60	

*Spectral equations are

A $E^{-\alpha}$

B $E^{-1.4}\exp(-E/kT)$

** A $E^{-\alpha}\exp[(E_c-E)/E_f]$

UNITS = photon $sec^{-1}cm^{-2}keV^{-1}$

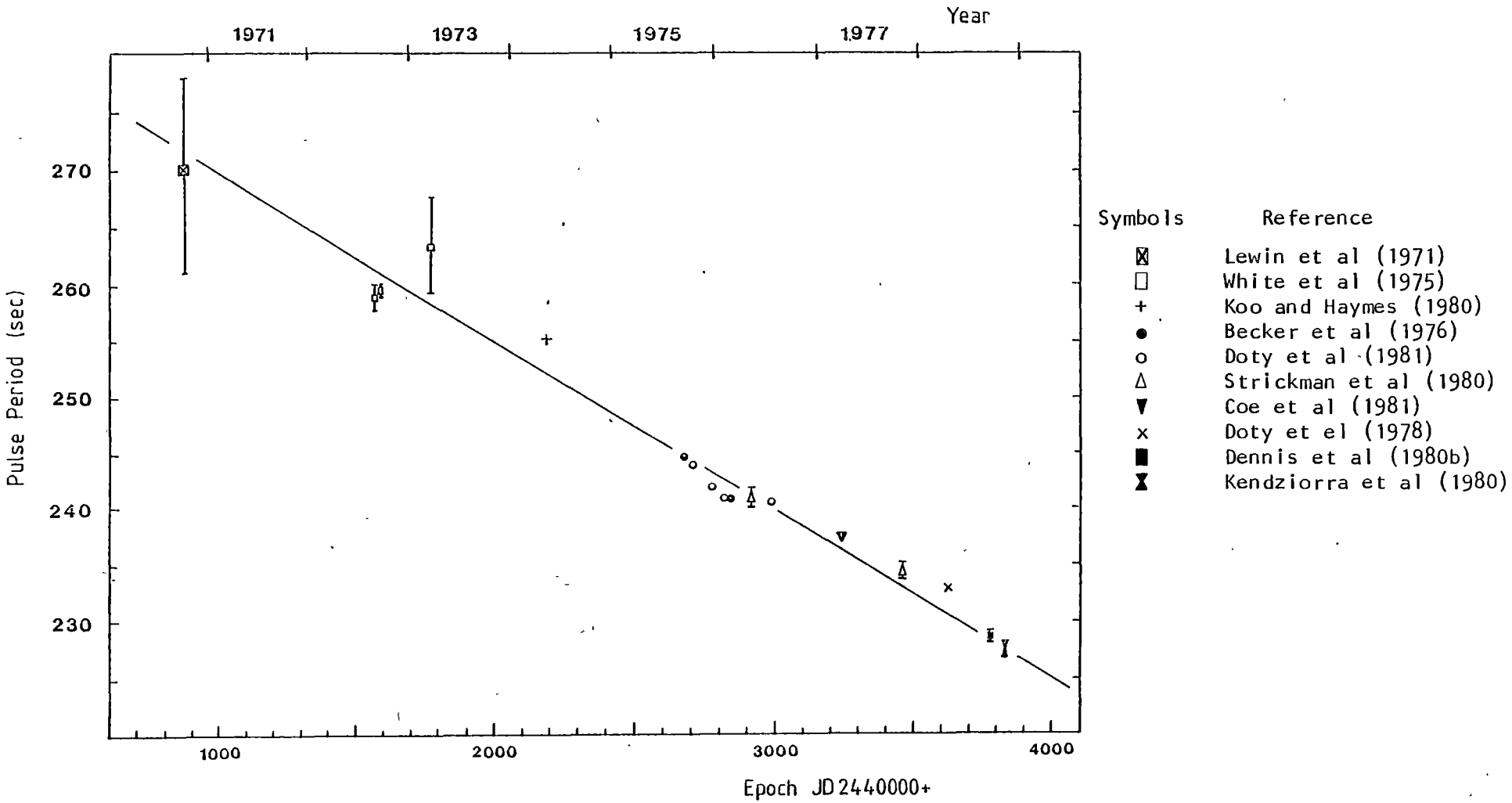

Figure 1.4 Pulsation period versus epoch for the pulsar GX1+4 and assuming the spin period is twice the observed fundamental period.

satellite data. A bright infrared source was found near the centre of the error box. Spectroscopy showed strong H_α emission with H_α/H_β intensity ratio ~55, indicating heavy reddening with A_V ~ 9 if normal nebular values are applicable. A finding chart of the optical candidate star GF is in Davidsen, Malina and Bowyer (1976) and in the SAS-3 galactic X-ray source position compilation (Doxsey et al., 1977).

A spectrophotometric study by Davidsen, Malina and Bowyer (1977) shows the optical counterpart is a symbiotic star consisting of an M6 giant and a variable blue continuum. They adopt an interstellar extinction of $A_V \simeq 5.1$ and deduce the intrinsic H_α/H_β ratio is ~20 and distance ~10 kpc. To explain the large Balmer line ratios, they suggest the presence of an optically thick envelope of radius 6×10^{13}cm at a temperature $1\text{-}2 \times 10^4$K and electron density $n_e \sim 10^9 cm^{-3}$. The observed X-ray column density of $4 - 10 \times 10^{22} cm^{-2}$ (White et al., 1976) is consistent with this suggestion.

A search for optical pulsations at H_α by Krzeminski and Priedhorsky (1978) at the X-ray pulsation period yielded a 3σ upper limit of 1.7% assuming a sinusoidal pulse shape or 0.7% assuming an X-ray pulse shape. From the Davidsen, Malina and Bowyer (1977) gas cloud model, the expected escape time for an H_α photon is $\sim 2 \times 10^5$sec or 10^3 longer than the pulse period. Any initial pulsation would be suppressed by a factor ~1000 and the upper limit does not contradict this model.

Long term infrared monitoring by Glass (1979) showed no significant changes. The mean magnitude and colours are K = 8.05, J-H = 1.52, H-K = 0.76 and K-L = 0.7. Radio observations by Duldig et al. (1979) during 1978 gave an upper limit of 5 mJy at 2 cm. They quote an upper limit of 15 mJy at 5000 MHz from A. Wright. Both are 1σ limits.

No doppler shifts or eclipses have been detected. The SAS-3 observations are compatible with an orbital period >10 days. If the companion star is a M6III star as proposed by Davidsen, Malina and

Bowyer (1977) then an orbital period >20 days is required. If there is a stellar wind of velocity ~10 km sec^{-1}, then the mass loss rate is $10^{-6} M_{\odot} yr^{-1}$ which is quite adequate to power the X-ray source via a stellar wind. Orbital separations as large as the cloud could be possible implying orbital periods of the order of years.

Bahtt (1982) has studied the pulse-period distribution of 17 X-ray pulsars. The pulsars tend to be either in the range 1 to 10 sec and 100 to 1000 sec but not in the decade 10 - 100 sec. He claims the gap is real and that for periods <10 sec mass accretion is driven by Roche Lobe mass transfer whilst for periods >100 sec, it is via stellar winds. This would imply that GX1+4 is driven by stellar winds. However Wang (1981) has made a detailed study of the exchange of angular momentum in massive X-ray binaries and has applied his models to GX1+4. He concludes that an analysis of the SAS-3 spin up data (Doty et al., 1981) is consistent with accretion from a disc.

1.8.2 Galactic Bulge Sources

The galactic bulge sources (Lewin and Joss, 1981) are a large class of low mass objects for which, with few exceptions orbital effects such as eclipses and optical heating light curves have not been seen. It is thought that the accretion discs are so thick that they shield the companion star from X-rays; hence only systems with low inclination angles are visible in X-rays (Milgrom, 1978). Typical luminosities are in excess of 10^{34} erg sec^{-1} and the ratio of X-ray to optical luminosities L_x/L_{opt} range from 10^2 to 10^4. The optical counterparts are generally faint (M_V ~ +2) and show no normal stellar absorption features. The class includes bursters, Sco-like objects, globular cluster sources and the low mass pulsars, e.g. Her X-1.

It is generally believed that they are neutron stars in low mass close binary systems with orbital periods less than a day and companion masses of the order 0.5 $M_{\odot}$. The faintness of the optical counterparts

rule out early-type main sequence companions which in turn requires small orbital periods in order to power the X-ray source via Roche Lobe overflow. The UV excess often seen is from reprocessing of the X-ray flux and not from the intrinsic luminosity of the companion.

The history of these systems is uncertain but one possibility is evolution from cataclysmic variables. The white dwarf degenerate accretes matter until its mass exceeds the Chandrasekhar limit (1.4 $M_\odot$) and becomes a neutron star. In the case of the globular cluster sources, where stellar space densities are much higher, the systems may have formed by capture.

Approximately 30 burst sources are known (Lewin and Joss, 1981). These can be divided into type I and type II depending on the characteristics of the burst. In type I sources, the bursts are consistent with thermonuclear flashes with temperatures of 1-2 keV on the surface of neutron stars. The mean derived blackbody radius is ~9 km if the source distance is ~9 kpc. Burst intervals can be of the order of hours or longer. Only one type II is known, the rapid burster, with burst intervals of seconds. The mechanism is considered to be instabilities in the accretion flow onto a neutron star. No bursts have been detected above 20 keV, consistent with the low blackbody temperature.

Objects that are of particular interest for hard X-ray observations are Sco X-1, 4U1626-67, GX339-4 and 4U1915-05. The question of the existence of a hard tail in the energy spectrum of Sco X-1-like sources (Greenhill et al., 1979b) is still not resolved, and more spectral measurements above 50 keV are required. The pulsar X Per has a hard tail above 30 keV superposed on a thermal spectrum (kT ~ 7 keV) (Worral et al., 1981). It will be interesting to compare them if Sco X-1 proves to have a hard X-ray excess. The 7.7 sec pulsar 4U1626-67 is in a ~2500 sec orbit about a 0.5 $M_\odot$ companion (Middleditch et al., 1981). It has highly phase-dependent spectra

above 15 keV (Pravdo et al., 1979) perhaps indicative of cylcotron absorption or emission. Measurements above 30 keV are required to test for this. The temporal characteristics of GX339-4 (Samini et al., 1979) between 1 and 20 keV make it a black hole candidate. High energy observations of Cyg X-1 (Nolan et al., 1981) reveal a spectrum that is consistent with a Comptonized spectrum expected from disk accretion onto black holes. Similar observations of GX339-4 are needed.

The 14th magnitude emission line object SS433 shows enormous Doppler shifts ($0.85 < 1 + Z < 1.2$) with a periodicity of 164 days. Models include relativistic beaming of plasma from double jets either formed perpendicular to an accretion disc or from the magnetic poles of a degenerate star, which precesses at a period of 164 days (for conference proceedings see Shaham, 1981).

SS433 has been studied up to 30 keV with Ariel VI (Ricketts et al., 1981) and HEAO-1 (Marshall et al., 1979a). The HEAO data can be described equally well by a power law ($\alpha = 2.1$) or a thermal bremsstrahlung spectrum ($kT = 14.3$ keV). The Ariel VI data indicate spectral hardening, and hard X-ray observations are necessary to determine the true spectral form, and hence the physics of the generating region.

1.8.3 Cataclysmic Variables

The understanding of galactic X-ray sources has increased dramatically with the data gleaned from the Einstein Observatory. One particular field which has benefitted enormously is the study of cataclysmic variables (CV). Prior to the Einstein era only 9 had been optically identified with X-ray sources; the polars AM Her (for review see Chiappetti et al., 1980), 2A0311-227 (Griffiths et al., 1979), AN Ursae Majoris (Hearn and Marshall, 1979), the dwarf novae SS Cyg during outburst (Rappaport et al., 1974), U Gem (Mason et al., 1978), EX Hya (Córdova and Riegler, 1979), AY Lyr (Córdova and Garmire, 1979), the old

nova GK Per during a minor outburst (King et al., 1979) and the novalike MV Lyr (Mason et al., 1979). The total X-ray detections are now ~55 with all classes of CV's being represented. The majority were detected in the surveys by Ariel V (Watson et al., 1978), HEAO-1 (Córdova et al., 1981b) and Einstein (Córdova et al., 1981a, Becker and Marshall, 1981 and Becker, 1981). Typical X-ray luminosities are from 10^{31} to 10^{33} erg sec^{-1}.

The closest CV is only 75 pc distant implying space densities of one per 3 x 10^{6} pc^{-3} or a galactic population of ~10^{6}. This can be compared to the galactic population of the luminous neutron star sources of ~100.

In the general model of CV's, a white dwarf orbits about a late type red dwarf with a period of 2 to 10 hours. The companion is generally on or near the zero age main sequence line and fills its Roche Lobe, permitting accretion onto the white dwarf. There are exceptions. The orbital period of GK Per is 1.9^{d} (Bianchini et al., 1981) requiring the secondary to be evolved. In this case, it is a K subgiant. TCrB is the largest period CV with an orbital period of 227.5^{d} and its companion is an M giant (see review by Robinson, 1976). In all, except the AM Her class, an accretion disc is formed and where the instreaming matter strikes this disc, a hot spot may form. With variable accretion rates this spot may move due to changing pressures.

Rapid random optical variations on timescales of tens of seconds, called flickering, is seen in most CV's, and is either from the hot spot or white dwarf.

The optical spectral energy distributions of CV's vary considerably from object to object as shown in the survey of Oke and Wade (1982). The distribution is composed of several components: a red component from the companion and blue from the white dwarf, the accretion column and/or the accretion disc and a hot spot if it exists. The H lines

can appear in emission or if the line of sight from the source is optically thick, in absorption. H lines in absorption can be seen for example in the spectra of dwarf novae in outburst.

Of the ~20 cataclysmic variables that have been detected with X-ray spectral temperatures, kT ≥ 5 keV (see, e.g. Córdova et al., 1981a), only the polars AM Her (Staubert et al., 1978, Rothschild et al., 1981) and 2A0311-227 (White, 1981) have been studied above 20 keV. Models by Kylafis and Lamb (1979, 1982), Imamura and Durisen (1982) and Wada et al. (1980) indicate the effects of magnetic fields on the observed spectra and observations are required for objects with fields $\leq 10^6$G. One possible candidate is 2A0526-328, which has a thermal bremsstrahlung spectrum with kT ~ 20 keV (Chapter 6).

There exist several classes of CV's. A summary is presented of the major classes with emphasis on the intermediate polars.

1.8.3.1 Novae Systems

Included in this class, characterised by outbursts, are the classical nova, the recurrent nova and the dwarf nova. Table 1.3 lists the observed properties of burst amplitude, energy, duration and recurrence interval. (See also review by Payne-Gaposchkin, 1977.) The classical example of a nova is DQ Her which erupted in 1934. TCrB is a recurrent nova whilst SS Cyg is the best known dwarf nova. The novae and recurrent novae outbursts are considered to be caused by unstable thermonuclear burning of hydrogen accumulated from accretion onto the surface of the white dwarf. The origin of the outbursts from the dwarf novae are instabilities in the accretion rate from the companion. The increased accretion leads to an increase in the size and luminosity of the disc. Bath and Pringle (1981) have studied the time evolution of model discs and can generate the observed properties provided the disc has a high viscosity.

TABLE 1.3

Characteristics of Novae-related systems

	outburst amplitude	duration	interval	energy (erg)
classical novae	9 - 14^m	months	10^4 - 10^5 yr	10^{45}
recurrent novae	7 - 9	months	10 - 100 yr	10^{45}
dwarf novae	2 - 6	days	10 day - 30 yr	10^{38} - 10^{39}

Considerable studies have been carried out on the nature of the outbursts of dwarf novae. For example: observations of rapid oscillations during eruptions by Patterson (1981) and Middleditch and Córdova (1982), broad band spectrophotometry from UV to near IR (Bath et al., 1980) and UV observations at outburst (Szkody, 1981). The rapid oscillations have periods between 10 and 30 sec and are thought to originate from non-radial oscillations of the white dwarf or the disc.

The spectra from UV to IR are generally consistent with accretion disc models, but the continua show a wide diversity of spectral shapes. Some do not seem compatible with steady state disc spectra (Szkody, 1981).

1.8.3.2 Nova-like objects

The Nova-like objects are systems which appear similar to novae from their spectra but have not been observed in outburst. The class can be split into four groups dependent on the influence of the white dwarf magnetic field on the observed properties. The magnetic fields in the AM Her objects are sufficiently strong to synchronise the white dwarf rotation to the orbital period by interaction of the field with the companion. At the other end is the disc stars, the UX UMa class where no effects from a magentic field have been detected. In between there are the intermediate polars and DQ Her types.

1.8.3.2 (a) AM Her stars

Ten AM Her stars are now known. The orbital periods range from 81 min for 2A0311-227 to 3.1 hr for AM Her (Chiapetti et al., 1980). As a class, they have the shortest periods of the CV's. They all exhibit optical and IR circular and linear polarization variations at the orbital period of the system. Typical values of polarization are 10%, with AN Ursae Majoris exceeding 35%. The source of the polarization is cyclotron radiation near the white dwarf surface from fields of $1 - 3 \times 10^7$ gauss. Little or no accretion disc can form in these systems and the bulk of the radiation is from the accretion columns. They have "low" and "high" states on timescales of months. During one such "low" state of AM Her, observation of Zeeman splitting enabled direct measurement of the field strength to be 2×10^7 gauss (Latham et al., 1981). Temporal structure as short as 2 seconds has been detected in the optical from H1405-451, and AN UMa but not AM Her (Middleditch, 1982). Quasi periodic oscillations of ~360 seconds have been seen in X-ray and optical studies of 2A0311-227 (Motch et al., 1982, Patterson et al., 1981). The source of the oscillations is not certain. Five possible explanations have been proposed by Patterson et al. (1981).

The X-ray spectrum of AM Her (Rothschild et al., 1981) is composed of two distinct parts, a soft X-ray blackbody (kT ~ 40 eV) component and a hard X-ray thermal bremsstrahlung (kT > 10 keV) component. The blackbody luminosity is larger than that of the bremsstrahlung component whereas in most CV's, the hard flux exceeds the soft. The blackbody component is considered to arise from heating of the surface of the white dwarf by the interception of half of the hard X-ray flux. Iron line emission is seen at ~7 keV.

Various attempts have been made to construct a consistent model of AM Her. (References in Chiappetti et al., 1980). The blackbody flux, from the white dwarf, should be comparable with the sum of the

cyclotron (i.e. optical) and bremsstrahlung (hard X-ray) fluxes but it exceeds the sum by at least a factor of five. Other sources of the soft X-ray component have been considered such as hot plasma clouds but none are consistent with the observed blackbody shape. Twin pole models and single pole models have been proposed to explain the light curves but none are completely satisfactory.

1.8.3.2 (b) Intermediate Polars

Intermediate polar is a term devised by Warner (1982) to name a class of objects where coherent pulsations of the order 100 sec are seen. The magnetic fields are sufficiently strong to have accretion columns with pulsed optical and X-ray emission but not enough to synchronise the white dwarf rotation as in the AM Her binaries. In the recent review by Warner (1982), he mentions two possible evolutionary histories. The magnetic field may be decaying and accretion torques may break synchronism. Alternatively, the system may be young and not yet have had time to achieve synchronism.

The relationship between the orbital period P_{ORB}, the white dwarf period $P_{WD.}$ and the beat period P_{BEAT} from reprocessing of the X-rays from the white dwarf is

$$P_{ORB}^{-1} = P_{WD}^{-1} - P_{BEAT}^{-1} \qquad (1.5)$$

Five intermediate polars are known H2252-035, H2215-086, V1223 Sgr, 3A0709+103 and 2A0526-328. All have been X-ray selected from precise positions from HEAO-1 and HEAO-2. All have periods longer than the AM Her class implying wider separation of the components. The lack of synchronisation is a possible result of the larger orbit since fields greater than for the AM Her types would be required for synchronisation. As the system evolves, the orbital period may decrease leading to an AM Her type. H2252-035 is regarded as the prototype of this class. It has a 3.59 hr photometric and spectroscopic period and two shorter optical periods of 14.3 and 13.4 min (Patterson and Price, 1981,

Warner et al., 1981). Modulation at the 13.4 min period has also been seen in the X-ray band (White and Marshall, 1981). The 13.4 min period is believed to be the rotational period of the white dwarf and the 14.3 min period results from the beating of the rotation period with the orbital period. The modulation arises from either the companion's X-ray heated atmosphere (Motch and Pakull, 1981; Wickramsinghe, Stobie and Bessell, 1982) or reprocessing from the disc and hot spot region. (Hassall et al., 1981). Motch and Pakull (1981) found the 13.4 min period was antiphased with the 14.3 min period at maximum light of the orbital period. This is consistent with the interpretation that the 13.4 min period arises directly from the X-ray beam. The optical spectrum of the 13.4 min pulsations is similar to the Rayleigh-Jeans tail of a hot blackbody and arises from direct X-ray heating of either the white dwarf or the inner regions of the accretion disc.

All the optical spectra of intermediate polars show strong emission lines of H, HeI and HeII superposed on a blue continuum which in general is described by the steady state disc spectrum of $F_\lambda \propto \lambda^{-2.3}$. H2252-035 is best described by a disc spectrum plus a blackbody of 12,000 K possibly from the hotspot. All the UV spectra show strong CIV emission and CII, SiIV and NV emission lines. The lines are generally broad (FWZI ~ 1000 km sec^{-1}).

The X-ray spectra of all five objects are hard (kT > 10 keV) with no evidence of a strong soft X-ray flux as seen in AM Her. Due to the recent discovery of these systems, little temporal X-ray data has been obtained. The only other object in which periodic X-ray modulation has been detected is 3A0729+103. The X-ray period has only been crudely determined. It lies between 900 and 1000 sec (McHardy et al., 1982); similar to the optical period of 913 sec. The expected beat period is 846 or 911 sec. Further X-ray data will be required to relate the 913 sec pulsations to either rotation or reprocessing origins. A HEAO-2 IPC

light curve of V1223 Sgr covering ~4 periods of the 794 sec pulsations revealed no X-ray pulsations at or near this period with an upper limit of ~20% (Steiner et al., 1981).

Two optical periods other than the orbital period have been detected in H2215-086 (Shafter and Targan, 1982; Warner, 1982). The dominant pulsation period is 20.9 min with a low amplitude 22.9 min period present from the beating with the 4.03 hour orbital period. If H2215-086 is similar to H2252-035, the 20.9 min pulsation is from reprocessing near the secondary but the orbit would need to be retrograde. For the orbit to be prograde, the 20.9 min pulsation must arise from the inner region of the disc and the 22.9 min pulsations from the secondary. All three periods (orbital, beat and rotation) have been detected in 2A0526-328, at approximately the same magnitude (Motch, 1981). Two models have been proposed. Hutchings et al. (1981) relate the 5.4864 hr period as the orbital period, the 5.19 hr period as the rotation period of the white dwarf and the 4.024 day period as the beat period. The alternative model of Watts et al. (1982) discussed in Chapter 7 requires the 4 day period to be the orbital period and the 5.4864 hr period to be the rotation period of the white dwarf. The orbit is required to be retrograde, to generate the 5.19 hr beat period.

Whilst the previous discussion has assumed the degenerate is a white dwarf, there is no explicit reason why the degenerate could not be a neutron star. The X-ray to optical flux ratio of ~1 for most CV's is generally considered to be an indicator of a white dwarf. However in the case of H2252-035, White and Marshall (1981) show reprocessing effects can reduce the X-ray to optical flux ratio from ~300 expected for a neutron star to near 1. Information on the spin up rate may be used to distinguish the nature of the degenerate. The theoretical spin up rate for a neutron star is $\dot{P}/P \sim -1.5 \times 10^{-5}$ whilst for white dwarfs it is $\sim -1.1 \times 10^{-7}$ (Warner, 1982). An upper limit for V1223 Sgr is $\sim -9 \times 10^{-6}$ which is not

yet sufficiently restrictive to exclude a neutron star.

Polarization has not been detected in any of the intermediate polars. Upper limits for circular polarization quoted by Warner (1982) are 0.07% in 2A0526-328 and H2252-035 and an upper limit of 0.2% for modulated linear polarization in H2252-035.

Several other systems are possible intermediate polars. TT Ari has a spectroscopic period of 0.13755^{d} (Cowley et al., 1975) which differs from the photometric period of 0.1327^{d} (Smak and Stępien, 1975) implying a beat period of 3.4 ± 0.4^{d}. The optical spectrum differs from the spectrum of intermediate polars because it shows broad absorption lines characteristic of optically thick accretion discs. The UV, X-ray and optical light curves which vary in a similar manner are all consistent with the intermediate polar model and not with emission from a hot spot. (Jameson et al., 1982 and references therein). EX Hya and V2051 Oph are very similar objects. The 98 min orbital period of EX Hya is established from eclipses and radial velocity studies whilst a 67 min period is seen optically and at X-ray energies (Warner, 1982). No beat periods are seen. The source of the optical 67 min pulsations is the inner edge of the accretion disc and the disc is sufficiently thick to prevent any significant X-ray flux to be reprocessed by the secondary. The 67 min period is changing at a rate of $\dot{P}/P \approx -3.6 \times 10^{-7}$ which is consistent with a white dwarf as the degenerate.

The following two sections are devoted to detailed reviews of 2A0526-328 and V1223 Sgr.

1.8.3.2 (b)i <u>2A0526-328</u>

The optical counterpart of the high galactic latitude X-ray object 2A0526-328 (TV Col) is now recognised to be a cataclysmic variable because of its broad emission lines of HeI, HeII and the Balmer series superposed on a flat continuum. Observations by Warner (1980a) showed rapid brightness variations typical of a cataclysmic variable. Charles et al. (1979),

who first identified the optical candidate, suggested it to be either nova-like (UX Ursae Majoris type) or a recurrent nova that has not erupted in recent times.

The optical spectrum of 2A0526-328 is very similar to the spectra of the AM Her class of polars. The magnetic field, however, is expected to be weaker than in AM Her since Tapia (see Charles et al., 1979) reports an upper limit of 0.5% for both optical linear and circular polarization. Stockman et al. (1982) (quoted in Warner, 1982) set a more stringent upper limit of 0.07% for circular polarization.

Motch (1981) gives a detailed study of colour and brightness variations as a function of his proposed orbital period of 0.21631^{d} and concludes that an accretion disc and hot spot are major contributors to the optical luminosity of the system. The B and V variations for the 0.22^{d} period are ~0.27 mag full amplitude whilst at U, it is ~0.22 mag. Brightness variations with a 4 day period are also seen but there is no correlated flickering or colour variations. Average flux changes are 0.33 mag. The phase of the minimum and maximum of the 0.22^{d} period are dependent on the phase of the 4 day period (Figure 1.5 from Figure 1 of Motch, 1981). Motch interpreted this behaviour as movements of the hot spot due to changes in the accretion rate and hence luminosity of the system.

UV observations, using IUE, have been reported by Coe and Wickramasinghe (1981), Mouchet et al. (1981) and Mouchet (1982). Coe and Wickramasinghe (1981) show that the UV spectrum is very similar to that of SS Cygni, where the UV is believed to arise in an optically thick blackbody disc rather than an accretion column. They also reported P Cygni profiles for the strong UV emission lines of CIV λ1550 and possibly SIV λ1400. The P Cygni profile is possibly present in the spectra of Mouchet et al. (1981).

The continuum from the optical to UV has not been uniquely defined

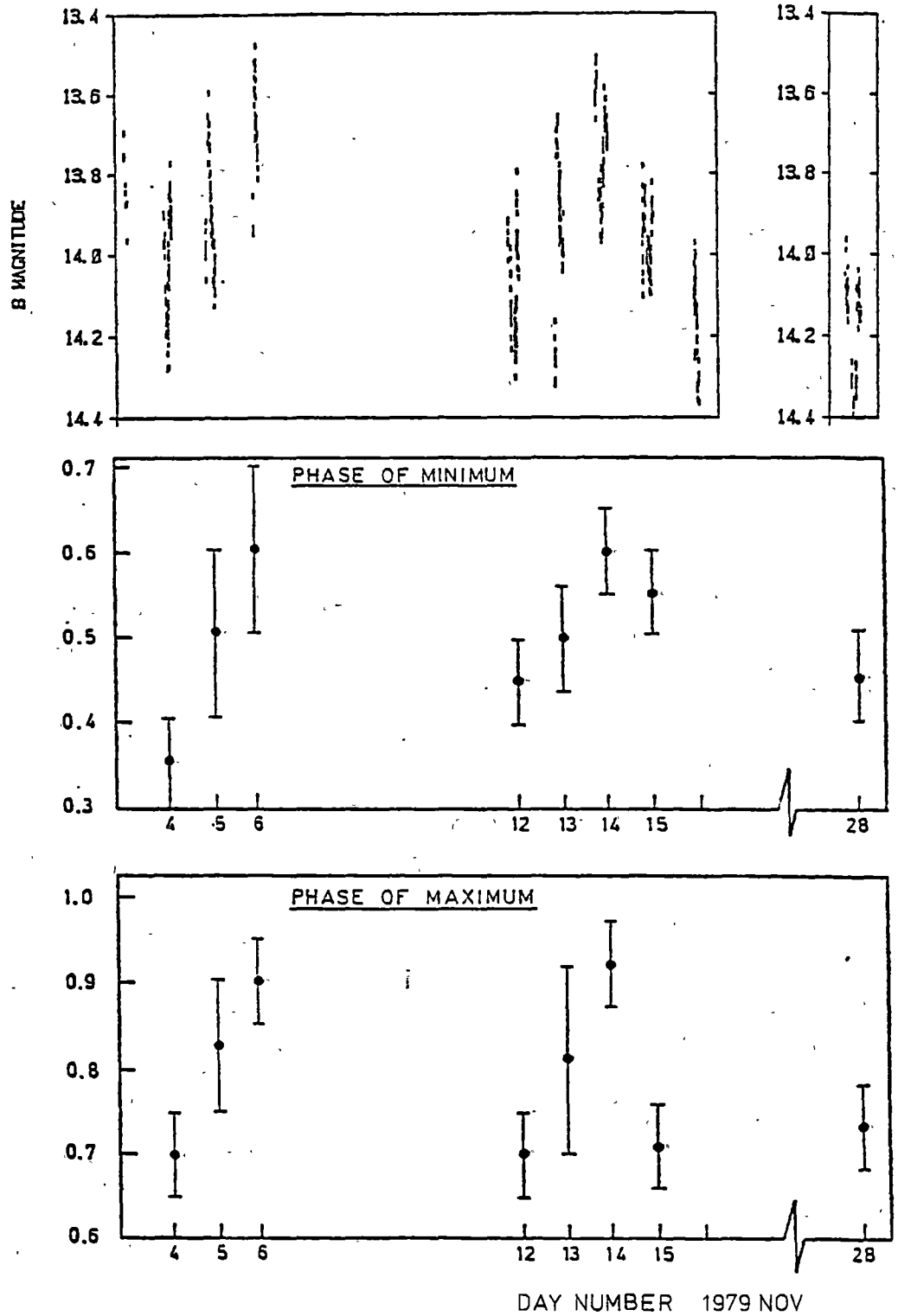

Figure 1.5 Photometry from 1979 Nov of 2A0526-328 from Motch(1981). Upper curve is B magnitude versus day of 1979 Nov whilst middle and lower curves represent the phase shift of the minima and maxima of the 5.19 hour photometric period.

due to the lack of concurrent data and large variability. Coe and Wickramasinghe (1981) fit the UV with a blackbody spectrum with a temperature of (2.25 ± 0.1) x 10^4K. They find $\alpha = 2.3$ (from $f_\lambda \propto \lambda^{-\alpha}$) expected from optically thick accretion discs is not an unacceptable fit. Mouchet et al. (1981) have fitted a variety of models to their UV data and find a superposition of a standard disc model with $\alpha = 2.3$ plus a blackbody component with a temperature 9300 ± 700 K gives a good description of the UV plus the mean UBV data from Motch (1981). Simultaneous data extending to the infrared would be required to test this. Mouchet (1982) has fitted steady state accretion disc models to three intermediate polars. In the case of 2A0526-328, the disc parameters are inner disc radius 1.2 x 10^9cm, outer disc radius 5.5 x 10^{10}cm, an accretion rate of 1.5 x $10^{-7} M_\odot yr^{-1}$ and a distance of $3650/\sqrt{\cos i}$ pc. The distance is unacceptably large for two reasons. The X-ray flux would be ~100 times the mean flux of cataclysmic variables and comparable to the luminosities of the bulge sources. Second, it would place it well above the plane of the galaxy at >1.8 kpc since its galactic latitude is -30°. A possible reason for the unacceptable fit is the presence of non disc spectral components such as cyclotron radiation from the accretion column. Spectroscopic studies by Hutchings et al. (1981), and using data from Watts et al. (1980) and Motch (1981) revealed three periods, a spectroscopic period of 0.228600^d, a photometric period of 0.21631^d, and a longer photometric period of 4.024^d. The ephemerides are listed in Table 2 of Hutchings et al. (1981) and are reproduced in Table 1.4.

The 4 day period is the beat period between the shorter periods. They discuss the system in terms of a near synchronously rotating white dwarf (rotation period 0.21631^d) in a 0.228600^d orbit about a late type main sequence companion. The 4 day light variation arises from the rotation of the white dwarf once within the system in a prograde

TABLE 1.4

Periods of 2A0526-328

	T_0 JD 2440000+*	Period (days)*	T_0
Radial Velocity	4227.631(2)	0.228600(5)	Balmer max velocity
Short light curve	4171.46(1)	0.31631(1)	maximum light
Long light curve	4191.5(3)	4.024(4)	maximum light

*Numbers in parentheses are errors in units of least significant figure.

direction. They found variations in the orbital solutions between the mean of the H lines and the He lines. For the H lines, V = 49 ± 6 km sec^{-1} and K = 116 ± 8 km sec^{-1} and phase by definition at the positive zero crossover. The HeI lines are similar with K = 103 ± 10 km sec^{-1} and phase at 0.966 ± 0.02 but V_0 = 91 ± 7 km sec^{-1} is markedly different. The HeII λ4686 peaks yield V_0 = 46 ± 15 km sec^{-1} and K = 276 ± 19 km sec^{-1} with phase zero at 0.285. The HeII emission is consistent with a hot spot on the trailing edge of the accretion disc if we associate the H lines with the disc. The large difference between V_0 for HeI and the H lines is not readily explained in this model nor is the large difference of V_0 for HeII λ4686 at different phases of the 4 day period. At maximum light V_0 = 73 ± 15 km sec^{-1} whilst at the 4 day minimum it is -2 ± 24 km sec^{-1}. Mouchet (1982) folded the fluxes at 1770 Å and 2700 Å from the IUE UV spectra at the 3 periods using the ephemerides of Hutchings et al. (1981). No regular variation was found at the two photometric periods but there was with the spectroscopic period (Figure 1.6 from Figure 2 of Mouchet, 1982).

X-ray observations of 2A0526-328 have been made by Ariel V, HEAO-1 and HEAO-2 (Chapter 6). The mean X-ray flux from the Ariel V data is 4.9 x 10^{-11} erg cm^{-2} sec^{-1} keV^{-1} corresponding to a flux of 3 x 10^{32} $(D/100)^2$ erg sec^{-1} where D is the distance in pc. A complete

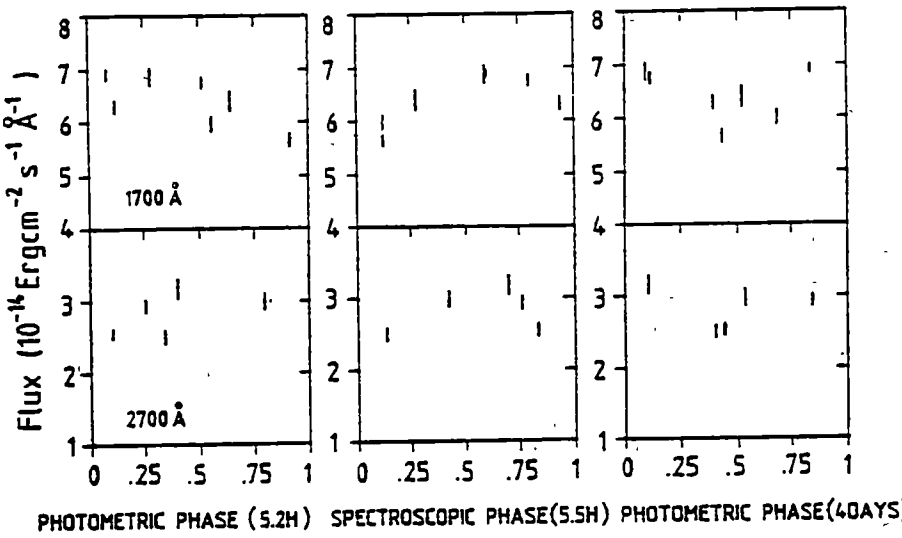

Figure 1.6 UV fluxes of 2A0526-328 at two wavelengths of 1770A and 2700A versus the phases of the three optical periods (from Mouchet 1982).

list of X-ray data including details of the HEAO-2 observations are given in Table 6.8.

The long term optical behaviour is unknown. Szkody and Mateo (1982) detected a flare from 2A0526-328 on 1982 November 22 during simultaneous IUE spectroscopy and optical photometry. The average magnitude rise was ~1.5 in 43 minutes followed by a 0.7 mag decrease over 2 hr.

1.8.3.2 (b)ii V1223 Sgr

Improved positional information on the X-ray source 4U1849-31 by HEAO-1 and HEAO-2 has shown the optical candidate to be the 13th magnitude cataclysmic variable V1223 Sgr (Steiner et al., 1981), making it the fifth cataclysmic variable to be discovered from its X-ray emission. Photometry by Steiner et al. (1981) revealed the presence of a coherent 13.2 minute period with a semi amplitude of 15% and spectroscopy, with a resolution of 15 Å shows it is a typical cataclysmic variable with strong emission lines of H_α, H_β, H_γ, HeII λ4686 and the CIII/NIII blend at 4640 Å. Weak HeI at 5860 Å is present and possibly FeII λ5150. The continuum from 4200 to 6700 Å is blue and can be described by $f_\nu \propto \nu^{+0.4}$. Extensive photometry by Warner (1983

private communication) shows a modulation at a period of 0.140239^{d}. No other periods have been detected.

UV observations by Bonnet-Bidaud et al. (1982) using IUE show a spectrum consistent with that expected from an optically thick accretion disc. They derive a distance of 600 pc from the ultraviolet interstellar extinction of $E(B-V) = 0.150 \pm 0.005$. The derived disc parameters from Mouchet (1982) are: mass accretion rate $5.8 \times 10^{-9} M_{\odot} yr^{-1}$; inner disc radius 5×10^{8}cm; outer to inner disc radius ratio ~90 and distance $625/\sqrt{\cos i}$ pc. The parameters are derived assuming the total observed flux is from the disc. Since a magnetic field is required to produce the 13.2 min pulsations, Bonnet-Bidaud et al. (1982) predicted an upper limit of $B \leq 10^{7} - 10^{8}$ gauss. Cyclotron emission from the accretion column will appear in the EUV. This will reduce the UV flux required from the disc and a larger inner disc radius is permitted.

The X-ray luminosity is 4×10^{33}erg sec^{-1} (2 - 10 keV) if the source distance is 600 pc. The spectrum is hard (kT > 10 keV) with no indication of a soft component as seen in AM Her (Tuohy et al., 1978). Three local maxima separated by ~800 sec appear in the IPC light curve (Steiner et al., 1981). More extensive X-ray studies are required to establish any X-ray periodicities.

The long term optical variations of V1223 Sgr from archival plates have been studied by Belserene (1981). V1223 Sgr is generally in a high state, with five low states observed that are 2 magnitudes or more lower than the mean high state. During one 12 year period, V1223 Sgr showed irregular variability at intermediate magnitudes.

1.8.3.2. (c) DQ Her types

The prerequisite to membership of this related class to the intermediate polars is pulsations with periods less than 1 minute. A similar model to that for the intermediate polars is proposed for

this class (Warner, 1982 and references therein). Notable examples are the protype of the class, the nova remnant DQ Her and the nova-like AE Aqr. Pulsation periods are 71 sec and 33 sec respectively. AE Aqr has also been seen to pulse at X-ray wavelengths. The high stability of the period of these systems requires the degenerate to be a white dwarf. Circular polarization is detected in both DQ Her and AE Aqr at 0.6%. The eclipse-related phase shifts seen in DQ Her are satisfactorily explained in terms of beamed light from the white dwarf reflected off the accretion disc (Petterson, 1980).

1.8.3.2 (d) "Disc" Stars

The last class of nova-like are the UX UMa class of objects reviewed by Warner (1976a). Most UX UMa stars possess broad shallow hydrogen absorption lines from optically thick accretion discs. No evidence has yet been found for the presence of magnetic fields. It is possible that fields exist but are too weak to appreciably influence the accretion disc. They provide the best laboratory for studies of discs and their structure, although simultaneous wide band observations are still needed. Even in this class, which is characterised by steady luminosities, unusual variability has been detected from UX UMa in the UV observations by Holm et al. (1982), and line profile changes in CD-42°14462 (Mayo et al., 1980). It is clear from this variability that further simultaneous observations at different bands are called for.

Several other problems exist which may be answered by study of the UX UMa class. The source of flickering is still not properly answered. In U Gem, this disappears during eclipse and is believed to be related to the hot spot on the disc. However, in AM Her it appears to be associated with the white dwarf. A particular question that can be answered by studying a variety of disc stars is the nature of the vertical Z structure of the disc. Mayo et al. (1980) have

constructed disc models with various disc thickness/radius ratios ranging from 0.01 to 0.05. The non-detection of X-ray flux from DQ Her is consistent with the idea that the disc is optically thick to X-rays, for inclination angles >85°. Combining X-ray and optical data, along with estimates of the system's inclination angle may allow an estimate of the height of the disc. The radius of the disc can be determined from procedures outlined by Sulkanen et al. (1981).

1.8.3.2 (d)i VY Scl

VY Sculptoris is a nova-like cataclysmic variables with a usual V magnitude of 13.2 which occasionally falls to ~17-18 mag (Warner, 1976a, 1980b). Observations by Burrell and Mould (1973) showed rapid flickering and an optical spectrum with strong emission lines of H, HeI and HeII. They detected oscillations at a period of 480 sec with an amplitude 0.01 - 0.02 mag. Warner and van Citters (1974) found no evidence for any periods at an upper limit 0.036 mag. Warner and van Citters interpret the 480 sec pulsations as the timescale of flares and not of any strictly periodic origin which are normally seen in dwarf novae at outburst. No other periods have been detected either by radial velocity studies or by photometry.

1.9 X-ray Detectors

There are four types of detectors that have been used for hard X-ray astronomy: the proportional counter, the scintillation detector, the gas scintillation detector, and the germanium detector. The most economical per unit area is the proportional counter detector. It is relatively uncomplicated, has modest resolution $E/\Delta E \sim 5 - 10$ and most importantly large areas can be easily constructed. Its big disadvantage is the low upper energy boundary that can be used. A 1 atm xenon detector is only useful up to 150 keV since at higher energies the probability of absorption becomes too small. Scintillation detectors have poorer resolution ($E/\Delta E \sim 2 - 3$) and are relatively expensive and

complex. Germanium detectors offer high resolution $E/\Delta E \sim 10\sqrt{E}$ but can only be constructed with small areas, are expensive and require croygenic cooling.

The University of Tasmania detector, outlined in Chapter 2 is a xenon-filled proportional counter detector. The following sections outline the process of detecting the X-rays and a mathematical representation of this process used in the spectral reduction procedures is discussed in Chapter 3.

1.9.1 Detection Theory of Proportional Counters

The interaction of X-rays with the counting gas xenon is a complex event with several means of ionising the gas. The dominant mechanism of photon interaction is the photoelectric effect. Another mechanism is Compton scattering but the probabilities of interaction are small at the energies being considered (<100 keV). The ratio of the mass attenuation coefficient for Compton versus photoelectric effect of photons in xenon between 20 and 100 keV varys from a minimum of 0.003 at 35 keV to 0.05 at 100 keV. We now consider only the photoelectric effect as an adequate description of the detection of X-rays.

Since xenon has a high atomic number (Z = 54), its principal absorption edge energies are also high and in the energy range being observed (15 - 100 keV). The K edge of xenon is at 34.56 keV and the mean energy of the three L edges is 5.1 keV. Following de-excitation from the photoelectric absorption event, the resulting fluorescence photon can in principle escape from the detector resulting in incomplete energy loss in the gas and consequent distortion of the pulse height distribution.

Since there are 3 sublevels of the L shell and 5 sublevels of the M shell, there are numerous de-excitation transitions that can be considered. Each transition can result in emission of a photon (fluorescence), with a probability known as the fluorescence yield,

or an electron (Auger effect). The K line transitions are listed in Table 1.5. The ratios of absorption by the K, L and M shells are respectively 0.86, 0.08 and 0.04 for an X-ray photon >34.56 keV and we can ignore all except K and L transitions in any spectral reduction analysis. Also listed in Table 1.5 is the relative probability of transition (Gorenstein et al., 1968).

TABLE 1.5

Name	Transition	Energy	Relative Transition Probability
K_{α_1}	$L_{III} \rightarrow K$	29.779	0.535
K_{α_2}	$L_{II} \rightarrow K$	29.459	0.267
K_{β_1}	$M_{I} \rightarrow K$	33.611	0.160
K_{β_2}	$N_{II} \rightarrow K$	34.446	0.037

In the Auger effect, after an X-ray photon has removed, say the K shell electron, then an electron from a higher level (e.g. L) fills this K vacancy. The fluoresence photon is immediately reabsorbed in the L shell. Consequently, the L shell electron is ejected as the Auger electron, leaving two L shell vacancies and a doubly charged atom. Typical ranges of electrons in one atmosphere of xenon range from 0.03 cm at 10 keV to 2.3 cm at 100 keV. (Evans, 1955). Hence very few of the Auger electrons escape the detecting medium and all the energy of the X-ray absorption event is deposited in the detector. The relative probabilities for fluorescence or the Auger effect are listed in Table 1.6 for the K and L shells (Bambynek et al., 1972), showing that fluorescence dominates above the K edge whilst nearly all interactions

TABLE 1.6

Shell	Fluorescence yield	Auger yield
K	0.894	0.106
L	0.103	0.897

below the K edge are by the Auger process. This means that the only significant source of photons that will escape the detector are from K transitions. The probability that a photon will leave the detector is counter geometry dependent and also dependent on gas pressure. It is only weakly dependent on the energy of the photon and in subsequent analysis it is assumed to be independent of energy. In 1 atm of xenon the radiation length of the K fluorescence photon is 18 cm which is comparable to the depth of the UT detector (21 cm). The escape peak ratio of a detector is an empirical measurement of this probability. It is defined by measuring the ratio of detected events at $(E_C - 30)$ keV to total events where E_C is the energy of a mono-energetic calibration source and provided $E_C >$ K edge. The escape peak ratio of the UT detector is ~0.51 (see Chapter 3) which means that ~57% of the fluorescence photons escape.

For every 1 keV deposited in the detector, ~37 electron-ion pairs are produced by ionization. The electron-ion pairs are accelerated to the anode and cathode respectively by the electric field in the detector and ionize further atoms in an avalanche effect, which produces a pulse proportional to the initial event. The gain may be between 10^3 and 10^5. Because the electron mobility is high, the electron pulse is collected at the anode in the order of 1 μsec whereas the positive ions drift to the cathode in a timescale of 10 to 100 μsec. The slow pulse is not measured because of the fast time constant of the anode amplifiers. Since the production process is statistical in nature, the final pulse

is distributed in a Poissonian distribution about its mean value. A mono-energetic source of X-rays will produce a gaussian pulse height distribution. If the X-rays have energies in excess of the K edge then a second gaussian peak occurs at a mean energy ~30 keV less than the first peak. The resolution of the detector is defined by the full width at half maximum (FWHM) divided by the energy of the peak and is proportional to the square root of the energy of the peak since the number of ion pairs produced by the X-ray photon is $\propto E$ and the standard deviation of this number is $\propto \sqrt{E}$.

1.9.2 Mathematical Description of Detector

The overall response of the proportional counter can be described by the following. Suppose $N(E, \gamma_1, \ldots, \gamma_j)$ is the photon differential spectrum as a function of energy (E) incident from a source at the top of the earth's atmosphere, and described by the parameters $\gamma_1, \ldots, \gamma_j$. Then the observed distribution as a function of pulse height E' observed from a balloon-borne proportional counter is given by (e.g. Stein and Lewin, 1967):

$$P(E')dE' = \int_0^\infty N(E,\gamma_1,\ldots,\gamma_j)T_A T_W (1 - T_G)[F_K R(E - E_K,E') + (1 - F_K)R(E,E')]dE\,dE'$$

$$= \int_0^\infty N(E,\gamma_1,\ldots,\gamma_j)Q(E,E')dE\,dE' \qquad (1.5)$$

where T_A, T_W, and T_G are the energy dependent transmission functions for the residual air in the line of sight, the counter window and the detection gas, respectively; F_K is the K shell fluorescence escape probability per detected photon for photon energies greater than the K-absorption edge of the detecting medium; R(E,E') is the Gaussian function given by

$$R(E,E') = \frac{1}{\sigma\sqrt{2\pi}} \exp\left[-\frac{(E-E')^2}{2\sigma^2}\right]$$

which describes the finite energy resolution of the detector by expressing the probability of an event of energy E being detected at

a pulse height E'; the standard deviation increases slowly with photon energy (as $\sqrt{E}$); E_K is the energy of the K fluorescence photon; Q(E,E') may be regarded as the total instrumental response function. Equation (1.5) simplifies the escape problem by treating the K_α and K_β resonances as one and by neglecting L fluorescence escape; however the resulting error is small.

The pulse height distribution P(E')dE' is sorted into a number of contiguous channels. The number of counts in the ith pulse height channel having boundaries (E'_i, E'_{i+1}) may be written as

$$C_i = \int_{E'_i}^{E'_{i+1}} P(E')dE' \quad , \quad i = 1,m \tag{1.6}$$

where m is the total number of channels.

CHAPTER 2

The UTIC Observatory and Ground Station

2.1 Introduction

The University of Tasmania/Imperial College, London (hereafter UTIC) platform was conceived as an economical means of flying large area X-ray detectors, for flight durations up to three days. The University of Tasmania (UT) proportional counter was initially designed and flown as a lightweight equatorially mounted telescope with the prime objective being temporal studies of X-ray sources. From this design concept, the UT detector evolved as a large area, one atmosphere pressure, xenon filled detector of relatively small depth (Greenhill et al., 1979c). It has been successfully flown twice in 1976 and 1978 (Duldig, 1981; Duldig et al., 1977; Greenhill et al., 1979d). During these flights, the viewing angle of FWHM 7° x 20° was defined by a pewter slat collimator. The pointing of the detector was not required to be accurate and typical azimuth pointing errors of 0.5° were acceptable. The disadvantage of a large viewing angle is source confusion especially for sources near the galactic plane. Observations of the galactic centre region in 1976 and the Circinus X-1 region in 1978 could only be crudely reduced due to the presence of many variable sources within the field of view near the targets. To eliminate these problems, the UTIC design required collimators of FWHM = 2° and hence, a considerable improvement to the pointing with maximum errors of the order 0.1°. Since equatorial mounts are unsuitable for accurate pointing due to balloon drift, the platform was changed to an alt-az configuration with an on-board microprocessor (μP) to control the pointing. A sun sensor was incorporated to provide an accurate platform azimuth and to check the pointing. Inclinometers measured the inclination of the platform relative to the two horizontal orthogonal axes.

2.2 The Platform

A schematic of the platform is shown in Figure 2.1. Principal features are marked and are discussed in further sections of this Chapter.

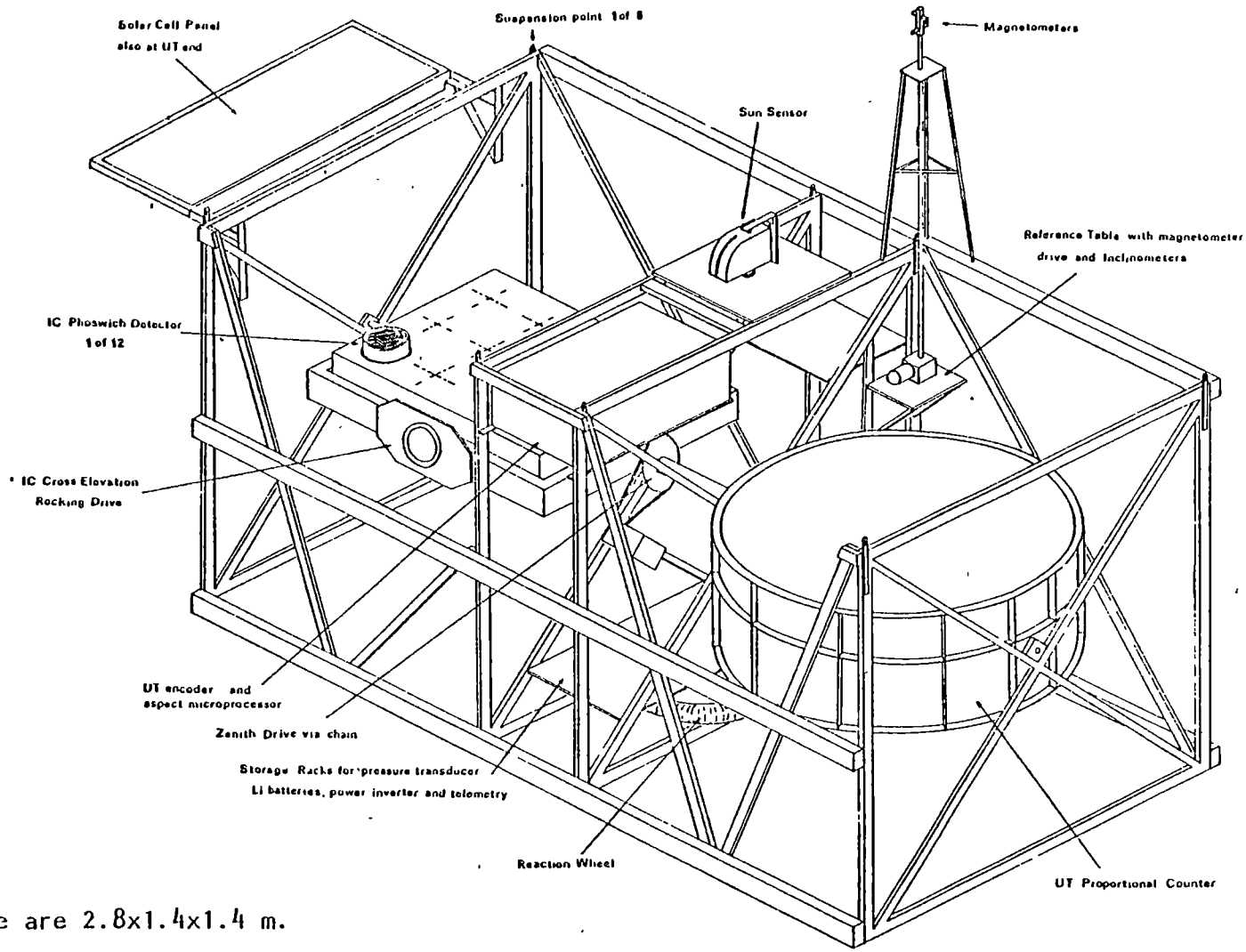

Figure 2.1

The UTIC platform.
Dimensions of the frame are 2.8x1.4x1.4 m.

Photographs of the platform during preflight tests at Alice Springs during November 1980 are shown in Figure 2.2. The thermal shield (see Section 2.10) surrounding the platform is not attached. The detectors are mounted on a common altitude shaft. The platform is stabilised relative to the local geomagnetic field using magnetometers, mounted well above any magnetic materials in the platform. A reaction wheel servo system mounted under the rotation axis of the platform maintains the reference magnetometer aligned to the earth's field lines. Changes in platform azimuth are obtained by rotating this magnetometer relative to the platform. The second magnetometer uniquely defines whether the reference magnetometer is pointing north or south. The magnetometer drive is mounted on a reference table. Optical flats glued to the top of the table are used as the absolute reference for levelling and alignment of the platform. Inclinometers, which can measure up to 10°, with an accuracy of $\sim 0.01^{\circ}$, are mounted under the table.

The structure of the platform, designed by M.W. Emery, is constructed from Al rectangular section. The four horizontal load bearing beams have dimensions of 5 cm x 8 cm. The central section, where the encoder, sun sensor, altitude drive and storage racks are located, is welded. The rest of the platform is bolted using high tensile steel bolts. Steel and brass plugs are located inside the tubing for location of these bolts. Flexure of the platform from a suspended state to resting on 4 jacks was less than 1mm over the length of the 2.8 metre load carrying beams, which is negligible with respect to the pointing requirements. Eight stainless steel plates, four on the inner section and four on the outer corners, are the anchor points for the suspension. Not shown in Figure 2.1 is the suspension bearing and torque relief motor to which the suspension cables are attached. To ensure the platform rotates freely and torque is not transmitted from the balloon to the payload, the torque relief motor "unsticks" the load carrying bearing using signals

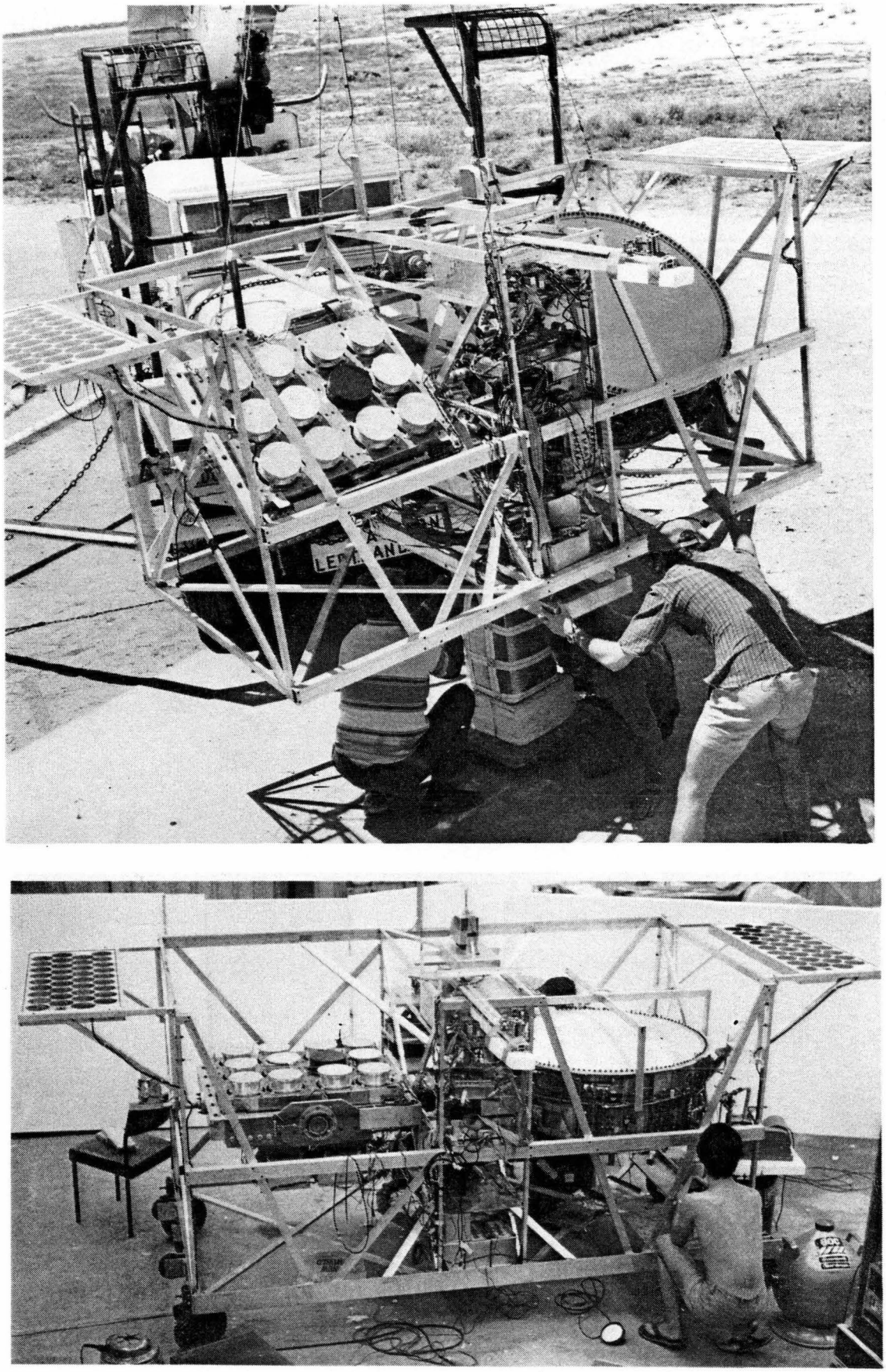

Figure 2.2 UTIC X-ray platform at Alice Springs, November 1980

derived from the magnetometers.

Ballast is usually carried and is suspended beneath the central section using the four outside corners of the central section for the suspension points. Total weight of the flight ready platform, excluding ballast, for the 1981 flight was 550 kg.

Solar cells are mounted at either end of the platform to supplement the power from Lithium batteries stored in the central section. A still frame camera was planned to be attached to the outside of the IC altitude shaft. It was designed for star photographs during the night for post flight determination of pointing errors. Unfortunately, it proved unreliable and was not used for the 1981 flight. However, the balloon flight did not extend into the night.

Two pressure transducers were carried. The low altitude transducer monitors the ascent and descent and covers the pressure range from 1000 mb to 10 mb with an error of ~1 mb. The high altitude transducer operates between 0 and 13 mb, with an accuracy of 0.06 mb.

2.3 The UT Proportional Counter

This is a multilayer, multianode proportional counter of wall-less construction with an effective sensitive area of ~5200 cm^2 and 21 cm active depth, filled with xenon at a pressure of one atm. It is contained in an aluminium pressure vessel of 1 metre diameter (Figure 2.3). The vessel is divided into two separate gas volumes by an 0.5 mm thick Al window. The top and bottom domed sections are filled with CH_4 and the top section contains the collimator (see Section 2.3.1). A tube links the two end sections. The middle section filled with xenon contains the detector itself. To quench the xenon , methane at 1% atmospheric pressure has been added. "O" rings seal the detector and collimator volume from gas loss or contamination from the exterior. Flexible windows composed of ten layers of mylar sheeting with a total thickness 0.134 gram/cm^2 seal the two ends of the detector. The design and construction of the detector

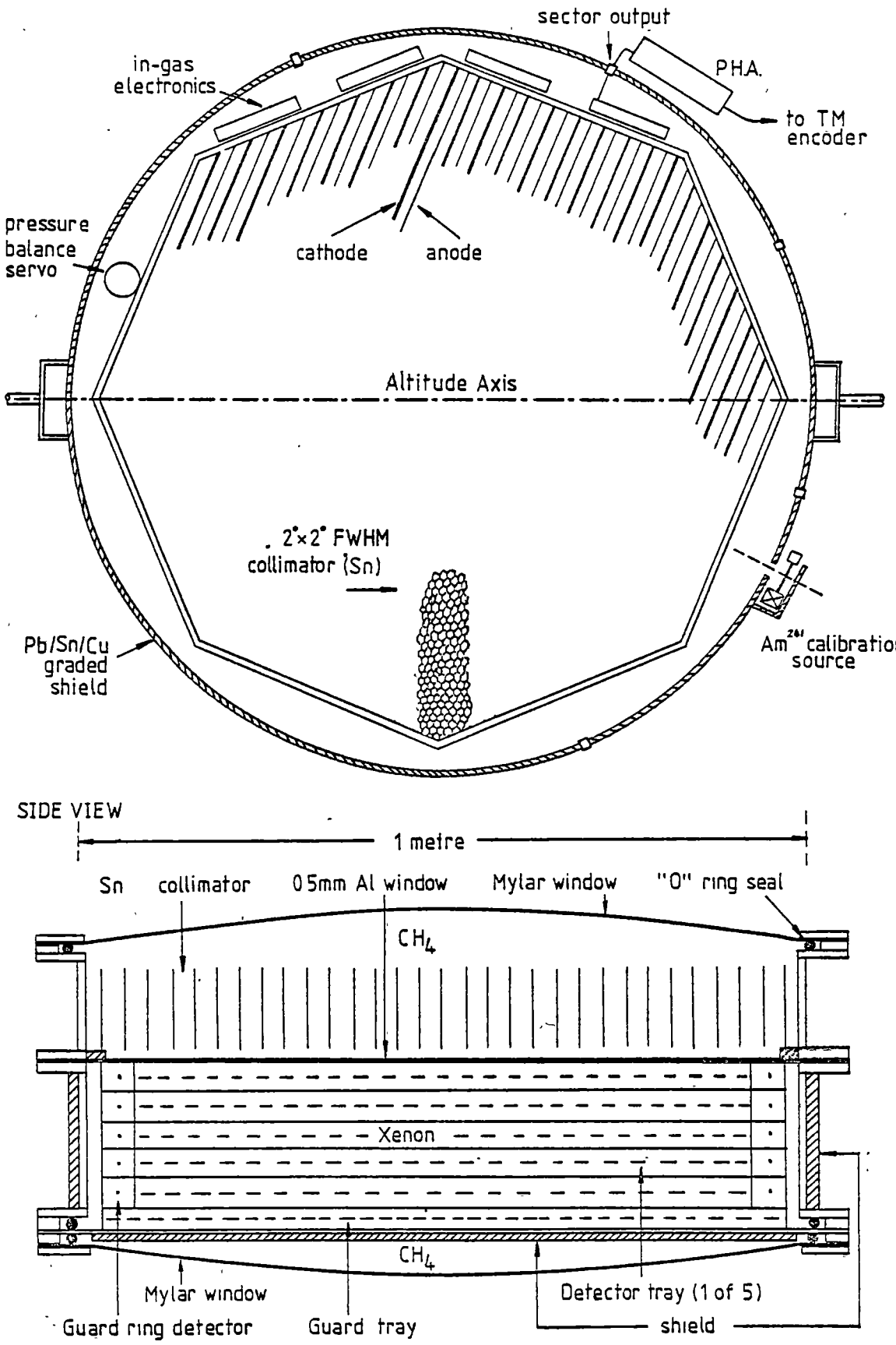

Figure 2.3 Sectional views of the UT proportional counter.

was conducted before the author joined the X-ray group.

As the outside air pressure changes from 1 atm at launch to ~3 mb at float the internal pressure of the vessel expands the mylar ends, causing a large pressure differential to occur across the Al window. The distortion of this window changes the gain of the detector since detector gain is very dependent on the counting gas pressure. To prevent such an occurrence, a pressure balance transducer mounted in the collimator section measures the differential pressure between the two volumes and accordingly valves in or vents methane from the collimator section to maintain the pressure difference to within a few mb. During ascent, gas is valved in whilst on descent, gas is vented out.

The actual detector itself is composed of six stacked octagonal trays. Figure 2.4 shows the six trays, with the preamplifier circuit boards mounted on the outside of the trays. Note that this is shown upside down. To maintain rigidity, each tray has its wires mounted perpendicular to the trays mounted immediately above and below. The bottom and sides of the detector are surrounded by guard detectors composed of cathode wires. The guard tray in Figure 2.4 is the thin tray at the top. Prior to the UTIC balloon flight, the ground plane of the tray nearest the window was the window itself. Distortion of the window during the 1978 flight changed the gain of this tray leading to poor energy resolution. To prevent any re-occurrence, a plane array of earthed wires, spaced 1 cm apart, was placed between the window and the top tray. This is not shown in Figure 2.3 or 2.4.

The active volume of the detector consists of the bottom five trays of Figure 2.4 of depth 21 cm and maximum width 95 cm. Each tray consists of 21 anodes, with a cathode wire between each anode and a plane of cathodes between it and the adjacent tray. The EHT supply unit is located in the collimator section. During the balloon flight discussed in Chapter 3, the EHT was set at 2300 volts. Three anodes are connected

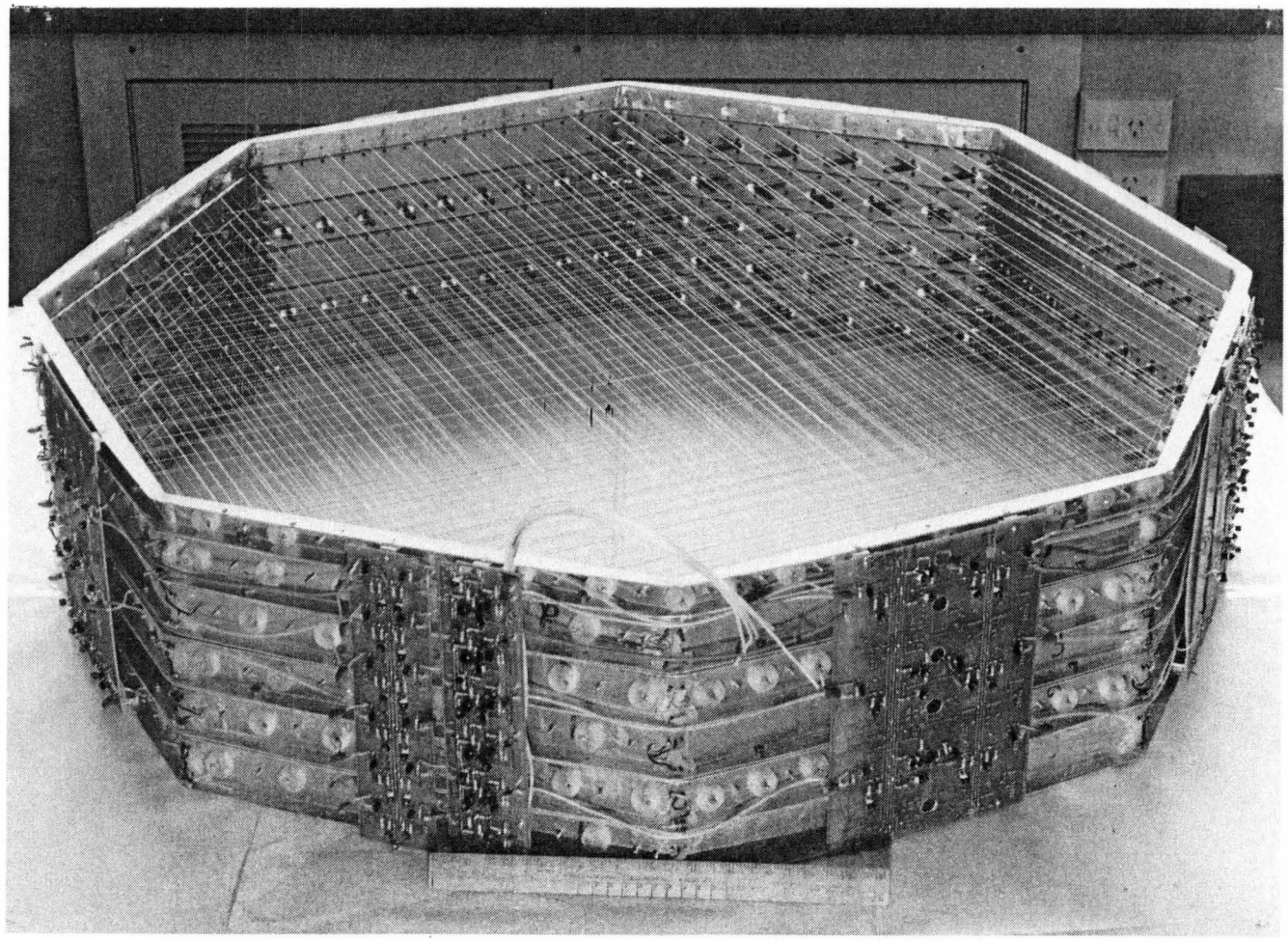

Figure 2.4 The 5 octagonal detector trays of the UT detector. Vertical boards are the preamplifiers.

Note the detector is shown upside down, with the guard tray at the top.

together in a unit called a cell. Each cell has its own preamplifier on the outside of the tray. The signals from each of the 35 preamplifiers are fed via five output ports through the wall of the pressure vessel to the amplifiers and peak detector circuits mounted on the outside of the vessel. Each output port is referred to as a sector. The design of the counter electronics was by Dr. J. Greenhill.

To match the gains of each cell and thus provide the best energy resolution, the gain of the amplifiers on the peak detector circuit boards were adjusted using potentiometers on the boards. The signals from the amplifiers are differentiated with a time constant of 10 μsec to remove low frequency noise. Up to four cells are added together using gain matching amplifiers and fed into one of the 11 peak detector circuits. The event signal voltage charges up a capacitor while it is increasing. The event signal also triggers a low level discriminator (LLD) which remains logically high for 10 μsec. The event signal decays with a time constant of 10 μsec whilst the capacitor retains the peak voltage of the event signal with a decay time of the order of seconds. When the LLD goes low, it closes a gate and the capacitor is discharged with a time constant of 2.2 μsec. The LLD triggers the pulse height analyser (PHA) so that the PHA can measure the peak voltage on the capacitor using an 8 bit analogue to digital converter.

Although 256 channels are available from this system, telemetry constraints, from the encoder, limit the telemetered (PHA) output to 19 contiguous linearly spaced energy channels. Events are rejected from the PHA if they trigger three or more detector cells within the 10 μsec sampling time of the peak detectors. This technique vetoes charged particle events which will normally trigger one cell in each of the five layers of the detector. Genuine X-ray events which result in emission and detection of a fluorescence photon will normally trigger at most two cells and are not vetoed. Events which trigger two or less

cells can also be rejected if they occur within +4 or -2 μsec of any pulses from the guard circuits. This is the principal background reduction technique. Charged particle events are transferred to the encoder by a separate channel, the veto channel. To accommodate the high count rate within the constraints of the telemetry, the veto count rate is rescaled by dividing by 128.

Background is also reduced by passive shielding surrounding the bottom and sides of the vessel. It consists of a graded shield of Pb (1.14 gram cm^{-2}), Sn (1.8 gram cm^{-2}) and Cu (0.022 gram cm^{-2}). The background rate at 50 keV was 5.0×10^{-4} counts $sec^{-1} cm^{-2} keV^{-1}$ at an atmospheric depth of 3.6 gram cm^{-2} over Alice Springs during a flight on 1981 December 2 (see Figure 3.4 for background spectrum).

The mylar window, collimator gas and Al window have respective column densities of 0.105 gram cm^{-2}, 1.25×10^{-2} gram cm^{-2} and 0.137 gram cm^{-2}. The combined transmission probability of the three is shown as the dashed line in Figure 2.5. The low energy cutoff, without any absorption from the atmosphere, is ~12 keV. The density of xenon, at 767 mm Hg pressure, is 5.61×10^{-3} gram cm^{-3} yielding a column density of 0.118 gram cm^{-2} for a sensitive depth of 21 cm. The absorption efficiency of the detector, including the transmission probability of the windows, is shown in Figure 2.5 as the solid line. The discontinuity at 34.5 keV is the K edge of xenon. The detector's upper energy limit is ~100 keV where the absorption probability has fallen to ~20%.

Under laboratory conditions, the energy resolution is ~25% FWHM at 60 keV. Inferior performance was obtained during flights prior to 1981 (Duldig, 1981). During 1976, xenon gas impurities affected resolution and in 1978 resolution was affected by the failure of the pressure balance servo and the consequent distortion of the Al window. The in-flight performance of the detector is monitored using an Am_{241}

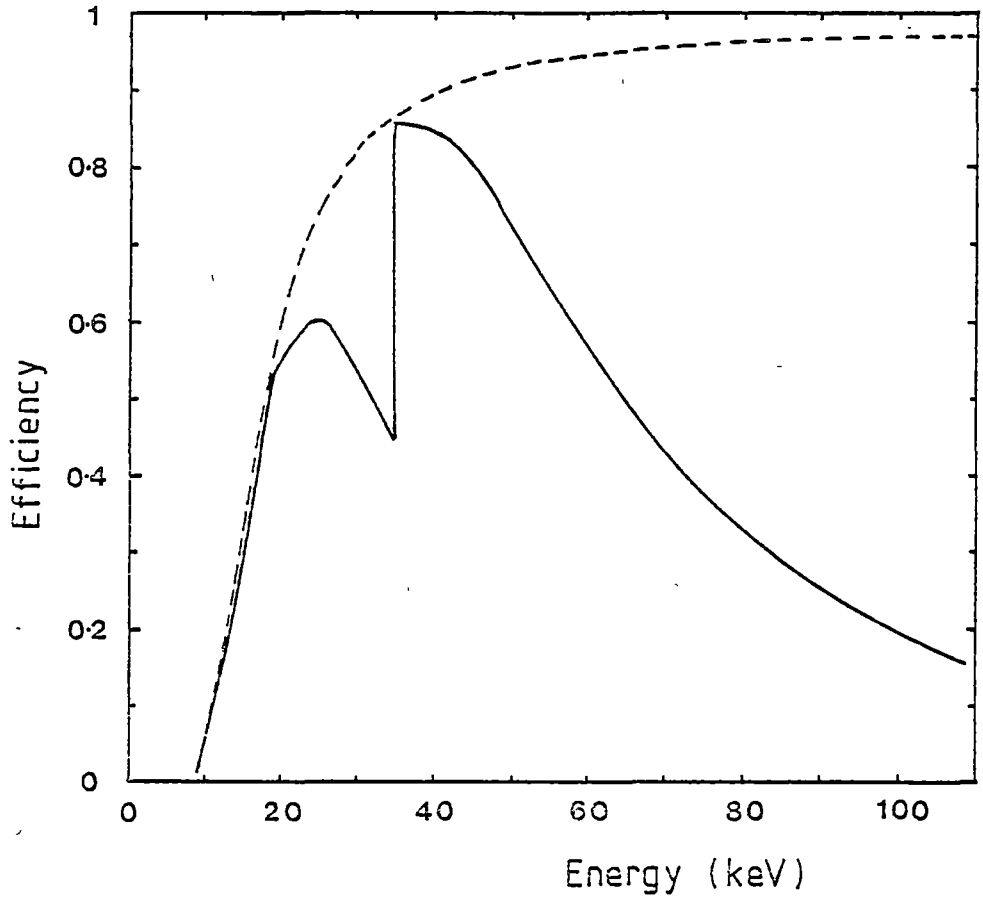

Figure 2.5 Probability of photon interacting with UT detector. Dashed line is transmission probability of the mylar window, collimator gas and Al window. Solid line is total absorption probability of the xenon including the transmission probability of the windows. Discontinuity is the K-edge of xenon at 34.5 keV.

calibration source attached to a rotating arm on the side of the detector. This is normally shielded from the detector. Under command, this source can be driven via a motor to illuminate the detector through a hole in the passive shield. Leakage from the source was found to be <5 counts sec^{-1} compared to the background level of ~200 counts sec^{-1}.

2.3.1 Collimator

The tin alloy collimator is mounted in the top section of the pressure vessel. It is composed of four square 33.5 cm x 33.5 cm elements surrounded by eight triangular sections 13.5 cm x 33.5 cm to match the octagonal shape of the detector tray. The depth of the honeycomb collimator is 6 cm and the internal diameter of individual holes is 0.4 cm with a wall thickness of 0.08 mm. The 12 elements are mounted in an Al frame which is attached to the sides of the pressure vessel and raised by 1 cm from the Al window. Collimator performance deteriorates rapidly above ~120 keV.

To align the 12 elements of the collimator, screws are located at three points equally spaced around the outside of each element. Since each element does not conform to the ideal design, due to manufacturing precision, the alignment of individual holes every square centimetre over the entire surface of the element was measured at Imperial College and a statistical average of the alignment determined for each collimator element. In the alignment of the complete collimator at the University of Tasmania by the author, the Al support frame was levelled and a vertical laser beam shone through the hole whose alignment was closest to the mean deviation. The alignment screws were adjusted until the pattern of light emerging from the collimator was axially symmetric. The result was confirmed by checking other holes with deviations near the mean deviation. After mounting the collimator in the pressure vessel, a mirror assembly was placed over the vessel and

aligned to the collimator to provide an optical reference to the X-ray axis. Tests using a 4.8mCi Am_{241} 60 keV gamma ray source at a distance of ~28 metres confirmed the alignment. Figure 2.6 is the count rate versus offset angle from the optical axis in the zenith direction. A similar result was obtained in the orthogonal direction. The dashed line is the idealised triangular response expected from a source at infinity. The rounded peak and shoulders are due to two effects. (1) Any misalignments and imperfections in the collimator will produce a flat top response near zero offset and also broaden the FWHM response. (2) The source, being a finite distance away, is shadowed by the collimator over a significant fraction of the sensitive area. The latter effect probably dominates. To test this satisfactorily requires the use of a source near infinity. For example, the ideal cosmic source is the Crab Nebula since the observed count rate can also provide an accurate estimate of the sensitive area of the detector.

The best estimate of the viewing angle is the FWHM of the peak marked in Figure 2.6. In the case of the zenith direction, FWHM = 2.11° and for the azimuth direction, FWHM = 2.20°. The average of 2.16° was adopted, close to the design criteria of 2° and the response of the collimator was assumed triangular and independent of the position angle of the source and optical axis. The alignment of the X-ray to the optical axis was found to be within 2 arc minutes for both zenith and azimuth directions. Total area of the collimator is 6000 ± 10 cm^2 which is reduced by 360 cm^2 because of the finite thickness of the walls. The area is further reduced because of misalignments and imperfections of the individual holes.

Since tin fluoresces at 25 keV, the cosmic ray radiation will produce a peak in the background spectrum at 25 keV. However, due to the small cross section of the collimator in the direction of the detector volume, the contribution to the background is found to be small

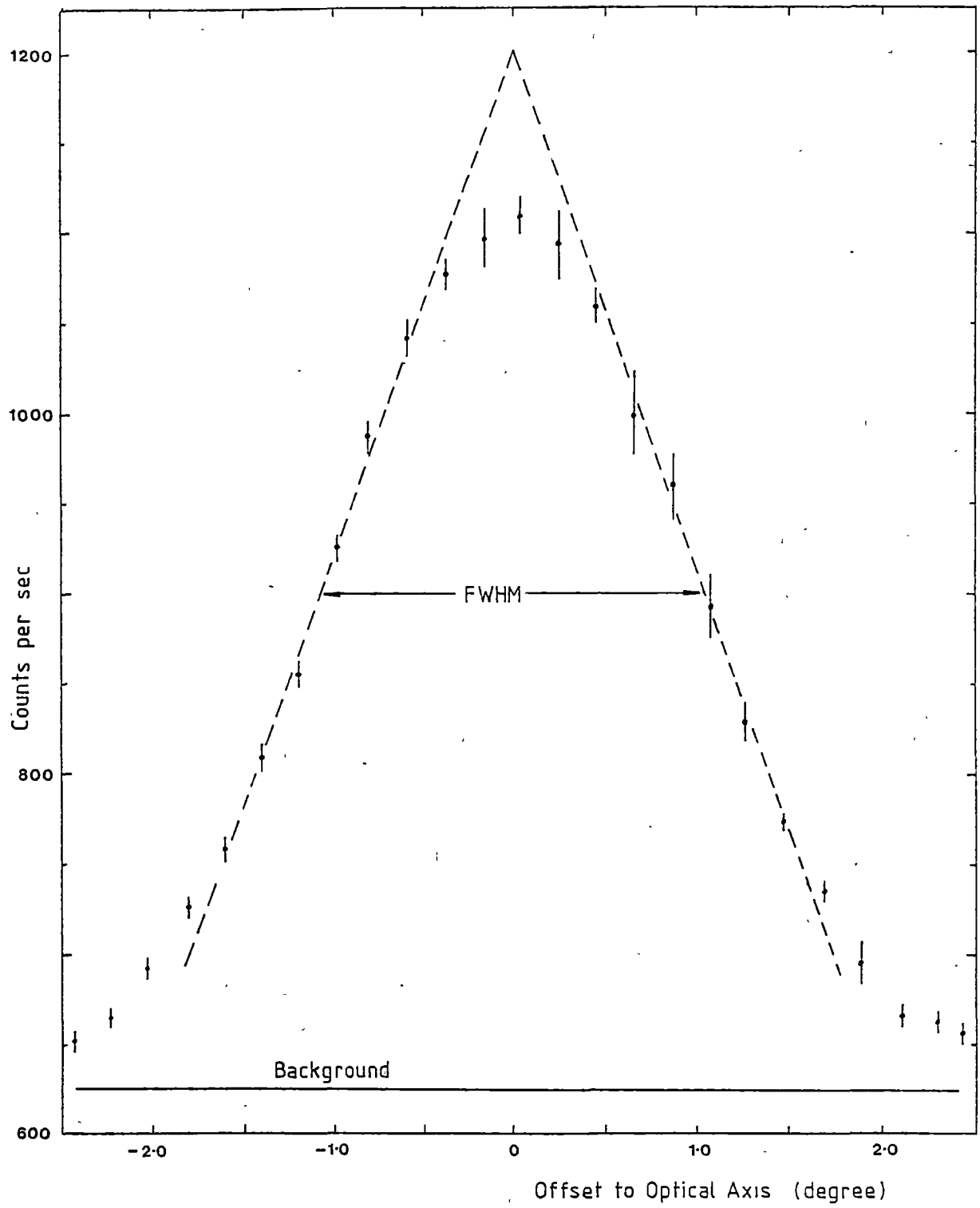

Figure 2.6 Count rate versus offset angle to the optical axis of the UT detector in the zenith direction. The dashed line is the ideal triangular response for a source at infinity. The full width at half maximum (FWHM) of the collimator is marked.

(see Figure 3.4 for background spectrum).

2.3.2 Gas Recirculation System

Impurities in the xenon can substantially affect the energy resolution of the detector. Sources of the impurities are small leaks and outgassing from electronics (principally the preamplifiers) and materials in the detector volume. To reduce outgassing, the detector volume is generally pumped continuously for periods of up to a week prior to filling with xenon. However deterioration of the gas over a timescale of days still occurs. To overcome this problem, a recirculation system is used. This pumps the xenon through a molecular sieve and, if necessary in extreme cases heated steel wool to eliminate oxygen. The gas can be cleaned in several hours and then maintained over periods of weeks via intermittent running of the circulation system.

After the balloon flight described in Chapter 3, the pressure vessel was modified to include an "O" ring between the Al window and the xenon compartment. This successfully eliminated any small leaks in this section with outgassing now being the dominant source of gas degradation. The lifetime of "clean" gas was thus extended to several months.

2.4 The Imperial College (IC) Phoswich Detector

This consists of 12 identical NaI/CsI phoswich scintillation detectors with a total sensitive area of 1680 cm^2 mounted in a 3 x 4 configuration. Above each detector is a tantalum honeycomb collimator with a field of view of 2° x 2° FWHM. The active depth of the scintillator material is 2 mm enabling observations between 20 and 200 keV. The number of PHA channels is software selected with a maximum number of 32. Resolution is ~22% FWHM at 122 keV. A plastic scintillator shield eliminates events due to charged particles entering the passive shield or collimator. The expected background, deduced from data from a test flight from Mildura, Victoria, in 1979, is ~3 x 10^{-4} cm^{-2} sec^{-1} keV^{-1} at

50 keV and an atmospheric depth of 3 gram cm^{-2} over Alice Springs. The detector is rocked on and off source in the cross elevation direction using a DC torque motor at a rate and amplitude under command control.

The IC encoder and electronic packages are mounted beneath the detector chassis. The encoder telemetry format is controlled by software enabling flexibility in formatting the data stream.

2.5 Comparison of UTIC with EXOSAT

Since EXOSAT is the only one of two satellites in the near future that can provide data at hard X-ray energies, a comparison of the UTIC detectors is of interest. The other satellite is Astro B (Tanaka, 1983) with a 640 cm^2 gas scintillator proportional counter of unknown sensitivity. The maximum energy is only 55 keV. Figure 2.7 shows the 3σ sensitivity curve of each detector for 10 keV bandwidth and a one-hour on-source observation at an atmospheric depth of 3 gram cm^{-2}. Also shown is the EXOSAT ME sensitivity for a 2×10^4 sec and 10^5 sec observation (Turner, Smith and Zimmerman, 1981). The UTIC detectors are much more sensitive in this energy range because of their larger areas and greater efficiencies. The true ME background is not certain but should give results close to those in Figure 2.7.

2.6 UT Flight Electronics

Figure 2.8 is a block diagram of the flight electronics package and ground station designed by Dr. J.G. Greenhill. It emphasises the central role of the on-board aspect control μP which is housed in the encoder package (Figure 2.1). The μP employs a hardware arithmetic unit (APU) to calculate the instantaneous altitude and azimuth of the desired source using time information from an on-board clock, together with source RA and declination, balloon geographic coordinates, and magnetic variation data telemetered to it by the command system from the ground station. The microprocessor also controls the altitude and

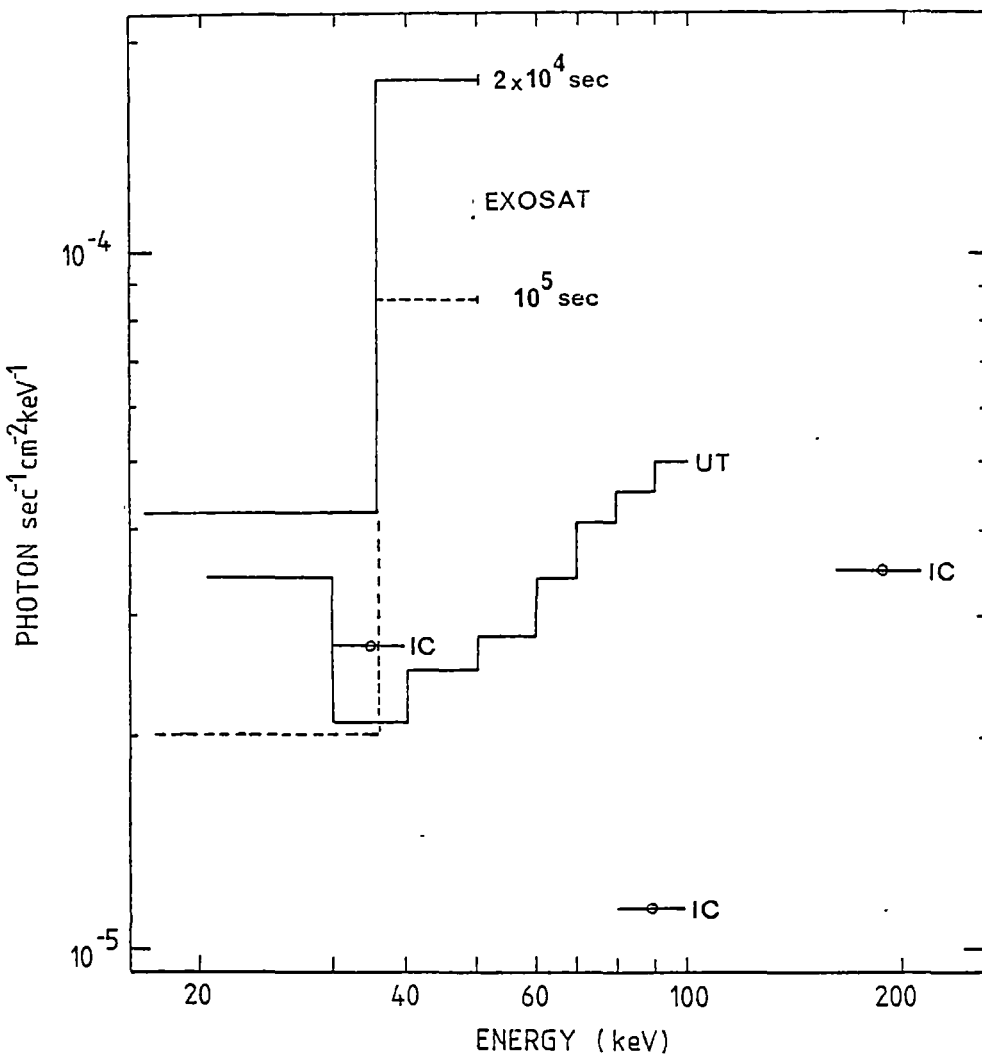

Figure 2.7

The 3σ sensitivity curve for the UTIC detectors with a 1 hour on-source observation at an atmospheric depth of 3 g cm^{-2} over Alice Springs. UT background from flight on Dec 2,1981; IC background from test flight in 1977. The EXOSAT curve is for a 6 hour and 28 hour observation.

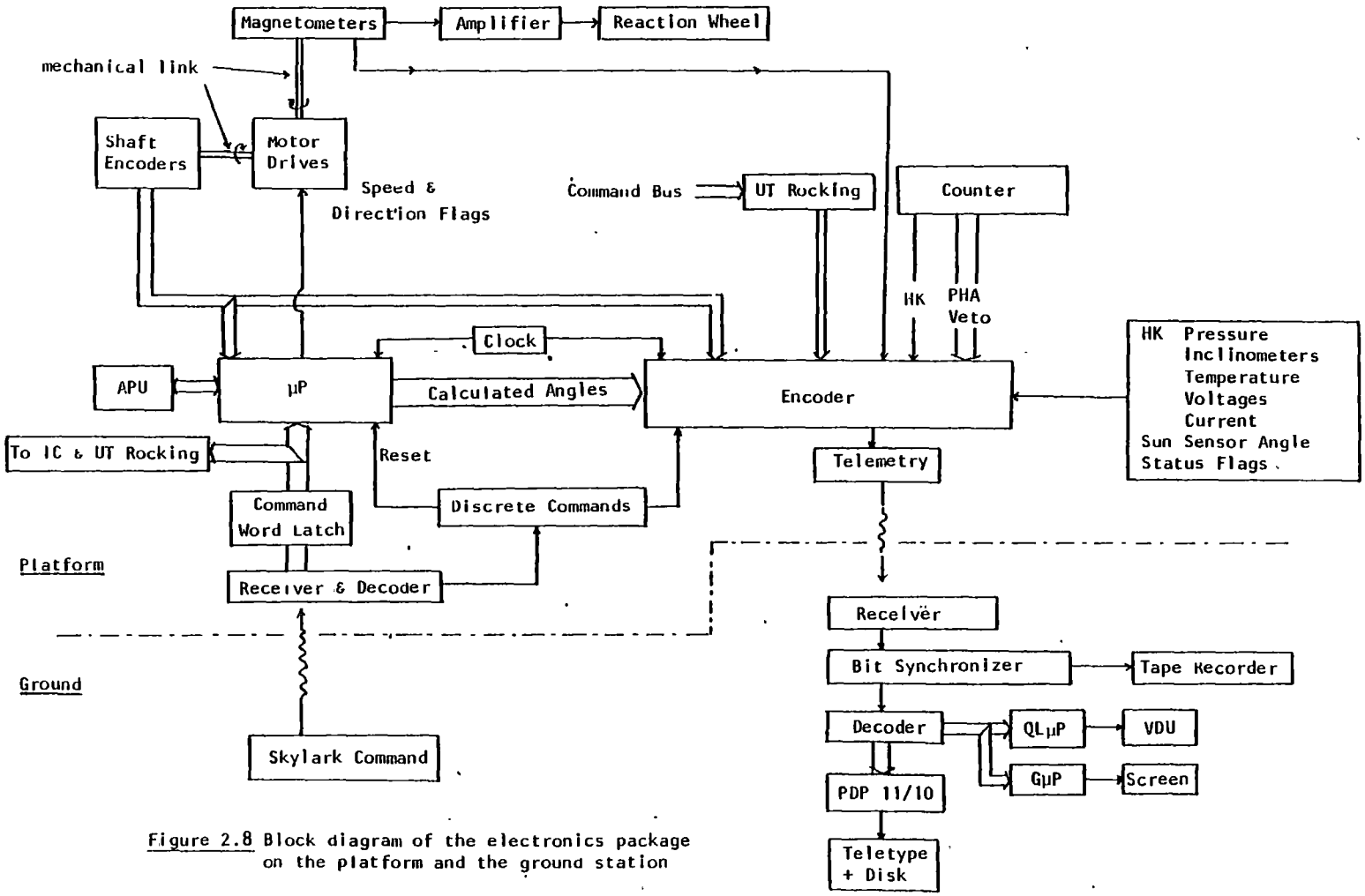

Figure 2.8 Block diagram of the electronics package on the platform and the ground station

azimuth axis drive stepper motors. The on-board clock is accurate to 2 seconds over ~4 days.

The command system used is the PCM Skylark system with 63 discrete commands available and the ability to transmit a sixteen bit data word. The data word upon being received on board is latched onto a data bus which can be read by the μP, IC electronics package and the UT rocking control hardware. Discrete commands are available for on/off operation of the EHT of the UT detector and azimuth servo, power supply control, operation of the calibration source and in the event of difficulties being experienced with the μP, manual driving of the zenith and azimuth drives. The μP can be reset to the start of the pointing program via a discrete command.

Other discrete commands are for ballast drops, balloon cutdown and parachute separation upon landing.

2.6.1 The Microprocessor (μP)

The μP is a Signetics 2650 8 bit processor using an AM 9511A arithmetic processing unit (APU) for hardware arithmetic including trignometric functions. The APU can operate on several data formats, single precision 16 bit, double precision 32 bit integer arithmetic or 32 bit floating point arithmetic. Data and commands are fed in and out as 8 bit words. Since all trignometric functions require floating point manipulation, instructions for the APU are available to convert data stored in the internal registers of the APU. The pointing program is stored in a 4K 8 bit word EPROM with a 1K 8 bit word RAM for temporary storage of data. The μP clock is run at 1 MHz. The μP and associated memory is TTL logic whereas the majority of the encoder is CMOS logic. Recently, CMOS μP's have become available which would reduce the power consumption from the present 20W to below 1W.

The μP reads the on-board clock as two 8 bit words. The 2 most significant bits (MSB) refer to day number since the clock was turned on,

the next five the number of elapsed hours in that day and the last nine bits represent elapsed seconds in that hour. Each increment represents 8 seconds, with a total of 450 per hour. The accuracy of timing information available to the μP is 4 seconds. Pointing errors from the clock are less than 1 arc min.

The azimuth and zenith shaft encoders are synchros and are converted to a 12 bit word by synchro-to-digital converters. Accuracy is ~0.07°. The data are split into 3 8 bit words for input to the μP. To monitor the calculated azimuth and zenith shaft angles, the μP outputs, via two 11 bit words, both angles to the encoder for telemetry to the ground station. The last output from the μP is the azimuth and zenith stepper motor speeds and directions. Each motor is controlled by a direction flag and three speed bits allowing a total of eight speeds each.

The data command words which the μP regards as valid are listed in Table 2.1. Other commands to the IC encoder and UT rocking hardware are ignored.

TABLE 2.1

Valid UT μP Commands

Name	ID (hex)	DATA
	15....12	11 10 9 0
Right Ascension	0	in 0.1° units
Declination	1	SIGN | in 0.1° units
Epoch	2	YEAR | Δ Julian Day
Latitude	3	SIGN | in 0.1° units
East Longitude	4	in 0.1° units
Zenith	5	in 0.1° units
Azimuth	6	in 0.1° units
Mode of Observing	7	see text
Azimuth Variation	A	SIGN | in 0.1° units

Each word is identified by the four MSB (bits 15 - 12) yielding a total of 16 12 bit words. The µP interprets words with ID from 0 to 7 and A. Word 8 is for UT rocking and the others are used by IC for their rocking, EHT control and selection of data acquisition and telemetry configurations.

Several observing modes are available and can be selected using the observing mode command (ID = 7). They are tracking a source at fixed celestial coordinates or driving to fixed azimuth and zenith angles previously sent using words with ID 5 or 6. Any combination of the two orthogonal dirve directions is possible. For example, one can track a celestial position in azimuth whilst maintaining a fixed zenith angle. The least significant bit (LSB) of the command word selects zenith track or position with a 1 or 0 respectively. The 2nd LSB is for selection of the azimuth observing mode. This design of the observing mode was selected to allow for maximum flexibility in control of the platform orientation.

Since the platform is aligned by using the horizontal component of the earth's magnetic field which changes direction at different geographic locations, the angle between geographic north and magnetic north must be telemetred to compensate, using the azimuth variation data word (ID = A). By using sun azimuth from the sun sensor, this angle can be estimated and for cases when the sun is not visible, either at night or by balloon shadowing, interpolated from existing information and/or the use of magnetic maps. Changes in the magnetic variation as large as $\pm 2^{\circ}$ can be expected during a balloon flight. All the angles to be telemetred (ID 0, 1, 3, 4, 5, 6 and A) are transmitted in units of 0.1°. For declination, latitude and azimuth variation, the MSB of the 12 bit data word represents the sign, 0 for + and 1 for -.

Epoch (ID = 2) is composed of 2 numbers, the Julian day at the start of the on-board clock and the year for precession corrections. The 2 MSB's of the 12 bit word represent years after 1980 whilst the Julian day that is transmitted, is number of days after JD2445000.5. The length of the numbers enables a maximum time of 3 years before the μP program requires a small modification for the determination of the year for the precession and the Julian day.

2.6.2 Pointing Algorithm

Given a celestial position, the epoch and the geographic position of the observatory, the required azimuth and zenith of the observatory can be determined from equations 2.1 to 2.9 (Lang, 1974). The definition of the variables are

Observatory latitutde	ϕ
Observatory east longitude	λ
Universal time	UT
Julian day of observation	JD
Right Ascension (1950.0)	α
Declination (1950.0)	δ

then Local Mean Solar Time (LMST) = UT + λ (2.1)

and Julian centuries since 1900.0 T = (JD-2415020)/36525 . (2.2)

Greenwich Mean Siderial Time (GMST) in hours

$$= 6.6461 + (8640184.542T + 0.0929T^2)/3600. \quad (2.3)$$

Local Mean Siderial Time Λ = GMST + LMST + UT * 9.8565/3600. (2.4)

The 1950.0 coordinates can be precessed, to first order, to current coordinates α' and δ' by

$$\alpha' = \alpha + (3^s.07327 + 1^s.33617 \sin\alpha\tan\delta)Y \quad (2.5)$$

$$\delta' = \delta + 20".0426 \cos\alpha\ Y \quad (2.6)$$

where Y is years since 1950.0. The accuracy of the precession calculation is ±20 arc sec, well within the required accuracy of $\pm 0.1^\circ$.

The final three equations yield the azimuth and zenith angles

$$\text{source hour angle} \quad h = \Lambda - \alpha' \tag{2.7}$$

$$\text{zenith angle} \quad Z = \arccos(\cosh \cos\delta'\cos\phi+\sin\delta'\sin\phi) \tag{2.8}$$

$$\text{azimuth angle} \quad AZ = \arccos\left(\frac{\sin\delta' - \sin\phi\cos Z}{\cos\phi\sin Z}\right) . \tag{2.9}$$

For reduction of azimuth and zenith angles to celestial coordinates, the following equations provide the inverse of equations 2.7 to 2.9.

$$\text{declination} \quad \delta' = \arcsin(\cos Z \sin\phi + \sin Z \cos AZ\cos\phi) \tag{2.10}$$

$$\text{hour angle} \quad h = \arccos \frac{\cos Z \cos\phi - \sin Z \cos AZ\sin\phi}{\cos\delta'} \tag{2.11}$$

$$\text{Right Ascension} \quad \alpha' = \Lambda - h . \tag{2.12}$$

The current celestial coordinates can be converted to 1950.0 coordinates by using equations 2.5 and 2.6. Equations 2.10 to 2.12 are used in post flight reduction of data (see Section 3.2) and in the real time display of the pointing of the telescope (see Section 2.12.2).

2.6.3 Pointing Program

The pointing program was initially written by the author. S. Ashton was responsible for the hardware and the testing of the integrated system and where necessary modified the program. Full details of the hardware and software are presented elsewhere (Ashton, 1980). The program was written, in Signetics 2650 assembly language, on a PDP 11/10 computer, cross assembled and the code file transferred to the μP and stored in a 4K RAM board for testing. Upon the successful testing of the system, the program was recorded permanently on a 4K EPROM board.

The program structure is outlined in Figure 2.9. It can be divided into 2 parts, the command interrupt subroutine (CIS) and the main program. The operation of the CIS is as follows. Upon receiving an interrupt, from the transmission of a data word from the ground station, the μP transfers to the CIS from the main program. The CIS reads the data bus and if it recognises the word to be valid, it will remove the ID and store the 12 bit data word in the appropriate location in RAM. Program

Figure 2.9

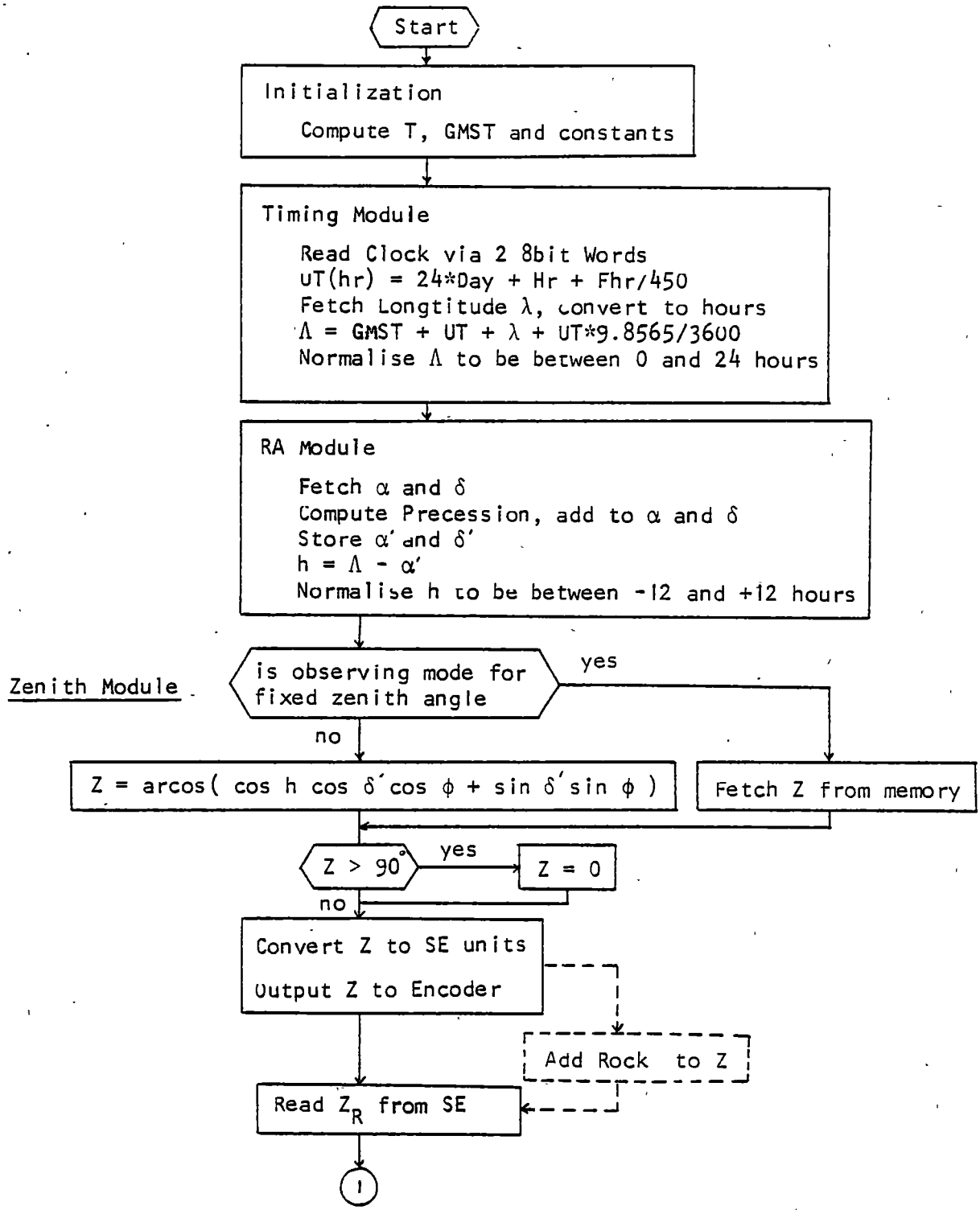

Figure 2.9 The UTIC μP pointing algorithm for UTIC81. The ROCK module for the post UTIC81 configuration is shown as the dashed box and in detail at the end of the flowchart.

Figure 2.9 cont.

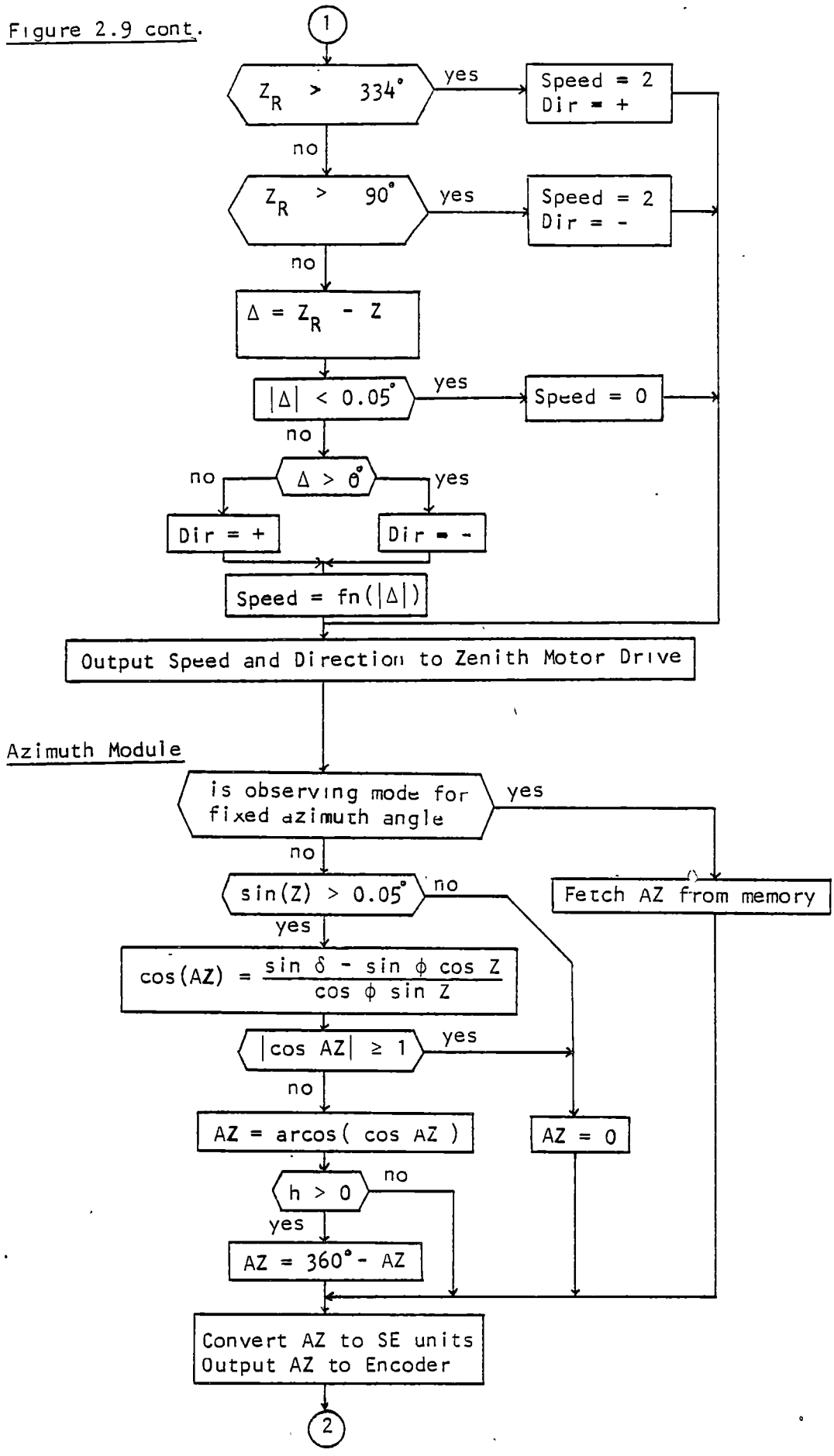

Figure 2.9 cont.

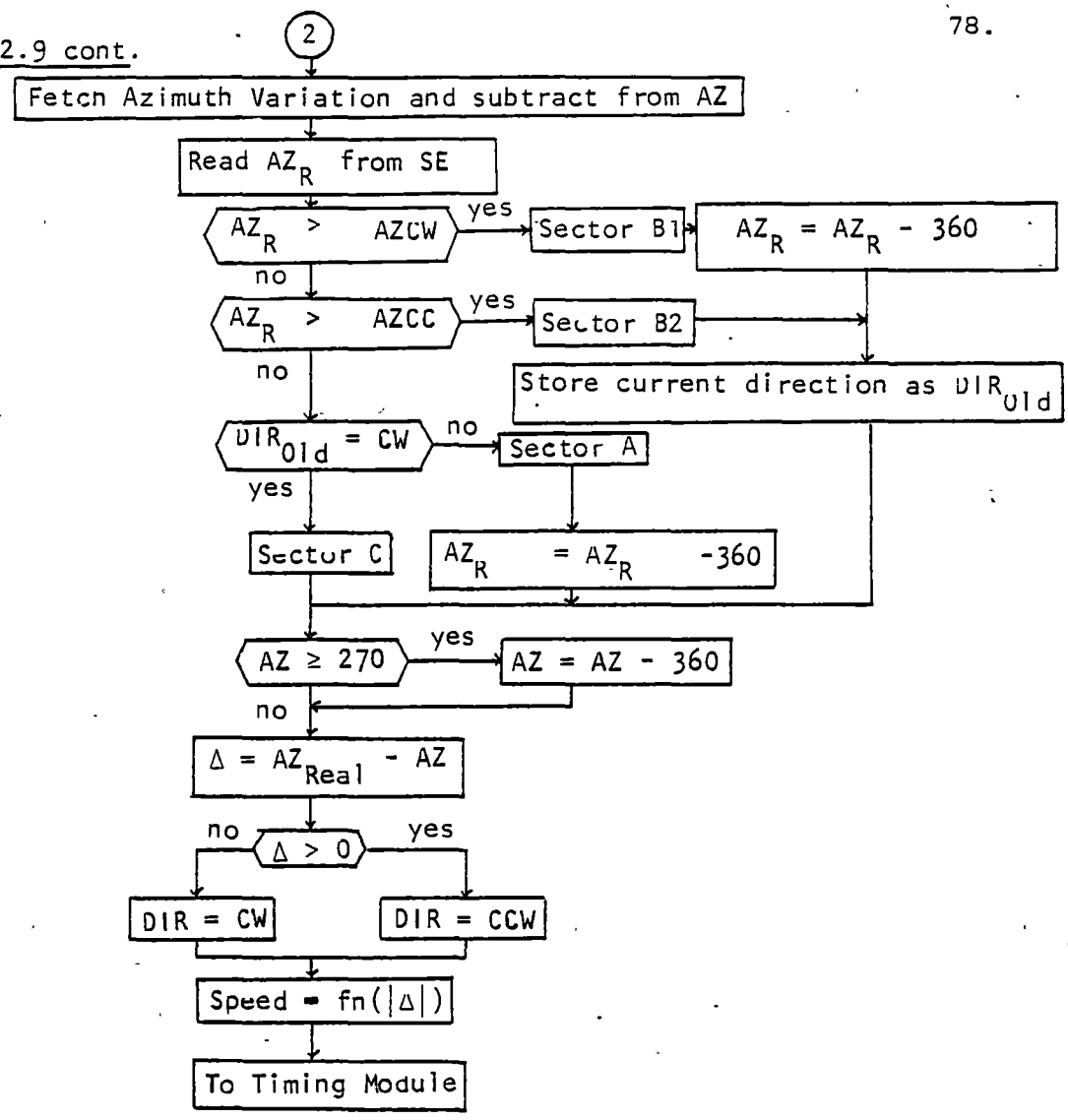

Rock Module post UTIC81

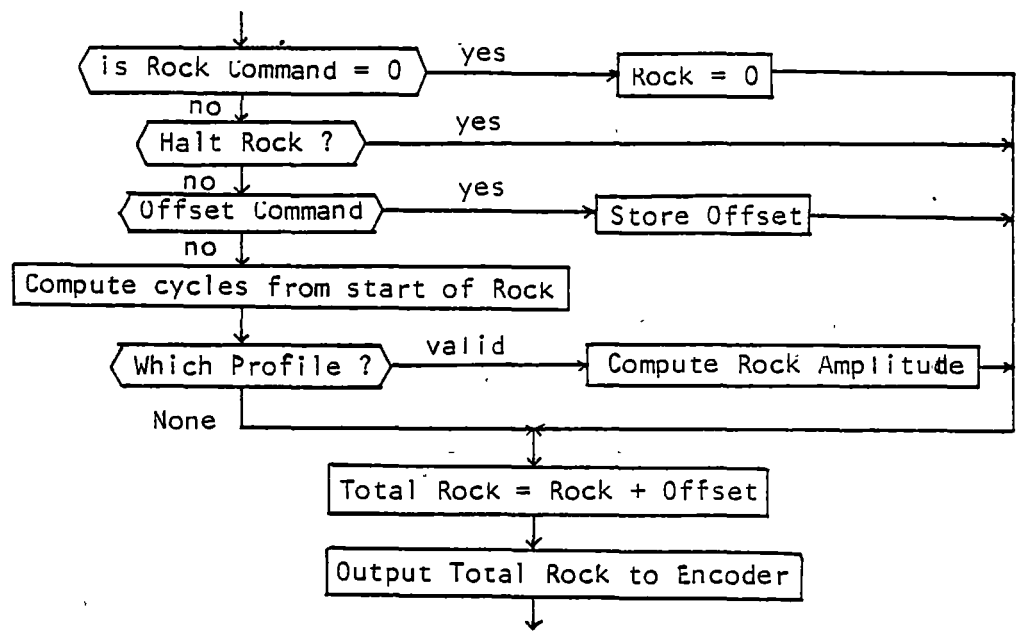

control is then transferred back to the point in the main program where it was interrupted. The main program is executed continuously upon power up, even if manual control of the drive motors has been selected. Manual control disables the control signals from μP to the drive motors.

The main program is divided into 5 blocks called initialisation, timing, RA, zenith and azimuth modules and for later flights, the rock module (see Section 2.8). The initialisation module computes the Julian centuries from 1900.0, and GMST (equation 2.1 to 2.3). Constants, common to several other calculations in other parts of the program are computed and stored in floating point format in RAM.

The timing module reads the clock and determines UT in units of hours. FHR in Figure 2.9 represents the number of "second" bits read from the clock. The local mean siderial time Λ is computed using equation 2.4 and then normalised to be between 0 and 24 hours. The RA module computes the current RA and Declination from equation 2.5 and 2.6. The hour angle of the source follows from equation 2.6.

The next section, the zenith module, determines the required zenith angle and issues instructions to the zenith drive motor. The zenith angle is either computed from equation 2.8 or fetched from memory, dependent on the selected observing mode (tracking a source or remaining at a predetermined zenith angle). The calculated zenith angle is converted to shaft encoder (SE) units and output to the encoder for telemetry. The dashed box labelled rocking in Figure 2.9 which allows the μP to rock the detector in zenith was inserted after the balloon flight discussed in Chapter 3 and full details are in Section 2.8. The detector zenith angle Z_R is read from the SE and checked to be within the limits of 0° (vertical) to 90° (horizontal). If $Z_R > 334^\circ$, the detector is pointing to the rear of the platform and the direction of the motor is set to drive the detector back through the vertical to point in the forward direction ($0^\circ < Z_R < 90^\circ$). If $Z_R > 90^\circ$, the

detector is below the horizon and the direction flag is set to drive the detector towards the vertical. If the detector zenith is within the allowed limits, the difference (Δ) between Z_R and the desired zenith angle is computed. If $(\Delta) < 0.05^\circ$, the zenith speed is set to zero and no driving is required. For $\Delta > 0.05^\circ$ the direction flag is set to drive the detector to the vertical, and the reverse direction for $\Delta < -0.05^\circ$. The drive speed is an increasing function of the magnitude of Δ, to ensure the platform is not perturbed by rapid deceleration of the detector and to prevent mechanical oscillations. Finally the speed (3 bits) and direction data (1 bit) including the equivalent azimuth data are output via an 8 bit word to the drive motors.

The final part of the program is the azimuth module. The first decision is the selection of the mode of observing: tracking a source or observing at a fixed azimuth angle. If observing at a fixed azimuth angle, the required azimuth is read from memory. For tracking sources, several tests are incorporated to ensure that no subsequent calculations will produce unacceptable or ambiguous answers. The first test is to ensure that sin Z is not too small. Otherwise the calculation of cos(AZ) in equation 2.9 may exceed the allowable bounds of +1 or -1 due to roundoff errors. If $\sin Z < 0.05^\circ$ then AZ = 0. Similarly if $|\cos AZ| > 1$, AZ is set to zero, otherwise the azimuth is satisfactorily determined. If the source is west, the azimuth is recalculated using $AZ = AZ - 360^\circ$ so that AZ is between 0° and 360°. The calculated azimuth is output to the encoder for telemetry. The magnetic variation is subtracted from the desired geographic azimuth to obtain the magnetic azimuth. The magnetometers are mounted on the end of the vertical drive shaft and are electrically connected via long cables to their amplifiers mounted on the frame. Hence the magnetometers cannot be continuously driven in the same direction. Figure 2.10 shows the azimuth range over which the magnetometers are allowed to drive.

Limit switches which override the μP, prevent the magnetometers exceeding the limits AZCW and AZCC. The centre of the overlap region is set at an azimuth of 270°.

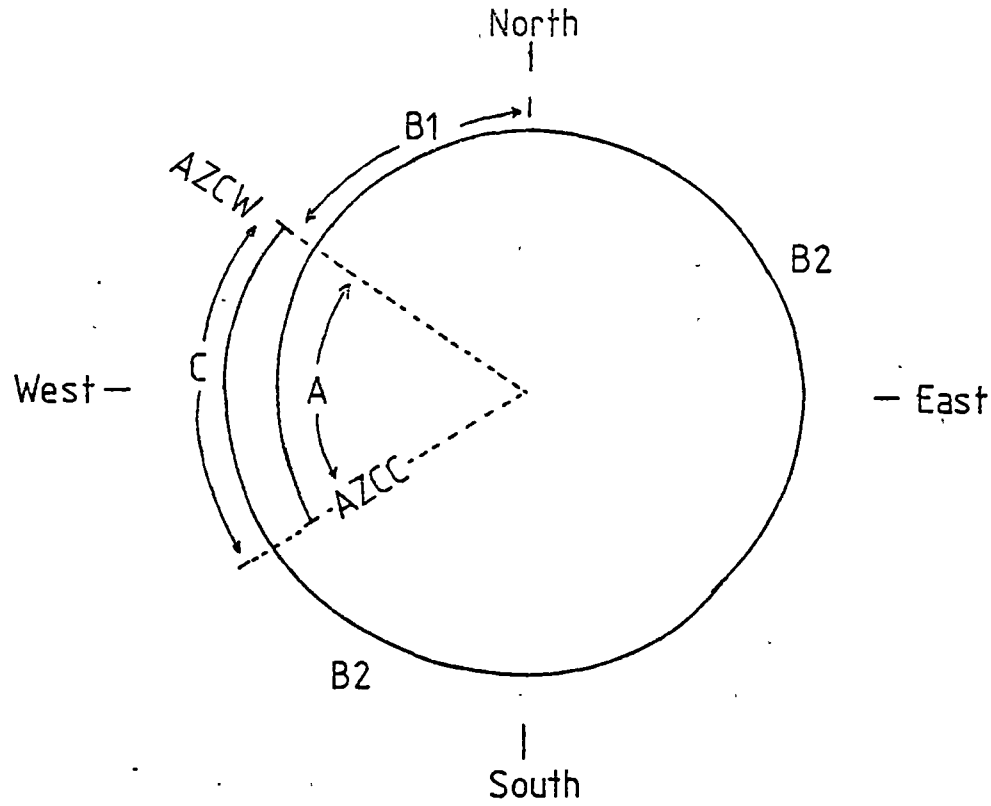

Figure 2.10 The allowed drive positions of the azimuth pointing system, with overlap at an azimuth of 270 degrees. The sector names are defined in Figure 2.9.

Sources with declinations further north than the current latitude of the detector will generally not have azimuths between 90° and 270° unless the zenith angle exceeds 60° and similarly southern sources will not have azimuths greater than 270° or less than 90°. Most X-ray observations are at zenith angles less than ~45°, due to the rapidly increasing atmospheric absorption at large zenith angles. Hence sources will not traverse through the east-west line and cause long delays by the requirement of driving through 360° when tracking through the azimuth angle of 270°.

The typical cycle time of the program is ~0.1 sec which makes pointing updates essentially instantaneous.

There are various sources of error which contribute to the total pointing error of the platform (Ashton, 1980). These are listed in Table 2.2.

TABLE 2.2

Pointing Errors

Quantity	Error (arc minutes)
Longitude	3
Latitude	3
Time	1
Shaft angles	2.5
Magnetic variation	~1.5
Total Mean Error	5.2

Other sources of pointing error are due to azimuthal oscillations which are typically 6 arc minutes RMS (see Chapter 3) and pitch and roll angles of the platform. The inclinometers have an accuracy of ~1 arc minute and any deviation from the horizontal can be removed in post flight analysis of the pointing solution. The magnetic variation can actually be specified to within 3 arc minutes but at zenith angles less than 45°, this translates onto the sky as ~1.5 arc minutes.

2.6 Azimuth Servo System

The platform is orientated in azimuth by means of a servo control system that uses the local horizontal component of the earth's magnetic field as the reference direction. The signal output from the sensing magnetometer is fed into an amplifier which includes a component of velocity feedback in its output. This error signal controls a voltage to frequency converter, each signal of which triggers a monostable pulse generator. The monostable drives a DC torque motor via a FET power amplifier. Thus the power input to the torque motor and hence to the reaction wheel which it drives is dependent on the pulse repetition frequency and hence on the magnitude of the error signal. The reaction

wheel is located in the lower part of the central section of the platform. The peak torque of the motor is ~0.55 kgm and the reaction wheel moment of inertia is ~1.3 kgm^2. The platform moment of inertia is ~300 kgm^2.

The suspension bearing, that connects the platform to the balloon rig is driven by a stepper motor, through a reduction gearbox. This motor is driven by the same signal that drives the reaction wheel to ensure both come to rest when the magnetometer is aligned to the field. There is sufficient friction in the suspension bearing to permit momentum transfer to the balloon.

2.7 UT Rocking

Since the UT and IC detectors are mounted on a common altitude shaft, the rocking for the UT detector had to be made independent of the altitude shaft. A separate rocking cam designed by M.W. Emery was inserted between the altitude shaft and the UT detector. It was capable of offsetting the UT detector $\pm 10^\circ$ relative to the zenith angle set by the μP. The cam was driven by a dedicated stepper motor and the angle measured by a shaft encoder accurate to 0.2°. The cam was driven by electronics located in the encoder box and used commands from the 16 bit PCM data word. Table 2.3 is a list of available commands and examples of rock profiles. The command word ID is 8.

TABLE 2.3

UTIC Rock Commands 1981 Balloon Flight

Function	ID	DATA		
	15....12	11....8	7....4	3....0
Set rock to 0°	8	X	D	0
Stop rock	8	X	0	0
Square rock amplitude to $+2^\circ$ duration 4 minutes	8	4	E	4
Triangular rock	8	0	0	8
Staircase rock	8	0	F	9

After the 1981 balloon flight discussed in Chapter 3, the altitude and rocking mechanisms were modified. Separate altitude drives were constructed for each detector allowing the UT rocking to be driven by the μP. The altitude shaft encoder was connected directly to the UT detector. The pointing program required little modification to incorporate a rocking subroutine after the calculation of the zenith angle (Figure 2.9). The CIS was modified to accept words with ID = 8. All program modification and testing were by the author. Table 2.4 lists the new rock commands.

TABLE 2.4

μP Rock Commands

Function	ID	DATA			
	15....12	11....8	7....4	3....0	
Set rock to zero	8	0	0	0	
Leave rock at current position	8	F	F	F	
Zenith offset	8	C	SIGN	in 0.1° units	
Triangular profile	8	0 0	PERIOD	SIGN	AMPLITUDE
Square profile	8	1 0	PERIOD	SIGN	AMPLITUDE
Staircase profile	8	0 1	PERIOD	SIGN	AMPLITUDE

The first command immediately sets the rocking offset to zero whilst the 2nd command halts the rocking cycle immediately. The modifications allowed the inclusion of a zenith offset in case pointing errors are apparent in the platform. Any known errors in the shaft encoder can also be corrected. The offset is added to the currently

determined zenith. The convention for the SIGN bit in this word and the rock profile is 0 = + and 1 = -. Each bit of the offset amplitude represents 0.1° giving a maximum offset to ±12.7°. Three rock profiles are currently available - triangular, square and staircase - although the flexibility of the system can allow the inclusion of any kind of profile. The period of the profile is determined by the 5 bit word located in bits 5 to 9 of the command word. Each bit increment represents 0.5 min steps. Upon receiving a rock profile command, the onboard clock is read and stored as reference to the start time of the rock profile. Every time the rock subroutine is run, the difference between the current time and the start time is used to determine the phase of the rock cycle and hence the rock offset. Since the clock is updated every 8 seconds, the rock profile will only change in 8 seconds or more. The amplitude of the rock profile is determined by the 4 bit word located in bits 0 to 3. Each increment is 0.5°, allowing a maximum semiamplitude of 7.5°. The sign of the amplitude defines the direction of the rock profile. In the case of the triangular and staircase rock profiles it defines the initial direction. It does not affect any bias of the rock to either side of the source position.

2.9 Sun Sensor

To determine absolutely the platform azimuth, a sun sensor designed by M.W. Emery, is mounted at the top of the central section of the platform (Figure 2.1). The box mounted above the plate rotates clockwise every second and two parallel vertical slits separated by 5 cm inside the rotating box define the entrance aperture. The detecting element is a photo-transistor. As the sun sensor passes through the point directly forward on the platform and parallel to the X-ray axis, an index pulse is generated and when the sun has been detected the difference in angle, measured with a 2048 bit shaft encoder, is stored and passed to the encoder for telemetry. The position of the sun is

refined by differentiating the gaussian profile of the output voltage from the photo transistor and determining the zero cross over point. The sun sensor is accurate to ~0.07° for sun zenith angles >5°.

The platform azimuth A can be determined from

$$A = SAZ - (\psi + \epsilon) \qquad (2.13)$$

where SAZ is the geographic sun azimuth, ψ the output angle from the sun sensor and ϵ the error between the optical axis of the detector and the position of the index pulse, measured in the clockwise direction.

2.10 Thermal Control

Thermal control of the platform is achieved using a passive shield of 5 cm thick styrofoam coated with titanium dioxide based paint enclosing the main structure. No active cooling or heating techniques are used. The selection of the shield and coating were determined with the assistance of a computer model of the thermal behaviour of balloon packages, developed by Carlson et al. (1973). The model predicts the payload temperatures at various locations including the skin of the package and allows for the time dependent effects of solar and earth radiation, albedo and convection. It also allows for internal power dissipation, internal heat transfer, package construction and temperature at launch. In the case of UTIC, the platform was treated as a box of volume 5.5 m^3 and surface area 20 m^2 with an internal power consumption of 120 W. The temperature range over which the platform can operate satisfactorily is from -10°C to +40°C. The IC phoswich detectors are temperature sensitive and stable temperatures over the duration of the balloon flight are desirable. A particular advantage of the large heat capacity of the platform is the slow thermal timescale. Previous University of Tasmania balloon flights have used small packages with individual thermal insulation packages and have suffered from rapid temperature changes in excess of 30°C over a few hours (Duldig, 1981).

The most stable results in computer modelling were obtained with a surface absorption coefficient of 0.32, with a maximum internal temperature of 30°C and minimum of -1°C over a 60 hour flight with 2 night/day cycles.

2.11 UT Power Supplies and Inverter

Power is supplied by 28 volt Li organic batteries, located in the central section of the platform. A power inverter converts the unregulated 28 volt supply to a variety of voltages, 5V, 12V regulated supply for TTL and CMOS logic, ±15V for linear circuits and 24 volts for the pulse amplifiers. The batteries are split into two packs and output can be switched from one to the other via relays under command control. If the duration of the balloon flight is prematurely short, the second pack of batteries need not be used. Total power consumption is ~120W.

An innovation for balloon flights is the use of two large solar cell panels to supplement the batteries during the day. These are located on the ends of the platform. Each panel is rated at ~2.5 amps at 15 volts.

2.12 UT Data Telemetry and Processing

Data from each detector is independently encoded into a pulse code modulated (PCM) bit steam and telemetered on separate subcarriers. Aspect and essential housekeeping data are duplicated on each bit stream, thereby providing an element of redundancy. Each bit stream is recorded separately at the receiving station and separate UT and IC computers are used for output on a VDU and teleprinter of housekeeping, aspect and quick-look X-ray data. A dedicated micro-processor-controlled graphics system obtains aspect information from the telemetry system and gives a visual representation of the instantaneous telescope aspect superimposed on a grid of equatorial coordinates. This facilitates telescope control during flight.

2.12.1 UT Telemetry Format

The UT telemetry format is fixed by hardware whereas the IC encoder format can be modified by software. This makes the UT data format somewhat inflexible. Each subframe is composed of 32 90 bit frames. Figure 2.11 illustrates the structure of one of the 90 bit frames. It is composed of two types of 16 bit data words referred to as type A and type B. Type A word is composed of two parts, the five MS bits represent the identifier for the complete frame. These bits cycle modulo 32. The remaining 11 bits of the A word can represent pulse height data (PHA) or housekeeping data (HK). Each type A word is followed by 4 16-bit B words. Each 16 bit B word is composed of 4 4-bit words known as PSR words and is used for high speed photometry of X-ray sources. The PSR word represents the number of pulses detected by the PHA in the energy channels six to fourteen inclusive during a 4 msec interval. The actual timing of the PSR data is derived from the position of the event in the subframe. B words must be compressed in time to 71% of the actual duration of the data to allow insertion of the A word and parity bits.

At the end of every 8 bits, a parity bit is inserted corresponding to odd parity, i.e. if every data bit is zero, then the parity bit is one. The format of the transmission code is non return to zero (NRZ). Each subframe is 2 seconds long yielding a transmission bit rate of 1440 bits per sec.

The allocation of the A word data (PHA and HK) is listed in Table 2.5. Frame 0 represents the number of subframes that have occurred in the hour. It is directly measured from the onboard clock which provides the time for the μP. Since each subframe is 2 seconds long, the data cycles from 0 to 1799. Frames 1 to 20 are for the twenty PHA channels. Frame 1 corresponds to PHA channel 1 and similarly up to frame 19. Frame 20 contains the veto count rate. Before

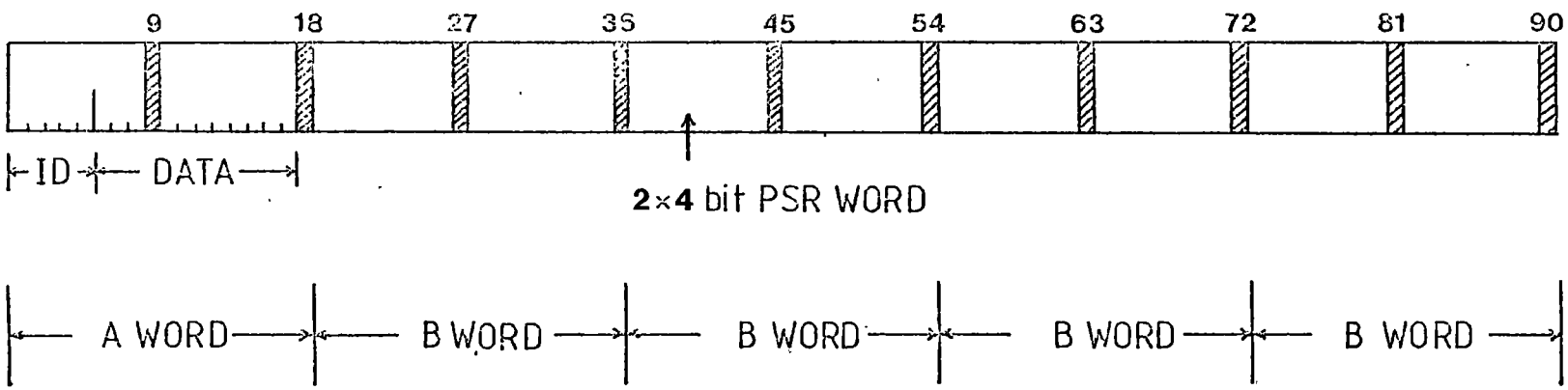

Figure 2.11 University of Tasmania PCM data format 1981. Only one frame of length 90 bits from the total of 32 frames making up the subframe is shown. ID is the identifier of the frame. Hatched areas are parity bits.

transmission the veto rate is divided by 128 so that it does not overflow the available 11 bits. The transmission format of the PHA channel is modulo 2048. Incoming PHA events are added to the previous total and transmitted at the appropriate time. If the total exceeds 2047, the MSB is lost so that the word now lies between 0 and 2047. To deduce the correct PHA count rates at the ground, the previous value of the PHA must be stored and then subtracted from the current value . If this value is negative, 2048 must be added to recover the original PHA rate.

Frames 21 to 24 inclusive are analog channels for transmission of voltages whilst frames 25 to 31 are digital. Frames 22 to 24 are multiplexed to include 4, 16 or 2 data words respectively to allow the monitoring of the HK data that are not expected to vary rapidly. The actual multiplexed HK data that is currently being transmitted is identified by the 4 least significant bits of frame 28.

Frame 21 contains the output voltage of the east/west magnetometer which is the prime azimuth direction sensing magnetometer. Frame 22 is a four-way multiplex with output of the north/south magnetometer being transmitted twice, i.e. every 2nd word. The other 2 multiplex positions are spare and were not used during the balloon flight. Frame 23 is the sixteen way multiplex. Table 2.6 contains a list of the voltages transmitted. Each voltage is sent every 32 seconds. Some voltages, e.g. EHT controlling voltage, and battery voltages are divided by 10 so they may fit in the maximum range of the analog to digital converter (0 - 10 volts). Multiplex words 8 and 11 are further multiplexed to allow for eight other HK voltages. No status bits were available for identification of these words so one word was set to zero. The identification of the other words is then determined by the order from this word. Cycle time for these words are 256 sec. Frame 24 is a two way multiplex transmitting alternatively the north/south (pitch) inclinometer voltage or the east/west (roll) inclinometer voltage.

TABLE 2.5

Allocation of Frames Within the Subframe

Frame Identifier	"A" WORD	
0	Timing in units of 2 sec	
1	PHA Channel 1	
2	" " 2	
3	" " 3	
4	" " 4	
5	" " 5	
6	" " 6	
7	" " 7	
8	" " 8	
9	" " 9	
10	" " 10	
11	" " 11	
12	" " 12	
13	" " 13	
14	" " 14	
15	" " 15	
16	" " 16	
17	" " 17	
18	" " 18	
19	" " 19	
20	VETO Channel	
21	east/west magnetometer	
22	north/south magnetometer + spare)	
23	16 way multiplex)	ANALOGUE
24	Inclinometers)	
25	Command word)	
26	Command word + rocking)	
27	Sun sensor angle)	
28	Day/Hr/Multiplex)	DIGITAL
29	Azimuth angle)	
30	Zenith angle)	
31	Status)	

TABLE 2.6

Multiplex Voltages Frame 23

Identifier		
0	Azimuth error voltage	
1	Motor drive current	
2	Electronics current	
3	EHT controlling voltage ÷ 10	
4	Electronics battery voltage ÷ 10	
5	Motor battery voltage ÷ 10	
6	0 - 1000 mb low altitude pressure transducer	
7	0 - 13 mb high altitude pressure transducer	
8	8 way multiplex	0 Electronics temperature 1 not used 2 not used 3 not used 4 not used 5 not used 6 zero 7 not used
9	Differential pressure transducer in detector	
10	Detector temperature	
11	8 way multiplex	0 Solar cell current 1 East/West magnetometer reference voltage 2 Sun sensor temperature 3 North/South magnetometer reference voltage 4 Inclinometer reference voltage 5 Sun sensor voltage 6 Zero 7 12 volt stabilised supply ÷ 10
12	Azimuth drive speed	
13	Zenith drive speed	
14	Zenith calculated angle from µP	
15	Azimuth calculated angle from µP	

Frames 25 and 26 contain the 16 bits of the command word sent up via the PCM command system and the six bits of the rocking shaft encoder output. Frame 27 contains the sun sensor shaft encoder angles. The day and hour bits are located in Frame 28 with the identifier for the multiplex words. Frames 29 and 30 respectively contain the azimuth and zenith shaft encoder angles. The last frame (31) is the status word. The allocation of bits is shown in Table 2.7. The identification of the multiplex status bit (bit 6) is from the multiplex identifier in frame 28 and was not used during the current balloon flight. The status words also contain direction and on/off flags for manual control of the drive motors. The status of the calibration source on the side of the detector, the star field camera and μP or manual operation of the platform are indicated by the three most significant bits. The next two bits monitor the state of the inlet and vent valves of the collimator section of the detector to see if they are open or closed.

TABLE 2.7

Status Word Allocation (Frame 31)

bit	11	10	9	8	7	6
type "1" "0"	calibration source on/off	camera on off	μP manual	inlet open closed	vent open closed	multiplex

bit	5	4	3	2	1
type "1" "0"	Altitude up/down	on/off	Speed slow/fast	Azimuth CW/CCW	on/off

2.12.2 Ground Station and Online Data Processing

A schematic of the ground station layout is shown in Figure 2.8. The incoming signal is synchronised using a bit sychroniser and the subsequent TTL signal is fed to various other recording or analysing devices. For recording the initial data signal a TEAC A-3300SX tape recorder was used. The signal was recorded on commercial tape using a head saturation recording technique. To represent a one on the tape, current was passed through the recording head in one direction and in the reverse direction for zeros. Up to 2 hours could be recorded without tape changes. Time signals from VNG can be recorded on the other track for absolute timing.

To process data in real time the bit synchronizer signal is fed into a decoder. To frame synchronize the decoder, the data are serially fed into a 185 bit shift register. A synchronizing pulse is generated when the detection of the three frame identifiers '29', '30 and '31' are achieved in bits 1 - 5, 91 to 95 and 181 to 185 respectively of the shift register. The data in location 1 to 8 and 9 to 17 in the shift register is then sent to a 16 bit buffer and the parity bits in location 9 and 18 are fed to a parity checker. If the data in the buffer has the correct parity, then a parity flag, which is sent to the PDP11/10 computer, is set to zero. The flag for synchronization of the "A" word is derived from the parity flag and is also passed to the PDP11/10.

The PDP11/10 outputs a hard copy of the data onto a Teletype Model 43 printer or if required the data can be dumped onto hard disk or floppy disc if there is a failure with the tape recorder. The software, written in machine code, was written by M. Duldig for the 1976 and 1978 balloon flights and has been modified by him to cater for the new telemetry format. Full details of the software are in Duldig (1981).

To monitor in real time the many functions onboard the platform, a dedicated μP system was constructed to output all the data in real time on a VDU and to estimate the pointing position of the telescope in celestial coordinates. The machine dedicated to the display of data is referred to as the quick look μP(QLμP) whilst the second machine for display of aspect information is called the graphics μP(GμP). Both machines act independently using data from the 16 bit buffer in the decoder. The data interrupt is generated from the "A" word flag in the decoder. Both machines were constructed by D. Warren who also wrote the software for the GμP. Details of the hardware and software are in Warren (1980).

The software for the QLμP was written by the author. Conversion of data to angles or voltages was done by machine code arithmetic and converted to ASCII characters for transmission at 9600 baud to a VDU. As data is received, it is converted and vectored to the appropriate place on the screen. Figure 2.12a is a photo of the VDU display from Warren (1980). The top left displays the time and count rate. Below this is the pointing data, i.e. azimuth and zenith angles, drive speeds and directions and calculated angles. Magnetometer, inclinometer, rocking and sun sensor data follow. The bottom block contains housekeeping voltages and all other slowly varying parameters. The block of 8 words to the bottom right is the 8 way non multiplexed voltages. The 1981 version used for UTIC81 is slightly modified and includes improved presentation and more data.

The GμP computes the celestial position of the optical axis of the detector from the azimuth and zenith angles of the detector, the rocking angle and the onboard clock using the equations listed in Section 2.6.2. Corrections to the azimuth from the sun sensor and magnetometer voltage are calculated. Latitude and longitude are input via a keyboard. Figure 2.12b is a photograph of the display from Warren (1980).

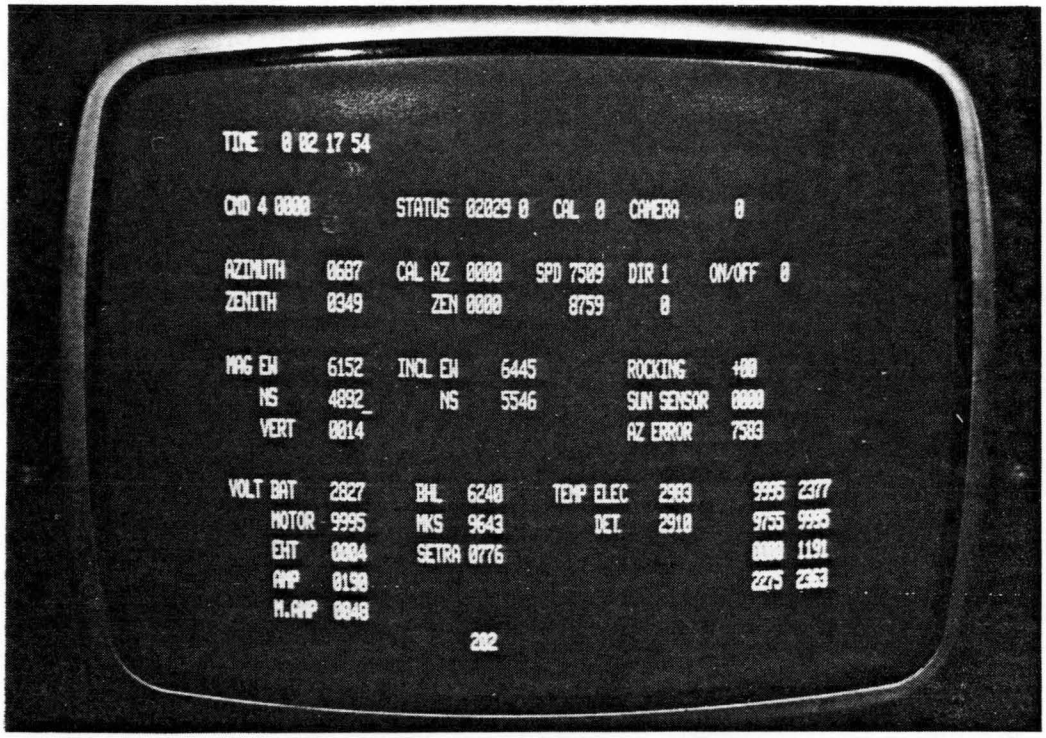

(a) QLµP VDU display

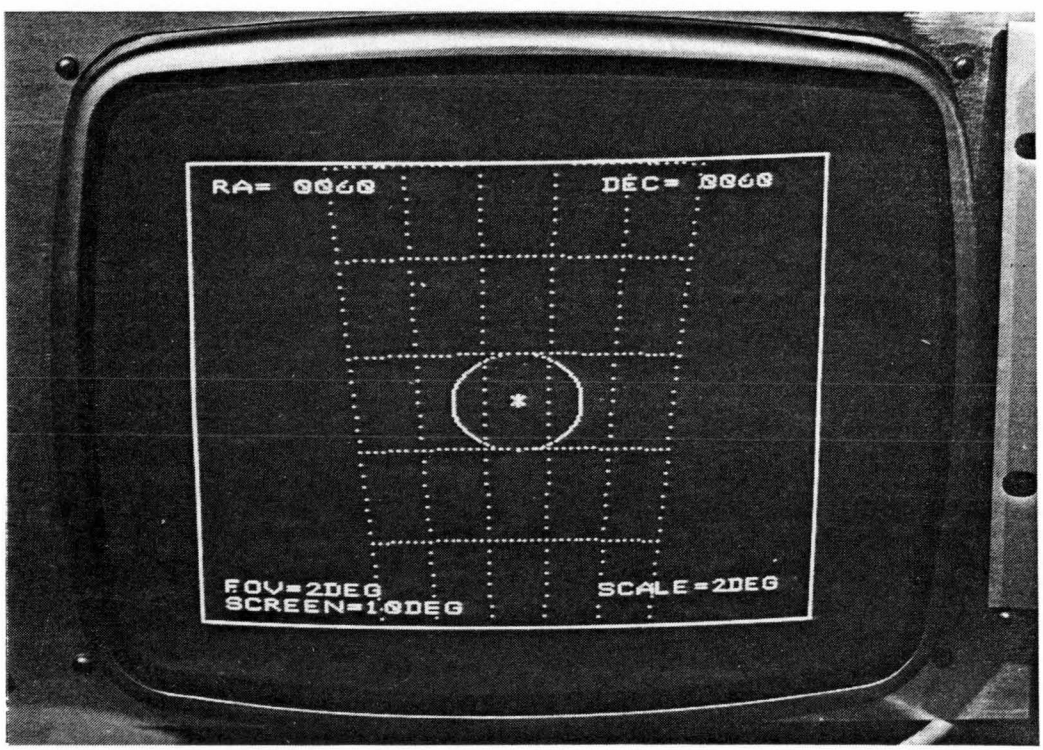

(b) GuP display

Figure 2.12

Vertical and horizontal dashed lines represent celestial grid lines with a spacing of 2 degrees centred at the position of the source under investigation. The circle is the 2° field of view about the actual pointing position. The centre position of the grid is displayed at the top of the screen in units of degrees. Further improvements to the system will permit display on the screen of star positions taken from a CCD camera mounted on the altitude shaft of the platform (Tholler, 1982). Star positions from the GμP memory will also be displayed. This will facilitate improved aspect control allowing the effect of pointing corrections to be observed.

CHAPTER 3

Observations and Data Reductions

3.1 The UTIC81 Balloon Flight

The platform was prepared for its inaugural balloon flight during November 1980. It was launched at dawn on 1980 November 25 at Alice Springs, Australia. Unfortunately the balloon burst at 60,000 feet, possibly from thermal shock from the cold of the stratosphere. There was insufficient time to dump ballast or to sever the balloon and the platform landed heavily on rocky ground north of Alice Springs. The frame was slightly bent and the magnetometers were lost. Approximately two weeks would have been required to fully test and realign the platform. By that time the launch window of the wind turn around at altitude would have finished. Flight durations would have been unacceptably short so no further flights were undertaken. Where mentioned in this chapter the abortive flight is referred to as UTIC80.

The next launch opportunity was during November 1981 and the flight name used in the following discussion is UTIC81. Due to unseasonally bad ground weather the platform was not launched until December 2nd at 0605 local time from Alice Springs airport (latitude -23.9°, longitude 133.9°E) using a 15 million cu ft balloon and carrying 150 kg of ballast. Since wind turn around at altitude (130,000 ft) was almost over, a duration of 6.5 hours at float was achieved before the platform reached the maximum telemetry range of 500 kilometres. The platform was recovered in excellent condition on the edge of the Gibson desert (latitude -23.0° longitude 130.5°E).

3.1.1 Flight Performance

Figure 3.1 represents some of the various housekeeping parameters as a function of the duration of the flight. Figure 3.1a illustrates the temperature profile of the sun sensor, UT electronics package and the detector. They respectively represent the outside skin of the platform, the principal source of power consumption and since the

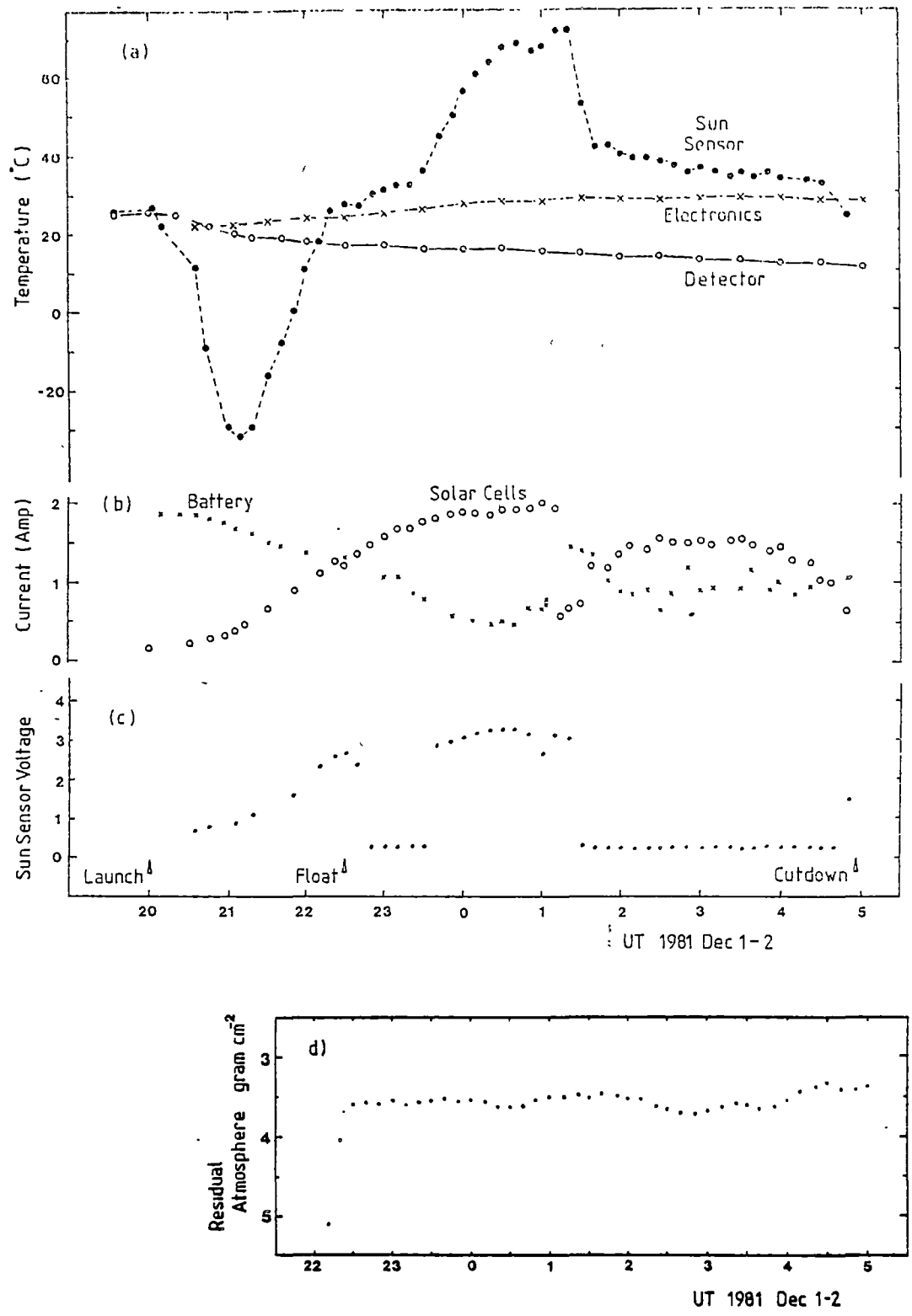

Figure 3.1 Housekeeping data during the 1981 Dec 2 flight

a) Sunsensor, electronics and detector temperatures
b) Solar cell and battery currents
c) Sunsensor voltage
d) Atmospheric depth

detector is massive and uses little power the best estimate of the mean temperature of the platform. The detector temperature varied from 26°C at launch to 10°C at cutdown whilst the encoder package stabilised at ~28°C by 0200UT. The sun sensor temperature varied dramatically. At 2100 UT it reached a minimum of -31°C whilst passing through the coldest region of the stratosphere. At altitude, it was 25°C but increased quickly to ~70°C by 0100 UT due to radiation of the rising sun. At 0100 UT the balloon shadowed the platform as the sun was now within ~30° of the zenith. This is indicated by the sun sensor voltage dropping to near zero in Figure 3.1c. The voltage is the output voltage of the sensing phototransistor and is proportional to the intensity of the detected solar flux. The period between 2245 UT and 2330 UT when the sun sensor voltage was again zero, was caused by shadowing of the sun sensor slit by the rear support for the rotating head. This occurs when the platform directly faces away from the sun. The current from the solar cells is shown in Figure 3.1b. As expected, it rose as the sun's elevation rises reaching a peak of 2 amps before the balloon's shadow reduced the current to ~0.5 amps. At 0300 UT, the sun was at zenith and the solar cell current was ~1.5 amps, compared to an expected current of ~2.3 amps if no balloon were in the way. The balloon's opaqueness reduced the power from the solar cells to ~70% of the maximum expected.

The atmospheric depth of the platform during the flight is shown in Figure 3.1d. Several ballast drops were made near 0100 and 0200 UT resulting in the increased altitude after these times.

Figure 3.2 shows the azimuth error of the platform as determined from sun sensor for a one-hour period at 0^{hr}UT. The azimuth of the sun was determined from equations 2.1 to 2.9. The apparent Right Ascension and Declination of the sun was interpolated from values listed in the Astronomical Almanac. After 0025 UT the platform changed

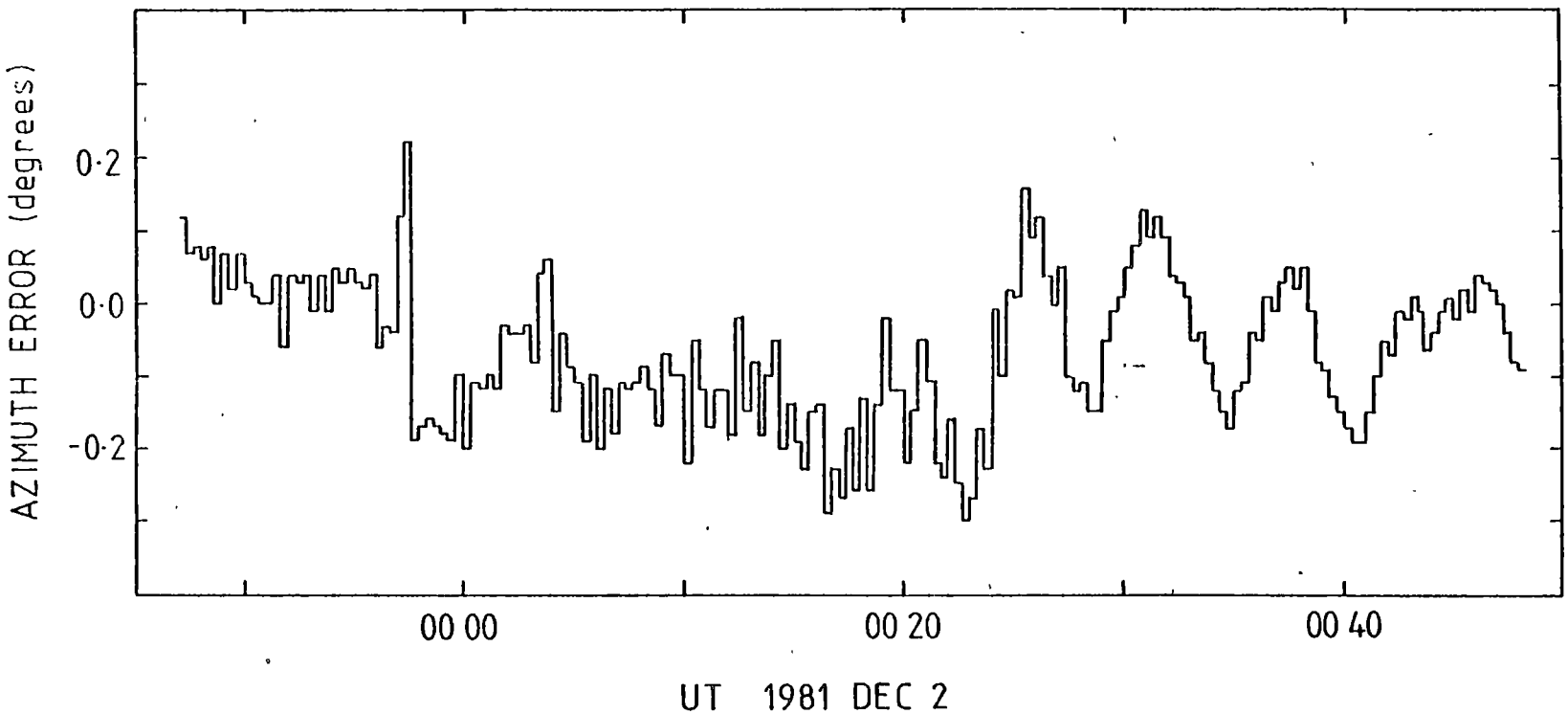

Figure 3.2 Azimuth error of the platform, in 20 sec bins, from 23 47 UT Dec 1 to 00 48 UT Dec 2,1981.

its mode of pointing from a slowly varying azimuth to an oscillation of peak to peak amplitude of ~0.2° and period 6 minutes. The azimuthal oscillations are known as dither. The rms deviation from the mean of -0.07° is 0.13° which projects onto the sky as a rms azimuth error of 0.04° for an average source zenith angle of 30°. This yields a collimator transmittance of 99%. Azimuth errors are therefore dominated by systematic effects on the local magnetic field from geographic changes or local effects. The variation in the direction of the earth's field due to change in the geographic coordinates of the balloon was about 0.9° during this flight. There is an uncertainty of ±0.25° in the magnitude of this variation. Magnetic material on the platform causes azimuth and elevation-dependent distortions in the field about the magnetometers. The amplitude of these errors was estimated during pre-flight calibrations. Corrective azimuth offsets were telemetered to the microprocessor during flight. An example of the offsets measured during ground calibrations is shown in Figure 3.3. In this case, the detector zenith angle was zero. The principal source of distortions to the local field is the IC detectors especially at azimuths such that the same field lines thread both the magnetometers and the IC detectors. This occurs at azimuths of ~90° and ~270°.

The technique for measuring the magnetic azimuth errors is as follows. The platform was placed in a region of no known magnetic materials and levelled by the use of jacks. The signal of the magnetometer, that is fed into the velocity feedback amplifier, was zeroed by driving the magnetometer drive until the sensing magnetometer was aligned to the local field lines. The angle of the shaft encoder was read and compared to the geographic azimuth of the platform. The true azimuth of the platform could be determined using a theodolite to a precision of 15 arc sec. The magnetometer shaft encoder angle measurement has a precision of 0.07°.

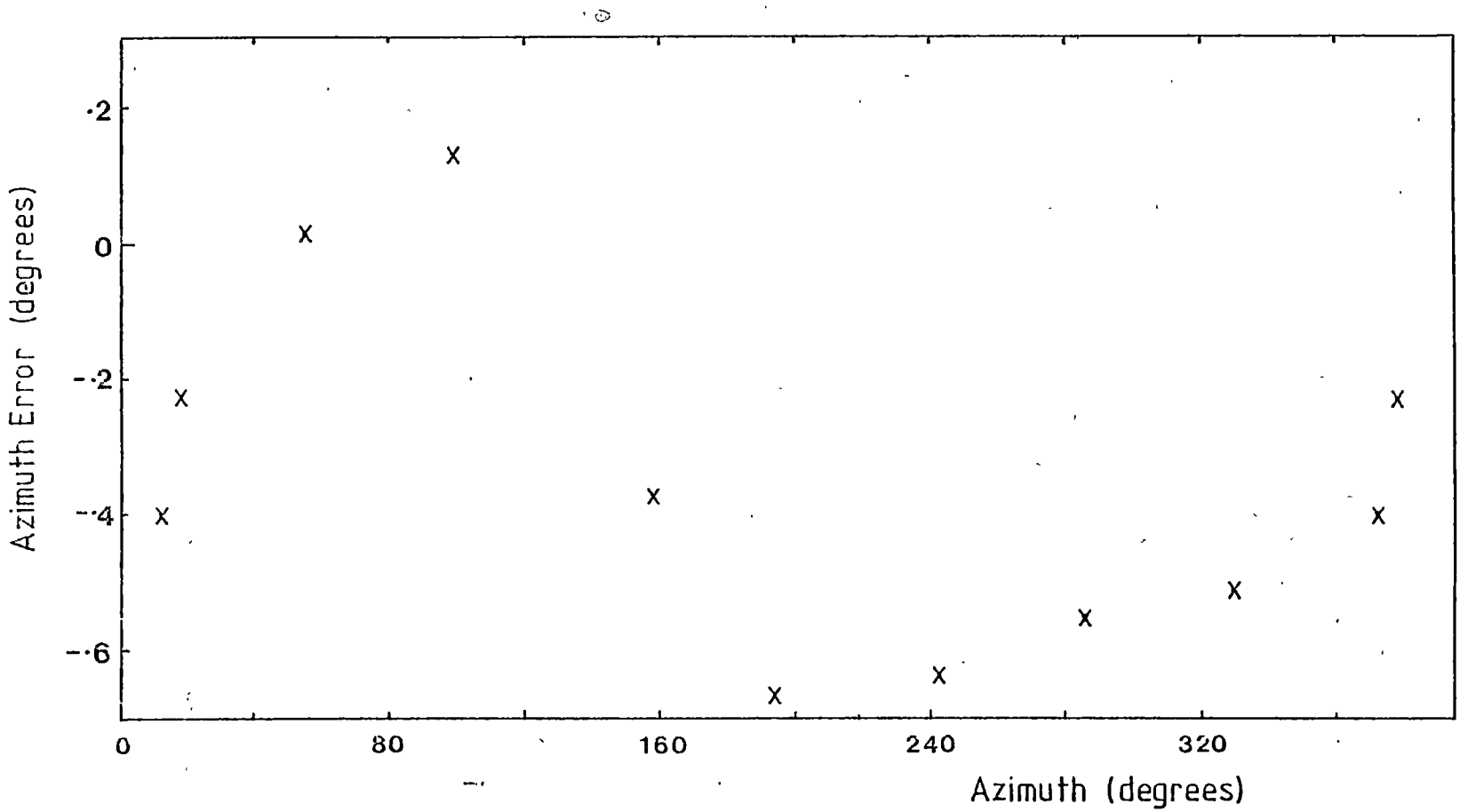

Figure 3.3 Error in geographic azimuth and magnetic azimuth from the distortions in the local magnetic field due to magnetic materials in the platform. The detector zenith angle was zero degrees.

The azimuth variations experienced during pointing tests when suspended during ground tests in the payload preparation building were of a comparable magnitude and frequency to the azimuth variations experienced during the flight. Even though the environments are markedly different, ground tests provide a satisfactory means of determining the pointing stability of the platform and of adjusting the time constants of the azimuth servo feedback amplifiers to achieve optimum dampening.

3.1.1 Inflight Problems

Several problems were encountered during the flight which limited or degraded the quality of the data that could be acquired. Approximately an hour after launch it was noted that the zenith drive would not move the detectors. After experimentation with the UT rocking in attempts to free the drive, it was concluded that the inboard bearing of the UT detector had seized and fixed the zenith angle of the UT detector at 6.2°, the angle it was at launch. The IC detector could be moved over a limited range by using the UT rocking cam to move the IC detector relative to the UT detector. In this way it was possible for the IC detector to view Sco X-1 whilst the object remained outside the field of view of the UT detector. The two objects that were observed by both detectors during the flight were IC4329A, an extreme Syl galaxy and the hard X-ray pulsar GX1+4.

At the recovery of the platform, the inboard UT bearing was free possibly from the impact of landing. However, the bearing surface appeared to have been bonded from some form of violent impact. The only source of such movement before or during the flight was the violent motion experienced during launch.

Two other problems which reduced the quality of the pulse height data were the excessive background in the lowest six PHA channels and electrical interference from the UT rocking drive. The source of the excess background counts is believed to be a large different-

iation time constant of 10 μsec in the veto amplifier circuits which reduces the efficiency of the veto circuits. Reducing the time constant of the veto circuits from 10 μsec to 1 μsec is expected to reduce the low energy background at balloon altitudes.

Figure 3.4 shows the background spectrum from various stages of the UTIC81 flight with a comparison of the UTIC80 background spectrum on the ground. The 9 GV cosmic ray cutoff rigidity at Alice Springs is relatively high. This assists in reducing the cosmic ray induced component of the background. The passive shield around the sides of the detector for the UTIC81 flight was increased with the addition of lead and extra pewter which substantially reduced the background count rates above 30 keV. The comparison at altitude and on the ground for the UTIC81 flight is shown in Figure 3.4b. Experience with background levels during the 1978 flight (Duldig, 1981) shows that background levels at float and on the ground are very similar. In future flights it is expected that the true float background will be similar to the UTIC81 ground background.

The last problem concerns the collimator. After the balloon flight the xenon in the detector volume was pumped out for cleaning and the detector was opened. The collimator was found to be severely damaged and distorted from pressure exerted by the Al window upon the detector side of the collimator. It is not certain when the damage occurred. It happened either during pumping out operations after the balloon flight or when the detector was flown back to Hobart for emergency repairs prior to the flight. The EHT supply inside the detector volume had developed a short-circuit and since the pressure tank for emptying or filling the detector was left in Hobart, it had to be air freighted back to Hobart for repairs. The collimator section was incompletely filled allowing the mylar ends to collapse. The resulting low pressure in this section relative to the xenon section

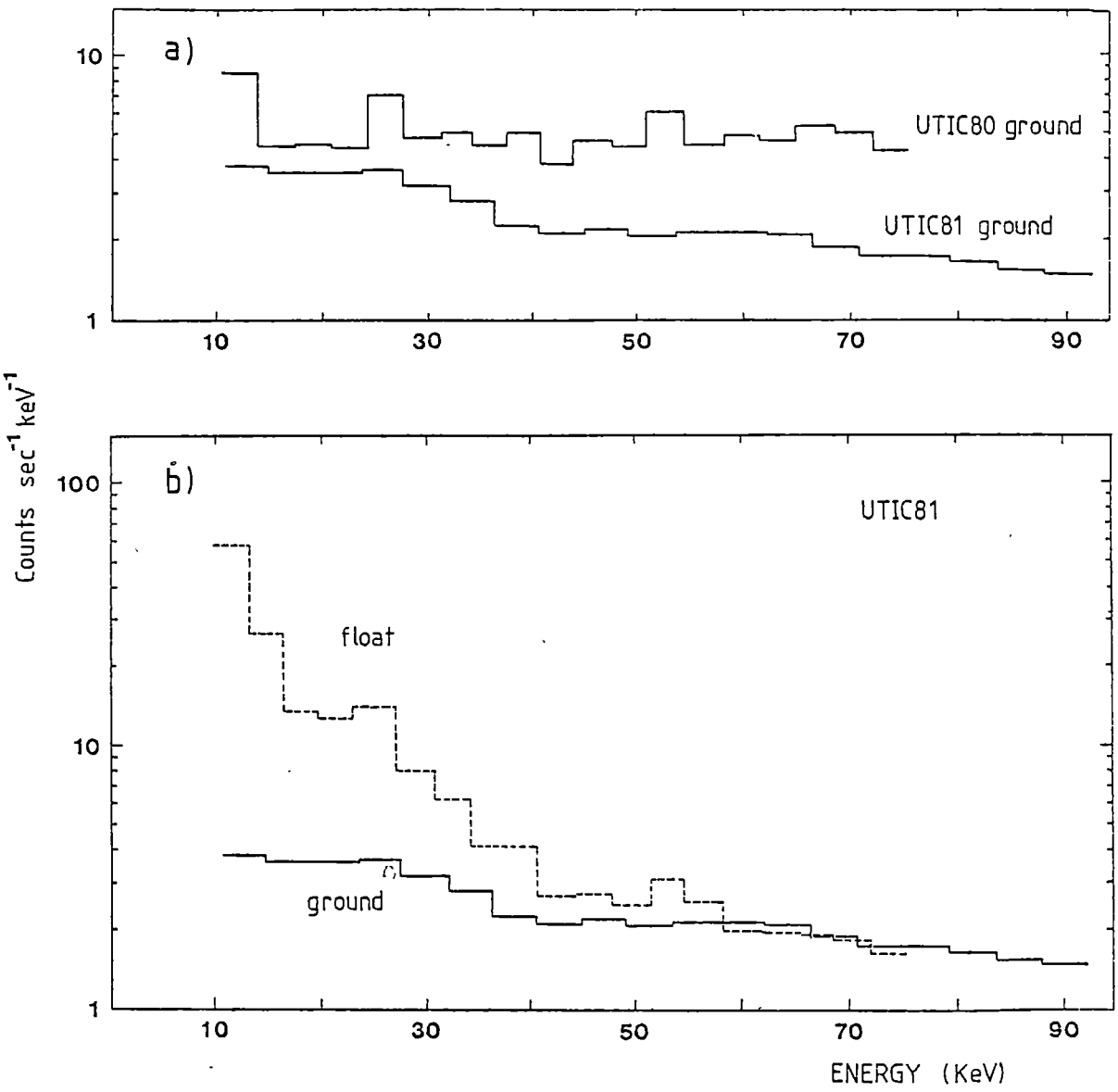

Figure 3.4 Background spectra from the UTIC80 and UTIC81 flights

a) Comparision of UTIC80 and UTIC81 on the ground. UTIC81 had increased passive shielding.
b) Ground and float backgrounds for UTIC81. The increase at low energies in the float background is believed to be due to the inefficiency of the veto system (see text).

may have forced the window against the collimator whilst in the aircraft.

To estimate the transmittance, the distorted collimator was treated as 4 separate quadrants of equal area. The shift in the supporting brackets around the outside and the bend in the support frame were estimated and hence the angle from the ideal was calculated for each quadrant. Figure 3.5 gives the estimated collimator efficiency as a function of azimuth and elevation. The dashed line represents the ideal conical response with FWHM = 2.1°. The dashed cross is the centre of this response with an efficiency of 1. The solid line is the efficiency curve for the distorted collimator with contours at efficiencies of 0, 0.2 and 0.4. The peak efficiency, marked by the solid cross, is 0.42. Since the exact state of the collimator was not known for the balloon flight, subsequent reductions of data have been carried out for both cases.

3.1.3 Count Rates

Figures 3.6 to 3.8 show overall count rates during the flight whilst at altitude. Figure 3.6 represents the total counts in PHA channels 1 - 3 corresponding to the energy range 9.7 to 20 keV (see Section 3.1.4). Integration time for all three graphs is 30 seconds. Immediately apparent in Figure 3.6 are the large spikes in the count rate, most noticeably during the 1st hour of the data. Several other events occur at odd intervals during the rest of the flight. These spikes are also present in Figure 3.7 of the plot of the summed PHA 4 to 19 (20 to 75 keV) and in the veto rates (Figure 3.8). Correlating the spikes with housekeeping data revealed the source was electrical interference from the UT rocking drive. Interference tests on the ground did not reveal the rocking drive to be a problem. Fortunately little rocking was done during the observations of GX1+4. The background data obtained before the scan of IC4329A is completely useless due to continuous rocking.

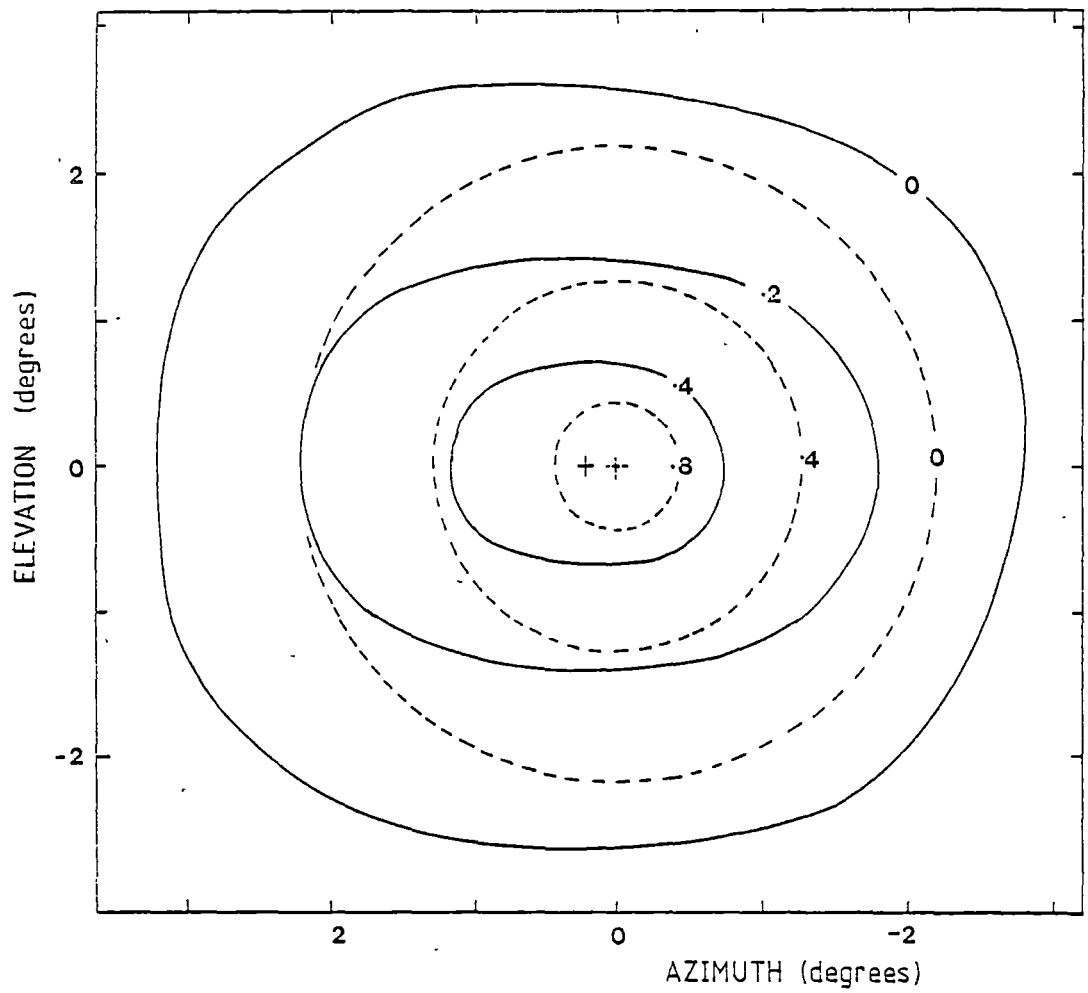

Figure 3.5 Collimator efficiency curves as a function of azimuth and zenith. Dashed line is ideal 2.1° FWHM response and solid line the response of the damaged collimator. Crosses are peak efficiency and numbers are the transmission factor.

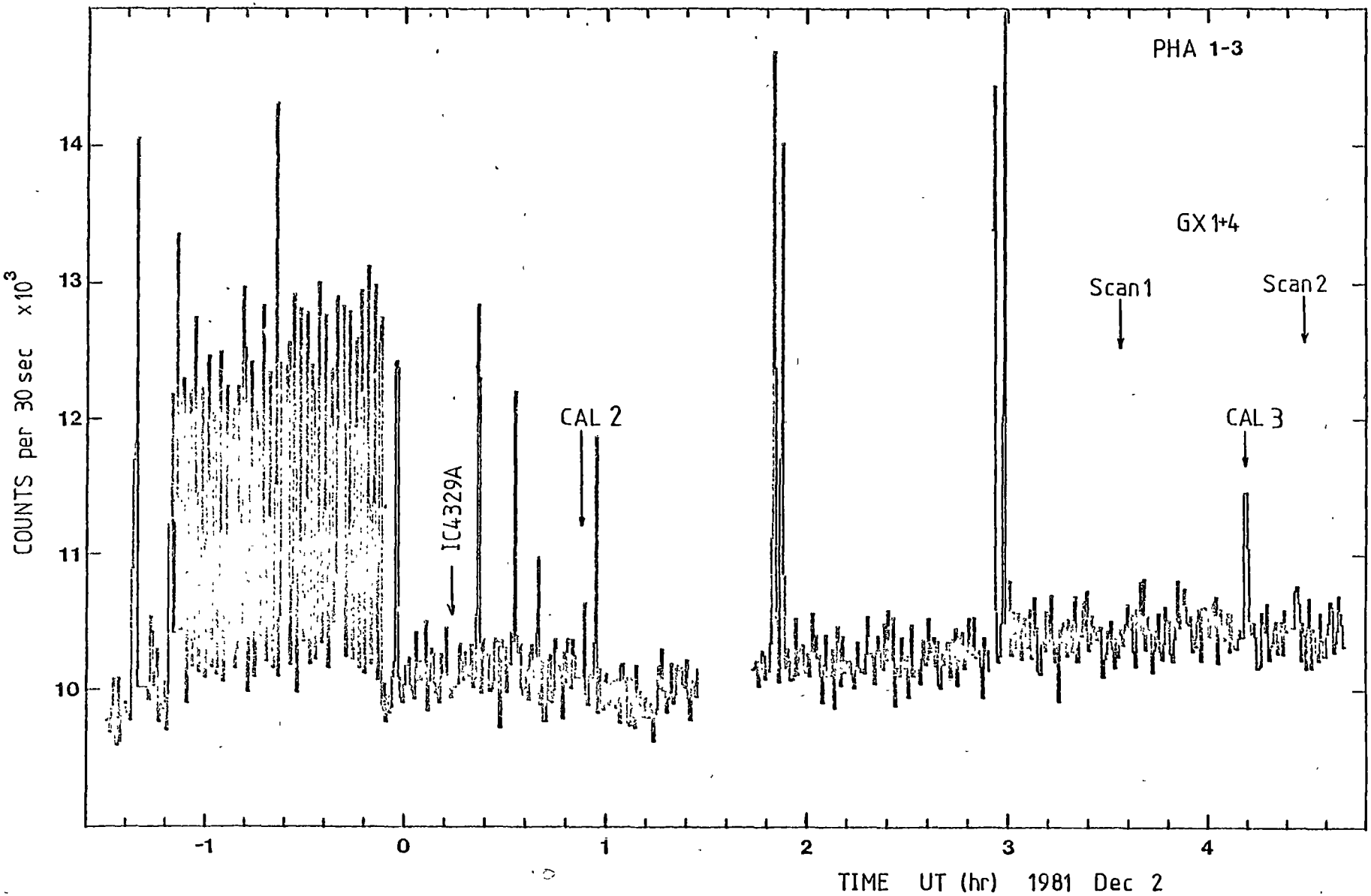

Figure 3.6 PHA count rates for channels 1 to 3 (9.7 to 22 keV). Integration time per data point is 30 sec. The times of the scans of IC4329A and GX1+4 and the two inflight calibrations are marked.

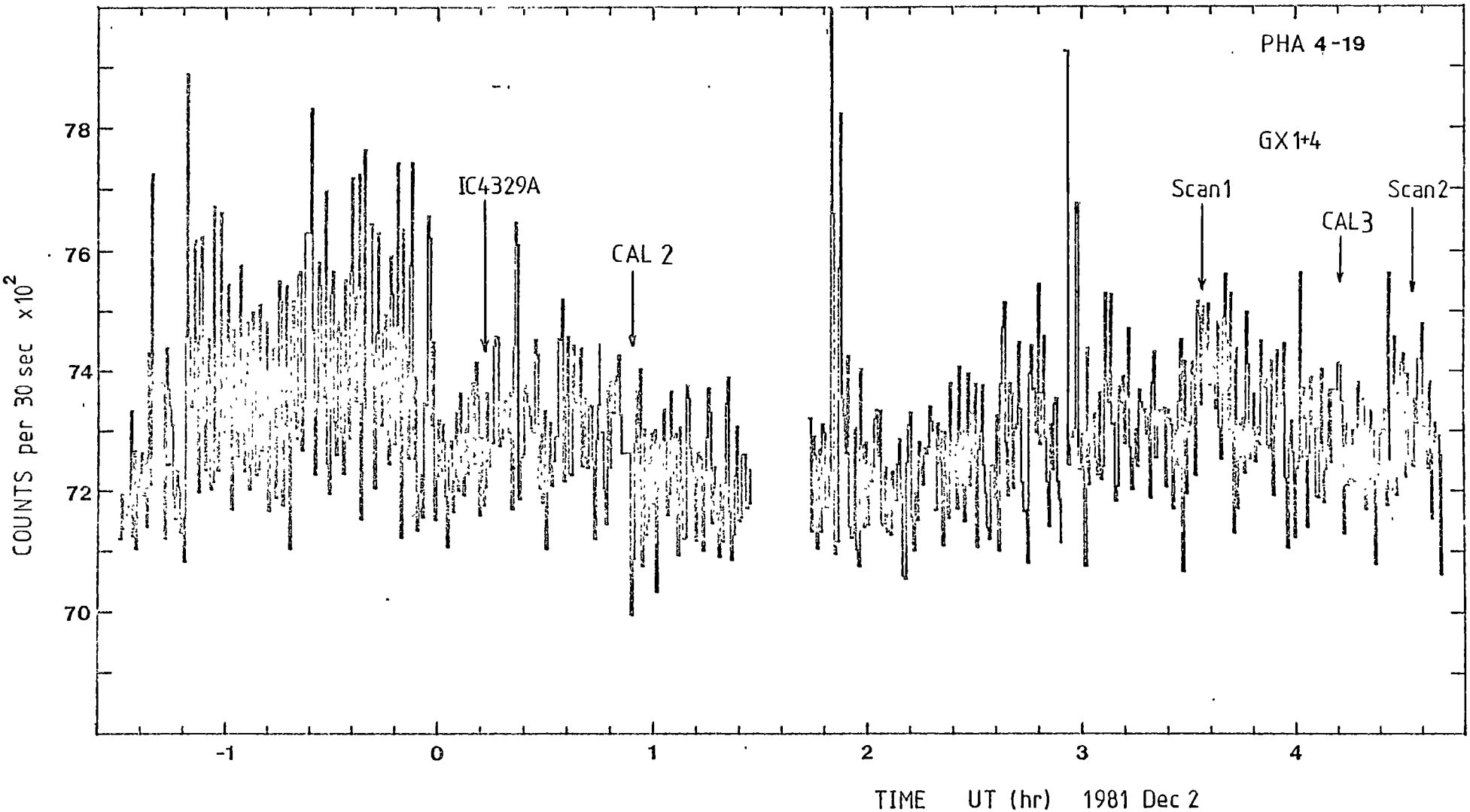

Figure 3.7 PHA count rates for channels 4 to 19 (22 to 76 keV). Integration time per data point is 30 sec. The times of the scans of IC4329A and GX1+4 and the two inflight calibrations are marked.

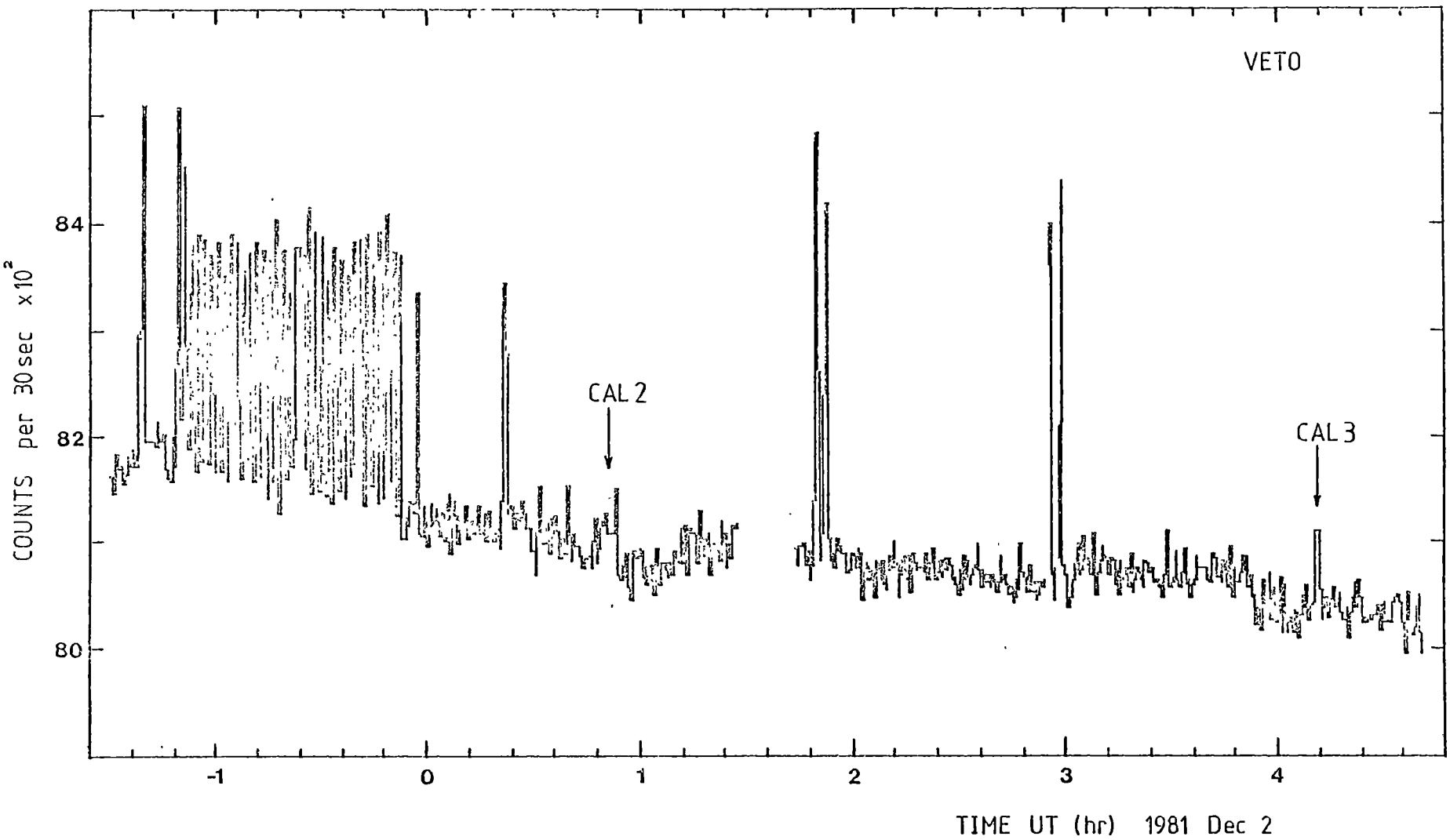

Figure 3.8 Veto count rate (divided by 128). Integration time per data point is 30 sec. The times of the two inflight calibrations are marked.

Three calibrations of the detector were made using the Am_{241} source on the side of the detector: one prior to the flight and two during the flight. The ground calibration was done at 1943 UT approximately 20 minutes before launch and is called CAL 1. The two inflight calibrations are called CAL 2 and CAL 3 and were taken at 0050 UT and 0412 UT respectively. Typical durations are 90 seconds. Both are marked in Figures 3.6 to 3.8. Most of the counts from the calibration source have been deleted from the count rate curves and just their positions have been marked. An analysis of the detector parameters using the calibrations is presented in Section 3.1.4.

The gap in the data at 0135 UT is due to failure of the telemetry system. Initially the only transmitter planned to be used was the transmitter mounted in the National Scientific Balloon Facility (NSBF) Consolidated Instrument Package (CIP) and operated in the L band. Due to the requirement of having an instantaneous pressure reading for safety purposes and the lack of a calibrated pressure transducer in the CIP, a second Australian Balloon Launching Service P band telemetry package, with its own pressure transducer, was added. This latter package was used for telemetry until its battery failed at 0130 UT. Telemetry was transferred to the CIP using a discrete command when the reason for telemetry failure was established. Unfortunately the error rate increased substantially from ~2 per hour to ~300 per hour. The error rates are for the errors detected in HK or PHA words and do not include possible errors in the PSR words which comprise 80% of the transmitted data (see Section 2.12.1). During the reduction of the data much time was spent in correcting or noting errors in the data files (see Section 3.2).

3.1.4 Detector Calibrations

As mentioned in the previous section, three calibrations were

taken prior to or during the flight. Figure 3.9 is a plot of the two flight calibrations from the onboard 59.9 keV Am_{241} source. Background has been removed and error bars are one sigma. The peak at PHA channel 15 corresponds to 59.9 keV and the peak in channel six is the escape peak at ~29.1 keV. CAL 1 made prior to the launch is similar except the gain of the detector is higher and the 59.9 keV peak occurs in PHA channel 12. The reason for the gain change is the small change in pressure in the detector volume as the outside air pressure changed. Gas gain in gas filled detectors is highly dependent on gas pressure. (Gain α Pressure^{-10}). For a gain change of 23%, the pressure must have decreased by 2.5% arising from the flexure of the Al window between the collimator and the detector volume.

Since no gain change occured between CAL 2 and CAL 3, the two were added together and by using a least squares fitting procedure, a model of the calibration PHA curve was fitted to the data. The equations describing the model are in Section 1.9. Table 3.1 lists the derived parameters.

TABLE 3.1

Counter Parameters from the UTIC81 Flight

	CAL 1	CAL 2 + 3
PHA low energy limit (keV)	10.6	9.7
high energy limit (keV)	92.3	75.6
energy/channel (keV)	4.30	3.47
Resolution (%) FWHM at 60 keV	44.6 ± 0.9	42.0 ± 0.7
Escape Peak Ratio	0.50 ± 0.01	0.50 ± 0.01

The energy resolution of 42% at 60 keV is significantly larger than normal with a xenon filled proportional counter. The reason for this result was stretch of some of the anode wires. Repairs after

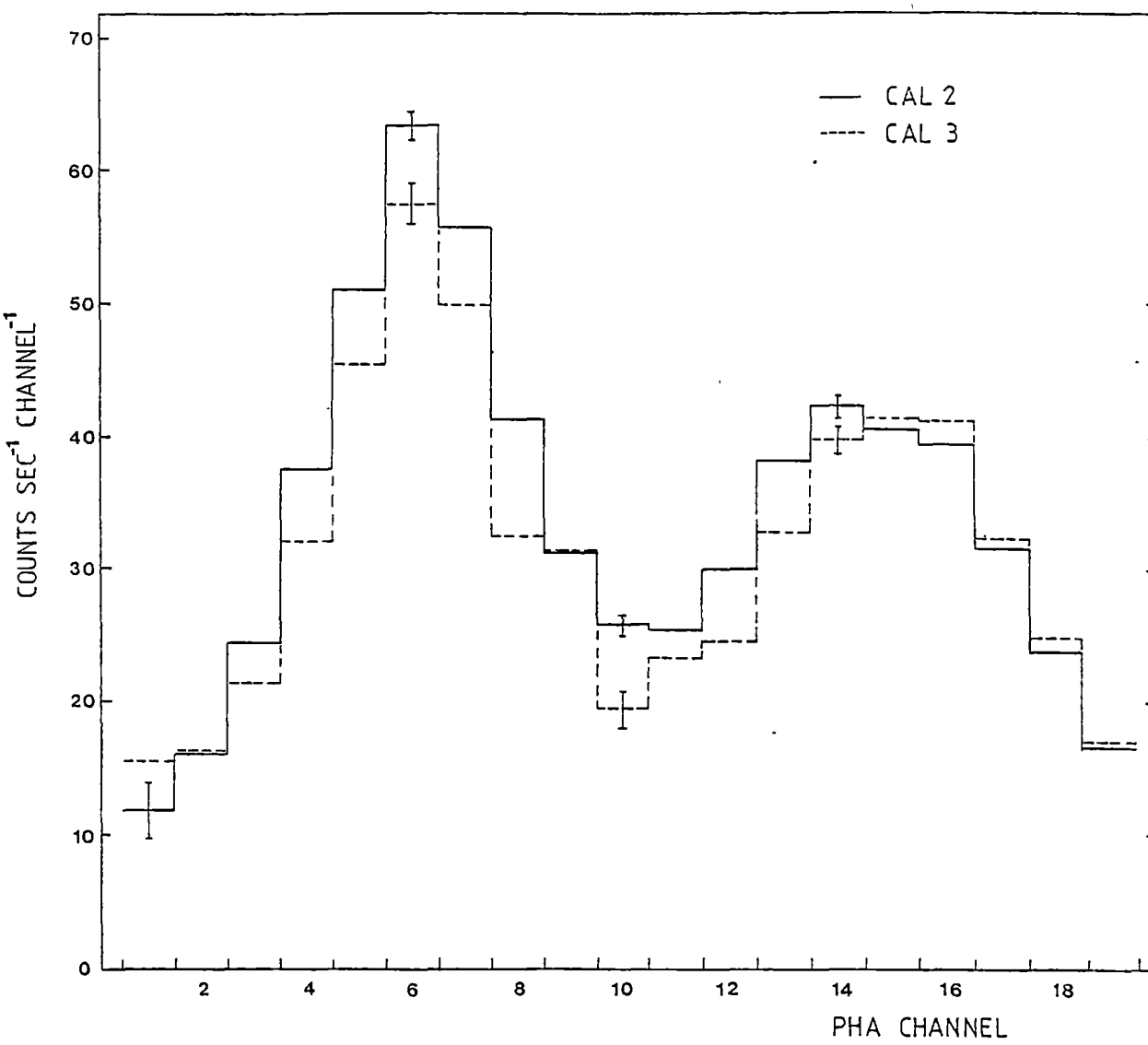

Figure 3.9 Count rate spectra of the two inflight calibrations from the Am_{241} source. Background has been removed and error bars are one sigma.

the flight improved the resolution to ~25% at 60 keV.

The majority of the X-ray events detected by the counter are measured in the tray nearest the window. However the calibration source principally illuminates the middle trays from the side. Comparison of calibration distributions from through the collimator and through the side revealed no significant differences. If the resolution of the detector were <25% FWHM the detection of any such differences would be more likely.

3.2 Data Reduction Procedures

As mentioned in Section 2.12.2, data are recorded directly from the bit synchronizer to the tape recorder. To transfer the data to the PDP11/10 after the flight, the program that provides quick look data and hard copy to the teletype during the flight was modified by the author with the assistance of M. Duldig. The modifications enable the transfer of HK and PHA data (the "A" words) directly onto hard disk in the form of ASCII data files. The program is called UTDUMP as it dumps UT data from tape into disk data files in the form of records. Each record of 128 ASCII characters represents a complete subframe and contains time in hours, minutes, and seconds, azimuth and zenith angles, sun sensor shaft encoder angle, the east/west magnetometer voltage, rocking angle, command and status words and the twenty PHA channels. Each record, when combined with the geographic location of the platform, is sufficient to provide the platform aspect in celestial coordinates (see Section 3.2.1). The status word is used to determine whether the calibration source is on or off by testing if the status bit for the calibration source is high or low. The command word is used principally to monitor any changes in the azimuth variation word telemetered to the platform since there is not a separate HK word which monitors the value of the azimuth variation word currently being used. The magnetometer voltage can be used to determine the precise azimuth

and hence to correct for any small azimuth variations knowing the azimuthal sensitivity of the magnetometer. Before the platform azimuth servo was turned on at float altitude, the freely rotating platform provided the required magnetometer calibration by using the sun sensor angle as azimuth reference. The sensitivity of the east-west magnetometer for UTIC81 was 0.0196 volts per degree.

Even though ASCII character files require considerably more storage room on disc than data formatted in binary, they provide several advantages. They can be read directly to monitor the data and more importantly, the data can be easily edited to correct for errors. All records with known rocking movements were removed. Records on either side of the calibration records were also removed since as a result of encoder sampling delays, the calibrator status flag was not a reliable indicator of the state of the data. A preamble was placed at the beginning of each UTDUMP file which contained the Julian day, various option flags and a list of possible sources for observation with their positions that may have been observed. The first stage in reducing the data was to deduce the pointing direction of each data record and to assign that record to a particular file. These files represent source, background or calibration source or if several sources were known to be present in the field of view, a separate file for confused observations. The equations for converting azimuth-zenith to celestial coordinates are listed in section 2.6.2.

Before the reduction software is described in detail, a flowchart of the overall reduction software is shown in Figure 3.10. UTDUMP converts taped data to a record-orientated disc file. The program ASPECT deduces the aspect solution of the detector with the use of a file which contains the geographic location of the platform and assigns the data record to either source, background, calibration source and/or sun sensor error files. The background data file is reduced by the

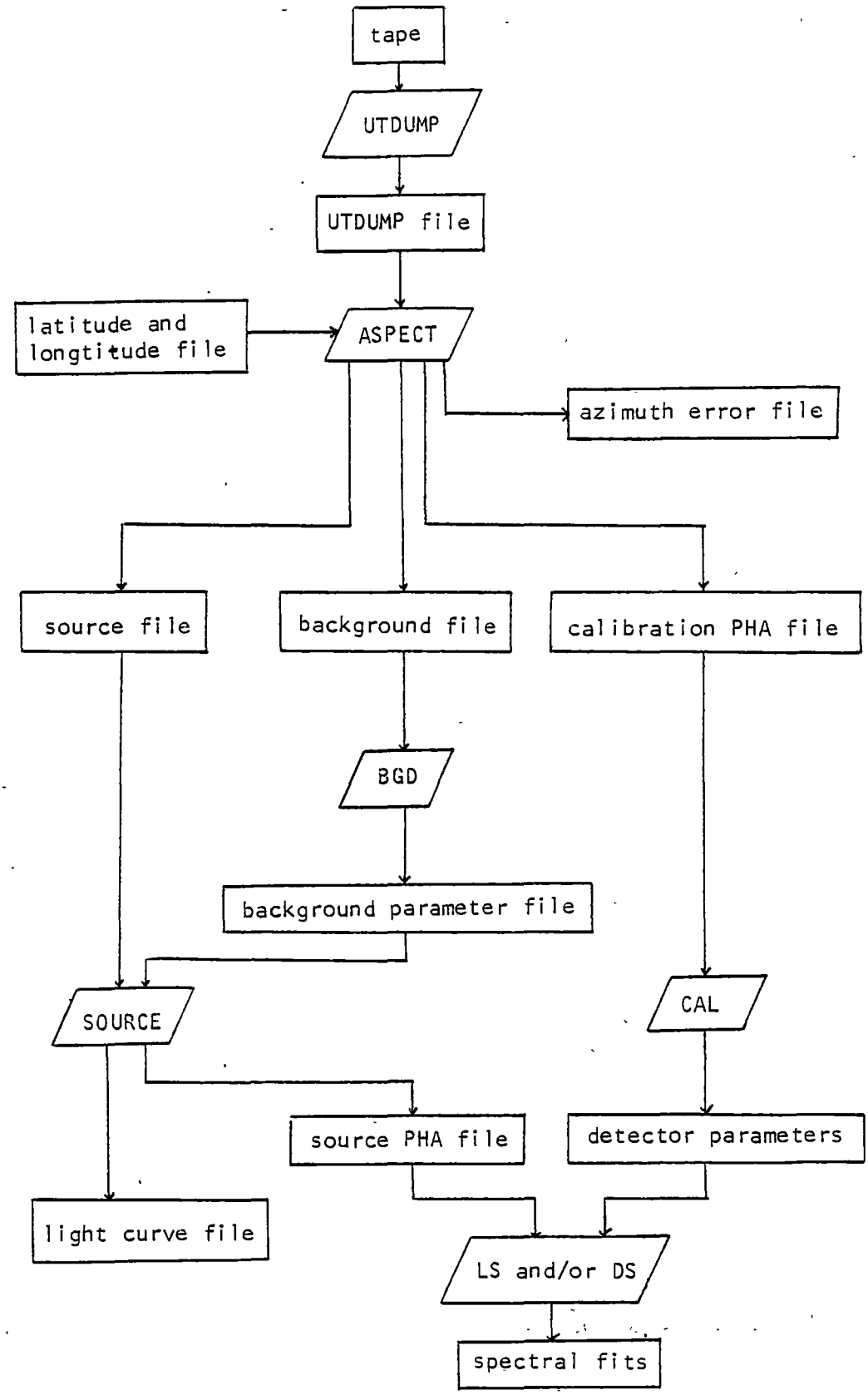

Figure 3.10 Flowchart of the data reduction software.

program BGD to yield background parameters which describe the shape of the background. The source data file, combined with the background parameters, are used by the program SOURCE to produce source fluxes and light curves. The calibration data in the form of background removed calibration source pulse height distributions are reduced to counter parameters by the program CAL. The source fluxes and counter parameters are converted to intrinsic fluxes using the counter model programs LS and DS. A more complete description of each program follows.

3.2.1 ASPECT

The program for deducing the pointing is called ASPECT and this program and all others for reducing the data except LS, were written by the author in FORTRAN. Figure 3.11 is a flowchart of ASPECT. The preamble to the UTDUMP data file is read followed by the data file containing the latitude and longitude of the platform. This file also includes the azimuth errors induced from the platform materials (Figure 3.3). All possible sources are listed with names, celestial positions and approximate source strengths. The reason for the inclusion of historic source strengths will be discussed later.

The start of the main program loop begins with the reading of the UTDUMP data record. If the end of file has been reached, the program stops and all data files are closed. Time and the interpolated geographic coordinates are computed next. The local solar and siderial times follow from equations 2.1 and 2.4. The command word is interrogated and if its ID is A, the azimuth variation data MAGVAR are updated. The calculation of platform azimuth AZ and zenith angle Z is next. The first includes the effect of MAGVAR and azimuth errors from platform materials and the latter includes rocking angle corrections.

If the sun is visible, as defined by the sun sensor voltage, the azimuth of the sun is computed using equations 2.7 to 2.9. The true

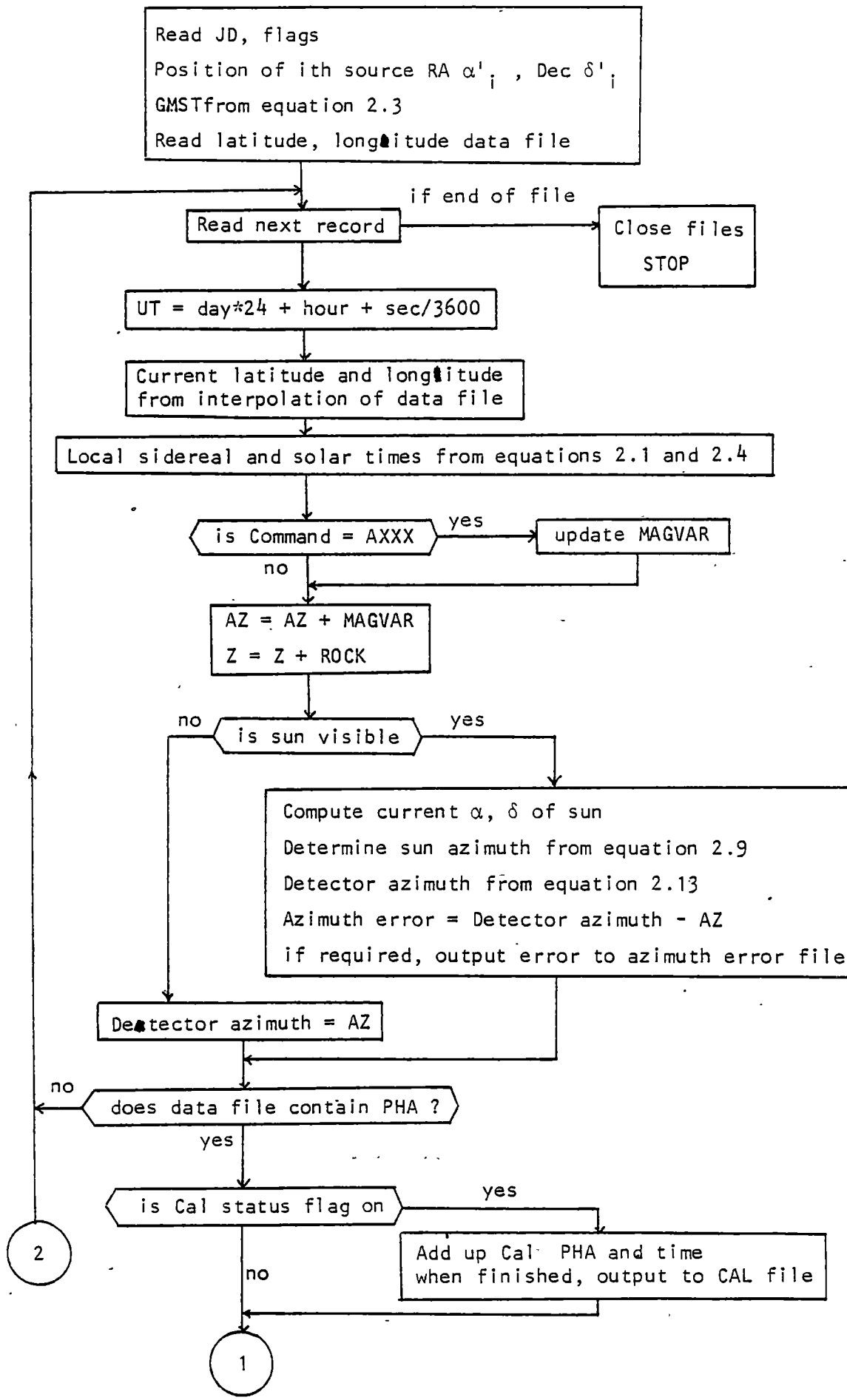

Figure 3.11 Flowchart of the program ASPECT.

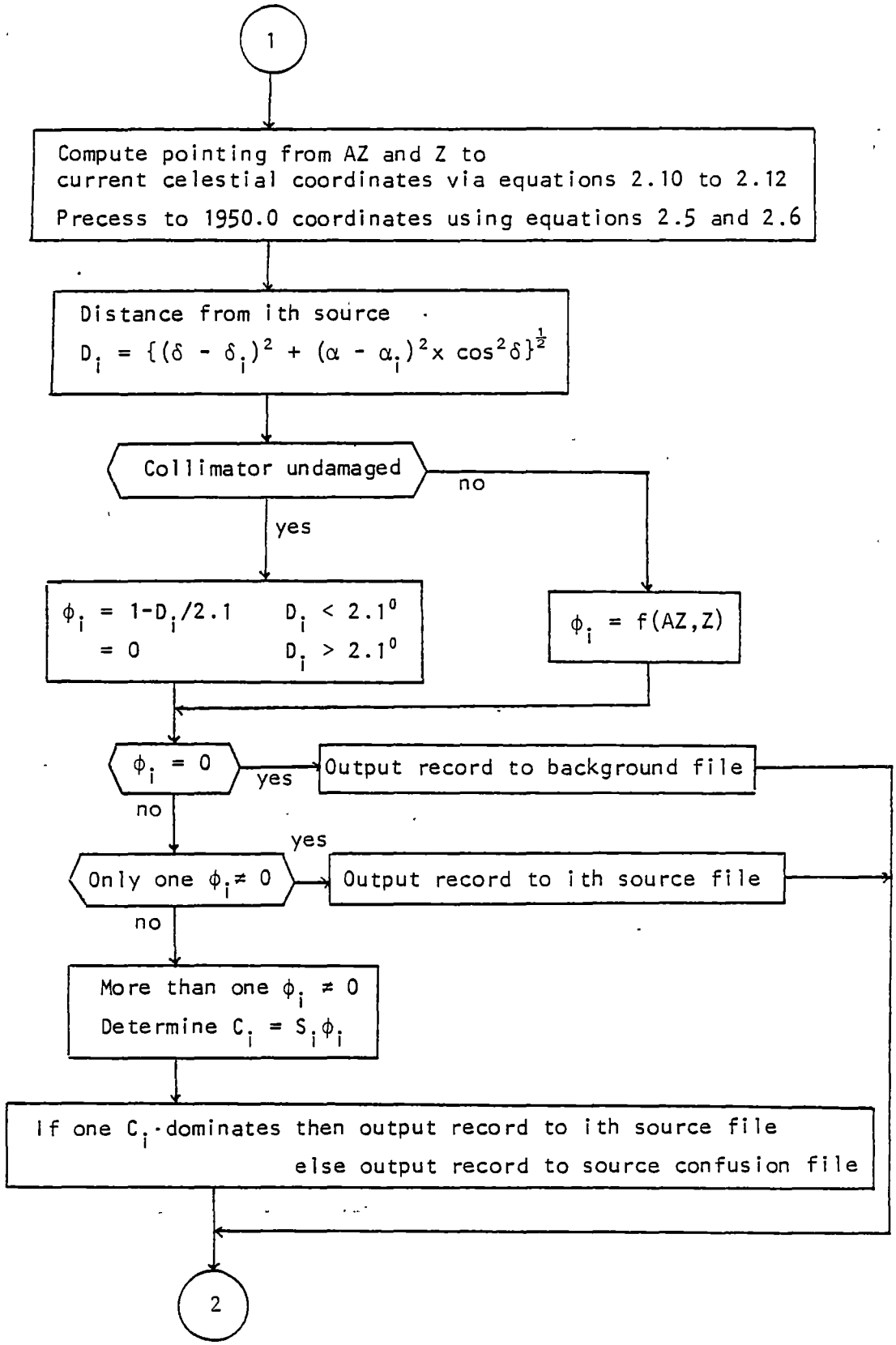

Figure 3.11 cont.

platform azimuth follows from equation 2.13. In the UTIC81 flight the sun sensor index error ϵ was $+0.04^{\circ}$. The difference between the sun derived azimuth and the magnetic azimuth can be written to an azimuth error data file. This allows estimates of the pointing stability and an example is shown in Figure 3.2. If the sun is not visible, the detector azimuth is taken to be the magnetic azimuth. If the file being read does not contain any PHA data the program loops back and reads the next data record. This option was included principally to generate azimuth error data files.

Next, the calibration source status flag is tested. If it is on, the record and subsequent PHA records are added. When the flag is reset to zero, the PHA data and time of integration are output to a CAL file for reductions using the CAL program.

The 1950.0 celestial coordinates are derived from the azimuth and zenith using equations 2.10 to 2.12 and precessed to current coordinates using equations 2.5 and 2.6. The distance D_i to the ith source follows. From this the collimator efficiency $\emptyset_i$ to each source follows from the assumption of an ideal triangular response, i.e. the collimator is assumed undamaged. To account for the possiblility of the collimator being damaged and since the response during UTIC81 was probably not independent of the position angle of the source with respect to the optical axis (see Figure 3.5), a separate subroutine for the calculation of $\emptyset_i$ was developed. The expected azimuth and zenith of the ith source is calculated from the ith source RA and Dec. Next the efficiencies of each individual quadrant and hence the mean collimator efficiency, $\emptyset_i$ (= f(AZ,Z)) is computed.

The last stage of the program deduces the nature of each record, i.e. source, background or confused. If all $\emptyset_i$ are zero, then the record is output to the background file. If all but one $\emptyset_i$ is zero, only one source is present in the field of view and the record is written

to the ith source file. If more than one $\emptyset_i$ is not zero, two or more sources are present. To test if any particular source dominates a new quantity $C_1 = \emptyset_i S_i$ is determined where S_i is the historic flux from the ith source. If any particular source dominates the other sources by more than a factor of 10, the record is considered unconfused and is output to that particular source file. Naturally X-ray sources are unpredictably variable and one must be aware of the records that are possibly confused. The threshold level for confusion can be easily reset from a factor of 10 to larger values if doubt exists. There are only a few areas in the sky where confusion is a problem with a 2° field of view, i.e. the galactic plane between 11^h and 19^h RA and the LMC and SMC regions. These regions do contain the majority of interesting galactic objects and require the careful selection of rocking directions for the determination of background. The program then loops back to the reading of the next data record.

3.2.2 BGD

The program BGD generates from a background file, the parameters describing the temporal slope of the background. Normally an observation has background before and after the observation of a source. BGD deduces the expected background during the source observation and outputs the parameters to a file. The program can work with any combination or sum of PHA channels. For weak sources, PHA data are generally added in 2, 3 or 4 channel groups to obtain a better signal to noise ratio.

3.2.3 SOURCE

For each source file generated by ASPECT, SOURCE will subtract the background using the background parameter files to generate any combination of light curves or summed spectra and output them to data files. Data errors are computed assuming Poisson statistics. The Poissonian nature of the detector count rate data was satisfactorily tested prior to launch and during earlier flights. The light curves can then be used

to test for any periodic structure in the data using subsequent programs. The PHA spectra can be inverted to intrinsic source spectra with absolute fluxes from either of the programs LS or DS, using the detector parameters from the CAL program.

3.2.4 CAL

CAL uses a non-linear least squares program to fit a model of the counter to the observed data. The model and equations are described in section 1.9.

3.2.5 LS and DS

LS stands for least squares spectral reduction whilst DS is direct spectral reduction. LS is in fact an implementation of the widely used minimum χ^2 technique. An intrinsic source spectrum $N(E,\gamma_1,\ldots,\gamma_j)$ is selected by the choice of initial estimates of the spectral parameters γ_1 to γ_j. This is then folded through the counter model described in equation 1.5. The χ^2 statistic

$$\chi^2 = \frac{1}{\text{dof}} \sum_{i=1}^{m} \left(\frac{O_i - C_i}{\sigma_i}\right)^2 \qquad (3.1)$$

is computed where m is the number of pulse height channels, O_i the observed data, C_i the expected data value from the model (see equation 1.6), σ_i the error and dof (= m - j) is the number of degrees of freedom where j is the number of spectral parameters.

The procedure is to minimise χ^2 by appropriate changes in γ_1 to γ_j after each iteration until the changes are smaller than a previously chosen level. The resulting spectrum is taken to be the best estimate of the source spectrum. Errors in γ_1 to γ_j can be estimated by plotting a grid of χ^2 versus γ_1 to γ_j and selecting contours that correspond to a known level of confidence. For 68% confidence the required contour is χ^2_{min} + 2.3 for 2 dof where χ^2_{min} is the minimum value of χ^2 from equation 3.1. The 90% confidence contour corresponds to χ^2_{min} + 4.6 for 2 dof. Information for estimating further confidence contours is given by

Lampton, Margon and Bowyer (1976).

The inherent disadvantage of the technique is the a priori choice of an intrinsic source spectrum. This biases the derived data and its interpretation. To overcome this disadvantage, direct spectral reduction (DS) from counts to flux can be achieved by two techniques, apodization (Dolan, 1972) and via eigen-solutions (Blissett and Cruise, 1979).

Apodization directly inverts the matrix equation 1.6. Unfortunately the resolution matrix is essentially singular resulting in poorly determined source spectra. To overcome this problem, Dolan (1972) simplified the inversion of the matrix describing the detector energy resolution. If we rewrite the equation describing the counter model (equation 1.5) as a matrix of dimension m, then

$$C = RF_K(I - T_G)T_W T_A N \tag{3.2}$$

where C is the observed data in column matrix form, R the resolution matrix, F_K the escape matrix, I the unit matrix, T_G, T_W and T_A the matrices describing the detecting gas, the window and atomsphere respectively. N is the source spectrum. All except R are easily inverted. To find $R^{-1}C$, Dolan used the following equation to determine the ith element of $R^{-1}C$

$$(R^{-1}C)_i = C_i - S_i[\tfrac{1}{2}(C_{i+\ell} + C_{i-\ell}) - C_i] \tag{3.3}$$

where ℓ (called apodization length) is dependent on the resolution at the ith channel such that $S_i = (\sigma_i/\ell)^2$. Dolan (1972) suggest $S_i = 1$ and modelling by Watts and Thomas (1979) confirm this choice.

The disadvantage of this technique is that errors propagated through the procedure are increased by a factor of ~3. For low signal to noise data they can become quite unacceptable. The method does provide an initial estimate of the spectral parameters for LS. We have used LS to refine the parameters knowing the non-uniqueness of the fit.

A recent and more powerful method of direct spectral reduction is the method of Blisset and Cruise (1979) which uses eigen techniques to reduce the resolution matrix. Errors are increased by a factor of ~2, which again is a serious disadvantage for low signal to noise data. The technique has not yet been implemented for UT data reduction.

3.2.6 Miscellaneous Programs

Several utility programs were written to merge files, search for particular values of data, compress files in time and/or to bin up PHA data. If the data available had had a higher signal to noise ratio, then period searching and analysis programs would have been developed to reduce the light curve data files. Some of these techniques are discussed in the reduction techniques for optical photometry in section 5.5.

3.3 UTIC81 Data Reductions

The data from the balloon flight were dumped into disk files via UTDUMP in blocks of ~1 hour. The data were corrected by editing the ASCII character files and checked by graphing all values. Obvious errors were readily apparent and corrected. Examples of such un-edited data are the count rate plots shown in Figures 3.6 to 3.8.

All data files were initially processed using ASPECT to provide a pointing solution and an azimuth error file using the sun sensor was generated. The sun sensor derived azimuth errors are shown in Figure 3.2. The overall celestial pointing is shown in Figure 3.12. The field of view is indicated by the circles of radius 1° (solid line) and 2.1° (dashed line). The thick solid lines represent telescope aspect during portions of the flight where tracking or slow scanning occurred whilst the thin solid lines represent aspect while driving. Each small dot represents the average position at thirty second intervals during driving. The gap at 1530 RA corresponds to the data loss at 0135UT. Sources marked are from pre-Einstein catalogues notably the 4U catalogue (Forman et al., 1978), the Ariel V 2A (Cooke et al, 1978) and 3A catalogues (McHardy et al., 1981;

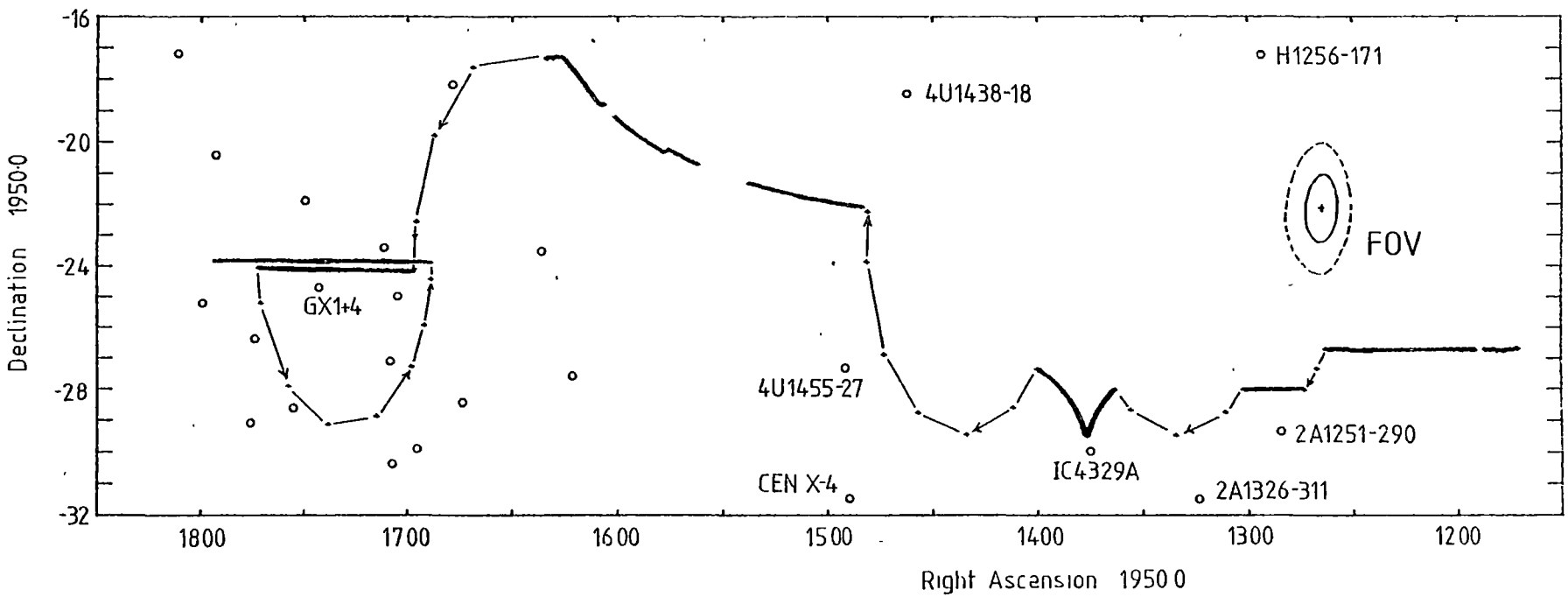

Figure 3.12 Celestial map of the overall flight trajectory of UTIC81. Thick lines represent tracking whilst thin solid lines represent rapid driving movements in azimuth. Also shown, as small circles, are all the known persistent X-ray sources from pre-Einstein catalogues. The region around GX1+4 is shown in more detail in Figure 3.13. Gap at 1530 RA corresponds to data loss at 0135 UT. The FOV is the field of view of the telescope for an undamaged collimator. Dashed line is maximum FOV.

Warwick et al., 1981), and the HEAO-1 catalogue (Piccinotti et al., 1982; Marshall et al., 1979b). The only sources not included are transients. The region about GX1+4 is shown in more detail in Figure 3.13. The field of view (FOV) is explained in Figure 3.12. As can be seen in Figure 3.13 the observations of GX1+4 are not confused by the galactic centre sources since our field of view is small.

Two objects were observed. The Seyfert galaxy IC4329A was tracked in azimuth whilst for GX1+4, the detector was set at a fixed azimuth and the source allowed to rise through the FOV. The azimuth was changed by ~180° and GX1+4 allowed to set through the FOV and so obtained two scans. A discussion on observations of each source follows.

3.3.1 GX1+4

The summed count rate for GX1+4 from PHA channel 4 to 19 (20 to 76 keV) is shown in Figure 3.14. Integration time is 30 seconds. The spikes between 0254 and 0300 UT are due to interference from rocking. The final detector calibration is marked as CAL 3. Also plotted is the collimator efficiency curves for undamaged collimator (solid line) and damaged collimator (dashed line). The broad nature of the damaged collimator response curve partially compensates for the reduced peak response. Consequently the total effective observation time for both possibilities are comparable.

At the end of the second scan of GX1+4 at 0439 UT, the tape recorder ran out of tape and before the tape was changed the balloon was cut down. Fortunately the background PHA rates during this time were being output to the teletype via the PDP11/10 as 20 sec integrations. To utilise this information the disk files were compressed into 20 sec integrations and the extra background added to the file by hand. It is this file that has been used in all subsequent reductions. Each scan was treated separately with the data file being split at the time of the 180° azimuth change at 0353 UT. All data during this change have been deleted from the analysis since background is dependent on the azimuth

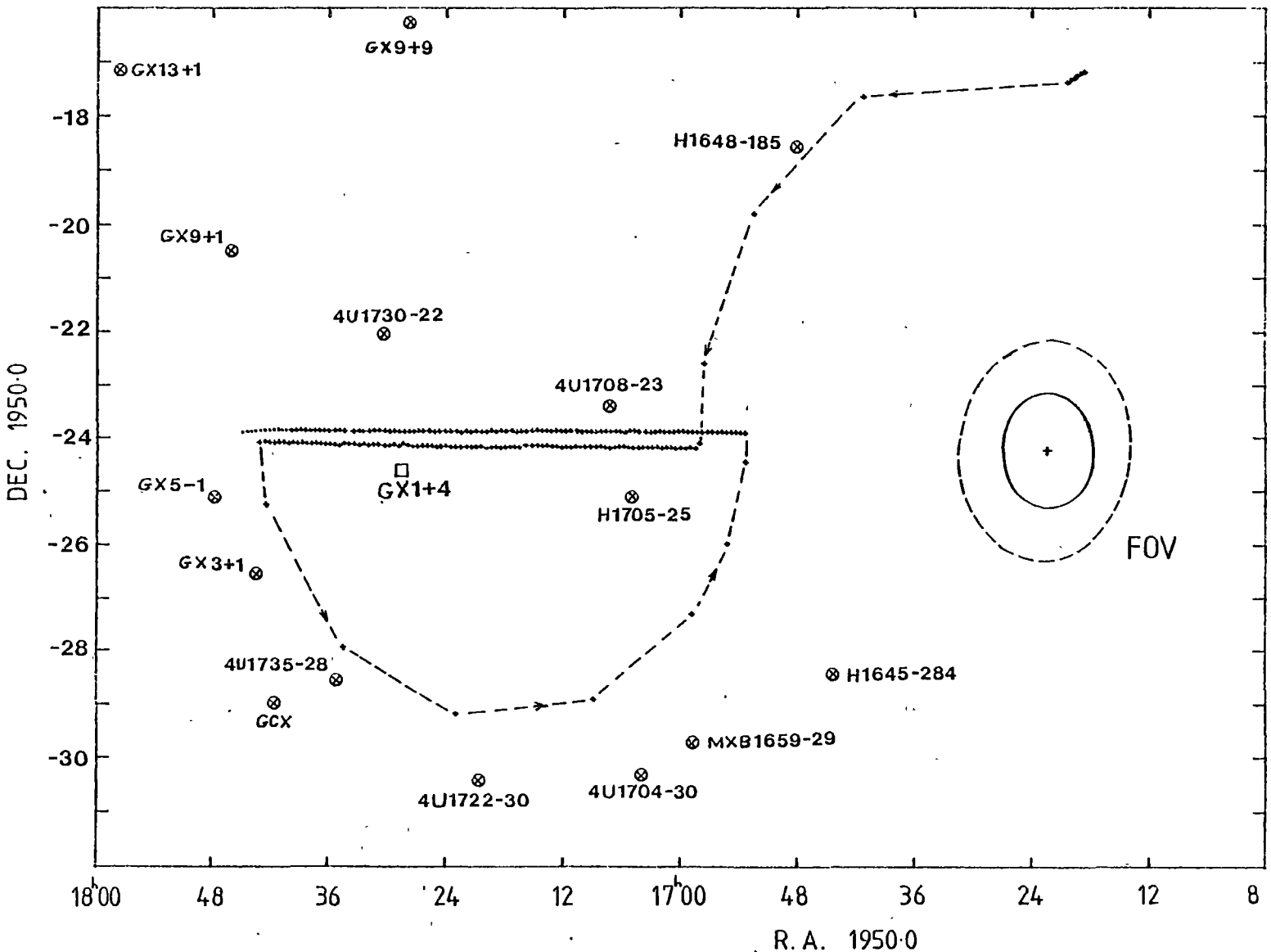

Figure 3.13 Scan map of the region of GX1+4. Each point in the scan is a mean of 30 seconds observation. The FOV is the same as in Figure 3.12. The map shows the scans of GX1+4 are not confused by other galactic centre sources.

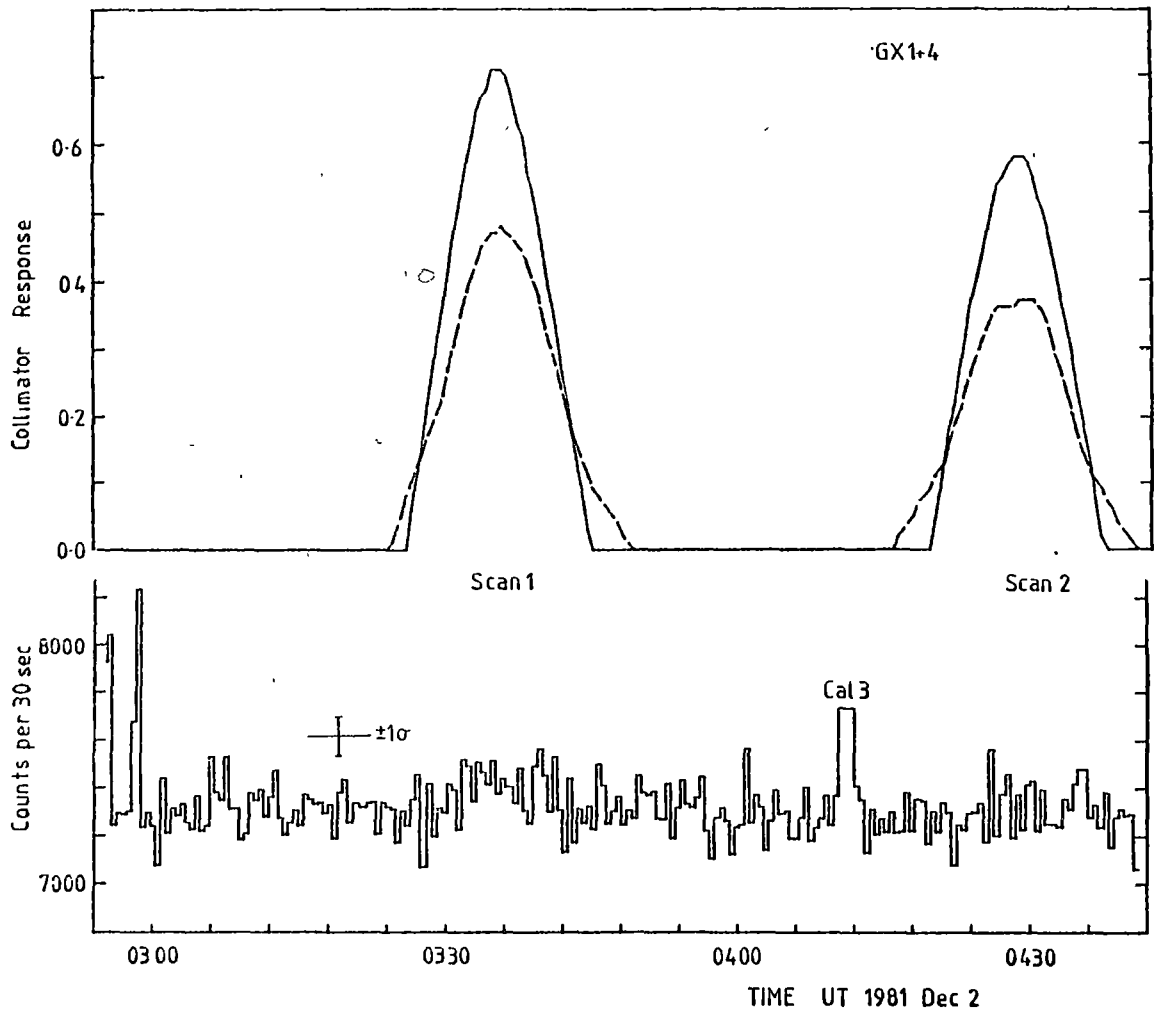

Figure 3.14 Summed PHA counts (channels 4 to 19) in 30 sec integrations during the two scans of GX1+4. The error of the data is indicated by the one sigma error bars. The solid line is the undamaged collimator response and the dashed line is for the damaged collimator. The time of the number 3 calibration is marked.

and zenith of the detector. In the case of azimuth changes, the variation with azimuth is due to the east-west asymmetry in cosmic ray fluxes. This is most obvious in the veto rates where at 0353 UT the veto count rate changed from 269.3 per sec to 268.0 per sec due to the change from an azimuth of 100.0° to 260.0° (Figure 3.8). Unfortunately the azimuth dependence of the PHA rates is not well established due to the lack of sampling at sufficiently many azimuth positions. The zenith dependence on background arises principally from the contribution of atmospheric X-rays but since the zenith was fixed, this had no effect on our data.

Table 3.1 contains counts and errors (assuming Poissonian statistics) for both scans and for both states of the collimator.

TABLE 3.1

UT Counts for the 2 Scans of GX1+4

SCAN (Mean Observation Date)	State of Collimator	Time (sec)	PHA bins (keV) 20-34	34-48	48-62	63-76
1	Undamaged	444	701±89	390±67	285±63	336±57
(JD 2444940.6492)	Damaged	353	565±102	415±77	129±72	313±66
2	Undamaged	337	11±125		333±79	
(JD 2444940.6867)	Damaged	267	0±125		238±95	

The spectral data from scan 1 was first processed using DS to obtain an initial estimate of the flux from GX1+4. We have adopted an effective detector area of 5200 cm^2. The procedure of DS always overestimates the high energy point due to incomplete knowledge of the contribution of flux energies above the upper threshold and at low energies the systematic errors are largely due to the rapidly changing attenuation factors (Watts and Thomas, 1979).

The data were then reduced using LS for a variety of spectral fits using the results from DS as an initial estimate. The data have low signal

to noise ratio and cannot be uniquely described by any particular standard spectrum. We have used power law, thermal bremsstrahlung with gaunt factor and blackbody models. The equations are listed in Table 3.2. A pivot energy of 40 keV was used for the power law fit. The resulting best fit parameters and χ^2 per dof are presented in Table 3.2. Errors have been derived from χ^2 contour plots shown in Figure 3.15. The best fit for either state of the collimator is the power law with a χ^2_{min} per dof of 4.7. The large χ^2_{min} is essentially due to the high flux point at 70 keV.

Figure 3.16 is a plot of the UT Scan 1 spectral points (filled circles) derived from the best fit spectral curves as quoted in Table 3.2 for an undamaged collimator and as a comparison spectral data from three previous observations from Table 1.2. The open circles are the IC spectra with 1σ error bars (communicated by K. Harper). The large difference between the IC and UT data cannot be reconciled by any reasonable assumptions about systematic or statistical errors such as in the effective area of the detectors or unknown pointing errors. The only way the UT data can be so different is if the collimator was not aligned as post flight measurements indicated. If the collimator was bent further upwards than estimated, its response to GX1+4 would be less than shown for the damaged collimator in Figure 3.14. Consequently the flux from GX1+4 would be underestimated. It seems plausible to assume that the large decelerations experienced during parachute opening and landing may have partially straightened the collimator leaving it in the state it was found. Since the exact shape of the collimator during the flight is not known, the data on GX1+4 are essentially useless. This can be confirmed by comparison of the flux levels of the two scans. The UT result indicates that GX1+4 was in a fainter state during the second scan (Table 3.1) whereas the IC data show that the flux levels during the two scans were similar. For the discussion on GX1+4 in chapter 4,

TABLE 3.2

UT Spectral Parameters for GX1+4 SCAN 1

Flux units are photon $sec^{-1} cm^{-2} keV^{-1}$.

	STATE OF COLLIMATOR					
	UNDAMAGED			DAMAGED		
Spectrum*	A	α or kT	χ^2_{min} dof^{-1}	A	α or kT	χ^2_{min} dof^{-1}
Power	$6.1\pm0.9 \times 10^{-5}$	0.77±1.0	4.7	$6.8\pm1.0 \times 10^{-5}$	1.0±1.3	4.7
Thermal Bremsstrahlung + Gaunt Factor	$3.1\pm0.3 \times 10^{-2}$	>100 keV	5.6	$2.5\pm0.5 \times 10^{-2}$	>100 keV	5.6
Blackbody	$\sim1.5 \times 10^{-7}$	24±6 keV	5.9	$\sim2.5 \times 10^{-7}$	21±9 keV	5.6

*Spectral equations are:

Power	$A(E/40)^{-\alpha}$
Thermal Bremsstrahlung + Gaunt Factor	$A/\sqrt{kT}\, e^{-E/kT}\, E^{-1} (E/kT)^{-0.4}$
Blackbody	$A E^2/(e^{E/kT} - 1)$

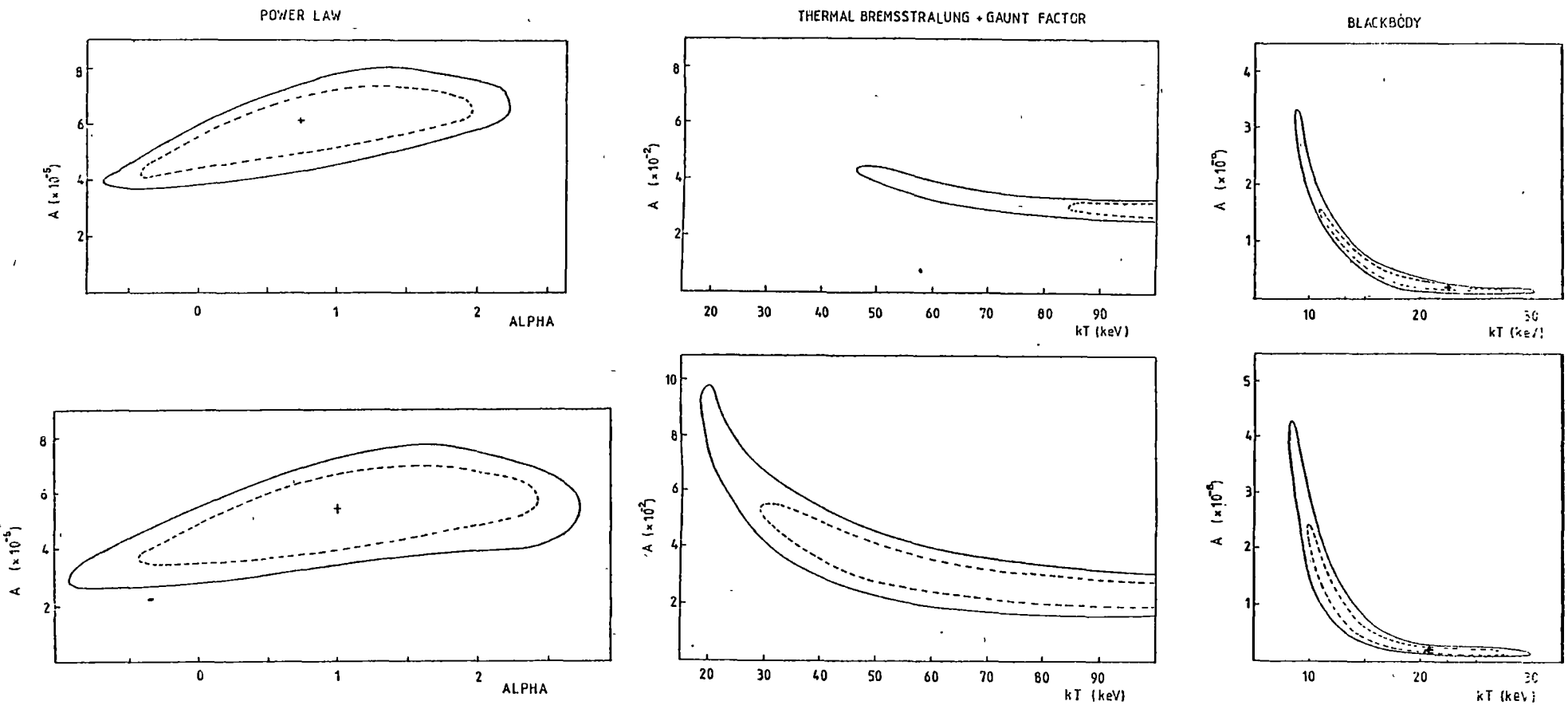

Figure 3.15 χ^2 contours for various spectral fits to the UT GX1+4 Scan 1 data. Dashed contour is 68% confidence contour, solid line is 90% confidence contour and cross is best fit. Upper row plots are for the assumption of an undamaged collimator and the lower row for a damaged collimator. Parameters and spectral equations are listed in Table 3.2.

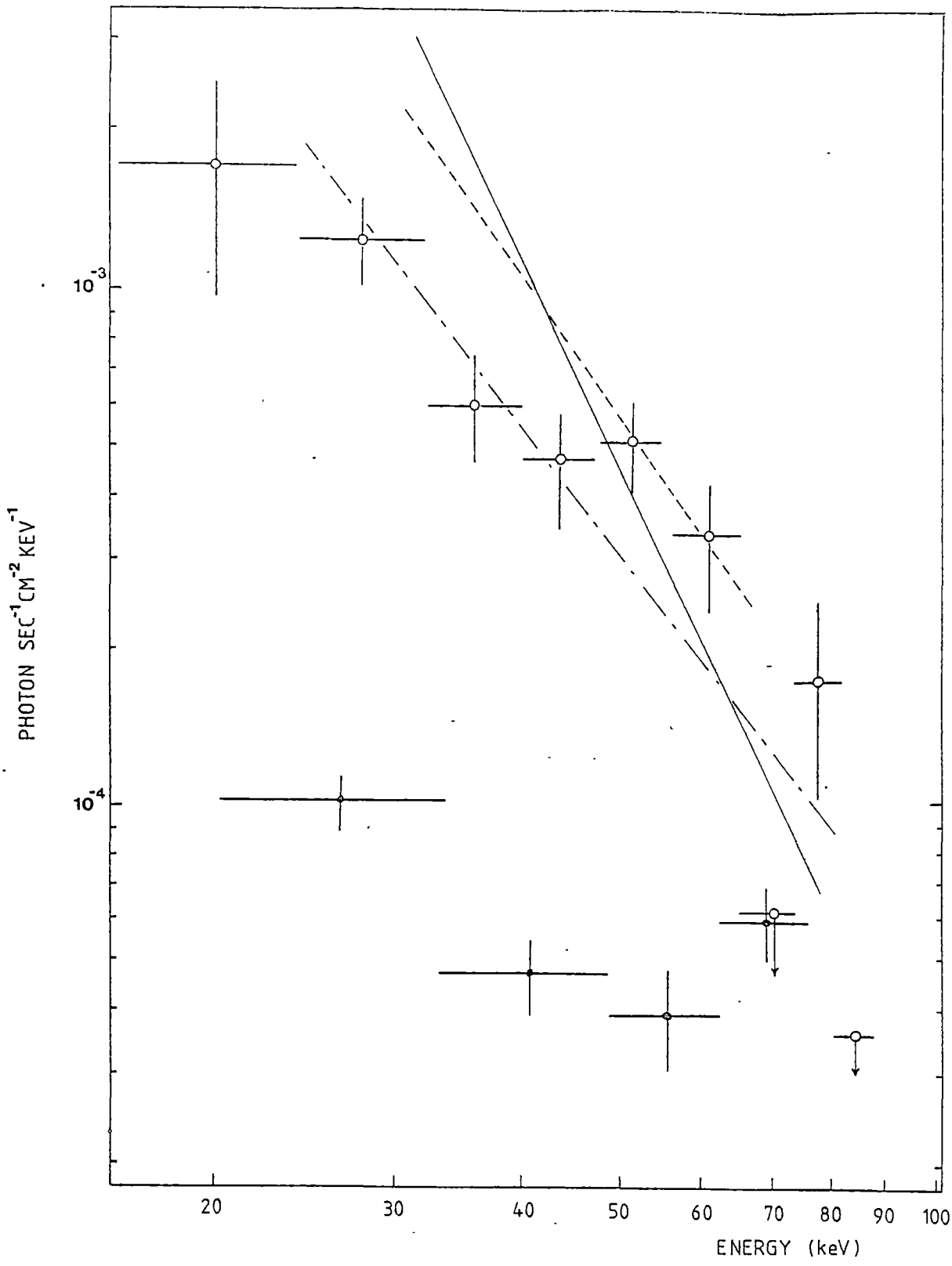

Figure 3.16 UT (filled dots) and IC (open dots) spectra of GX1+4. (SCAN 1) Error bars are one sigma and upper limits are 2 sigma. Also shown for comparision are best fit power law spectra from previous observations.

——— OSO-8 (Dennis et al 1980a)
- - - - NRL (Maurer et al 1982)
—·— AIT/MPI (Kendizorra et al 1980)

the IC data have been used. The discussion on the reduction of the data has been left intact as an example of the method of reducing UT data.

The best fit parameters to the IC data are listed in Table 3.3. The errors are derived in a similar manner to the UT results.

TABLE 3.3

IC Spectral Parameters for GX1+4

Spectral equations are as listed in Table 3.2.

	A	α or kT	χ^2_{min} dof^{-1}	dof
Power Law	0.15±0.04	1.5±0.5	1.80	6
Thermal Bremsstrahlung + Gaunt Factor	0.29±0.09	64^{+50}_{-20} keV	2.00	6

The spectral parameters indicate that GX1+4 was in a hard low flux state. The previous lowest flux state at hard energies was the data from Kendziorra et al. (1980). The IC data are comparable or slightly harder than this state. Whilst the absolute intensity of the UT data is not known, the spectral shape of the UT data is independent of the state of the collimator response, since the collimator response is independent of energy. There is however a decrease in the signal to noise ratio of the spectral data, which in turn increases the errors on the derived parameters. The UT data confirms the hard state of GX1+4.

3.3.2 IC4329A

IC4329A was observed from 2348 UT to 0036 UT (mean JD 2444940.004). Table 3.4 contains derived fluxes for IC4329A from the IC experiment. The upper limits are 2σ. The fluxes have been derived from the program LS using the power law fit to the low energy Einstein data (see Section 1.4.1) as representative of the spectral form. The only free variable is the intensity.

TABLE 3.4

Upper Limits (2σ) for IC4329A
from IC Detector

Energy (keV)	16-48	48-104	104-200
Flux photons $sec^{-1} cm^{-2} keV^{-1}$	2.3×10^{-4}	3.7×10^{-5}	4.8×10^{-5}

Figure 3.17 is a spectral plot of Einstein data from Holt (1981) and the IC upper limits. The Einstein data have been adequately fitted with a power law of photon spectral index -1.86 and a low energy cutoff of 1.0 keV (see section 1.4.1). The solid sloping line is the extension of this power law. The lines marked maxima and minima are the maximum and minimum flux states of IC4329A assuming no spectral hardening or softening from the previous X-ray observations of IC4329A (see Table 1.1). The IC upper limits are marked on the extreme right. The IC results are consistent with the known properties of the soft X-ray data. The flux at soft X-ray energies was not known for this epoch.

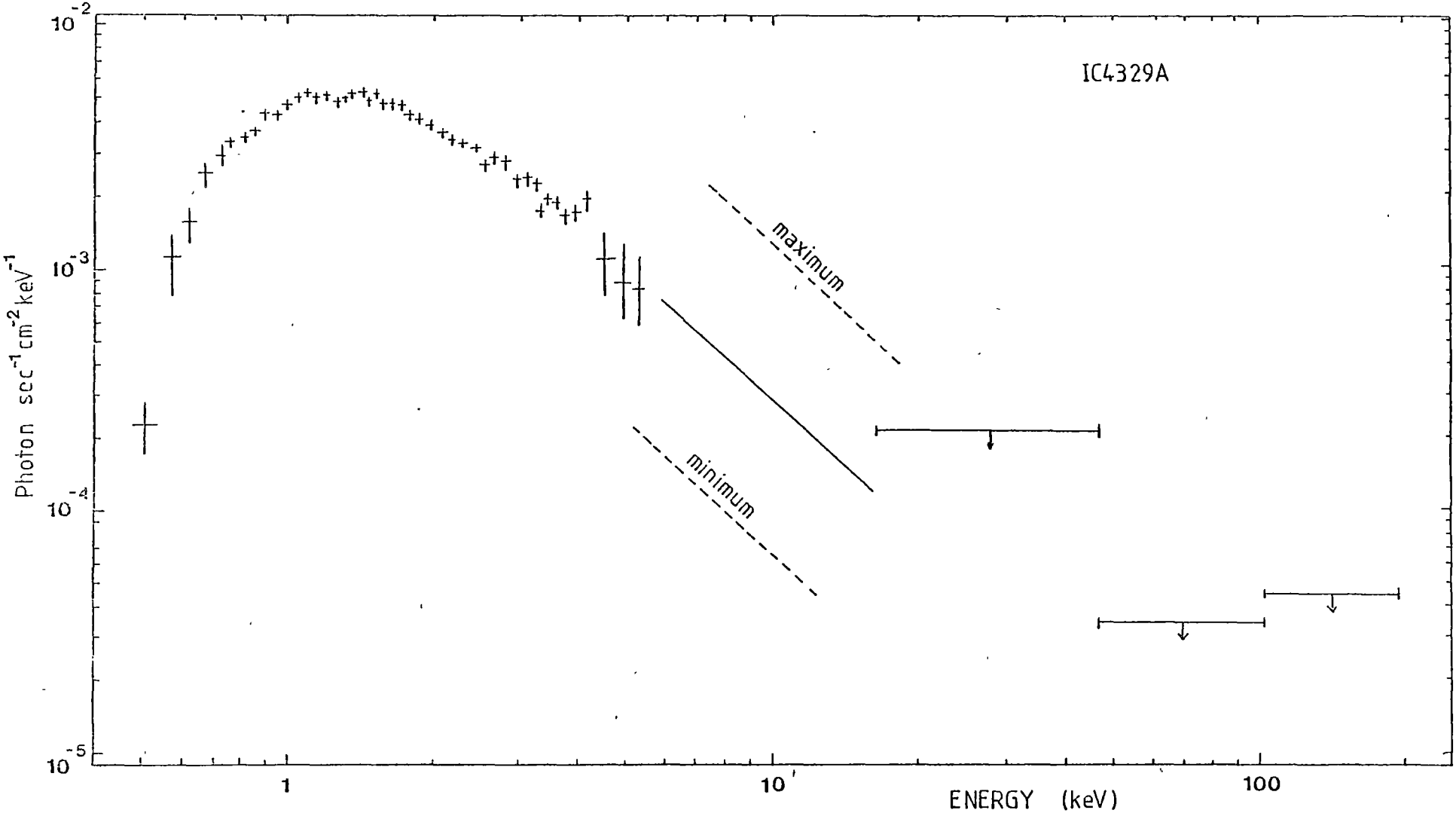

Figure 3.17 X-ray spectrum of IC4329A. Low energy data from HEAO-2 and solid line is extension of this data to high energies. Maximum and minimum lines are the limits of observed spectra assuming no spectral changes from the Einstein SSS spectrum. IC upper limits (2σ) are on the right.

CHAPTER 4

DISCUSSION OF UTIC81 OBSERVATIONS

The discussion on the UTIC81 X-ray data is divided into two sections. The first is on the Seyfert galaxy IC4329A and the second on the pulsar GX1+4. This chapter concludes with a discussion on proposed improvements to the platform and detector and brief details of the last balloon flight UTIC83 conducted in Brazil on March 26, 1983.

4.1 IC4329A

In a recent review, Lightman (1982) discussed the nature of the power source in the nuclei of active galaxies (AGN) and quasars and outlined the various X-ray production mechanisms that are currently envisaged.

The standard model of the power source is accretion onto a massive black hole of mass 10^6 to 10^9 $M_\odot$. The observed X-ray luminosities are $\sim 10^{44}$ to $\sim 10^{46}$ erg sec^{-1}. The source of the accreting gas is not certain. Five models have been proposed (Lightman, 1982). They are: (i) stellar collisions, (ii) tidal stripping of stars by the central black hole, (iii) infall of intergalactic gas, (iv) galaxy mergers, and (v) intragalactic gas from normal stellar evolution. Each model provides a different evolutionary scenario of the AGN and its surroundings.

As mentioned by Lightman (1982), the actual X-ray production mechanism is not certain because of the complex environment that is presumed to exist. However the observed spectra are all well fitted by power law models. In the 0.1 to 5 keV energy range, the spectra of 28 Seyfert galaxies can be represented by a power law with photon number index $\alpha = 1.65$ with a dispersion of 0.13. This represents the most homogeneous group of X-ray objects with respect to the similarities of their spectrum (Urry et al., 1982). Comparison with IR to UV data suggest Compton processes dominate in the X-ray region.

To generate power law spectra there are 2 possible mechanisms. The first method is synchrotron radiation. If an electron distribution of number density $de/dE \propto E^{-r}$ exists then the observed photon number index is $(r+1)/2$. In the case of IC4329A the soft X-ray spectral index of 1.86 implies $r = 2.72$. A test for this model is detection of polarization at X-ray wave-lengths. A variant of this model is the synchro-Compton model where relativistic electrons ($\gamma \sim 10\text{-}10^3$) produce optical and infrared synchrotron radiation. These photons can Compton scatter into the X-ray and γ-ray regions (Liang, 1979). Several problems exist with this model. They are: (i) the initial source of relativistic electrons, and (ii) the need to maintain the electron energy because of their fast cooling time.

The second model is Compton scattering of cold photons at energy E_0 from a flux of hot electrons of temperature T and Thomson scattering depth τ. The observed photon index α follows from

$$\alpha = -0.5 + (9/4 + 4/y\,\pi^2/3)^{\frac{1}{2}} \qquad E_0 < E < 4kT$$

where

$$y = 4kT/m_e c^2 \, \mathrm{Max}(\tau, \tau^2) \ ,$$

(Guilbert, Fabian and Ross, 1982 and references therein). For IC4329A, $y = 4.0$ implying τ between 4 and 6 for T of the order 20 keV. This is the regime of unsaturated Comptonization. In saturated Compton scattering, $y \gg 1$ and the maximum energy that a photon can attain through multiple scattering is ~3 to 4kT. Further scattering does not increase the photon energy. Saturated Compton scattering can occur when there is an insufficient supply of soft photons. In either case, the power law spectrum will extend up to photon energies ~4kT and will exhibit an exponential decrease at this energy.

Liang (1979) discusses two models for the source of hot electrons (i) a hot inner disc model similar to the Cyg X-1 model of Shapiro et al. (1976) and (ii) a corona model of hot electrons surrounding a disc.

In the Shapiro et al. model, the inner disc is optically thin to free-free absorption and is gas pressure dominated. The ion temperature T_i exceeds the electron temperature T since electron cooling is very efficient. A copious supply of soft photons are Compton scattered to higher energies to produce the observed hard X-ray spectrum. The source of the soft photons is either from cooler regions surrounding the inner disc or from infalling material near the compact object. Shapiro et al. found in the case of Cyg X-1 that the energy of the soft X-rays must be between 50 eV and 5 keV and that the emergent hard X-ray spectrum is insensitive to the initial soft photon spectrum. Liang (1979) mentions several problems associated with this model. They are:

(i) the predictions of the model are highly dependant on the disc viscosity;

(ii) the difficulty in explaining the large range of AGN X-ray luminosities given the requirement of unsaturated Comptonization;

(iii) the model critically requires $T_i >> T$;

(iv) it is an unstable model due to the two temperature regions.

Liang proposes a corona model which is stable and requires fewer assumptions regarding the geometry of the emission region. A turbulent disc will transport energy via twisted magnetic field lines and waves into the region surrounding a disc and produce a hot corona. The disc is the source of the soft photons. This simple model also explains why Comptonization appears unsaturated. In the Shapiro et al. model it is required as an assumption because of the requirement of a copious supply of soft photons. Comptonization produces both an outgoing flux from the corona and an ingoing flux because of the random nature of the scattering process. The outgoing flux is observed at infinity but the ingoing flux is intercepted by the optically thick disc and reemitted as soft photons. y is maintained near 1 if the disc intercepts a significant fraction of the Comptonized photons. This is certainly

the case for a corona enveloping the disc.

Lightman and Rybicki (1979) have calculated the reflected spectrum of soft photons incident on a semi-infinite slab of hot plasma. Under the conditions that the slab has large τ and small absorption depth, the emergent spectrum is similar to a power law with photon index α = 1.2 to 1.8 and is insensitive to the parameters of the plasma. A high energy turnover at photon energy >kT exists.

Our X-ray results are not sufficient to provide any constraints on the energy of the spectral turnover and hence the electron temperature. Even in unsaturated Compton conditions, a high energy turnover is still required since the energy output would otherwise be infinite (since the energy spectral index is <1). If the soft X-ray state of IC4329A was at the previously observed maximum then the UTIC data suggests a turnover near 20 keV. Unfortunately the soft X-ray flux at this epoch is not known.

4.2 GX1+4

The main question regarding GX1+4 is how does the UTIC data compare to other spectral information from previous observations. Most, if not all, observations of GX1+4 have suffered from poor signal to noise in the hard X-ray regions. Even with the high quality results of Kendizorra et al. (1980), they could not distinguish between power law (PL) or thermal bremsstrahlung (TB) and only selected the latter because the model fitted the soft X-ray data of Becker et al. (1976) better than a power law. Figure 4.1 illustrates the spectral variability of GX1+4 using PL (a) and TB with Gaunt factor (b). The data are listed in Table 1.2 and data symbols and equations are compiled in Table 4.1. The UTIC result is indicated by the asterisk. Most of the historic data have been presented in the form of PL and not TB spectra.

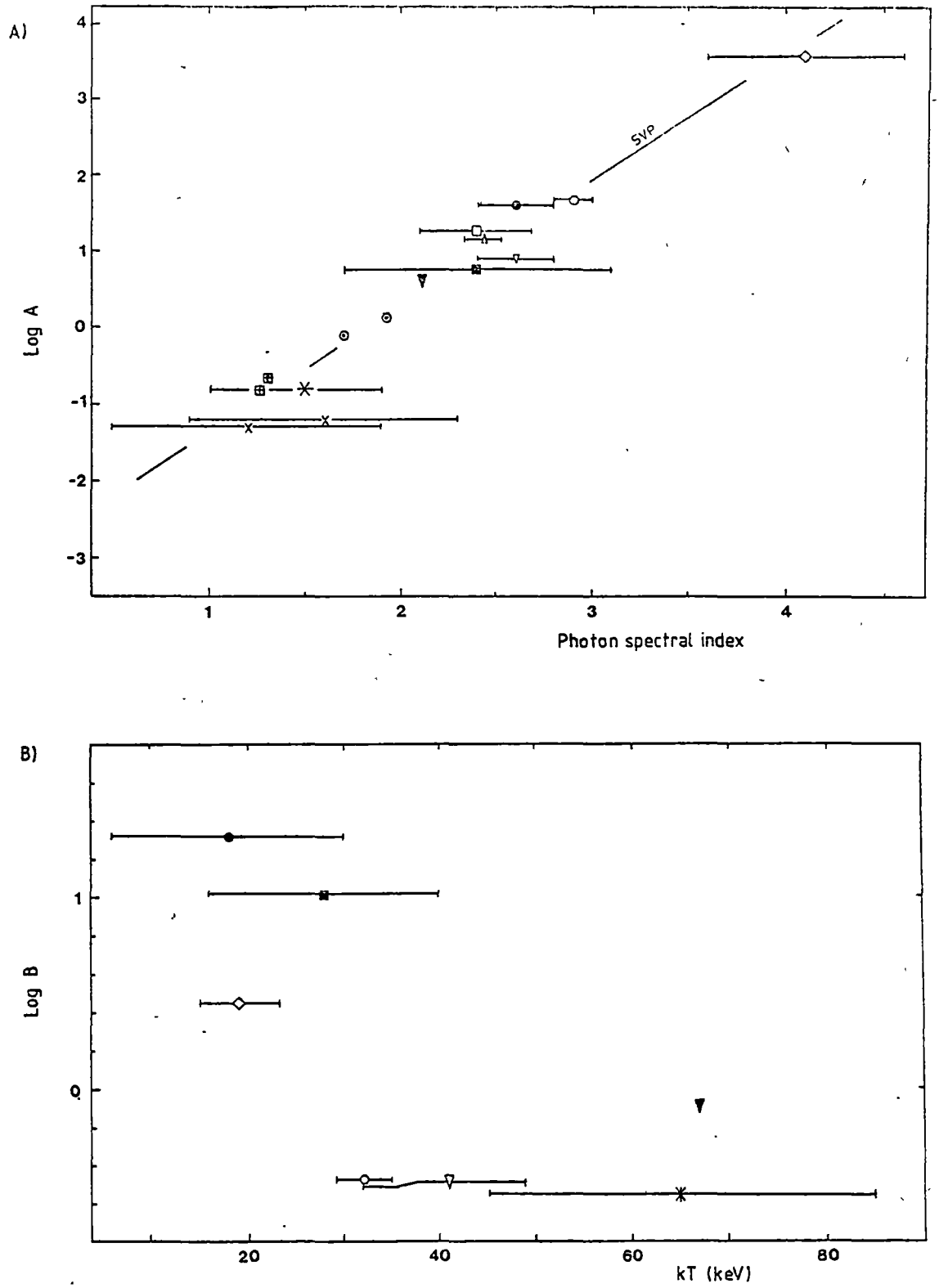

Figure 4.1 The spectral variability of GX1+4 expressed as either power law (A) or thermal bremsstrahlung with Gaunt factor (B). The line marked SVP in (A) is the line of best fit (see text). Symbols are defined in Table 4.1.

The HEAO-1 and HEAO-2 spectra from White et al. (1983) have been fitted with PL and TB over the energy range 20 to 100 keV so as to validate a comparison with the other data.

TABLE 4.1

Symbol	Energy Band (keV)	Reference
Δ	30 - 2 MeV	Johnson et al. (1972)
O	20 - 250	Maurer et al. (1982)
□	30 - 130	Thomas et al. (1975)
X	1 - 28	Parsignault and Grindlay (1978)
⊞	2 - 20	Becker et al. (1976)
◇	21 - 197	Dennis et al. (1980a)
o	15 - 60	Ricker et al. (1976)
■	18 - 150	Lewin et al. (1971)
∇	18 - 130	Kendizorra et al. (1980)
⊖	1 - 50	Ricketts et al. (1982)
*	20 - 100	This work
▼	2 - 60	White et al. (1983)

PL $A\,E^{-\alpha}$

TB $B/\sqrt{kT}\; e^{-E/kT} E^{-1} (E/kT)^{-0.4}$

Units are Photon $sec^{-1} cm^{-2} keV^{-1}$

It must be emphasised that simple spectral models are not realistic but they do provide an easy means of equating observations from different epochs. This is especially so if the data have low signal to noise ratio. It is for this reason that the modelling of the behaviour of GX1+4 and similar sources discussed later are related to the spectra via their two parameters A versus α and B versus kT.

Particularly striking about the data presented in Figure 4.1a is the linear relationship between log A and α. Similar behaviour is seen in other bright X-ray sources. Thomas et al. (1977) showed that anticorrelated spectral variability was not only seen in the black hole candidate Cyg X-1 but in the X-ray nova A0620-00, the pulsars Cen X-3 and Her X-1, the eccentric binary Cir X-1 and the 4.8 hr binary Cyg X-3. They noted that the variability appears to be pivoted about an energy point E_p to yield power law spectra of the form

$$A'(E/E_p)^{-\alpha} \quad \text{where A is a constant.}$$

This is related to the normal PL equation $A\,E^{-\alpha}$ by

$$\log A = C + S\alpha \quad \text{where } S = \log E_p \text{ and } C = \log A'.$$

Spectra that pivot about an energy E_p will have a linear relationship between log A and α. Thomas et al. (1977) refer to the log A versus α plots as spectral variability plots or SVPs. Table 4.2 is a list of sources that exhibit this behaviour and their derived parameters. N is the number of observations for each source and errors are 1σ. Also listed are the ranges of α that are observed.

TABLE 4.2

Source	Type	N	S	E_p (keV)	Range of α	Reference
Cyg X-1	black hole candidate	25	1.3±0.1	20^{+5}_{-4}	0.6-2.8	Thomas et al. (1977)
A0620-00	nova (recurrent?)	8	0.9±0.1	8±2	1.6-5.0	Thomas et al. (1977)
Cyg X-3	4.8 hr binary	5	1.1±0.3	13^{+14}_{-7}	1.5-4.0	Thomas et al. (1977)
Cir X-1	eccentric binary	10	1.3±0.3	20^{+20}_{-10}	1.1-3.9	Thomas et al. (1977)
Her X-1	pulsar	9	1.3±0.3	20^{+20}_{-10}	~1 -2.5	Thomas et al. (1977)
Cen X-3	pulsar	5	0.9±0.5	8^{+17}_{-6}	1.1-2.5	Thomas et al. (1977)
GX1+4	pulsar	15	1.65±0.14	44^{+18}_{-12}	1.2-4.1	See Table 4.1
GX339-4	black hole candidate	2	0.72±0.12	5^{+2}_{-1}	1.5-4.5	Ricketts (1983)

The data for GX339-4 is from Ariel VI observations of the low and high states measured between 1 and 50 keV.

The line of best fit to the GX1+4 data is marked on Figure 4.1a as SVP. The fit excludes the low energy data of Parsignault and Grindlay (1978) and Becker et al. (1976) and includes only the high energy data from Ariel VI above 15 keV (Ricketts et al. 1982). Excluding the value of S from GX339-4 because of the low number of observations, the mean value of S is 1.21±0.26 corresponding to $E_p \sim 16^{+12}_{-7}$ keV.

We now consider the various means of generating spectral variability that can mimic the behaviour seen with the SVPs. Shapiro et al. (1976) showed the effect of varying y between 0.6 and 1.2 to obtain changes in the emergent Comptonized spectra. In this case they adopted kT = 200 keV. The photon number spectral index for power law fit, measured between 10 and 100 keV varied from 1.9 for y = 0.6 to 1.4 for y = 1.2. Similar phenomena may occur in the sources listed in Table 4.2. Compton scattering is believed to occur in several galactic sources. Lamb and Sanford (1979) found that Compton spectra yielded better fits to 2 to 15 keV data from Sco X-1-like sources than TB spectra. For Sco X-1, τ varied between ~12 and ~19. In the other sources (Sco X-2, 4U1813-14 and 4U1728-16) τ ranges from ~12 to ~25. High quality hard X-ray data from Cyg X-1 can be fitted by Compton spectra with kT = 32 keV and τ = 3.9 or 1.6 for spherical or disc geometry scattering regions respectively (Nolan et al., 1981). Fabian, Guilbert and Ross (1982) have constructed a model of the bulge source 4U1822-37 in which a cold shell surrounds the source and scatters the emergent X-ray spectrum to lower energies. This shell may be an atmosphere around an accretion disc. In the case of GX1+4, the broad iron line at 6 keV suggests large τ (White et al., 1983).

To test the Compton scattering model we have used the analytical solutions of Chapline and Stevens (1973) to generate Compton scattered

spectra under a variety of conditions. They have divided their solutions into 2 regimes dependent on τ and kT. The equations are as follows:

Regime 1 $\qquad \tau < (m_e c^2/2kT)^{\frac{1}{2}}$

Let $\quad d = E/kT$ where E is the energy being observed

then $\quad P(d) = 1.5\ (d^3 - d^2 - d)$

$\quad Q(d) = 1.5\ d^2 - 0.75\ d^3.$

Let $\quad f = 2kT/m_e c^2 \tau^2$

then the emission spectrum J is

$$J = J_0\{1+0.375d^3 f - P(d) f^{-1}(e^{-f} - 1 + f) + Q(d) f^{-1}(e^{-f}(f+1) - 1)\} \qquad (4.1)$$

where J_0 is the initial TB spectrum. J_0 includes the free-free Gaunt factor $g_{ff} \sim (E/kT)^{-0.4}$.

Equation (4.1) is only applicable in the non-relativistic limit, i.e., kT < 20 keV. Modifications by Shapiro et al. (1976) and references therein allow for kT up to $m_e c^2$. At kT ≥ 20 keV, Monte-Carlo simulations are >10% different from the analytical solution. However comparison of spectra corrected for relativistic effects with the non-relativstic spectra for kT = 50 keV (Cooper, 1971) show little difference in the energy range being considered (10-100 keV). The ratio of flux at 30 keV to the flux at 100 keV differed by only 1%. The major difference occured in the normalisation (~9%). This indicates that a non-relativistic spectral regime is adequate for modelling Compton spectra at the level of accuracy we require (~30% in A and 0.2 in α).

Regime 2 $\qquad \tau > (m_e c^2/2kT)^{\frac{1}{2}}$

Let $\quad k_c = 6.6 \times 10^{-11} kT^{-1.25} n_e^{\frac{1}{2}}$

and $\quad k_d = 7.8 \times 10^{-4} kT\, \tau^2 k_c$

then $\quad \bar{K} = e^{\frac{k_d}{kT}} \{Ex(\frac{k_d}{kT}) - Ex(\frac{k_c}{kT})\}\{(\frac{k_d}{kT})^2 + 2\frac{k_d}{kT} + 2\}^{-1}$

where Ex is the exponential integral.

The observed spectrum is then

$$J = J_0(1 + \bar{K}\, g_{ff}^{-1}\, d^3) \ .$$

In the limit $\tau >> (m_e c^2/2kT)^{\frac{1}{2}}$ J becomes a Wien spectrum, i.e. $J \propto d^3\, e^{-d}$.

The model spectra are then fitted with PL models between 20 and 100 keV and the parameters A and α plotted on an SVP diagram. Figure 4.2 illustrates the behaviour of TB at various temperatures (10, 20, 30, and 50 keV) under various τ which are marked at each point. The dashed line between $\tau \sim 2$ and $\tau \sim 10$ signifies the transition between regime 1 and regime 2 and possibly represents the area of greatest error. The normalisation of the TB spectra, marked on the right on each curve are varied in steps of 10 for each temperature to avoid confusion.

The average shape of each curve closely follows the required value of S listed in Table 4.2. This is especially so for kT = 20-50 keV. For kT = 10 keV, increasing τ above 15 does not change α significantly. There is an increase in log A by 0.6. Also at this temperature, $\tau = 5$ produces a softer spectrum contrary to the results at higher kT. This may be a result of the break down of the equation (4.1). Nevertheless, in general the results of Figure 4.2 bear close resemblance to the observed behaviour. Listed in Table 4.3 are the values of S modelled from Figure 4.2 and the range in α that can be obtained. Note in Figure 4.2 that there is no strong variation of normalisation of the PL spectra as a function of kT. For constant B (i.e., constant ion and electron densities in the plasma) the model data all lie on a line of slope ~1.22 with a dispersion of log A ~ 0.3. Also marked on Figure 4.2 is the line of constant luminosity between 10 and 100 keV.

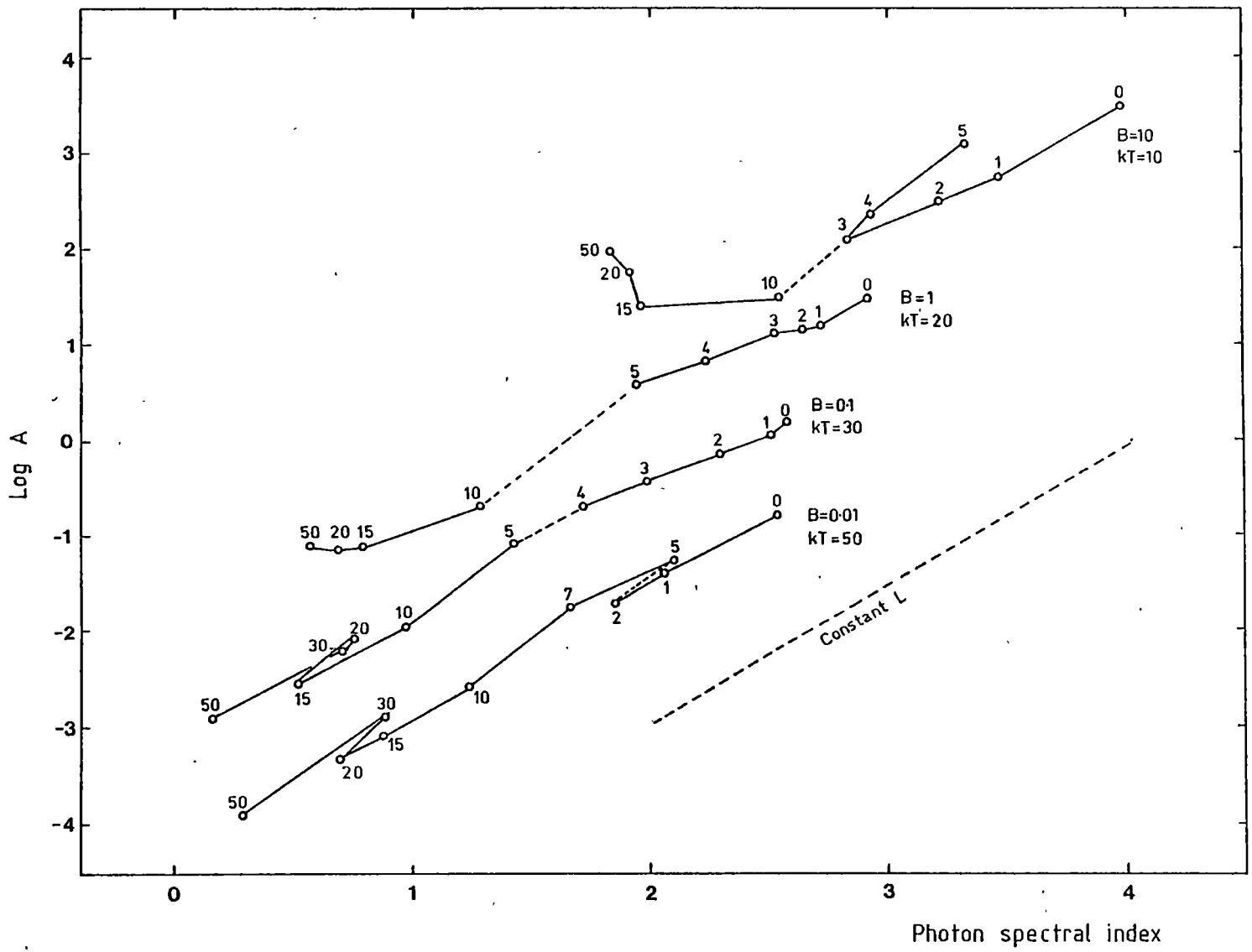

Figure 4.2 The loci of the best fit parameters A and α (from PL spectra) to TB spectra at various kT (10,20,30 and 50 keV) and τ. The value of τ is indicated at each point. Note the normalisation B of the TB spectra varies from 10 to 0.01 to avoid confusion. The dashed line is the loci of constant luminosity between 10 and 100 keV.

TABLE 4.3

kT (keV)	S	Range of α
10	0.89	1.9 to 4.0
20	1.18	0.6 to 2.9
30	1.33	0.2 to 2.6
50	1.34	0.3 to 2.5

Similar methods can be applied to fitting TB spectra to the Comptonized spectra. Figure 4.3 illustrates the behaviour of varying τ at different electron temperatures. The results are not as consistent as the PL fits in Figure 4.2. This is most evident for kT = 10 keV. At τ = 5 (Regime 1) the best fit parameters are B = 1.3 and kT = 17 keV whilst for τ = 15 (Regime 2), B = 1.13 and kT = 62 keV. The transition between the two states is not smooth because Comptonized spectra are quasi-power laws and TB spectra do not give good descriptions of this shape especially at large kT or τ when spectra are flat (α < 2.5). The parameters from fitting TB spectra are very sensitive to the signal to noise of the data compared to the parameters derived from fitting PL spectra. In particular kT (and hence B from $J \propto 1/\sqrt{kT}$) is not well determined for hard spectra. For these reasons, we use PL as the basic description of the spectral shape.

We can now fit the parameters τ and kT to the spectra on the basis of the range α that is observed and our predictions from Table 4.3. The parameters for the sources in Table 4.1 are listed in Table 4.4. The relationship between the variations in τ and α are dependent on kT so a unique parameter range is not possible. This is especially so for kT > 25 keV. We have selected the minimum kT that yields the desired range in α .

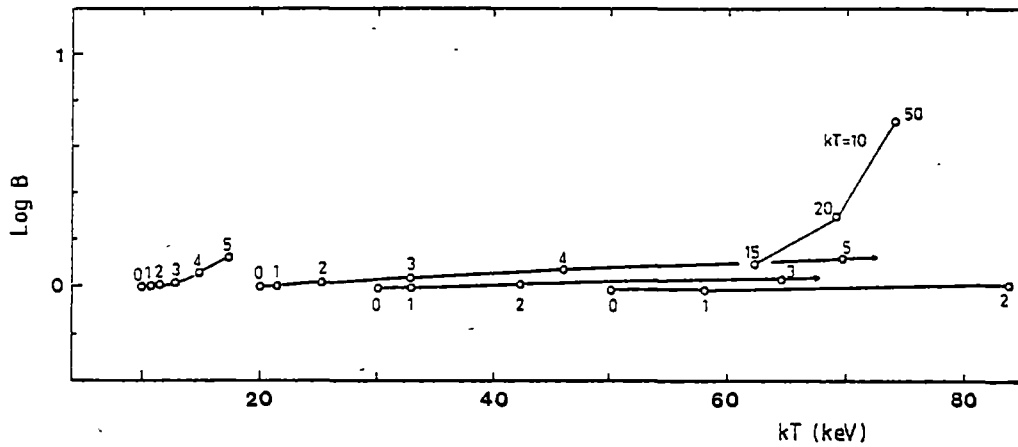

Figure 4.3 The loci of the best fit parameters B and kT of TB spectra with no Comptonization to TB spectra with Comptonization at various kT (10,20,30 and 50 keV). The value of τ is indicated at each point.

TABLE 4.4

	kT	Range of τ
Cyg X-1	≥30	0-15
A0620-00	<10	0-50
Cyg X-3	~10	0-50
Cir X-1	10-20	0-12
Her X-1	~20	0-12
Cen X-3	~20	0-10
GX1+4	10-20	0-12
GX339-4	~10	0-50

In some cases (Cir X-1 and GX1+4) kT must vary to obtain the necessary range of α. Such effects are certainly possible in Cir X-1 where strong shocks are presumed to occur when the compact object is at periastron. These shocks will heat the accreting matter (Murdin et al., 1980). In the case of GX1+4, no models have been constructed which require constant kT. This does not mean that the other sources have constant kT but that by only varying τ, their behaviour can be

modelled satisfactorily. The value of kT ~ 30 keV for Cyg X-1 would imply a spectral turnover at 90 keV (~3 kT). This is consistent with the known turnover at ~100 keV (Nolan et al., 1981). White et al. (1983) found a turnover at ~45 keV for GX1+4 which agrees with the derived value of kT ≈ 10-20 keV. The results for the pulsars Her X-1 and Cen X-3 are not as good with observed turnover energies of ~25 keV and ~20 keV respectively (White et al., 1983). The model predicts turnovers near 60 keV.

The variations in τ can be achieved by varying n_e or the path length R_c of the scattering region (or cloud) using the following.

$$\begin{aligned} \tau &= n_e \sigma_T R_c \\ &= \frac{3\sigma_T}{4\pi} N R_c^{-2} \end{aligned} \tag{4.2}$$

where σ_T is the Thomson cross section and N is the total number of electrons in the cloud (assuming constant n_e). Expansion (contraction) of R_c by a factor a can decrease (increase) τ by a^2 provided N is constant. In the case of A0620-00, Cyg X-3 and GX339-4, a ~ 7 and for Cen X-3 the minimum value of a is ~3.

The equations of Chapline and Stevens (1973) do not consider the cooling of the electron gas by the photons. They require kT to remain constant. Guilbert and Fabian (1981) relax this constraint in their Compton cooling model for Cyg X-1. If the size of the cloud can change α through variations in τ, it may modify the cloud's X-ray luminosity. To estimate the true variations in the integrated flux in terms of kT and τ the line of constant luminosity from 10 to 100 keV is marked on the SVP diagram (Figure 4.2). It has a slope of 1.49 which is larger than the value of S for all but one source (GX1+4). The mean observed value of S (= 1.21) implies hard flux ≈ 7 x soft flux but for GX1+4, the reverse is observed with soft flux (α=4) ≈ 2 x hard flux (α=1.5).

We now derive the expected luminosity from the cloud as a function of R_c using the Compton cooling model of Guilbert and Fabian (1982). The maximum X-ray luminosity L_{max} from a scattering region is

$$L_{max} = n_e 3kT\frac{4\pi}{3} R_c^3 t_e^{-1} \tag{4.3}$$

where $t_e = \tau^2/n_e\sigma_T c$ is the escape time of a photon (Guilbert and Fabian, 1982). Using the condition of constant N, equation (4.3) becomes

$$L_{max} = 3kT \frac{4\pi}{3\sigma_T} c R_c \ . \tag{4.4}$$

The actual X-ray luminosity L depends on the relative rates of heating and cooling of the gas cloud (Guilbert and Fabian, 1982)

$$L = (t_e/t_{cool})L_{max} \tag{4.5}$$

where

$$t_{cool} = \frac{3E_0}{L_s} \exp(t_{therm}/t_e)\frac{4\pi}{3} R_c^3 \tag{4.6}$$

is the cooling time of the cloud and E_0 is the energy of the soft photon source which has a total luminosity L_s.

$$t_{therm} = W(n_e\sigma_T c)^{-1} \tag{4.7}$$

is the thermal heating time of the cloud,

and $$W = \log(\frac{kT}{E_0})/\log(1 + \frac{4kT K_3(m_e c^2/kT)}{m_e c^2 K_2(m_e c^2/kT)}) \ , \tag{4.8}$$

K_3 and K_2 are modified Bessell functions.

Combining equation (4.7) with t_e yields

$$t_{therm}/t_e = W/\tau^2 \ . \tag{4.9}$$

From equation (4.6) and (4.2), we obtain

$$t_e/t_{cool} = \frac{\tau^2}{n_e\sigma_T c} \frac{L_s}{3E_0} \exp(-W/\tau^2)N^{-1} \ . \tag{4.10}$$

In terms of R_c, equation (4.10) becomes

$$\frac{L}{L_{max}} = \frac{t_e}{t_{cool}} = \frac{L_s \sigma_T}{4\pi E_0 c} \frac{1}{R_c} \exp(-G R_c^4) \qquad (4.11)$$

where $$G = \frac{16\pi^2 W}{9\sigma_T^2 N^2} .$$

Inserting L_{max} from equation (4.4) and assuming the cloud is at a distance D from the soft photon source, we have

$$L = L_s \frac{kT}{E_0} \exp(-G R_c^4) \cdot \left(\frac{R_c^2}{4D^2}\right) \qquad (4.12)$$

L is the total flux emanating from the cloud. The total flux from the system L_T will also include the soft photon source if it is not obscured by the gas cloud. Guilbert and Fabian (1982) estimate that only 10% of the soft component is intercepted by the gas clouds in Cyg X-1. If this is true for the majority of the sources then $L_T = L + L_s$.

The cloud parameters are only known for Cyg X-1 because of detailed concurrent low and high energy observations. Such observations have not been carried out for the other sources. From Guilbert and Fabian (1982), the parameters of a typical cloud are

$n_e = 2.7 \times 10^{16}$ cm^{-3} $\qquad$ $L_s = 10^{36}$ erg sec^{-1}

$R_c = 1.1 \times 10^8$ cm $\qquad$ $N = 1.5 \times 10^{41}$

$E_0 = 0.5$ keV $\qquad$ $\tau \sim 2$.

Inserting into equation (4.12) and adapting $D = 1.6\ R_c$ so that 10% of the soft flux is intercepted by the cloud as in Cyg X-1, yields the following

R (cm)	τ	L/L_s	L_T/L_s
0	∞	0	1
2×10^7	25	0.6	1.6
4×10^7	12	2.4	3.4
6×10^7	5.5	4.2	5.2
8×10^7	3.1	3.4	4.4
1×10^8	2.4	2.2	3.2
2×10^8	0.5	0	1
3×10^8	0.2	0	1

By including L_s in the total source flux the minimum L_T occurs when $\tau < 1$. Our predicted range of τ for Cyg X-1 was 0 to 15 corresponding to changes in L_T/L_s from 1 to ~5. The observed relative increase in L_T from the high state ($\alpha \sim 3$) to the low state ($\alpha \sim 1$) is <5. To compensate for the lack of increase in L_T, variations in kT and/or L_s leading to changes in L (equation 4.12) may have occured. When $\alpha > 2$, R_c must increase. This could arise from an increase in L_s due to an increase in $\dot{M}$. This would have the effect of increasing S nearer to the observed values.

Equation (4.12) is highly dependent on the cloud parameters and the sources cannot be easily modelled without concurrent data from the soft and hard X-ray regions. Only one set of observations have covered the transition from high to low spectral states (or vice versa). These are the Ariel V observations of Cyg X-1 during 1975 May (Chiapetti et al., 1981) and have enabled estimates of E_0. The time lag between the hard X-ray and soft X-ray fluxes have enabled estimates of n_e and R_c (Guilbert and Fabian, 1982 and references therein).

In the case of pulsars, large τ may smear out the X-ray pulsations that originate near the surface of the neutron star. Maraschi et al. (1977) suggest a correlation exists between the existence of a pulsation period and the hardness of the X-ray spectrum. At large τ, a surrounding cool cloud softens the emergent X-ray spectrum but will also reduce the pulsed fraction. At low τ, the intrinsic pulse spectrum and pulsations are seen. The time of escape of a photon is

$$t_e = 0.22 \left(\frac{R_c}{10^9}\right)^2 \left(\frac{n_e}{10^{16}}\right) \text{ sec} .$$

This will only affect fast rotators like SMC X-1 if R_c and n_e are comparable to the cloud parameters of Cyg X-1. Fabian, Guilbert and Ross (1982) estimate $R_c \simeq 10^8$cm and $n_e \simeq 6 \times 10^{16}$cm^{-3} for the scattering cloud of 4U1822-37 corresponding to $t_e \sim 0.01$ sec. If $R_c > 2 \times 10^8$cm

then the gas will not be completely ionized. For the fast rotator Her X-1, changes in R_c (and n_e) will not affect the pulse shape but will harden the time average spectrum leading to the observed variability.

In conclusion, the anticorrelation between spectral index and the normalisation of the X-ray spectrum seen in GX1+4 and other luminous galactic sources can be explained by changes in the size of the hot cloud (R_c) causing Compton scattering of a soft photon source. In the case of GX1+4, changes by a factor of ~3.5 in the radius of an electron cloud of temperature kT ≃ 20 keV can mimic the variations of the observed power law photon number index of 4.1 to 1.2. At low τ, corresponding to a large cloud, little Comptonization occurs and the spectrum is soft. If the cloud contracts and conserves the total number of electrons, then τ increases ($\propto R_c^{-2}$) and the spectrum hardens. The size of the cloud may be dependent on $\dot{M}$.

At low τ, the cloud's X-ray luminosity is negligible. In order to agree with the observed flux at large α, the soft photon source must be visible. This would occur if the Compton region does not surround the soft photon source. One possible geometry is that the soft source originates near the compact object and the cloud(s) reside in the accretion disc.

As a final note, SS433 shows similar spectral variability. Ariel VI observations show α varies between 1.3 and 2.25 indicating S ~ 0.75 (Ricketts et al., 1981). Further observations are required to test if Compton scattering is responsible for the variability.

4.3 Update on the UTIC Project and the UTIC83 Balloon Flight

Several improvements have been planned for the detector and platform based on the experience of UTIC81 and previous flights. The reliability of the counter was decreasing rapidly due to damage from parachute landings and the design was a compromise based on costs and

simplicity. Dr. A.B. Giles has been designing a new modular rectangular detector. Each module of area 2500 cm^2 is filled with 2 to 3 atm of xenon for operation over the energy range 20 to 150 keV. The decrease in area for a single module is compensated for by substantial improvements in background rejection techniques so that the sensitivity of the new detector is expected to be considerably improved over the UT detector. One particular powerful background technique that is being considered is escape gating.

The last balloon flight (UTIC83) of the current UTIC platform was on March 26, 1983 from Cachoeira Paulista, Brazil. None of the problems encountered during UTIC81 were experienced. Energy resolution was 25% FWHM at 60 keV compared to 42% for UTIC81. The flight duration was 7 hours at float before the balloon inexplicably failed at altitude. Unfortunately the parachute failed to deploy and the payload was destroyed. Excellent data were obtained on three sources, SS433, the QSO MR2251-178 and the binary pulsar SMC X-1. Analysis of the data is now currently under way by members of the group.

Current plans call for the construction of the new detector and a similar platform to the UTIC design. The IC detector will not be incorporated in this new platform. The encoder will be controlled by a microprocessor so that the data format can be rapidly modified. With count rates expected to be less than 100 sec^{-1}, information on the precise time and energy of each detected event will allow post-flight analysis of phase-dependent pulsar spectra. This was not possible with the old telemetry configuration for fast pulsars (periods <5 sec). The tracking of the UTIC83 flight was less than desirable and an onboard Omega receiver is essential to directly input the current geographic position to the aspect microprocessor.

CHAPTER 5

OPTICAL AND SOFT X-RAY OBSERVATIONS - EQUIPMENT AND METHOD

As a complement to hard X-ray observations of galactic objects, a program, initiated in 1978 to conduct optical observations of binary X-ray systems, has been continued. The emphasis has been on the study of cataclysmic variables where the components are thought to be a late type star and white dwarf whereas many of the hard X-ray objects are binary X-ray pulsars with components of an early type star and a neutron star.

With the greater sensitivity of the HEAO-1 and HEAO-2 satellites and the substantial reduction in the error box areas of X-ray source positions, there has been a rapid increase in the number of X-ray emitting cataclysmic variables. Currently ~50 are known covering all the types. We have restricted detailed studies to two of the five members of the class of intermediate polars as defined by Warner (1982).

The principal optical telescope used was the 3.9 metre Anglo-Australian Telescope. The Mount Stromlo Siding Spring Observatory (MSSSO) 1 metre reflector at Siding Spring and the University of Tasmania 1 metre telescope at Mt. Canopus, Hobart, Tasmania, have been used for photometry. Soft X-ray observations of the intermediate polar 2A0526-328 and the nova-like variable VY Sculptoris were made using the Einstein Observatory (HEAO-2).

5.1 Anglo-Australian Telescope

The Anglo-Australian Telescope (AAT) on Siding Spring mountain near Coonabarabran, New South Wales, is a 3.9 metre equatorially mounted reflector of Ritchey-Crétien design. Five foci are available, f/3.3 prime focus, f/8, f/15 and f/36 Cassegrain and f/36 Coudé. The telescope is under complete computer control and essentially appears as an "ideal" telescope with its pointing corrected for atmospheric refraction, flexure and gear errors. The rms absolute pointing error whilst working at Cassegrain is ~3 arc sec. Pointing whilst offsetting is accurate to ~0.1 arc sec.

5.1.1 The IPCS and RGO Spectrograph

The Royal Greenwich Observatory (RGO) spectrograph is mounted at the Cassegrain f/8 focus of the AAT (Wampler and Morton 1977). It has two cameras, an 82 cm focal length f5.5 spherical mirror and a 25 cm f/1.67 Cassegrain-Maksutov system. All spectroscopic observations used the 25 cm camera. Figure 5.1 from Blades (1980) shows the light path in the spectrograph. The camera can view direct or the image off the mirrored surface of the slit. The limiting magnitude is ~18 in moonlight and ~22 in moonless conditions. The dispersion range of the spectrograph is from 5 to 160 Å/mm. The slit width can be varied from 0.07 to 16.75 arc seconds. Neutral density and colour filters are mounted above the slit. A copper-argon arc lamp is used for wavelength calibration. The tungsten lamp is for determining the pixel to pixel sensitivity of the image tube and this procedure is referred to as flat fielding.

For low dispersion observations, grating 250B with 250 grooves per mm was used. For the 1979 February 16-17 observations, the grating was set blaze to camera giving a dispersion of 140 Å/mm. For the other low dispersion observations, the grating was set blaze to collimator for a dispersion of 156 Å/mm. The high dispersion observations on 1979 February 21, 1980 February 10, 1982 January 16 and June 10-11 used grating 1200B set blaze to collimator with a dispersion of 33 Å/mm.

The University College, London, Image Photon Counting System (IPCS) (Boksenberg 1972) is a two-dimensional detector. It is the principal detector used with the RGO spectrograph although CCD detectors have now been developed for spectroscopy. The IPCS detects individual photons using a high gain 4-stage image intensifier tube optically coupled to a continuously scanning television camera. Its central sensitive area is ~30 mm across with an S20 response. Event-centre-detection logic identifies the centroid of the photon event and records it in a 512 k

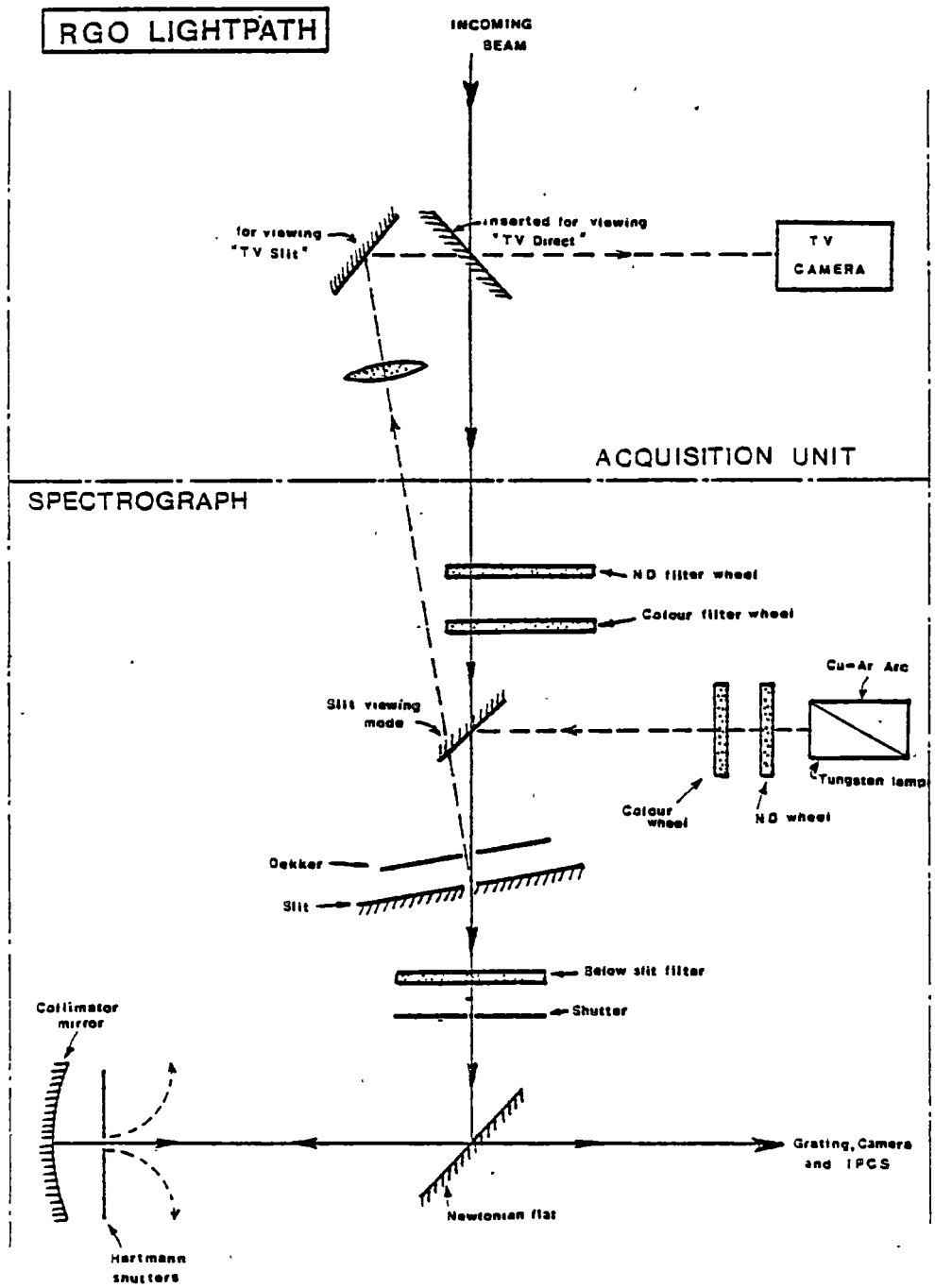

Figure 5.1 RGO light path at the Cassegrain focus of the AAT

digital memory. The gain is ~10^8 per primary photo-electron.

There are several modes of acquiring data when used in its spectroscopic mode. Data can be recorded in 1 to 3 pairs of one dimensional spectra (1D) or as a two-dimensional rectangular window (2D). All our observations used the 2D mode. The window format can be selected by the observer. The spectral resolution is determined by the number of lines on the camera. Highest resolution is 2048 lines which means spectra are recorded in 2048 contiguous channels. The number of image elements parallel to the slit (and perpendicular to the spectral lines) can be set from 18 to 514. Each increment can be either 0.36 or 0.7 arc sec dependent on whether the X-gain is high or low respectively. This can be further scaled by factors of 2, 4, or 8. This projects onto the sky as a series of continuous points where one acquires the data. Memory constraints limited the 1979 February data to 1987 spectral by 8 spatial increments. By using the external memory installed after that date, the camera area was set at 2040 spectral by 15 spatial elements. There are several advantages of the 2D mode. Sky background is taken directly next to the star being observed and allowance can be made for varying seeing. If studying variable stars and if a second nearby star (assumed non-variable) can be centred on the slit by suitable rotation of the instrument mount, then, that star can be used to monitor the relative brightness of the candidate star.

A significant problem of the image tubes used, was small shifts in the spectral channel dependent on the physical orientation of the IPCS. This problem, referred to as 'flop' excluded observations within ~½ hour of zenith and for position angles of the slit at ~135° or ~315°. To move the telescope across the meridian, it was necessary to ensure that the zenith angle was always > 5°.

Software is provided to focus the spectrograph, rotate the camera until the scan lines are perpendicular to the dispersion direction and

to remove S-distortion caused by the image tube. On-line manipulation and display of data is available to monitor the progress of the observation. Observations can be acquired continuously using the IPCS in the continuous mode. A dwell time is set via the controlling computer and observations are automatically stopped, data logged and restarted. There is ~1 second deadtime between each observation to dump data to tape, and initiate the new run.

At the end of each observation, the data are logged onto 9 track magnetic tape for reduction using the Scanner Data Reduction System (SDRSYS) programs. SDRSYS is an interactive language system. Each observation is first flat-field corrected by dividing by the relative response of each pixel. Calibration arc spectra are then reduced to provide a polynomial fit between wavelength and bin number. For most reductions a third order polynomial was used. Sky data are subtracted from the star+sky data and then 'scrunched' with the calibration polynomial. 'Scrunching' assigns a wavelength to each bin and then the bins are rearranged to be of equal width. Counts are adjusted so that the total counts are preserved. Corrections can then be made for atmospheric extinction, earth radial velocity, neutral density filters if used, and the IPCS instrumental response if a calibration star was observed. Some of the calibration stars used by SDRSYS are the white dwarf stars of Oke (1974).

5.1.2 The Hatfied optical/infrared polarimeter

The polarimeter is designed to make simultaneous optical and infrared polarization measurements. Figure 5.2 shows the layout of the instrument. It differs from the previous description by Bailey and Hough (1982) in that the IR dewar is attached to the side and the optical photometer to the bottom of the instrument. The IR dewar is from the AAO infrared photometer (IRPS) and employs an InSb detector described by Barton and Allen (1980).

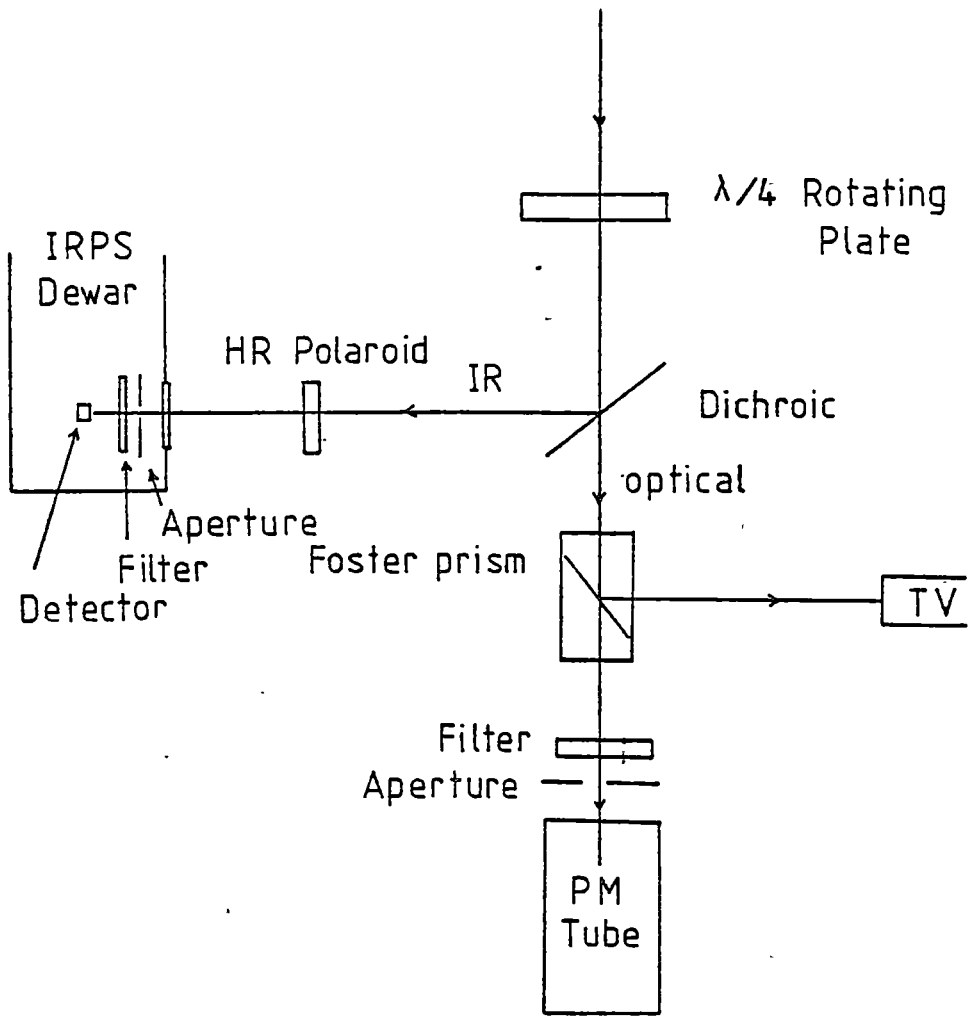

Figure 5.2 The configuration of the Hatfield Polarimeter at the Cassegrain focus of the AAT during 1982 June.

The rotating $\lambda/4$ plate produces a sine wave modulation of the signal, the amplitude of which is a measure of the circular polarization. The phase of the modulation is fixed and is determined by the alignment of the optics in the instrument.

The controlling software assumes it is measuring linear polarization in which both the amplitude and phase are relevant and thus measures both the sine and cosine components of the modulation which it calls Q and U. They are obtained by sampling the data every quarter of the modulation circle. If A, B, C and D represent the counts per quarter of a sine modulation then

$$\text{total intensity } I = A + B + C + D$$

$$\text{and} \qquad Q = (A-C)/(A+C)$$

$$U = (B-D)/(B+D).$$

The required circular polarization V is a linear combination of Q and U:

$$\text{i.e.} \quad V = aQ + bU$$

where a and b are constants which change from run to run due to the fact that changing the filter on the IRPS changes the synchronization of the data sampling with the rotating wave plate. The values of a and b are listed in Table 5.1.

TABLE 5.1

	optical		IR	
	a	b	a	b
1982 June 7	0	-1	0.56	-0.83
June 8	0.39	-0.92	-0.32	-0.94

For the observations of V1223 Sgr and the AM Her binaries PG1550 + 195, CW1103 + 254, H1405 - 45 and HO139 - 68 during 1982 June, the polarimeter was configured for circular polarization only.

Beamswitching was used for background determination. The cycle was six seconds on source followed by a 1 sec beamswitch to a sky point 15 arc sec from the source. A six second integration on background was followed by a beamswitch back to source.

The data from the photometers is fed into a Z80 microcomputer which analyses it in real time. At the end of a star-background cycle, the cumulative mean and error are output to a line printer. Q and U are printed out, both in counts and in percent of the total counts. No facility was available for output to tape. After an average of six cycles the run was aborted and restarted with UT times from a master clock recorded by hand.

No TV guidance was available so the auto-guider was used. Every twenty minutes, the centering of the star in the aperture was checked by peaking the IR signal whilst offsetting in declination and hour angle.

5.2 MSSSO 1 metre telescope at Siding Spring

This is an equatorially mounted 1 metre reflector with a single channel 1P21 phototube at the Cassegrain focus. Standard Johnson UBV filters were used. Data were logged onto PDP cassettes and onto a line printer.

5.3 Mt. Canopus 1 metre telescope

Located in the foothills of Hobart, Tasmania, it is a 1 metre reflector (Waterworth 1980) with folded Cassegrain and Coudé focus. The twin channel photometer mounted at the folded Cassegrain uses EMI9658B photomultipliers. Data are logged onto floppy discs via an LSI-11 minicomputer.

5.4 Einstein Observatory (HEAO-2)

The Einstein satellite observatory consists of a 0.6m diameter Wolter I grazing incidence mirror with five inter-changeable focal

plane instruments. They are the image proportional counter (IPC), the high resolution imager (HRI), the solid state spectrometer (SSS), the objective grating spectrometer (OGS) and the focal plane crystal spectrometer (FPCS). Coaligned with the X-ray optical bench is the Monitor Proportional Counter (MPC). The effective area of the mirror ranges from ~400 cm^2 at 0.25 keV to ~30 cm^2 at 4 keV. The instruments used during the guest observations of the cataclysmic variables 2A0526-328 and VY Scl were the MPC and IPC. HRI positions have been searched for optical counterparts (Chapter 8). Brief details are described below. For further details of the platform and the other instruments see Giacconni et al. (1979).

5.4.1 The Monitor Proportional Counter (MPC)

The MPC is an Ar-CO_2 gas filled proportional counter of area 667 cm^2 sensitive in the range 1.5 to 22 keV, with 8 contiguous pulse height channels. The collimator provides a circular 1.5° FWHM field of view. Background rejection is by two mechanisms, pulse shape discrimination and anticoincidence. Photon timing resolution is 1 μs for count rates less than 33 sec^{-1} and ~1.6% of the interval between events for count rates > 33 sec^{-1}. Accumulated counts in the pulse height analyser channels are read every 2.56 sec.

5.4.2 The Image Proportional Counter (IPC)

The IPC is a position sensitive proportional counter of active depth 4 cm filled with 84% argon, 6% xenon and 10% CO_2. The spatial resolution is ~1 mm which corresponds to 1 arc min when projected on the sky. The total field of view is 75' x 75'. Timing resolution is 63 μs and energy resolution is < 100% FWHM above 1.5 keV and 200% at 0.28 keV. Thirty two pulse height channels are available from 0.1 to 4 keV. Differential gain changes over the counter area have made it difficult to calibrate the spectral data from the IPC and in the case of our observations has only been solved for the analysis of VY

Sculptoris. Two effects have contributed to this problem: differential gas loss through the entrance window and temperature changes when the instrument was driven to focus.

5.4.3 The High Resolution Imager (HRI)

The HRI is used for high spatial (~1 arc sec) and temporal (~7 μ sec) studies. It has no spectral capacity apart from absorption filters and has a maximum count rate of 100 counts per second. The detector consists of two cascading microchannel plates and a crossed grid charge detector and operates over the central 25' of the focal plane.

The initial reduction of the Einstein data of 2A0526-328 and VY Sculptoris by P.W. Hill used the standard software available at the Einstein ground station located at the Centre for Astrophysics, Harvard University, U.S.A.

5.5 Temporal Analysis Methods

The technique used for temporal analysis of the photometric data are outlined and definitions follow

x_i, y_i	ith element of data set x and y respectively
t_i	ith time element of data
N	number of elements in set x and y
f	frequency
τ	lag time in units of temporal bins

then mean is $\bar{x} = \frac{1}{N} \sum_{i=1}^{N} x_i$.

To use the auto and cross correlation functions the Hatfield photometric data were interpolated and sampled at 14 second intervals to provide an equally spaced data set.

Correlation Functions

Auto correlation function (ACF)

$$A_\tau = \frac{1}{N} \sum_{i=1}^{N-\tau} (x_i - \bar{x})(x_{i+\tau} - \bar{x}) \,/\, \sigma^2 \qquad \tau \neq 0$$

$$= 1 \qquad \tau = 0 .$$

Cross correlation function (CCF)

$$C_\tau = \frac{1}{N} \sum_{i=1}^{N-\tau} (x_i - \bar{x})(y_{i+\tau} - \bar{y})$$

$$C_{-\tau} = \frac{1}{N} \sum_{i=\tau}^{N} (x_i - \bar{x})(y_{i-\tau} - \bar{y}) .$$

Least Squares Fourier Analysis

Let $$yc = \sum_{i=1}^{N} y_i \cos 2\pi f\, t_i$$

$$ys = \sum_{i=1}^{N} y_i \sin 2\pi f\, t_i$$

then the reduction factor RF of Lomb (1976) is

$$RF = \{ (\frac{2}{\sqrt{N}} yc)^2 + (\frac{2}{\sqrt{N}} ys)^2 \} / \sum_{i=1}^{N} y_i^2 .$$

RF corresponds to the fraction by which a best-fitting sine wave at that frequency reduces the variance in the data. By definition, RF varies between 0 and 1.

Q Method

The Q method of Warner and Robinson (1972) is a particularly convenient analysis technique for large unequally spaced data sets since no trigonometric computations are required. The data are folded at the trial period into B phase bins. Then Q is calculated by

$$Q = \frac{1}{B} \frac{\sum_{i=1}^{B} s_i n_i}{N}$$

where s_i is the mean in the ith phase bin and n_i the number of data points in that bin.

CHAPTER 6

OBSERVATIONS OF INTERMEDIATE POLARS 2A0526-328 AND V1223 Sgr AND NOVA-LIKE OBJECT VY Sculptoris

6.1 2A0526-328

6.1.1 Spectroscopy 1979 February

The optical candidate for 2A0526-328 was observed during 1979 February on three separate occasions using the RGO spectrograph and Image Photon Counting System. Low dispersion spectroscopy at 140 Å/mm was carried out on February 16 and 17, and higher dispersion spectroscopy of 33 Å/mm on the night of February 21. Our AAT setting position for the candidate is $\alpha = 05^h\ 27^m\ 34.5^s$, $\delta = -32^\circ 51'22''$ (1950.0).

Low Dispersion Observations

Spectroscopic observations at 140 Å/mm were carried out from 1230 UT on 1979, February 16, and again on 1979, February 17, from 1327 UT. The integration periods were 1030 seconds and 2100 seconds respectively. Wavelength calibrations were made at the start and end of each observation by observing a Cu-Ar arc. The reduced spectrum from February 16 (JD = 2443920.52) is shown in Figure 6.1. Visible in emission, on a very flat continuum, are the Balmer series H_α to H_{10}, HeI (4026, 4387, 4471, 4922, 5876), HeII (4686), the CIII NIII blend (4640-50) and CaII (3933). It is similar to the spectra of AM Her (Cowley and Crampton, 1977; Stockman et al., 1977) and the members of its class of accreting magnetic white dwarfs 2A0311-277 (Griffiths et al., 1979), VV Pup and AN Ursae Majoris (Liebert et al., 1978). Table 6.1 lists the equivalent widths and full widths at half maximum (FWHM) for all lines from both observations. The ratio of equivalent widths for all lines from the first to second observations is ~0.8. This is a consequence of observing at different binary system phase as will be discussed later. The continuum decreased to 43% of the first observation. There was no change in the shape of the continuum. The strongest line observed by Charles et al. (1979) was H_α with an

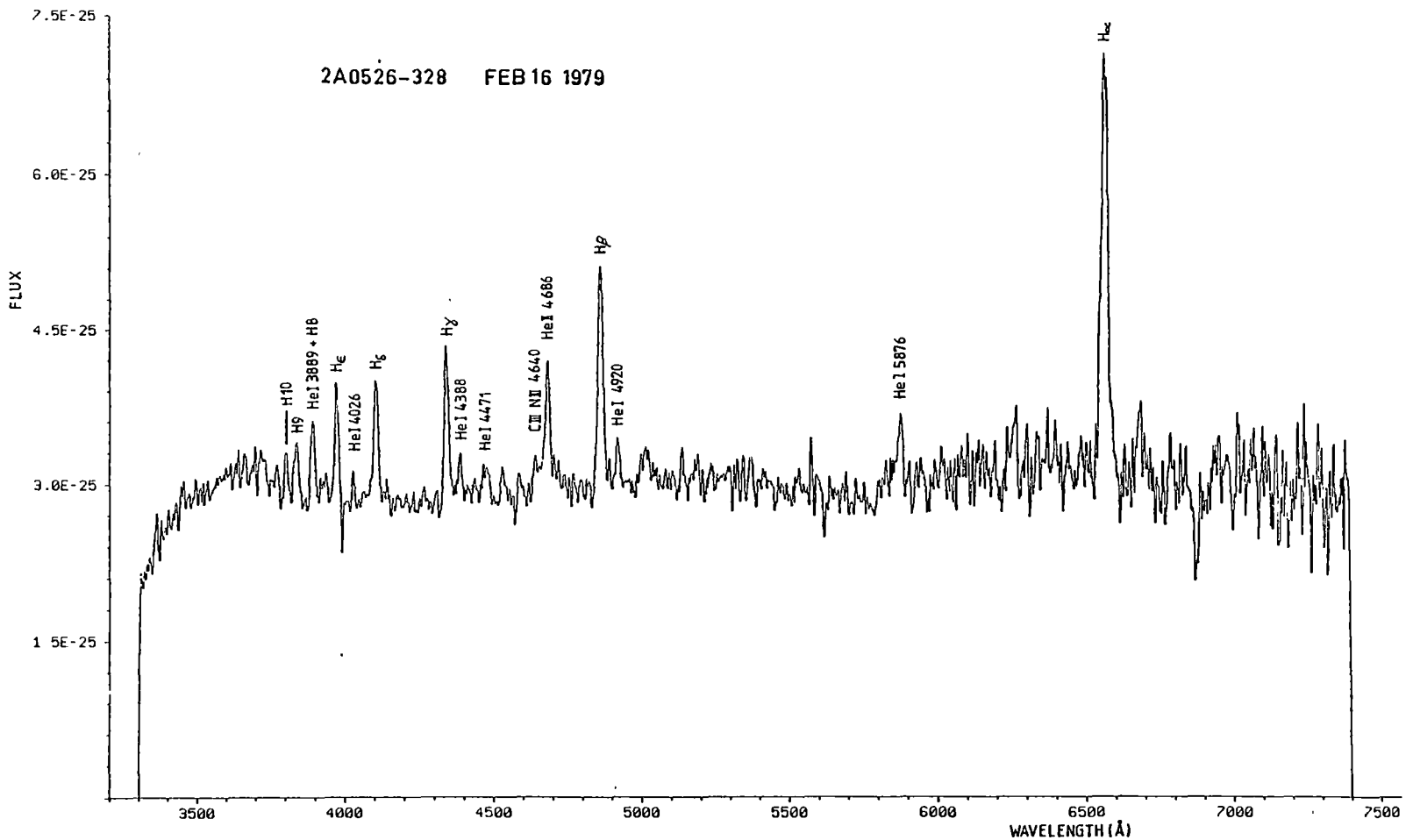

Figure 6.1 Spectrum of the optical counterpart of 2A0526-328, taken at 1230 UT, February 16, 1979. Flux units are erg cm^{-2} sec^{-1} Hz^{-1}. Resolution is $\sim$ 6 Å.

Table 6.1

Identification	Wavelength (Å)	February 16, 1979 Equivalent width (Å)	FWHM (Å)	February 17, 1979 Equivalent width (Å)	FWHM (Å)
H_{10}	3797.6	2.7	15	3.7	15
H_9	3835.4	3.7	24	4.3	15
H_8	3889.1	4.7	18	6.0	15
CaII	3933.7	1.6	24	1.3	18
H_ε + CaII	3968.5 + 3970.1	6.0	13	6.4	15
HeI	4026.3	0.9	9		
H_δ	4101.4	6.5	18	9.6	15
H_γ	4340.5	8.9	15	11.8	15
HeI	4387.9	0.8	$\sim$ 10	3.2	22
HeI	4471.6	$\sim$ 1.0	$\sim$ 24	3.3	24
CIII NIII	4640	$\leq$ 1.5	$\sim$ 10	4.1	33
HeII	4685.7	7.9	18	9.0	18
H_β	4861.3	15.3	19	20.6	21
HeI	4921.9	1.4	12	< 1.6	9
HeI	5875.7	3.1	19	7.6	19
H_α	6562.8	38.4	27	43.9	24

Equivalent widths and full widths at half maximum (FWHM) for all observed lines of 2A0526-328 taken from the Anglo Australian Telescope February 16 and February 17, 1979. The uncertainty in the equivalent widths is $\sim$ 0.5 Å.

equivalent width of ~23 Å. This is well below the values obtained in our observations (Table 6.1).

Using the response curve of the Johnson B and V filters in Allen (1973) the approximate magnitude for 1979 February 16 is m_B ~13.0, m_V ~12.8 and 1979 February 17, m_B ~13.9 and m_V ~13.7. The error is difficult to estimate because of the use of a narrow slit (1.3 arc sec) and poor seeing (~3 arc sec) but should be within 30% or 0.3 mag since the calibration star was measured under similar conditions. The B magnitude on 1979 February 16 is 0.5 mag brighter than the maximum B magnitude that Motch (1981) measured, suggesting that light variations other than the periodic modulations have occurred. Recent photometry by Szkody and Mateo (1982) indicate the presence of flares up to ~1.5 mag.

The quoted line-intensity ratios in Watts, Greenhill and Thomas (1980) are in error due to measuring the line fluxes from a plot of λ versus F_ν and not versus F_λ. Correct results are listed in Griffiths et al. (1980) but only apply for 1979 February 16 spectrum. We have averaged both low disperion spectra to obtain an improved estimate.

The Balmer decrement H_α: H_β: H_γ of 1.24 : 1.00 : 0.69 is not consistent with electron densities $n_e \leq 10^6 cm^{-3}$ the regime studied by Brocklehurst (1971) but is similar to that calculated by Adams and Petrosian (1974) (Case A and Case B) for plasma with n_e ~3×10^{12} per cm^{-3}. The Balmer decrement is sensitive to the electron density in this range, principally because the radiative transition probabilities for the lower energy levels of the hydrogen atom are dependent on n_e when collisionally induced transitions become significant at n_e ~$10^{13} cm^{-3}$. Case A is when the emitting region is assumed to be optically thick in all lines and Case B is defined as optically thick to the Lyman lines but optically thin for all other lines. The line ratios of 2A0526-328

fit all the temperature regimes of Case A (6000 to 20,000 K) studied by Adams and Petrosian (1974) but for Case B only for temperatures ~6000K. In either case, the electron densities of the emission region are lower than estimated for AM Her for which $n_e \sim 10^{13} cm^{-3}$ (Stockman et al. 1977). A value of $n_e \approx 10^{13} cm^{-3}$ has also been reported for 2A0311-227 (Griffiths et al. 1979). The ratio of HeI λ5876/λ4471 = 1.5 ± 0.2 is significantly different from that of AM Her (~0.6) (Stockman et al., 1977) or for 2A0311-277 (~0.3) (Griffiths et al., 1979) but still consistent with $n_e \leq 10^{12} cm^{-3}$.

Figure 6.2 is the Balmer decrement for 2A0526-328 compared to the polar 2A0311-227 (Griffiths et al., 1979) and the intermediate polars H2252-035 (Griffiths et al., 1980; Hassal et al., 1981) and V1223 Sgr (Steiner et al., 1981). 2A0526-328 has values considerably lower than 2A0311-227 for lines shorter in wavelength than H_β but nestled around values for the intermediate polars. This suggests that as a class the intermediate polars have less dense line emission regions than the polars.

High Dispersion Observations

1979 February

A 2.5 hour observation covering the spectral range 4240 Å to 5200 Å at a dispersion of 33 Å/mm was commenced at 1017 UT, February 21, 1979. The initial integration time was 1000 seconds, but thereafter the observations were of 500 seconds duration interspersed with wavelength calibrations, until cloud interfered at 1250 UT. These spectra have been combined into 5 sets to improve the signal to noise ratio. The time dependence of the H_γ emission line during the period of observation is illustrated in Figure 6.3. Similar variability was observed in H_β. The HeII λ4686 was very weak in the first spectrum but, like H_γ and H_β, was clearly split in the 1215 to 1241 UT spectrum.

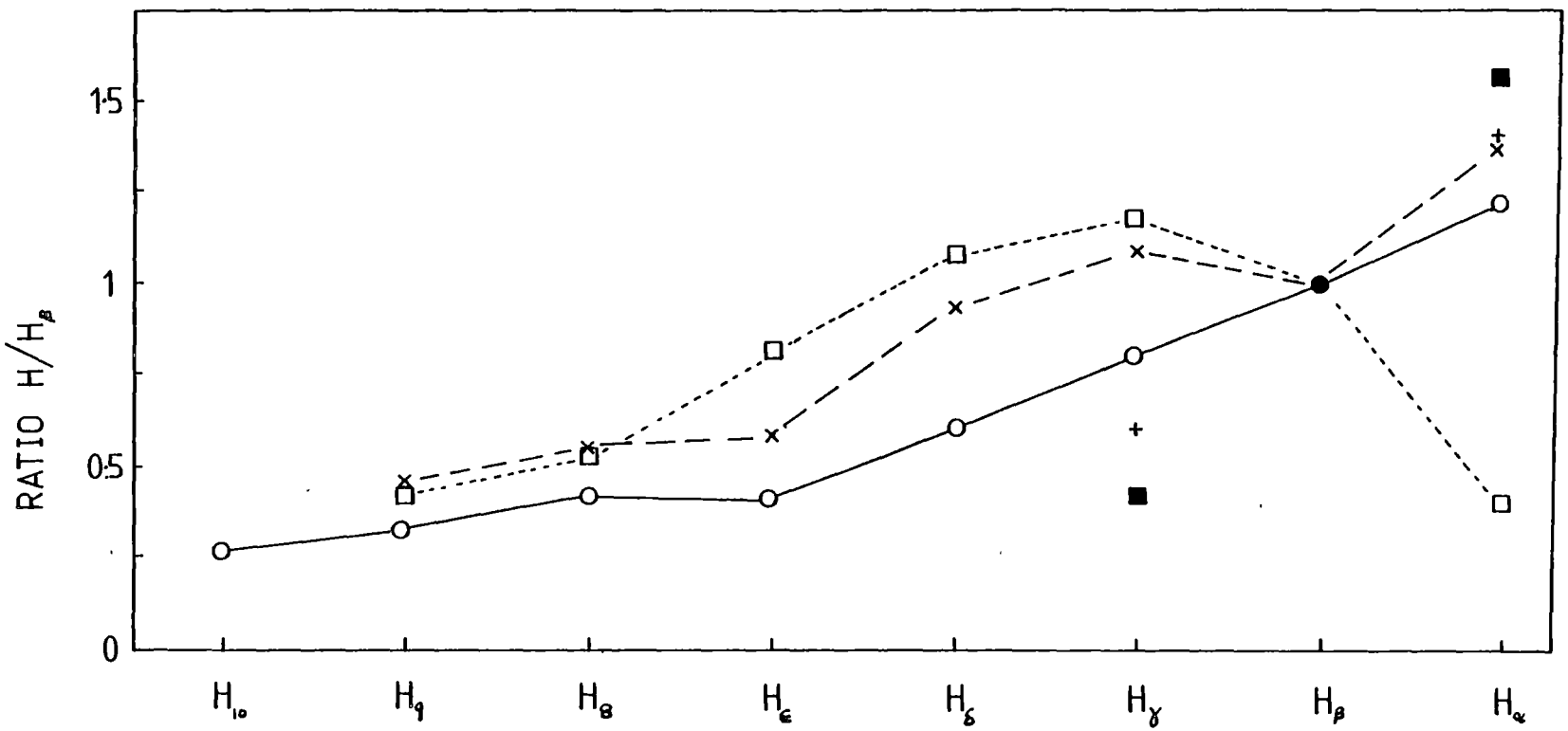

Figure 6.2 Balmer decrement for the intermediate polars 2A0526-328 (open circle), H2252-035 (crosses), V1223 Sgr (filled squares) and the polar 2A0311-227 (open squares

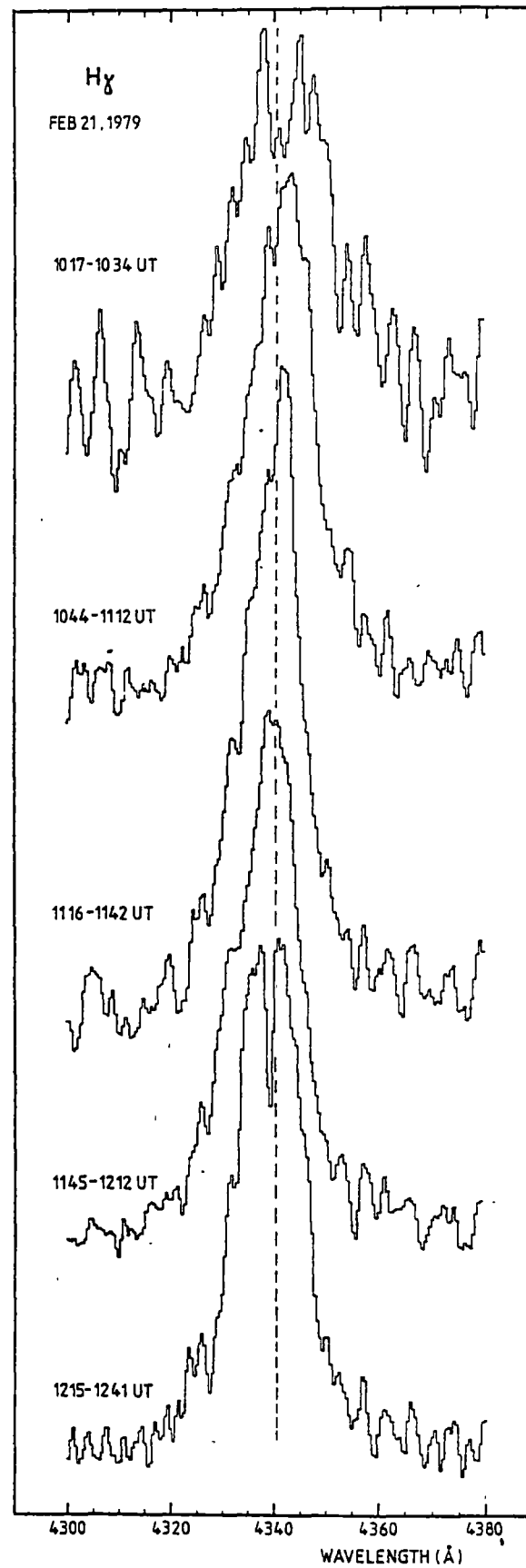

Figure 6.3 H_γ emission line profiles, at 33 Å/mm, from 1017 UT to 1241 UT, February 21, 1979. Resolution is ∿ 2 Å. The dashed line represents the rest wavelength of H_γ. The intensity of each line has been adjusted to the same height.

Of particular note is the narrowness of the absorption feature compared with the width of the line. The mean separation of the split components was 5.9 Å for H_γ and 5.2 Å for H_β. There is evidence of marginal statistical significance for splitting of the H_γ line in one of the 500 second integrations at ~1115 UT. This is not apparent in the combined data sets (Figure 6.2).

Radial velocity calculations were carried out for H_β, H_γ, HeII λ4686 and HeI λ4471 by two different methods. The first method was to estimate the wavelength by measuring the centre of gravity of the profile and the second to measure the centre wavelength at the half height of the profile. The results were consistent for each method. However, the centre of gravity method resulted in less random fluctuations and the results obtained were used in the subsequent radial velocity analysis.

The radial velocity curve for the H_γ and H_β lines is illustrated in Figure 6.4(a). The HeI λ4471 velocity curve is systematically different from the others by ~100 km sec^{-1}. However, the data are statistically poor. This was the first radial velocity study of the object and gave the first estimate of the period. The formal least squares fit to H_γ and H_β data yielded the orbital parameters listed in Table 6.2, indicating a close, low mass system, unless the inclination angle is very small. Subsequent observations and analysis by HCCTC and including the data illustrated in Figure 6.4 have refined the radial velocity period to 5.48^{hr}.

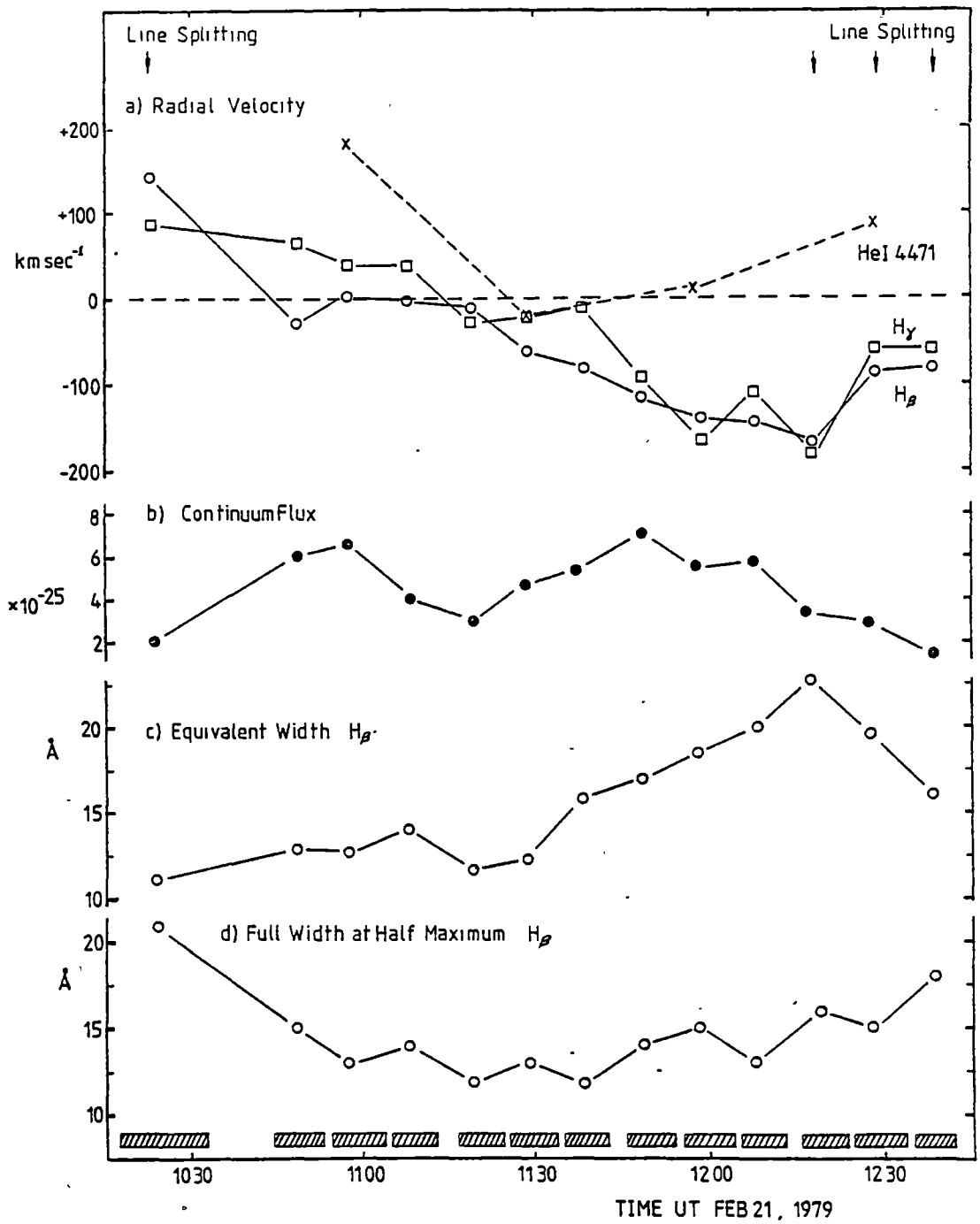

Figure 6.4

Data from observations of 2A0526-328 on February 21, 1979. The shaded blocks represent the duration of each observation.

(a) Radial velocity curves for H_γ(O), H_β(□) and HeI λ4471 (Ẋ). Scans centred on 1100, 1130, 1200 and 1230 UT have been added together to provide an adequate signal to noise ratio for HeI λ4471.

(b) Continuum flux (erg cm^{-2} sec^{-1} Hz^{-1}) near H_β.

(c) Equivalent width of H_β.

(d) FWHM for H_β.

TABLE 6.2

Orbital Elements of 2A0526-328 from 1979 February 21 Observations

Period	3.5 ± 0.7 hr
Projected velocity	111 ± 18 km sec^{-1}
Centre of mass velocity	-25 ± 20 km sec^{-1}
Eccentricity	<0.3
Projected radius	(2.2 ± 0.8) x 10^{10} cm
Mass function	(2.1 ± 1.4) x $10^{-2} M_{\odot}$

The emission lines of H_{γ}, H_{β}, HeI λ4471 and HeII λ4686 show similar variations in equivalent width which appear to be phase dependent. The time dependence of the equivalent width of H_{β} is illustrated in Figure 6.4(c).

The width of H_{β} at half height (FWHM) is shown in Figure 6.4(d) and a similar phenomenon is seen in H_{γ} and HeII λ4686. The profile of HeI λ4471 was too noisy to determine if there were any variations in broadening. Figure 6.4(b) illustrates the time dependence of the continuum flux level near H_{β}. There are indications of a dip at about 1115 UT, but we cannot exclude the possibility of instrumental effects, an increase in atmospheric extinction or changes in seeing at that time due to the use of a narrow slit. Photometry by Motch (1981) did not reveal any eclipses and his ephemeris indicates maximum light occurs during the middle of the observations. No changes in the shape of the continuum were observed. The intensity of the continuum was, on average, three times greater than that observed by Charles et al. (1979). A correlation appears to exist between the FWHM of the emission lines, their equivalent width, and radial velocity. At maximum recessional velocity, the FWHM was large, the line was split (see Figure 6.3), and its equivalent width was a minimum. When the emission region velocity approached its mean level (~-20 km sec^{-1}), the continuum flux

dropped by 55%, and the FWHM of the line reached its minimum level. As the radial velocity approached its maximum negative value, the continuum flux increased, the FWHM of the line increased, line splitting occurred, and the equivalent width reached its maximum. The phenomenon of maximum line emission at the time of maximum negative radial velocity is also observed in 2A0311-227 (Boley et al., 1979).

1980 February

Spectroscopic observations at a dispersion of 33 Å/mm were carried out at the AAT on February 10, 1980, from 1036 to 1542 UT, and on February 11, 1980, from 1420 to 1538 UT. The measurements were made using the RGO spectrograph, 25 cm camera and the image photon counting system (IPCS). The wavelength range used (3800Å to 4800Å) includes the lines H_ϵ to HeII 4686. Dwell times of integration were 10 minutes except for the period on February 10 from 1143 to 1258 UT, where it was 5 minutes. A Cu-Ar arc was used for wavelength calibrations every 20 minutes. Observations were planned at a position angle of 135° so that the nearby companion ($m_v \approx 14.7$) could also be observed for estimating photometric variations of 2A0526-328. Unfortunately, at that position angle, flop occurs at hour angles between -2 and +2 hours and another position angle was required.

Radial velocity measurements of the emission lines were calcuated by the method of cross correlation (Tonry and Davis, 1979) using the summed spectra as template.

Briefly, all available spectra are added to provide an accurate representation of the continuum. A running mean through a large number of points provides a smooth approximation to the integrated continuum. The integrated data are then normalised by dividing by this smooth continuum and subtracting the mean. After apodising the ends of the data with a cosine bell function, we obtain the template. The wave-

length shifts obtained by correlating individual spectra against the template are applied to the individual spectra and an improved template is then constructed. The process is repeated until it converges and, from the final wavelength shifts, the velocities of the lines are calculated relative to the template. The region in which the radial velocities were calculated was centred on H_γ since this was the only line in common with the data from 1979 February. The template velocity was estimated by measuring the centre of gravity of the template profiles. Errors were estimated using the width of the cross correlation function. The reliability of the method was confirmed by comparing the results with velocities obtained by measuring the centre of gravity of emission line profiles.

The results are listed in Table 6.3 for both 1979 and 1980 data. The 1979 February velocities are within 30 km sec^{-1} of the measurements used for the radial velocity estimates in Figure 6.4. The phase of the data has been determined from the elements of HCCTC. (See Table 1.4). The radial velocity curve is shown in Figure 6.5 and confirms the ephemeris. Note that our radial velocity measurements are from the complete line and not measured at 20% of the line height as done by HCCTC, hence the shift in average velocity due to the asymmetric profile but not in the peak-to-peak amplitude.

Figure 6.6 shows H_γ line profiles from the February 1980 AAT observations combined into 20-minute dwells. Immediately apparent is the variability of the shape of the lines. These data are derived from narrow slit spectra, so apparent intensity variations are open to large errors. The rapid variability of the line profiles, however, is source-related. Profile changes from asymmetric with a blue excess to a red excess, or to symmetric, occurred on several occasions. For a brief period (1108 to 1118 UT, February 10) HeI λ4026 and HeI λ4471 were seen as absorption lines with emission wings (Fig. 6.7) indicating

Table 6.3 2A0526-328 Radial Velocities

Radial velocity of H_γ line determined by cross correlation. Phase of observation from HCCTC. ϕ_{phot} - photometric phase of 5.19^h period, ϕ_{spec} - spectroscopic period, and ϕ_{4day} - 4 day photometric period. S.D. - standard deviation of velocity.

Date	UT	JD(2444279)	Radial velocity	S.D.	ϕ_{phot}	ϕ_{spec}	ϕ_{4day}
10 Feb 80	1041	.945	138	24	.52	.84	.98
	1051	.952	225	32	.58	.88	
	1102	.960	245	34	.59	.91	
	1113	.967	314	37	.63	.94	
	1125	.976	240	25	.67	.98	
	1136	.983	250	19	.70	.01	
	1145	.990	232	22	.73	.04	
	1150	.993	249	18	.75	.06	
	1156	.997	231	21	.77	.07	
	1202	1.001	271	16	.78	.09	
	1210	1.007	230	16	.81	.12	
	1215	1.010	267	17	.83	.13	
	1222	1.015	192	18	.85	.15	
	1228	1.019	155	20	.87	.17	
	1236	1.025	50	32	.90	.20	
	1241	1.028	12	20	.91	.21	
	1247	1.033	-40	25	.93	.23	.00
	1328	1.061	31	28	.06	.35	.01
	1336	1.067	46	22	.09	.38	
	1341	1.070	81	20	.10	.39	
	1346	1.074	40	25	.12	.41	
	1351	1.077	12	26	.14	.42	
	1359	1.083	54	27	.16	.45	
	1405	1.087	60	21	.18	.47	
	1410	1.090	6	23	.20	.48	
	1416	1.094	71	19	.21	.50	
	1423	1.099	-15	21	.24	.52	
	1429	1.103	22	23	.26	.54	
	1435	1.107	72	22	.27	.55	
	1440	1.111	1	19	.29	.57	
	1451	1.119	18	21	.33	.61	
	1501	1.126	-8	22	.36	.64	
	1515	1.135	1	27	.40	.68	.03
	1536	1.150	127	32	.47	.74	
	1548	1.158	52	45	.51	.78	

Continued:

Table 6.3 cont.

Date	UT		Radial velocity	S.D.	ϕ_{phot}	ϕ_{spec}	ϕ_{4day}
		JD(2444281)					
11 Feb 80	1425	.101	31	22	.87	.90	.26
	1435	.108	144	22	.90	.93	
	1447	.116	166	22	.94	.97	
	1458	.124	174	17	.98	.00	
	1510	.132	176	22	.01	.04	
	1520	.139	266	20	.05	.07	
	1532	.147	262	19	.08	.10	
	1543	.155	212	27	.12	.14	
		JD(2443925)					
21 Feb 79	1025	.934	47	20	.93	.24	.00
	1048	.950	27	10	.01	.31	
	1058	.957	81	9	.04	.34	
	1108	.964	19	11	.07	.37	
	1120	.972	-25	11	.11	.41	
	1129	.978	-17	8	.14	.43	
	1138	.985	-64	10	.17	.46	
	1149	.992	-1±1	6	.20	.49	
	1158	.999	-104	8	.24	.52	
	1208	1.006	-123	8	.27	.56	
	1219	1.013	-87	9	.30	.59	
	1228	1.019	-48	8	.33	.61	
	1237	1.026	-76	12	.36	.64	.03

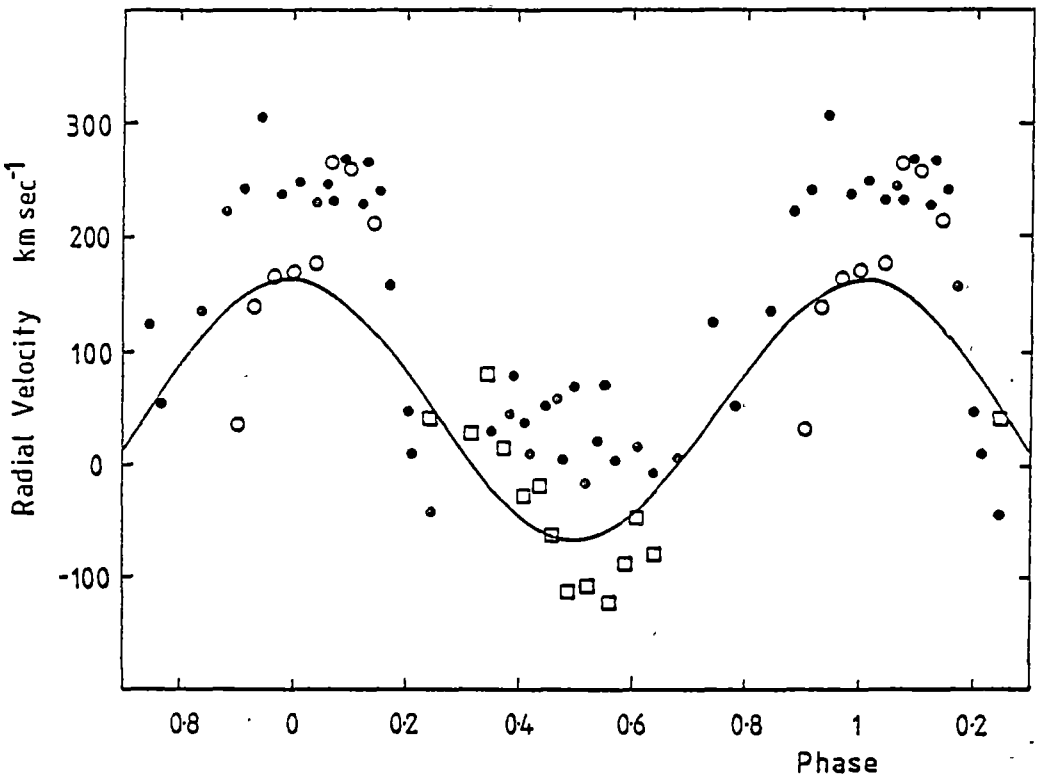

Radial velocity curve for the H_γ line determined by the method of cross correlation, and folded using the ephemeris of HCCTC. Filled circles are from 10 Feb. 1980; open circles from 11 Feb. 1980; squares from 21 Feb.1979. Solid line is the Balmer radial velocity curve of HCCTC measured at the base of the emission lines. $K = 116$ km s^{-1}, $V_o = 49$ km s^{-1}.

Figure 6.5

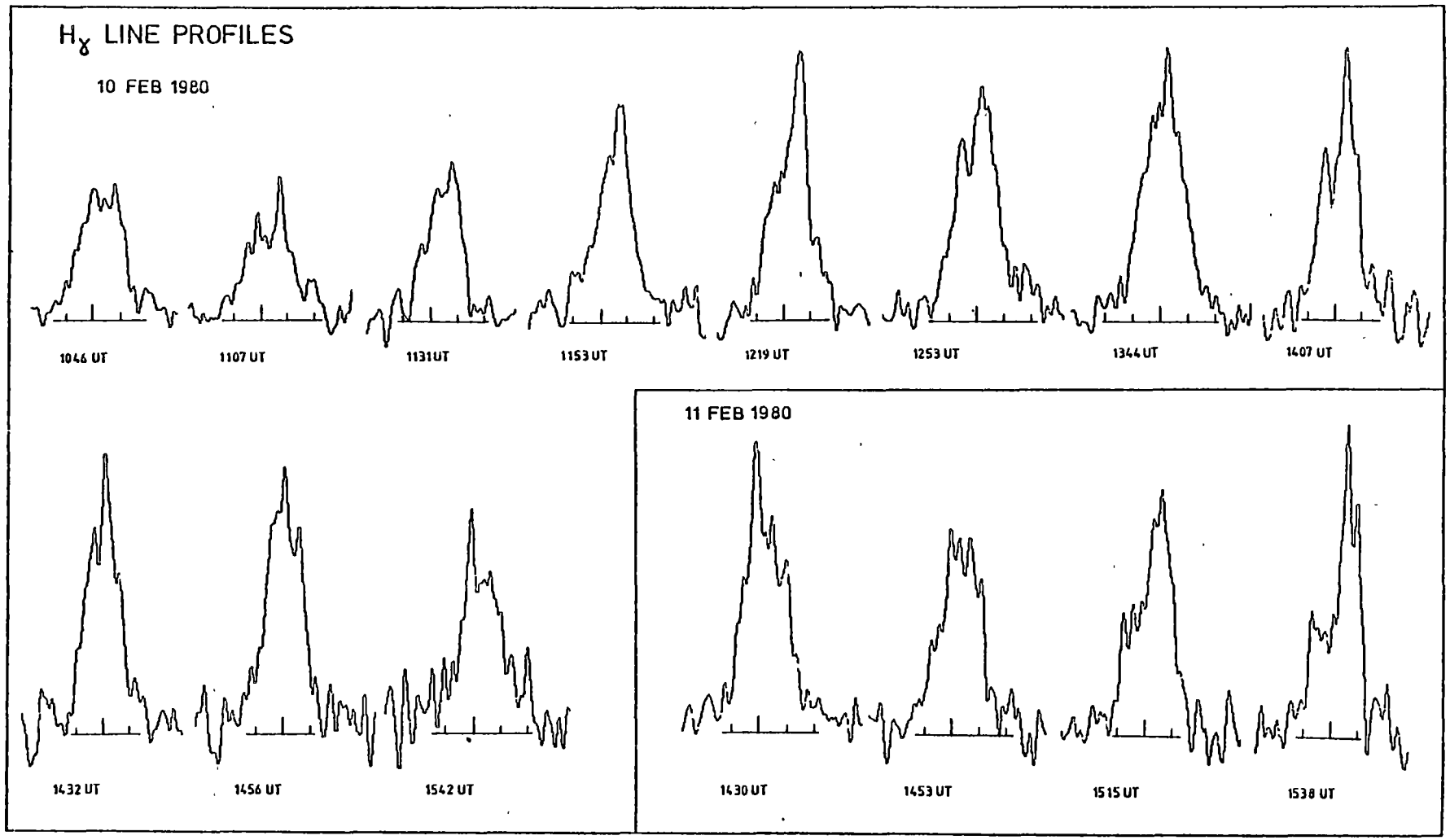

Figure 6.6

H_γ line profiles of 2A0526-328 taken at AAT, February 10 and 11,1980. Dwell time is 20 minutes and the time refers to the centre epoch of the observation. The large x-scale mark is 4340Å with 10Å marks on either side. Blue is to the left and red to the right.

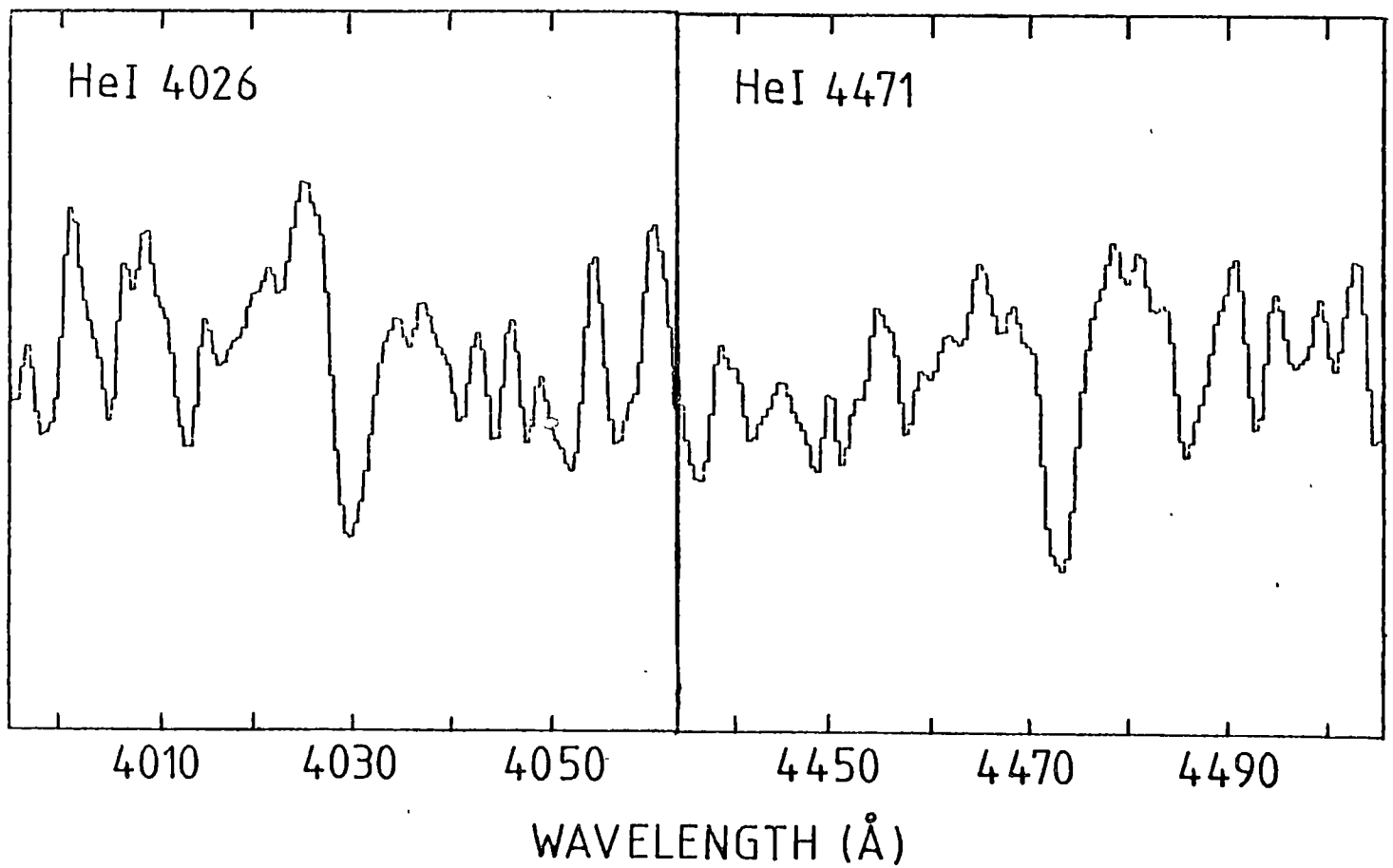

Figure 6.7 Absorption line profiles of HeI 4026 and HeI 4471 lines from 1108 to 1118 UT, February 10,1980.

absorption by a relatively cool foreground gas. At all other times these lines were seen in emission. The only time the Balmer line profiles were symmetrically split was on February 10 at 1046 UT for H_γ and 1107 UT for H_δ. In the 1979 February observations this phenomenon was observed at 1017 to 1034 UT and 1215 to 1241 UT, February 21, 1979, as shown in Figure 6.3. There is no evidence of any phase dependence for this phenomenon.

It is important to note that at about 1230 UT, February 10 (spectroscopic phase 0.18), a large radial velocity change occurred. The velocity changed from +200 to -40 km s^{-1} in 25 minutes, but there were no significant changes in the line profiles, even at 5-minute dwells, for any of the emission lines. The rapid change at this time, the fact that the radial velocity curve is significantly different from a sinusoid, and the asymmetric nature of the line profiles all suggest strongly that the emission originates from a gas stream or hot spot and not from the outer parts of an accretion disc. The profiles are similar to those seen in VV Pup, AN Ursae Majoris, and 2A0311-227 (Schneider and Young, 1980a,b).

In 1979 February 21, there were large changes in the equivalent widths (EW) and full widths at half maximum (FWHM) of the HeI, HeII, and H lines. Similar phase-dependent changes in the equivalent width of the H_β have also been reported by van Paradijs et al. (1980). The changes are most strongly correlated with the photometric period (5.19 hours) rather than with the spectroscopic period. Both data are shown in Figure 6.8. The peak occurs at photometric phase 0.4, just before minima. The observed peak to peak modulation in the photometric period of 0.27 mag (Motch, 1981) does not account for all the changes in the EW. The shift in peak EW is probably due to the variable phase shift of the minima, a consequence of different 4 day phases.

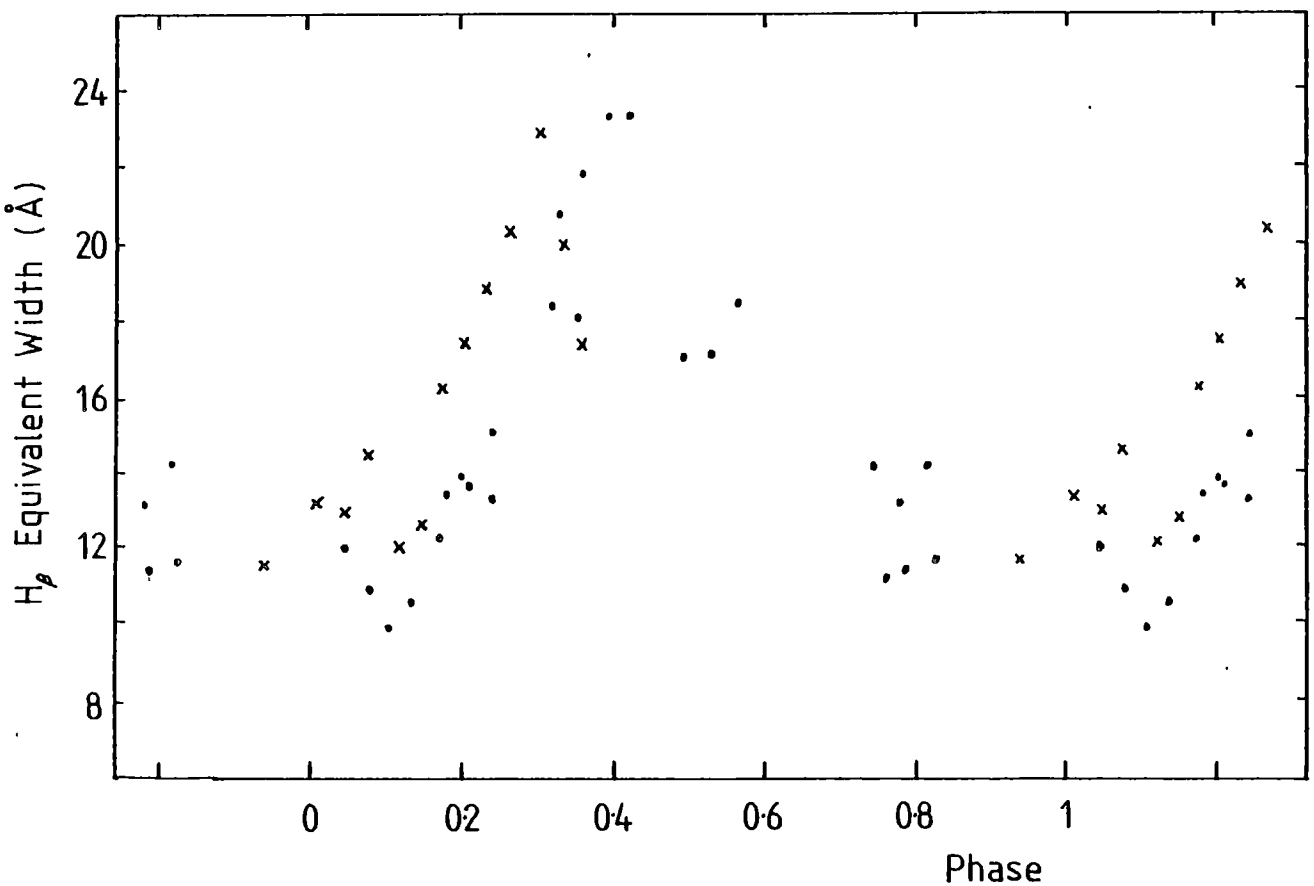

Figure 6.8 Photometric phase-dependent H_β equivalent widths. Dots from 1979 Nov. 10-14 (van Parajıdis et al 1980) and crosses, 1979 Feb. 21.

No significant changes in EW or FWHM were detected during 1980 February observations. The EW and FWHM of all lines stayed approximately constant with no obvious phase dependence. The results are listed in Table 6.4. HCCTC did not detect any phase-dependent effects from the lines except the CaII λ3933 line.

TABLE 6.4

EW and FWHM of emission lines from 2A0526-328 during 1980 February

Line	EW (Å)	FWHM (Å)
H_γ	15	14
H_β	14	14
HeII λ4686	3.0	8
HeI λ4026	2.0	8
HeI λ4471	2.5	7.5

The CII λ4627 line was detected in emission when all the 1980 February spectra were added, with an EW ≈ 0.5Å and FWHM ≈ 3Å . This is considerably weaker than that found in AM Her where it has an EW of ~2Å (Crampton and Cowley, 1977).

1982 January 15

Further spectroscopy was planned for 1982 January 15 and 16. However, poor weather allowed the acquisition of only one spectrum, at January 15, 1042 UT. Dwell time was 429 seconds. The instrumental set-up was the same as the 1980 February observations, except the wavelength range covered was from 3950 to 5100 Å. The mean radial velocity of H_β, H_γ and H_δ from centre of moment estimates was -45 ± 15 km sec^{-1}. From the phase of HCCTC the spectroscopic phase should be 0.21 ± 0.07 corresponding to an expected velocity of 20 ± 50 km sec^{-1}. Our data are consistent with the HCCTC emphemeris.

6.1.2 Photometry

1979 November, Siding Springs

During the period 1979 November 24 to November 29 we conducted photometry at the 1 m telescope of the Mount Stromlo and Siding Spring Observatory with a single channel photometer using an IP21 phototube. B photometry was carried out on the nights of November 24, 25 and 26, UBV photometry on November 27 and 28, and white light photometry on the last night, November 29. The system was calibrated using Cousins' (1973) photoelectric standards in the equatorial zone. Due to poor seeing over most of this period principally caused by high winds, inexperience of the observer and the close proximity of a star of similar magnitude, data from only two nights (November 24, 27) and a small portion of the night of November 28 were suitable for futher analysis.

An aperture of 9.2 arc seconds was used and observations were 20 seconds long for white light and B photometry and 10 seconds for UBV photometry. Corrections for atmospheric extinction used the empirical extinction coefficients of Lee (1976) for the Siding Spring site. They are:

$$K_V = 0.16$$

$$K_{B-V} = 0.13 - 0.04\ (B-V)$$

$$K_{U-B} = 0.36$$

Data were recorded onto PDP cassettes and on-line hard copies for monitoring the data were produced at a terminal next to the telescope. All subsequent reductions had to be carried out by hand from the hard copy because of the incompatability of the recording media to the author's available computing equipment.

After completion of the observations, Motch (1979) published his analysis of data from observations at the European Southern Observatory during 1979 November. He detected a period of 5.186 hr or 4.26±0.01 hr.

Subsequent work by HCCTC refined it to 5.1905±0.0002 hr. The B filter data has been folded at that period and shown in Figure 6.9. It confirms the ephemeris. The colour to magnitude changes observed on November 27 agree with Motch's (1981) observations, and are shown in Figure 6.10. The error bars represent intrinsic fluctuations of the object and not just statistical fluctuations. U-B changes from ~-0.85 at maximum light to ~-1.0 at minimum. There are no corresponding changes in B-V.

Three minima and two maxima were observed and are listed in Table 6.5. These confirm the variable phase of the observed photometric minima and maxima seen by Motch (1981).

TABLE 6.5

Phase of observed photometric minima and maxima during 1979 November and 1981 November

Date	JD	ϕ_{phot}	ϕ_{4day}
Minima			
1979 Nov 24	2444202.104	0.66 ± 0.04	0.64
1979 Nov 27	205.107	0.54 ± 0.05	0.38
1979 Nov 29	207.106	0.79 ± 0.05	0.87
1981 Nov 22	391.150	0.64 ± 0.06	0.82
1981 Nov 23	392.000	0.56 ± 0.06	0.62
Maxima			
1979 Nov 24	2444202.165	0.94 ± 0.06	0.64
1979 Nov 27	205.150	0.74 ± 0.05	0.39

1981 November, Mt. Stromlo

Four nights on the 76" reflector at Mt. Stromlo were allocated during 1981 November for linear polarization studies of 2A0526-328. Poor weather reduced the time to two intervals: November 22 1457 to 1611 UT and November 23 1133 to 1226 UT. Two minima were observed and are listed in Table 6.5. Data reductions by N. Visvanathan yield a result of 1.26 ± 0.4% linear polarization at position angle 90 ± 20°.

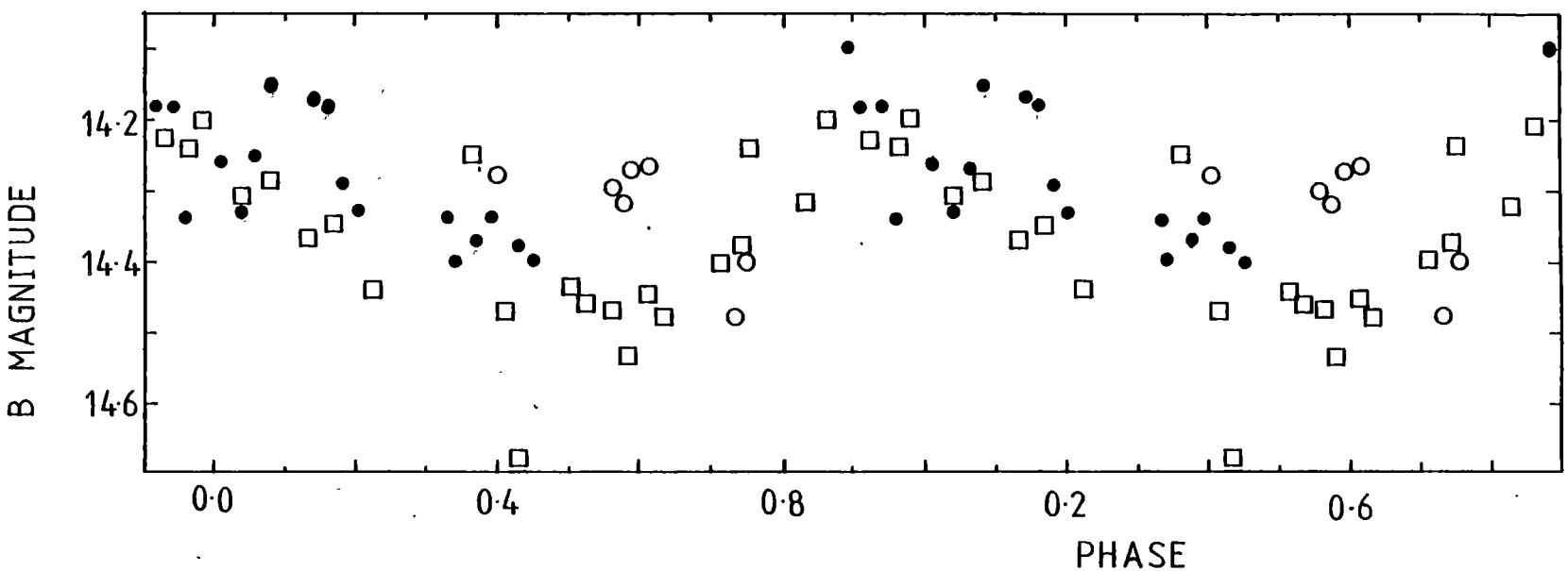

Figure 6.9 B Photometry of 2A0526-328, from Siding Spring Obsevatory during 1979 November, folded twice for clarity, using the photometric period of 5.19 hr. Squares from Nov. 24, filled circles Nov. 27 and open circles Nov. 28.

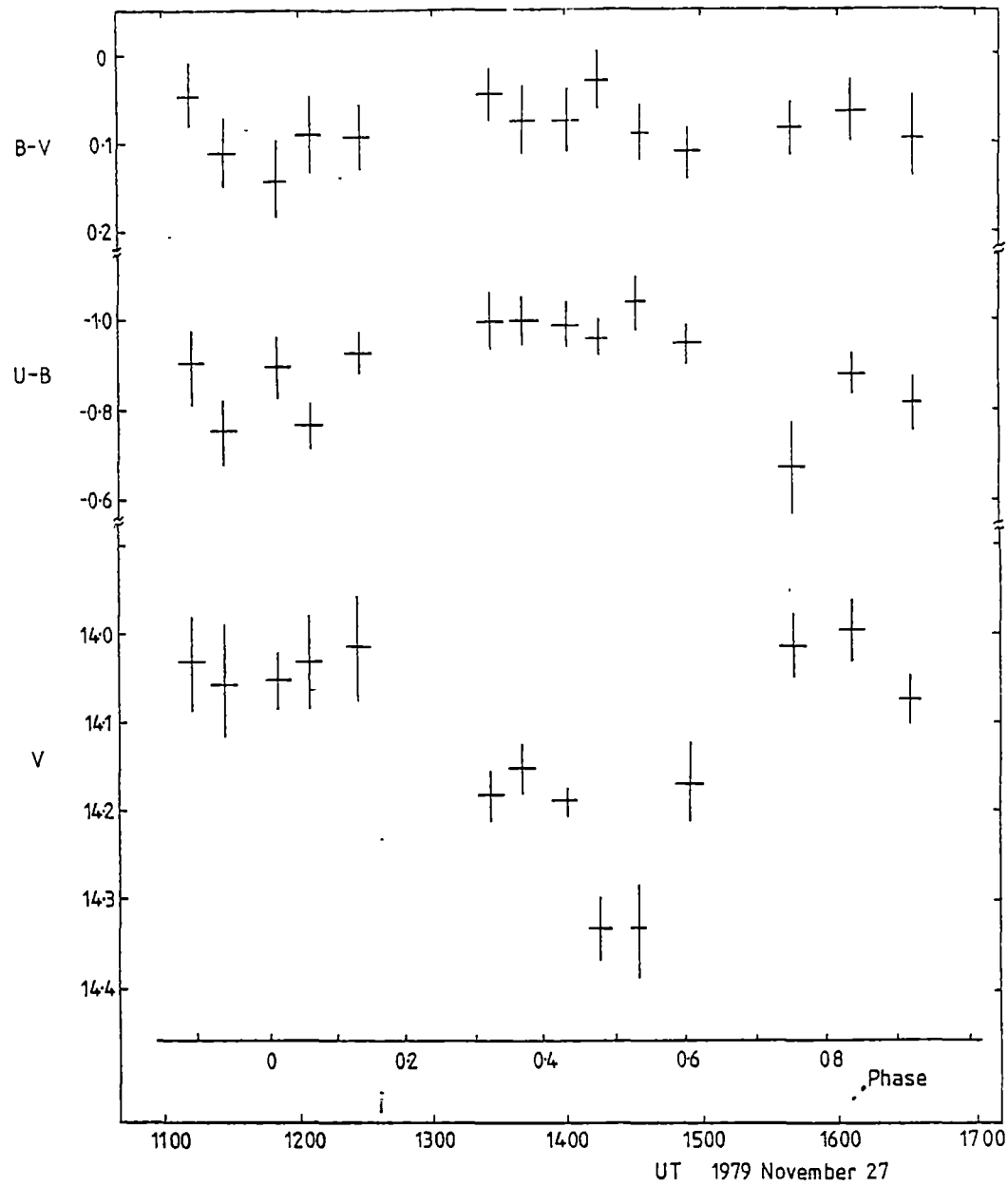

Figure 6.10 UBV photometry of 2A0526-328 during 1979 Nov. 27. Phase is 5 hr photometric period. Vertical error bars represent intrinsic source fluctuations not just statistical errors.

The significance is 3.2σ which is marginal. Observations by Stockman, Liebert and Moore (1982) give an upper limit of circular polarization of 0.07%. Further observations are needed to confirm our result.

6.1.3 X-ray

During September, 1979, HEAO-2 made two pointed observations of the region of 2A0526-328 using both the IPC and MPC instruments (Giaconni et al., 1979). The dates of observations are listed in Table 6.6 with phases from HCCTC. Owing to poor weather at the Anglo-Australian Observatory during the Einstein observations, concurrent spectroscopic data were not acquired.

TABLE 6.6

HEAO-2 observation dates of 2A0526-328

Date	Observation No.	Effective observation time (sec)		JD	ϕ_{phot}	ϕ_{spec}	ϕ_{4day}
1979 Sep 10	4497	1743	START	2444127.173	0.26±.01	0.55	0.01
			END	.224	0.50	0.78	0.02
1979 Sep 11	4498	4394	START	2444128.132	0.69±0.1	0.75	0.25
			END	.212	0.07	0.10	0.27

At the time of the reduction of the data by P.W. Hill, the IPC gain behaviour was not well known and we cannot deduce with any precision the spectral content of the data. The flux detected was $6.49\pm0.08 \times 10^{-12}$ erg $cm^{-2}sec^{-1}$ in the energy band of 0.15 to 4.5 keV, or $1.5 \times 10^{31} (D/100)^2$ erg sec^{-1} where D is the distance in pc. The IPC count rate was 0.284 ± 0.004 counts sec^{-1} which corresponds to ~0.8 UFU, three times fainter than the Ariel V observations (Cooke et al., 1978). Long-term monitoring by Ariel V (McHardy et al., 1981) indicates that the X-ray flux is constant on timescales exceeding 10 days, and that the mean flux is about a factor of three higher than that reported here. The IPC position for the source was $05^h27^m34.6^s$, $-32^\circ51'52''$ (1950.0), 30" south of the candidate but within the one arc minute error circle of

the IPC.

The mean hardness ratio of the IPC data as defined by Córdova et al. (1981a) of counts (0.55-4.5 keV)/counts(0.16-0.55 keV), is 4.7±0.1 which is typical of other cataclysmic variables. To monitor any crude spectral changes, the hardness ratio has been defined to be counts (~1.15-3.4 keV)/ counts (~0.37-1.15 keV). This corresponds to counts in PHA channels 15 to 23 and in 7 to 14 respectively.

Figure 6.11 is the X-ray light curve and hardness ratio from the IPC data for both observations, binned into 100 sec intervals. 2A0526-328 is highly variable in soft X-rays with flux changes of 300% on timescale of ~100 seconds. The hardness ratio is also variable. During observation 4997 and the first half of 4998, it was ~1 whilst the IPC count rate was ~0.3 counts per sec. The hardness ratio changed to ~1.4 during the last half of 4998 and the count rate dropped to ~0.14 counts per sec. To illustrate this behaviour, the hardness ratio versus count rate is shown in Figure 6.12. At count rates ≈ 0.2 per sec, there is substantially more variation in the hardness ratio.

To further study the X-ray variability, the IPC observation on 1979 September 11 (observation nos. 4998) has been plotted with an integration time of 50 sec (Figure 6.13). An interesting feature is the large variations in the first half of the observation on a time-scale of ~700 seconds, the same characteristic time-scale that Motch (1981) found for flickering at amplitudes up to 0.15 mag in B. In the second half, smaller variations occur with a time-scale of ~300 seconds between the 5600 and 7000 second marks of the observation.

There were no significant spectral differences in the MPC data (1.1 - 21.0 keV) for both observations. The combined spectrum from both observations is shown in Figure 6.14(a). There was no unique fit, but it can be described by a thermal bremsstrahlung spectrum with a temperature of 19.7±8.8 keV. The 68% and 90% confidence contours for

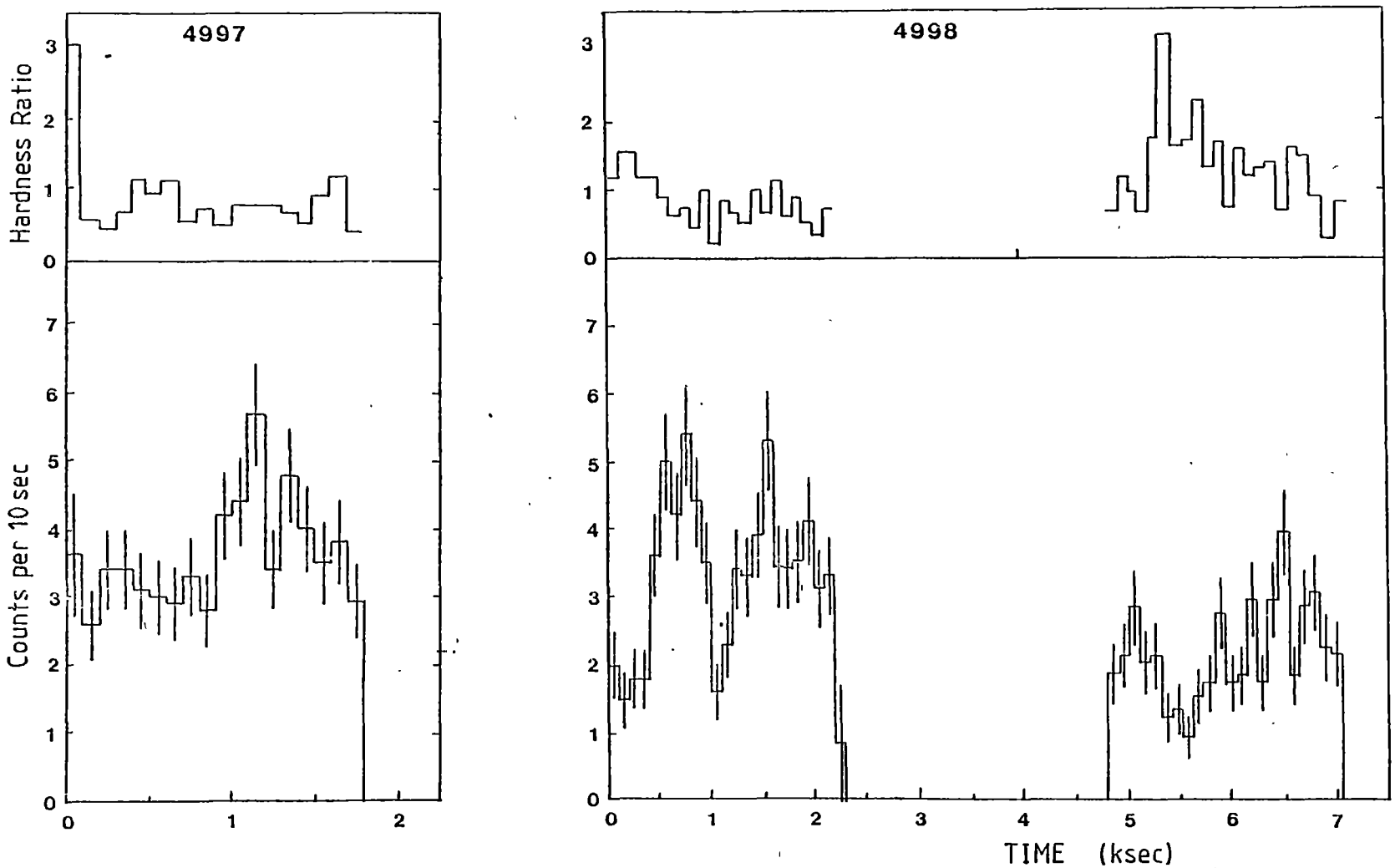

Figure 6.11 IPC light curve of 2A0526-328. Zero time for observation 4497 is at 1979 Sept. 10 1646 UT (JD = 2444127.1991) and for observation 4498 at 1979 Sept. 11 1510 UT (JD = 2444128.1317). Count rate is from 0.1 to 4.5 keV whilst hardness ratio is counts(1.15-3.4 keV) / counts (0.37-1.15 keV).

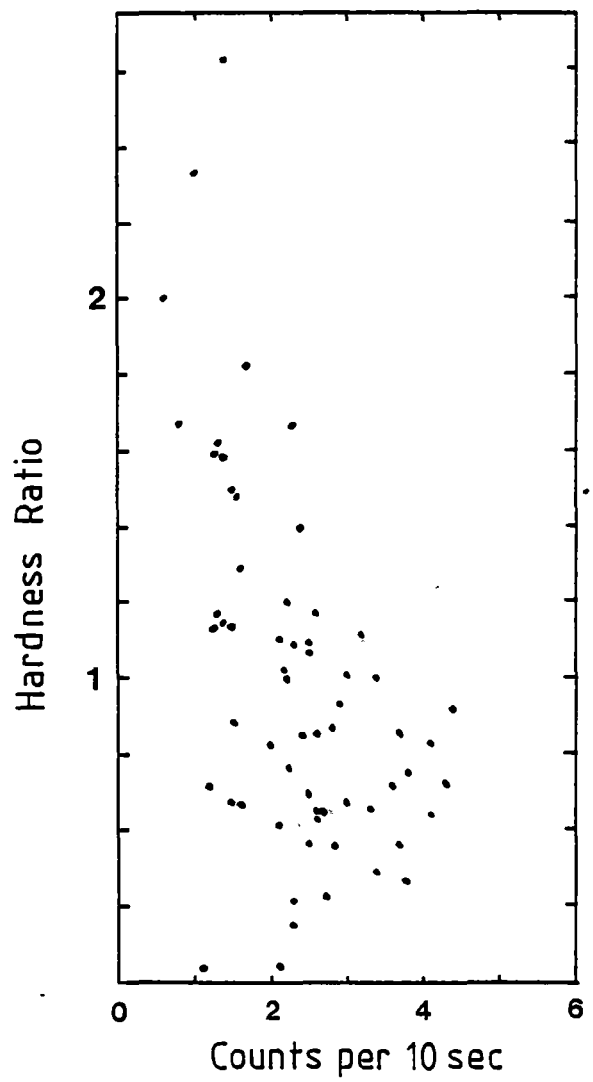

Figure 6.12 Hardness ratio versus count rate for observations 4497 and 4498 of 2A0526-328

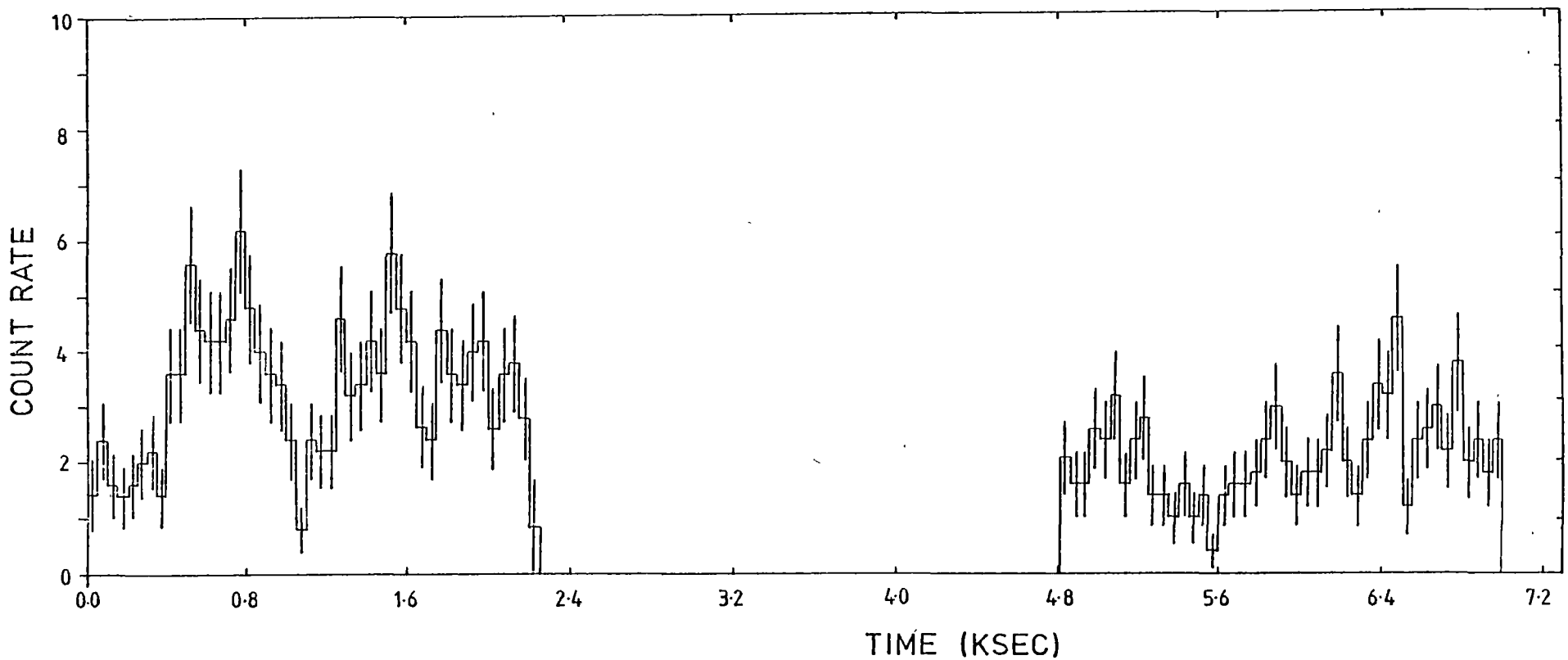

Figure 6.13 IPC light curve of 2A0526-328. Zero time is at 1979 Sept. 11 1510 UT (JD = 2444128.132). Count rate is counts per 5 sec. Bin size is 50 sec.

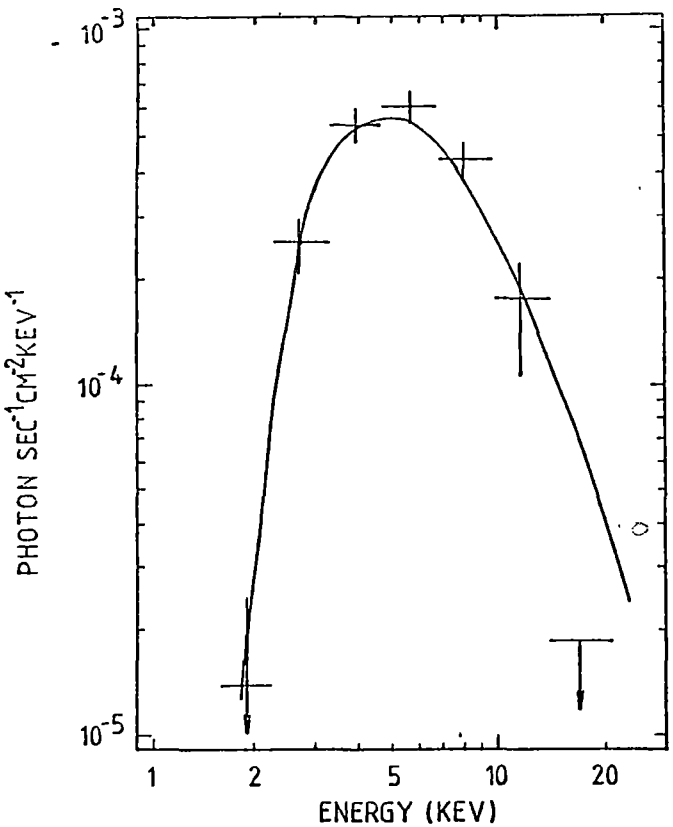

MPC X-ray spectrum of 2A0526-328 during September 1979 with the line representing the best fit thermal bremsstrahlung spectrum. Error bars are 1σ, whilst the upper limit is 3σ.

(a)

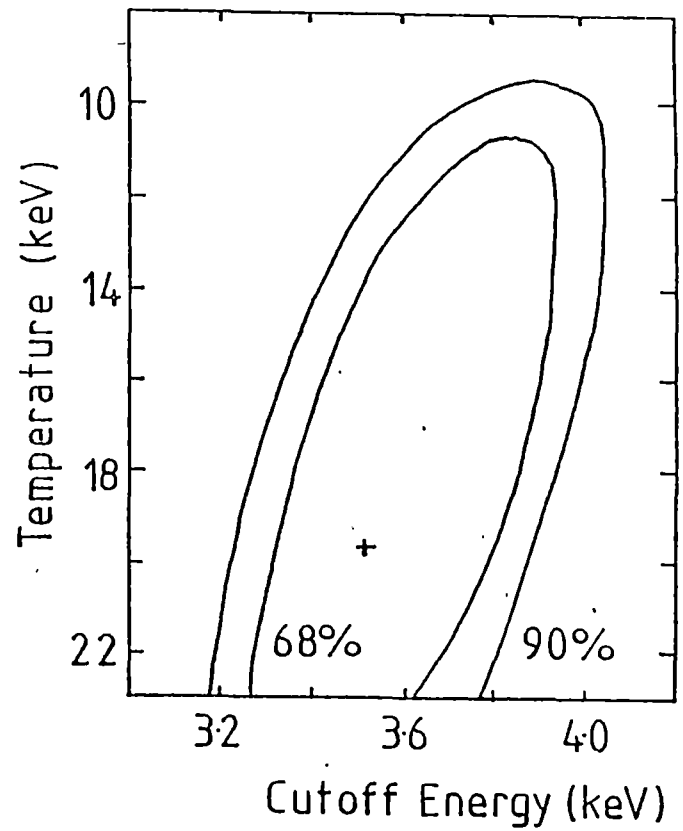

68% (χ^2_{min} + 2.3) and 90% (χ^2_{min} + 4.6) confidence contours for thermal bremsstrahlung spectral fit to the MPC data of 2A0526-328.

(b)

Figure 6.14

thermal bremsstrahlung with X-ray absorption cut-off are shown in Figure 6.14(b). The spectral parameters and χ^2_{min} for the various possible spectra are listed in Table 6.7.

TABLE 6.7

Spectral Parameters for Einstein MPC Data of 2A0526-328

Model*	kT or α	A ($keV\ sec^{-1}\ cm^{-2}keV^{-1}$)	Cutoff (keV)	χ^2_{min}	d.o.f.
Thermal Bremsstrahlung and Gaunt factor	19.7±8.8 keV	3.6×10^{-3}	3.5	29.8	5
Thermal Bremsstrahlung	9.7±2.5 keV	6.5×10^{-3}	3.5	28.1	5
Power	0.86±.18	1.9×10^{-2}	3.8	33.5	5
Blackbody	~2 keV	3.0×10^{-4}	2.9	26.7	5

* spectral equations are:

Thermal bremsstrahlung and gaunt factor	$A \exp(-E/kT)(E/kt)^{-0.4}$
Bremsstrahlung	$A \exp(-E/kT)$
Power	$A E^{-\alpha}$
Blackbody	$A E^3/(e^{E/kT-1})$

The integrated MPC X-ray flux is $1.2\pm0.3 \times 10^{32} (D/100)^2 erg\ s^{-1}$. The 3σ upper limit for the equivalent width of iron emission at either the 6.4 keV fluoresence peak or the 6.7 keV thermal peak is 1.6 keV. This is not inconsistent with the results obtained for AM Her and SS Cyg of 940 eV and 550 eV respectively (Pravdo, 1979). The photo-electric absorption cut-off of 3.5 keV is equivalent to a column density $n_H = 1.2 \times 10^{23} cm^{-2}$, a factor of three higher than for AM Her (Swank et al., 1977). This would imply a source distance D ≈ 1 kpc if it were inter-stellar in origin, but absorption by circumstellar accreting matter seems much more likely. Interstellar extinction is E(B-V) = 0.06

(Mouchet, 1982) or $n_H \cong 4 \times 10^{20}$ cm^{-2} suggesting matter near the source dominates the absorption.

AM Her, 2A0311-227, and SS Cyg are the only known cataclysmic variables of ~50 studied to have a separate strong UV/soft X-ray component in their spectra (Tuohy et al., 1978; Fabbiano et al., 1981). This flux generally exceeds the hard X-ray flux. There is no evidence in the spectrum of 2A0526-328 for this component from either the UV (Coe and Wickramasinghe, 1981) or our soft X-ray observations. Thus the 0.15 - 0.5 keV energy flux measured with the IPC was 6.5×10^{-12} erg cm^{-2} sec^{-1}, about a factor of 8 less than the 1 - 21 keV energy flux measured with the MPC.

Table 6.8 presents a summary of all published X-ray observations. There is some difficulty in equating fluxes from different detectors. However, by integrating the MPC spectrum from 2 to 10 keV, the band compatible with Ariel V and HEAO-1 A2 data, it is obvious that 2A0526-328 was in a low X-ray state at the time of the observations.

Further observations by the Einstein observatory were approved, using the HRI and MPC instruments. Unfortunately, pointing problems due to failure of the gyroscopes, excluded sources with declinations $>22^{\circ}$. The problems were not solved before the Einstein observatory was shut down.

6.2 V1223 SGR

Polarimetric observations of V1223 Sgr were made on the night of 1982 June 7 and 8 using the Hatfield polarimeter on the AAT. It is a dual channel polarimeter using a dichroic mirror to direct IR flux to the IRPS. Standard Johnson UBV and Kron-Cousins IR filters were used in the optical region. The observing mode was 6 seconds on source followed by a 1 second beamswitch to a 6 second background measurement giving a timing resolution of 14 seconds. Optical standards were HD128211 and HD189226 (Vogt et al., 1981) and BS7340 for the IR.

TABLE 6.8

X-ray Observations of 2A0526-328

Instrument	counts/sec	flux x 10^{-11} erg $cm^{-2} sec^{-1} keV^{-1}$	band keV	Date	Reference
Ariel V	0.8 ±0.1	4.24±0.53	2-10		Cooke et al. (1978)
Ariel V	0.99±0.08	4.92±0.42	2-10		McHardy et al. (1981)
HEAO-1 A2	1.99±0.16	4.32±0.34	2-10	1977 Sep 7-13	Piccinotti et al. (1982)
	2.55±0.20	5.53±0.43	2-10	1978 Mar 5-12	and Schwartz et al. (1979)
IPC	0.284±0.004	0.65±0.01	0.15-4.5	1979 Sep 10-11	This work
MPC		2.42	2-10	1979 Sep 10-11	This work

The spectroscopic observations on 1982 June 11 used the RGO spectrograph, 25 cm camera and IPCS. We used the 1200 B grating at a dispersion of 33 Å/mm from 3940 Å to 4940 Å. Spectra were taken every 79 seconds using the IPCS in the continuous mode and a Cu-Ar arc was used for wavelength calibrations at the beginning and end of the observation. Any shifts in the arc lines were less than 0.1 Å. Further spectroscopy was planned for the next two nights however the weather was not suitable.

White light photometry from the Mt. Canopus Observatory was obtained in 1982 June, with a dwell time of 1 second and using an aperture of 15 arc sec. Table 6.9 is a journal of all the observations.

TABLE 6.9

Journal of observations of V1223 Sgr

Instrument	Telescope	JD 2440000+	Pass Band
Hatfield Polarimeter	AAT	5128.0991 - 5128.1944 5128.1960 - 5128.2512 5129.1583 - 5129.2284	Optical R IR J R K V K
IPCS	AAT	5132.2307 - 5132.3194	3940Å - 4940Å
2 channel photometer	Mt. Canopus	5139.0993 - 5139.2232 5147.1557 - 5147.1858 5148.0707 - 5148.1056 5149.1274 - 5149.1760 5150.1438 - 5150.3067 5151.0023 - 5151.0276	white light

6.2.1 Photometry

The R band light curve of V1223 Sgr on 1982 June 7 is shown in Figure 6.15. It covers a complete period. The phase marked on Figure 6.15 is derived from the photometric ephemeris of Warner (1983, private communication). The ephemeris of maximum light is

$$T_0 = \text{HJD } 2444749.9866 + 0.140239\ E \quad . \qquad (6.1)$$

No errors are quoted but an error of less than 5 least significant numbers in the period corresponds to a phase error of less than 0.1.

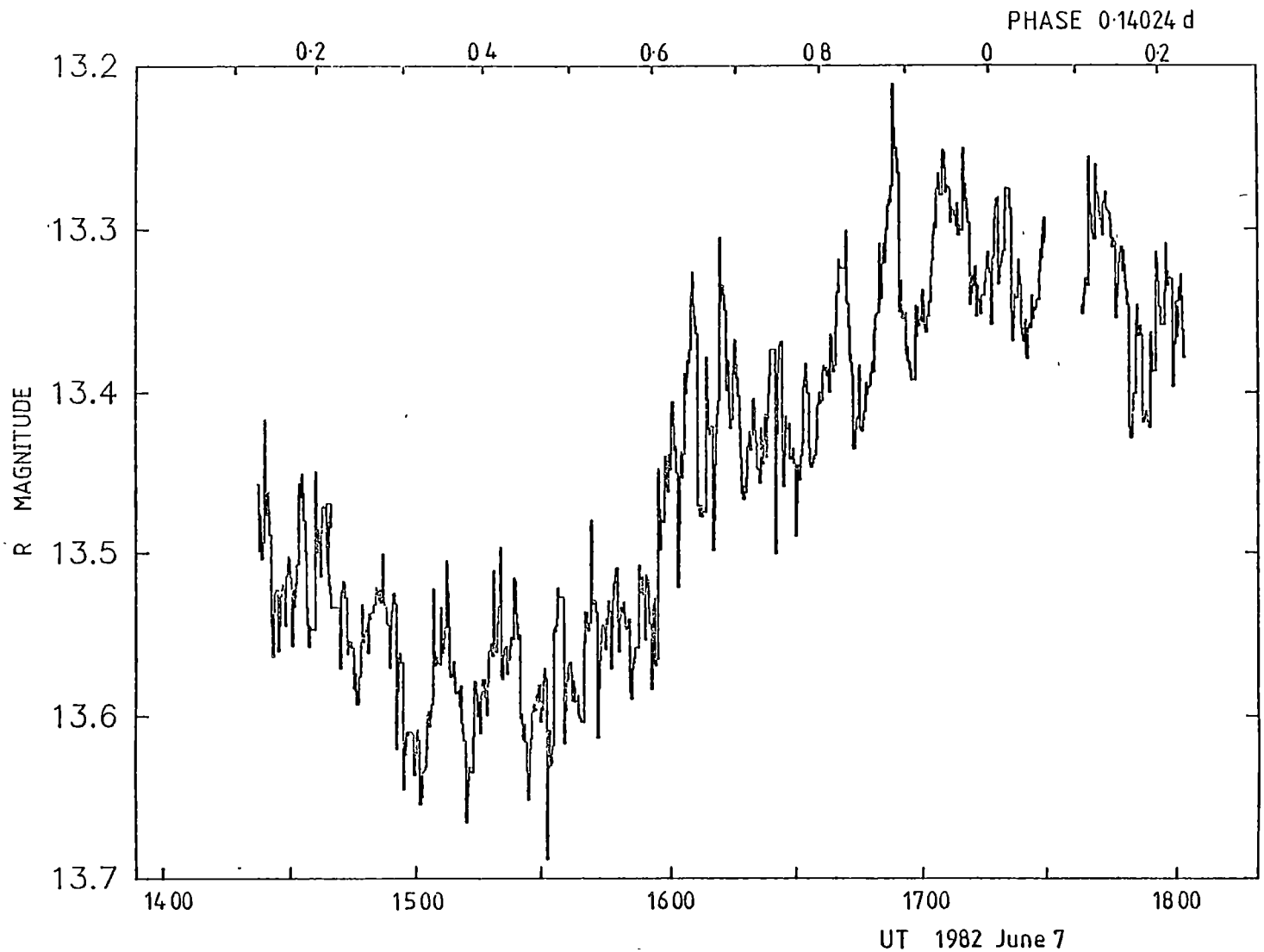

Figure 6.15 R band light curve of V1223 Sgr on 1982 June 7. Error per data point is ~ 0.012 mag.

During the R band observations from 1422 UT to 1640 UT, we simultaneously, observed the J band (Figure 6.16). At 1532 UT it was apparent that the IR beam was not centred on the IR aperture whilst the optical beam did not show any such effect. The IR beam was realigned by maximising the signal whilst offsetting in hour angle and declination. Thereafter, every twenty minutes, the beam was checked for centre. This is the reason for the eight minute gap in data at 1730 UT. Note that the J magnitude in Figure 6.16 is not symmetric about the minimum. At phase 0.2 it is ~0.05 mag brighter than at phase 0.8, whilst in R the difference is -0.8 mag. This is apparent in the colour R-J (Fig. 6.17). It changed from 1.33 mag at 1430 UT to 1.15 mag at 1630 UT in a smooth linear fashion. It is important to note that the system was reddest before minimum light. The difference in time was at least 0.03^{d} or 0.2 of the period.

From 1640 UT to 1800 UT, the IR filter was changed to K. The mean K magnitude was constant at ~12.50 mag although there were variations above the expected noise level of 0.03 mag (Figure 6.18). The R-K colour variations are principally due to changes in K. On 1982 June 8, from 1548 UT to 1730 UT data from the V and K bands were acquired (Figure 6.19). The average fluxes of V and R are lower than observed by Bonnet-Bidaud et al. (1982) by 0.38 mag and 0.75 mag respectively. There is no hint of a maximum in the V light curve as expected from the ephemeris given by equation 6.1.

Figure 6.20 is adopted from Figure 2b of Bonnet- Bidaud et al. (1982) and their dereddened UV spectrum is shown as crosses above the observed fluxes (diamonds). The UV can be fit with a power law $F_{\lambda} \alpha \lambda^{-1.96\pm0.05}$). The IR points are well below the extrapolation of the UV to the infrared and indicating a spectral break at ~5000Å. The slope between V and K cannot be well determined since the measurements are not simultaneous. The best estimate is obtained by interpolation

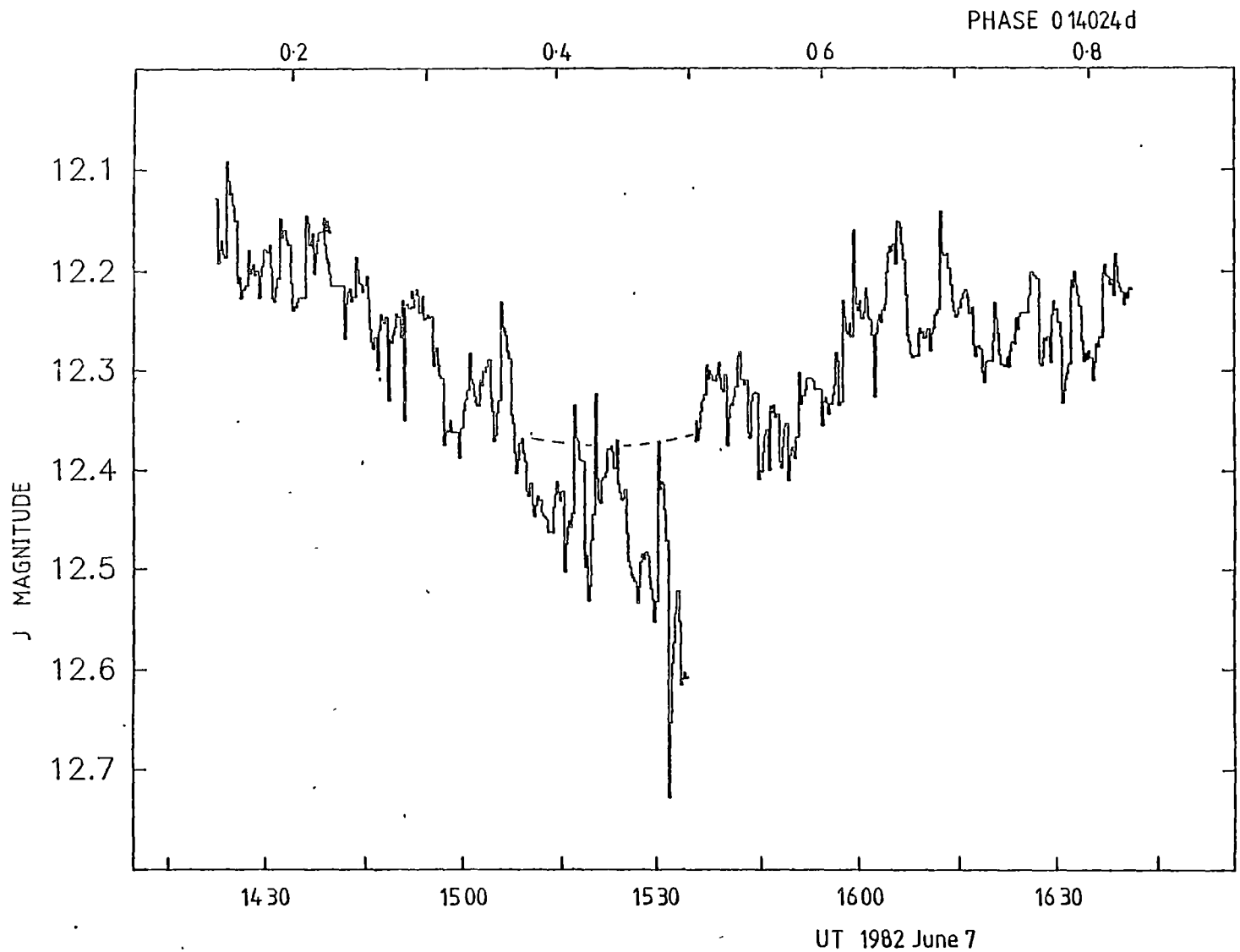

Figure 6.16 J band light curve of V1223 Sgr on 1982 June 7. Error per data point is ~ 0.015 mag. The dashed line is the expected mean curve after correction for guiding errors.

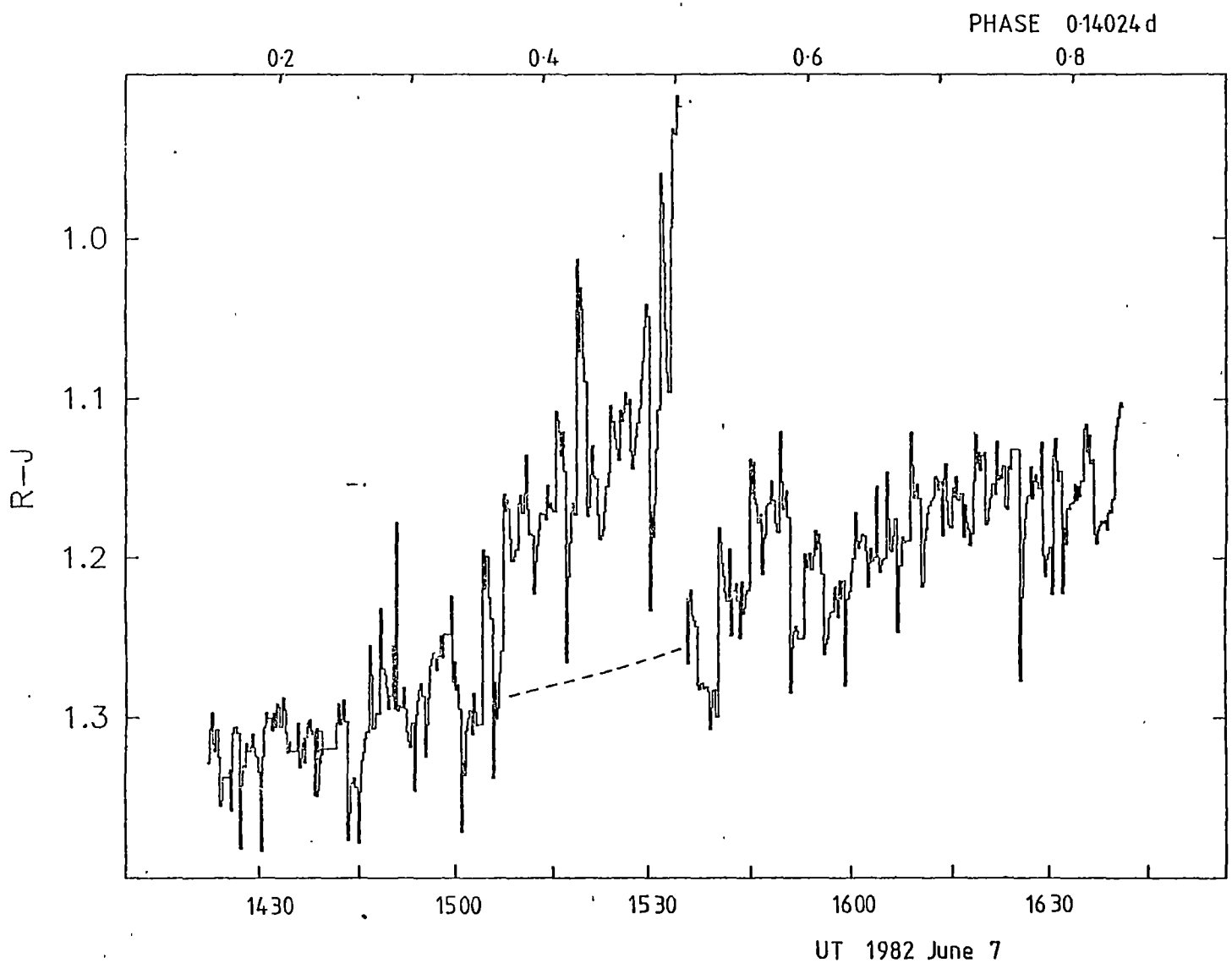

Figure 6.17 R-J lightcurve of V1223 Sgr on 1982 June 7. The dashed line is the expected mean curve after correction for guiding errors.

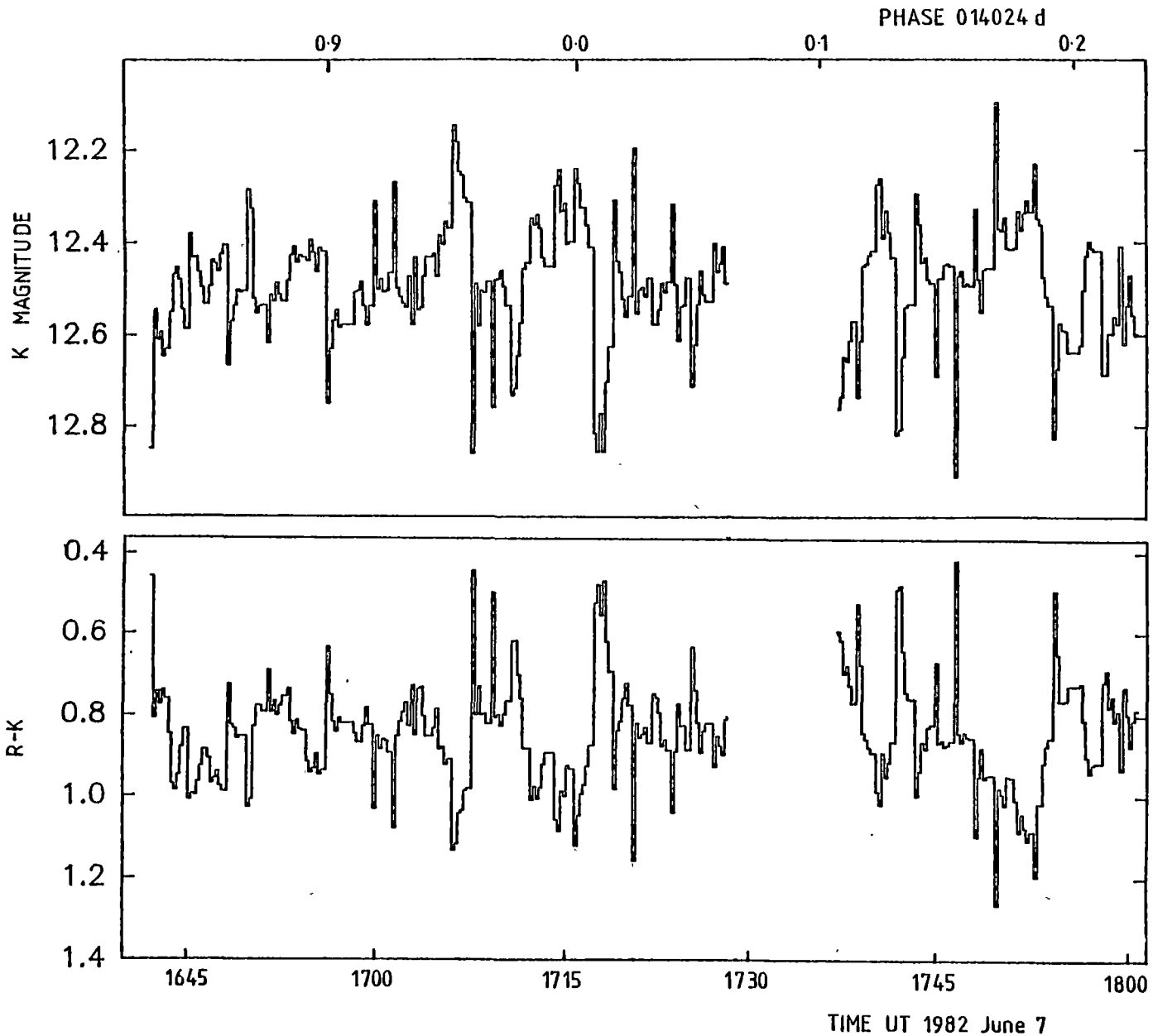

Figure 6.18 K and R-K light curves of V1223 Sgr on 1982 June 7.
Errors per data point are 0.02 and 0.025 mag respectively.

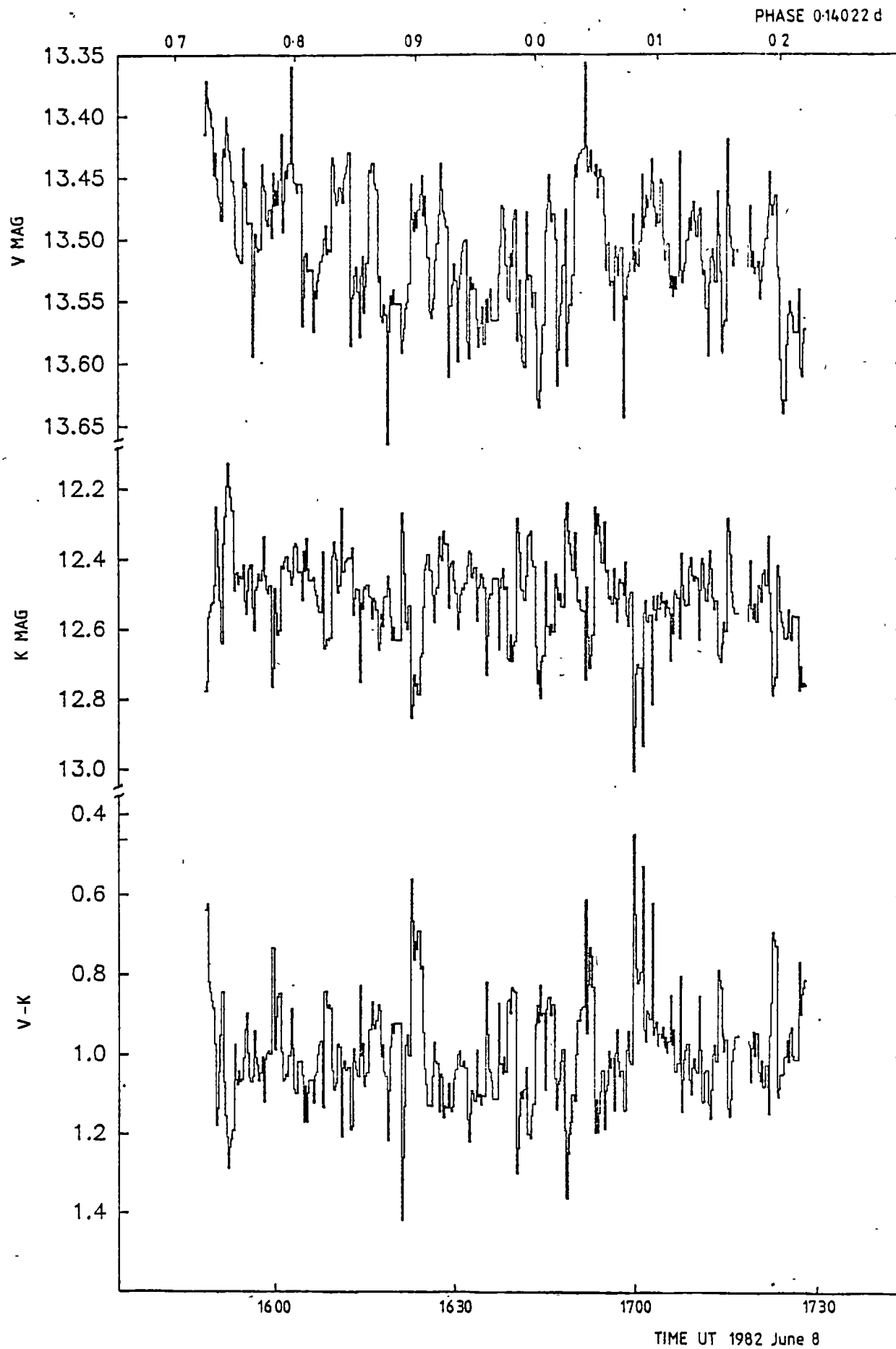

Figure.6.19 V, K,and V-K light curves of V1223 Sgr on 1982 June 8. Respective errors per data point are 0.01, 0.02 and 0.025 mag.

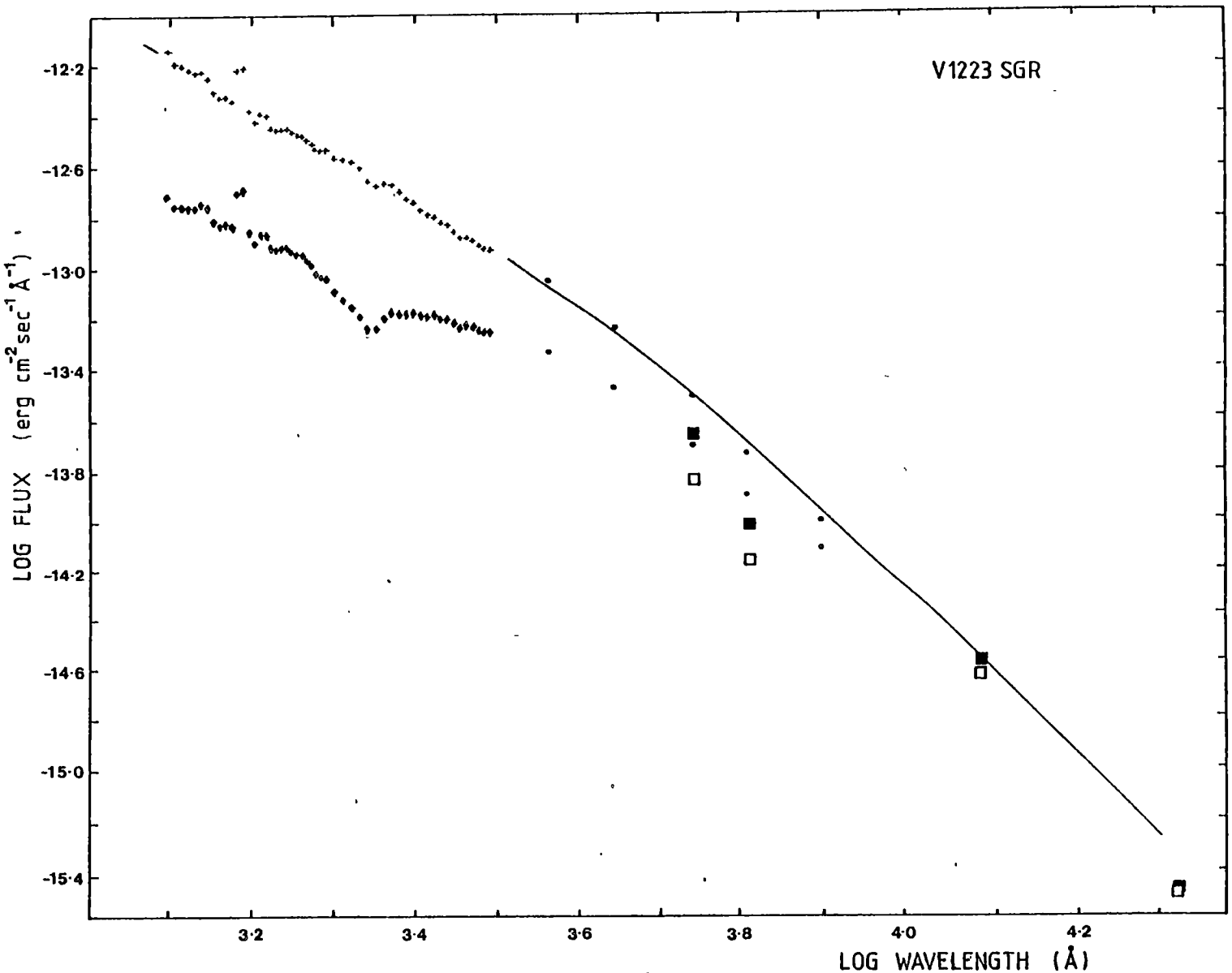

Figure 6.20 Spectrum of V1223 Sgr. UV (crosses and diamonds) and optical (dots) from Bonnet-Bidaud et al (1982). Open squares are mean observed data from AAT and filled squares are corrected for reddening. Solid line is best fit disc model from Mouchet (1982).

between the simultaneous R and K data from 1982 June 7 1640 UT to 1800 UT. The mean R magnitude during this interval was 13.03 mag implying $F_\lambda \alpha \lambda^{-3.0\pm0.10}$. There is no obvious IR excess expected from a secondary or cool dust. The flux from J appears to be above the power law fits but nonsimultaneity of the data makes it difficult to justify it as an excess.

To determine the temporal characteristics of V1223 Sgr, the data have been analysed using auto correlation , cross correlation, least squares Fourier analysis (Lomb, 1976) and the Q method (Warner and Robinson, 1972). As is evident in Figure 6.15, there are distinct 13.2 minute (794 sec) pulsations as initially reported by Steiner et al. (1981). Individual pulsations are quite strong on occasions whilst others are not apparent. Figure 6.21 is a plot of the least squares Fourier analysis of the R (Figure 6.15) and J (Figure 6.16) light curves. The data have been prewhitened by the removal of the orbital modulation via a running mean. The 794 sec pulsation is apparent in R but not in J. Other periods are marked and are discussed later. To derive an accurate ephemeris for the 794 sec pulsation, the Mt. Canopus photometry has been analysed using the Q-method of Warner and Robinson (1972). For maximum light, the ephemeris is

$$T_0 = \text{HJD } 2445139.0101 + 0.0091937\ E \quad . \qquad (6.2)$$
$$\pm 0.0004 \quad \pm 0.0000004$$

The photometry from the AAT has been folded at the period of 794.4 sec (Figure 6.22) after removal of orbital modulation via a running mean. Phase zero is at HJD 2445127.5048. The number of cycles folded for each filter are V band 7.6, R band 16.6, J band 10.4 and K band 13.6. The small number of cycles for V is the reason for the erratic nature of the pulsation profile since individual pulse profiles vary dramatically from pulse to pulse and cancel out when more than ~10 are added together. Folding the Canopus white light data, covering

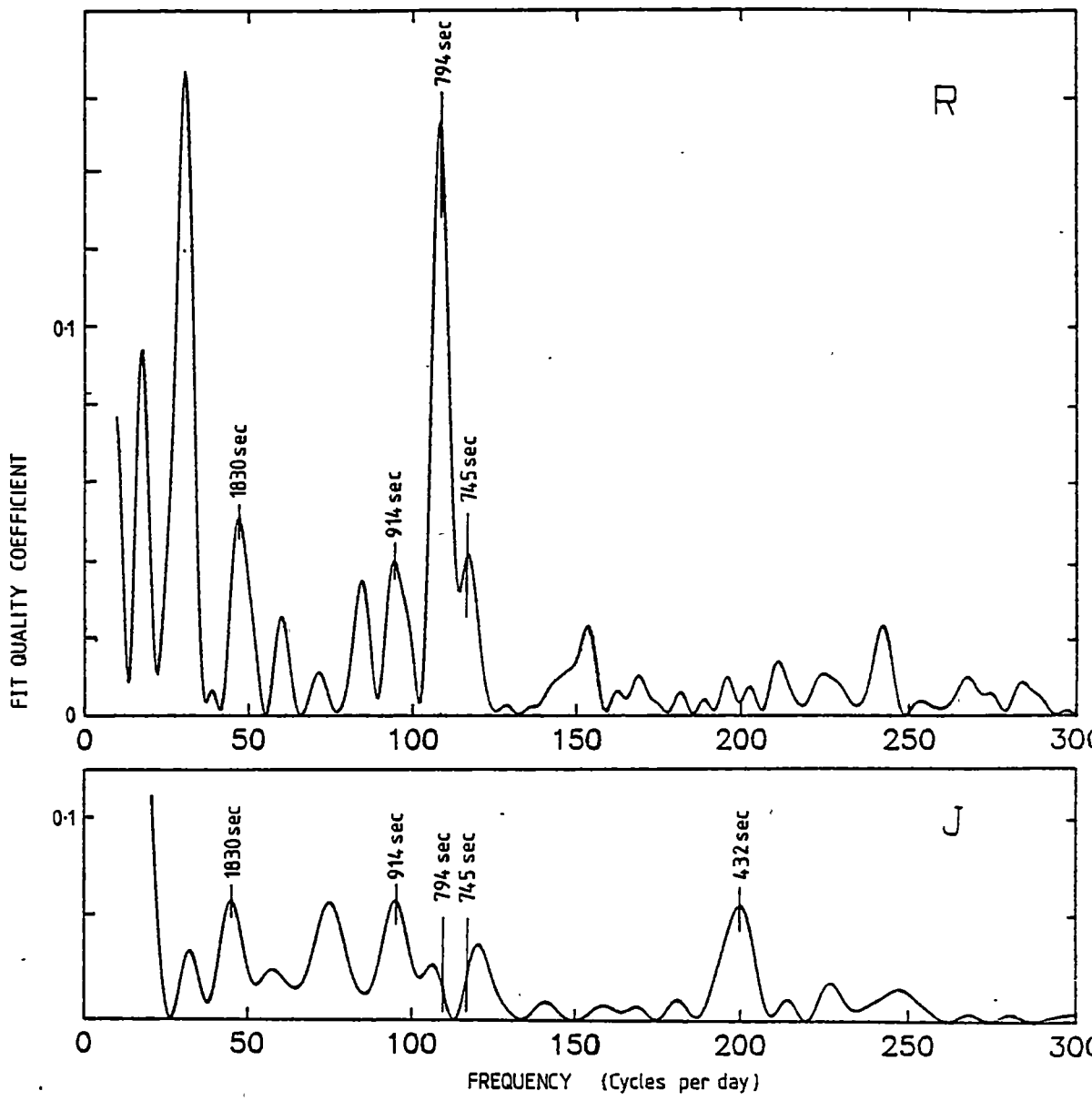

Figure 6.21 Least squares Fourier analysis of 1982 June 7 R and J light curves of V1223 Sgr. Marked periods are discussed in text.

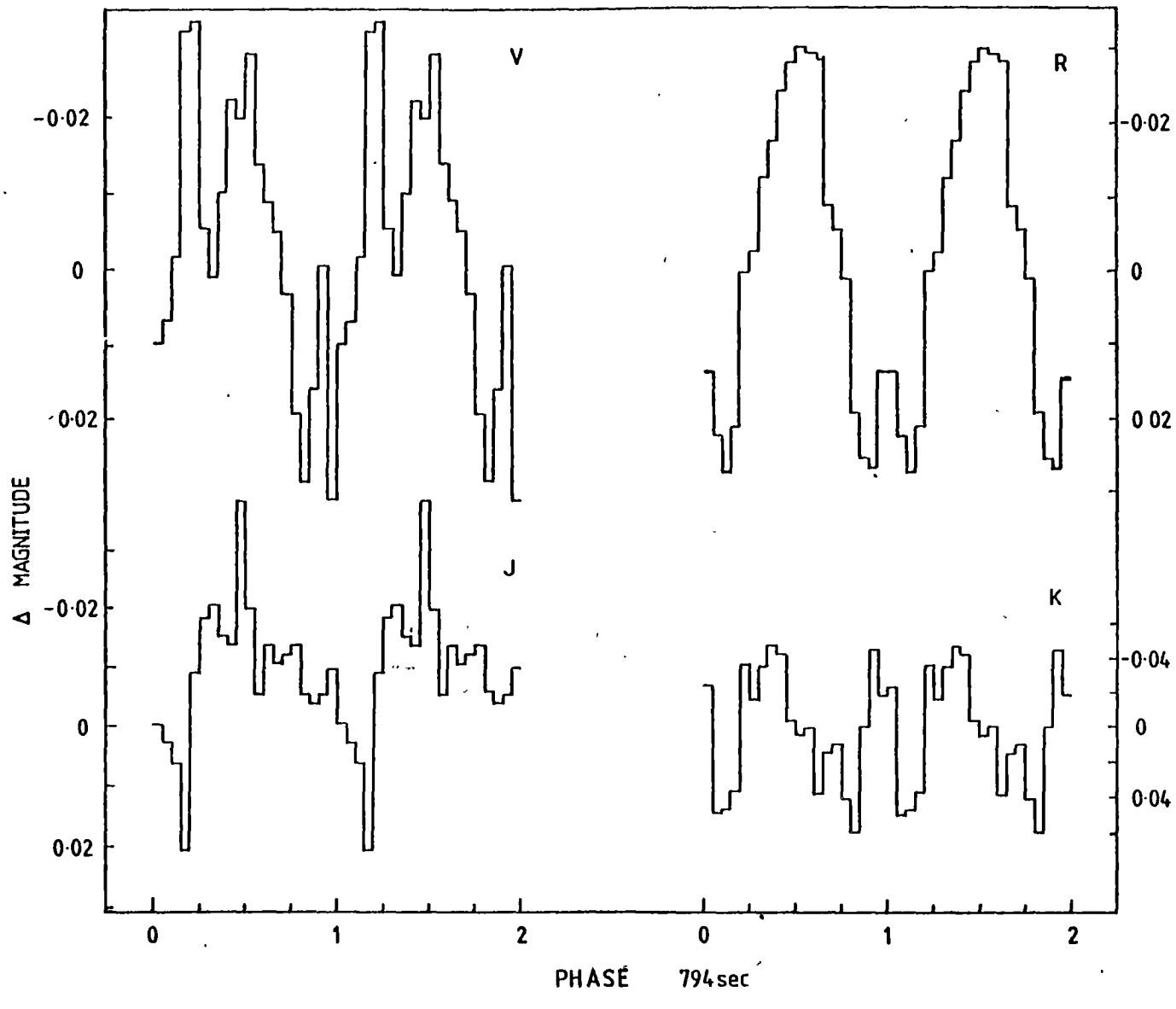

Figure 6.22 Photometry, folded twice for clarity at the period of 794.4 sec. Phase zero is HJD 2445127.5048

47 cycles, yields a smooth sinusoidal light curve of peak to peak amplitude 0.045 ± 0.004 mag. There was no statistical difference between odd and even pulse profiles. This suggests that either one pole is dominant in the optical yielding a fundamental period of 794 sec or twice this with both poles contributing equally to reprocessing the X-ray flux. No other periods were detected with an upper limit of 0.025 mag. Peak to peak fluxes of the AAT pulsations are listed in Table 6.10 assuming a sinusoidal profile and using the absolute fluxes for the various filter bands from Johnson (1966). The pulsation fluxes and the UBVRI pulse fluxes from Bonnet-Bidaud et al.(1982) are shown on Figure 6.23 with fluxes at other periods. Our V and R fluxes are ~44% less than those of Bonnet-Bidaud et al. Bonnet-Bidaud et al. comment that their fluxes are compatable with the theoretical X-ray heated atmospheres of Milgrom (1976) which predict power law $F_\lambda \alpha \lambda^{-\alpha}$ with α between +3.1 and +3.5. Using the R and J data since they are concurrent, yields $\alpha = 3.1$.

TABLE 6.10

Full-amplitude fluxes (erg $sec^{-1} cm^{-2} \text{Å}^{-1}$) of pulsations from V1223 Sgr at various periods

Pass Band	Period (sec) 794.4	745.4	914.2	431
V	5.3×10^{-16}	$<1.8 \times 10^{-16}$	$<4.0 \times 10^{-16}$	-
R	4.7×10^{-16}	1.2×10^{-16}	1.86×10^{-16}	$<1.5 \times 10^{-16}$
J	6.2×10^{-17}	$<4.9 \times 10^{-17}$	8.5×10^{-17}	7.8×10^{-17}
K	$<2.5 \times 10^{-17}$	$<7.6 \times 10^{-18}$	$<2.6 \times 10^{-17}$	-

There are two possible sources for the 794 sec pulsations. It is reprocessed X-rays from either the companion star or hot spot region or the reprocessed radiation is from the inner edge of the accretion disc. The relationship between the orbital period, the white dwarf rotation period and the beat period for a prograde orbit is

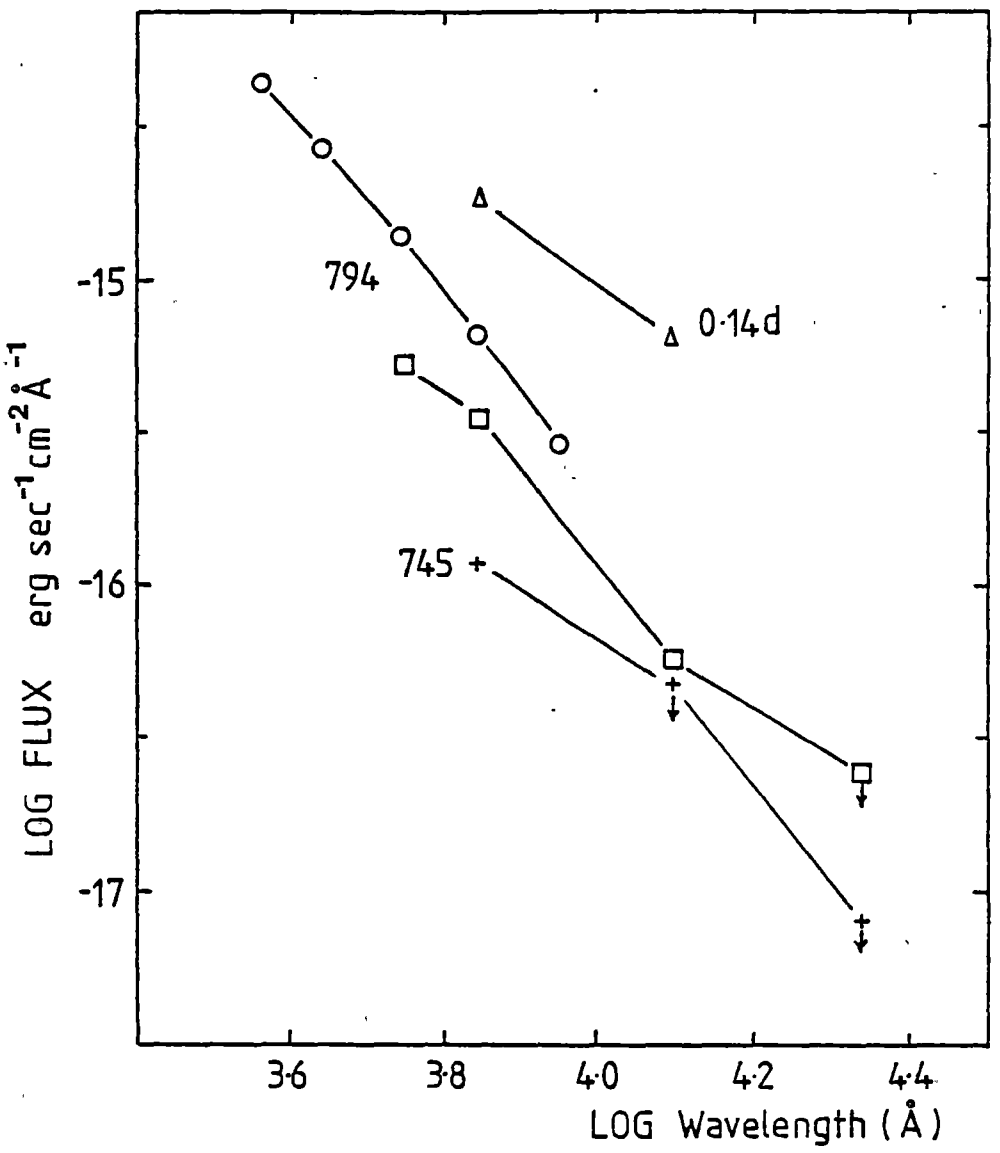

Figure 6.23 Pulsation flux spectrum for the orbital modulation (triangles), the 794 sec pulsation (squares) and the 745 sec period (crosses). Open circles are from the 794 sec pulsations seen by Bonnet-Bidaud et al (1982).

$$\frac{1}{P_{orb}} = \frac{1}{P_{WD}} - \frac{1}{P_{HEAT}} \qquad (6.3)$$

where P_{orb}, P_{WD} and P_{HEAT} are the orbital period, white dwarf rotation period and the beat (or heating) period respectively. We first consider the model of reprocessed light from a source fixed in the orbital frame (i.e. the companion/hot spot). In this case P_{HEAT} = 794 sec for a single pole model or twice this for a twin pole white dwarf. For a single pole system P_{WD} = 745.46 ± 0.22 sec using equation 6.3. This period is marked on Figure 6.21 and coincides with a peak on the shoulder of the main peak in R. No peak is evident in J or K.

Only the R, J and K light curves are sufficiently long to separate adequately the white dwarf period and the beat period. If the white dwarf has two equal strength poles then P_{HEAT} = 1588.8 sec implying from equation (6.3) that P_{WD} = 1404.5 sec. The profile at this period should be a double sinusoid and the period analysis should reveal a period of 702.3 sec (or 123.0 cycles/day). No peak is evident in R. In J, the periods of 745 and 702 sec are either side of the small peak at 120 cycles/day (Figure 6.21). If this model of the dominant pulsation originating in the orbital frame is correct then the data suggests that the rotation period of the white dwarf is 745 sec and one pole dominates the light curve. A consequence of this model is the 794 sec and 745 sec pulsation should be in antiphase at maximum orbital light. This is observed in H2252-035 (Patterson and Price, 1981). However, the pulsations are in phase at maximum light.

The second model relates the observed pulsation to the rotation period of the white dwarf, with the reprocessed light coming from the inner edge of a thick accretion disc. Letting P_{WD} = 794.4 sec (or twice this), then from equation (6.3), P_{HEAT} = 850.1 ± 0.3 (101.63 cycles per day) for one pole or P_{HEAT} = 1828.4 ± 0.5 (47.2 cycles/day) for the two pole model. The expected peak at 101.6 cycles per day is not evident in Figure 6.21 but both the fundamental and harmonic for the two pole model are coincident with peaks in the

least squares Fourier analysis.

A prominent periodicity at 431 ± 5 sec appears in the J analysis (Figure 6.21) but no corresponding peak in R. To check the coherence of the 431 sec period, the J light curve was separated into 4 equal blocks. In each case the pulsation was evident with the same phasing, and amplitudes were within 30% of the mean. No other periods were seen with frequencies above 50 cycles per day. A peak at ~30 cycles per day occurs in R and is possibly related to small deviations from a true sinusoid variation of the 0.14^d photometric period. Further photometry would be required to establish this.

To determine the fluxes for the three periods, the data have been pre-whitened by removing the 794 sec period. The light curves at 914 sec, 745 sec and 431 sec, plotted twice for clarity, are shown in Figures 6.24, 6.25 and 6.26 respectively. Phase zero is the same as for Figure 6.22. Fluxes are listed in Table 6.10. Since there are no peaks in the least squares Fourier analysis for V, J and K at the period 745 sec or R at 431 sec, the scatter in the light curve represents the upper flux limit.

The correlation functions (ACF and CCF) according to the definitions in Chapter 5, are shown in Figures 6.27 to 6.29. The R filter and J filter data are clearly correlated with no significant delays ($\Delta t < 14$ sec) (Figure 6.27). The maximum separation of the optical and infrared emission regimes is $c\Delta t$ where $\Delta t = 14$ sec or 4×10^9 cm which is comparable to the size of the binary system. The e-folding time of the RxJ CCF is ~180 sec which probably corresponds to the rise or decay timescale of the pulsations. The RxK CCF (Figure 6.28) shows no correlation or lag. The peak at +800 sec in RxR and RxK corresponds to the prominent optical period. The VxK CCF (Figure 6.29) is remarkably different. The dominant peak occurs at a lagtime of 190 ± 10 sec,

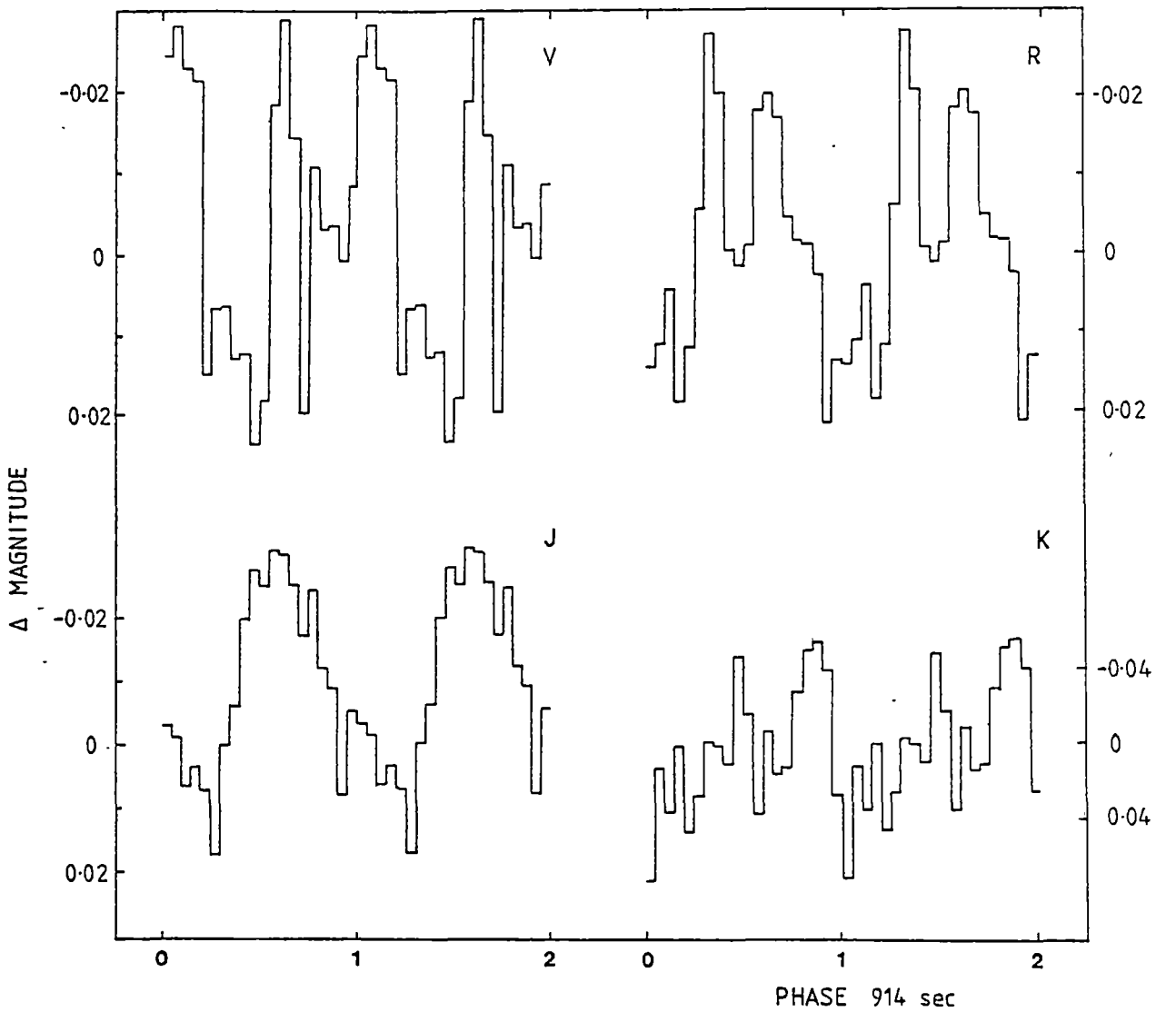

Figure 6.24 Pulse profiles, plotted twice for clarity, at the period of 914 sec. The data have been prewhitened by the removal of the 794 sec period. Phase zero is at HJD 2445127.5048.

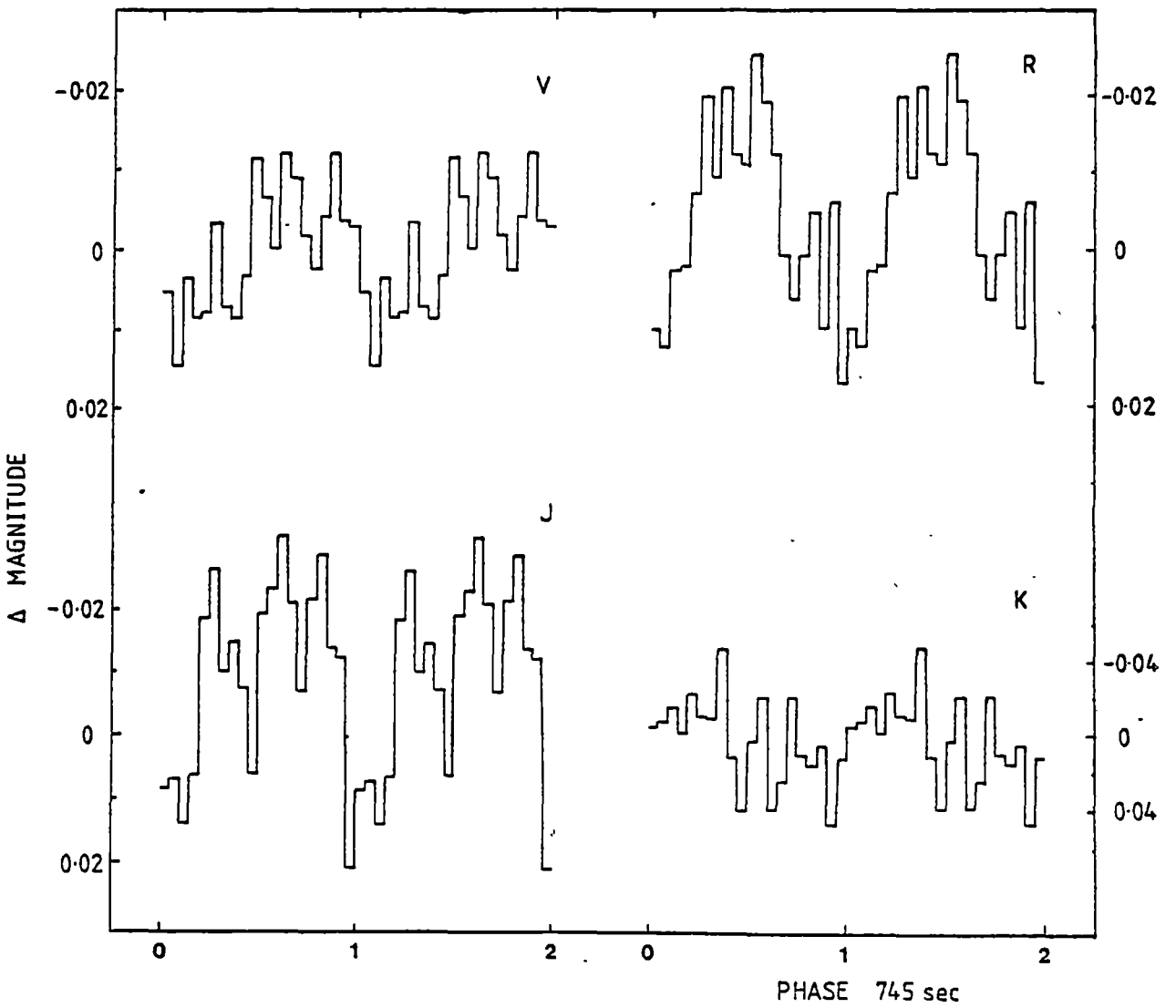

Figure 6.25 Pulse profiles, plotted twice for clarity, at the period of 745 sec. The data have been prewhitened by the removal of the 794 sec period. Phase zero is at HJD 2445127.5048.

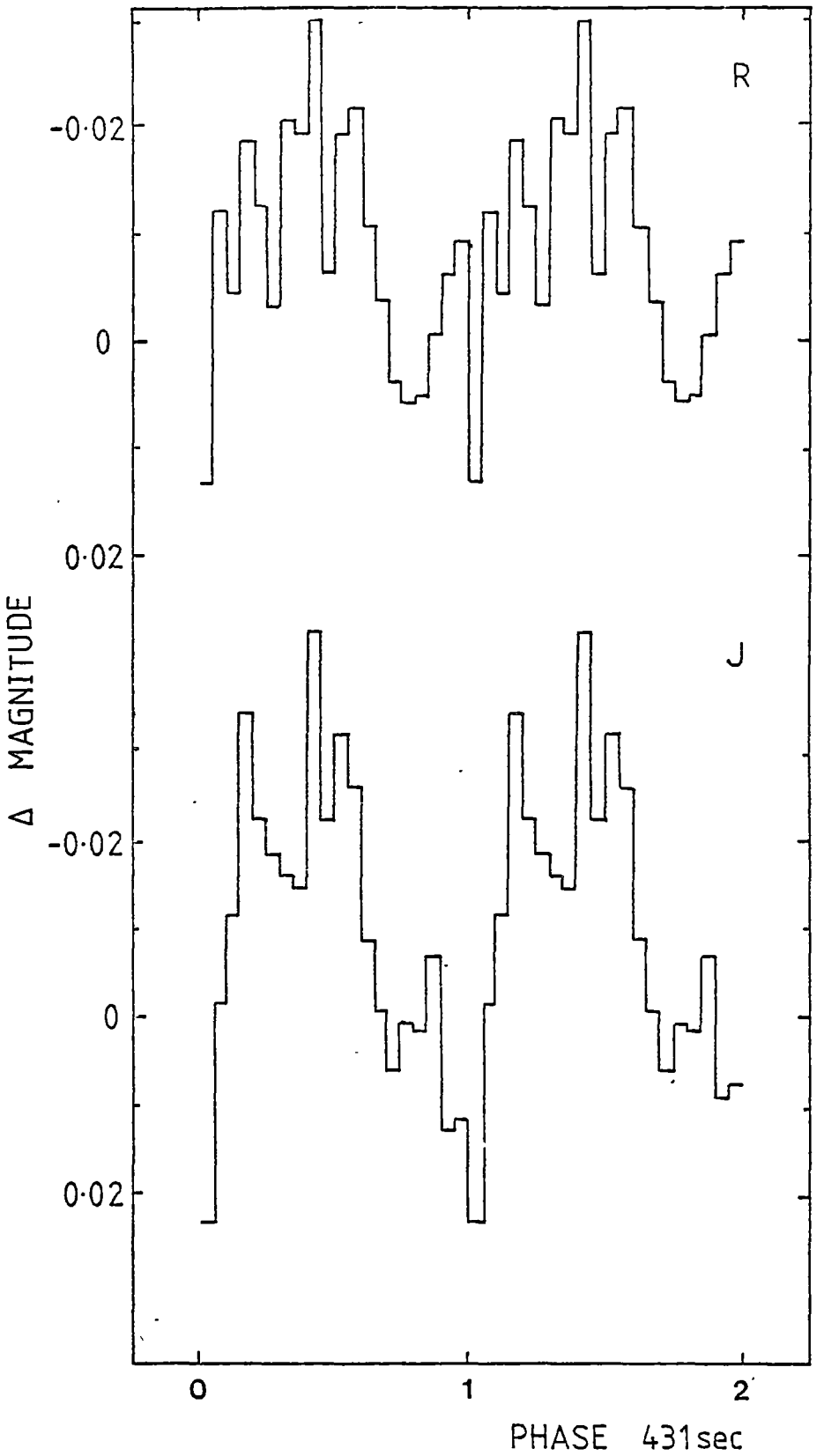

Figure 6.26 R and J pulse profiles, plotted twice for clarity, at the period of 431 sec. The data have been prewhitened by removal of the 794 sec period. Phase zero is at HJD 2445127.50488

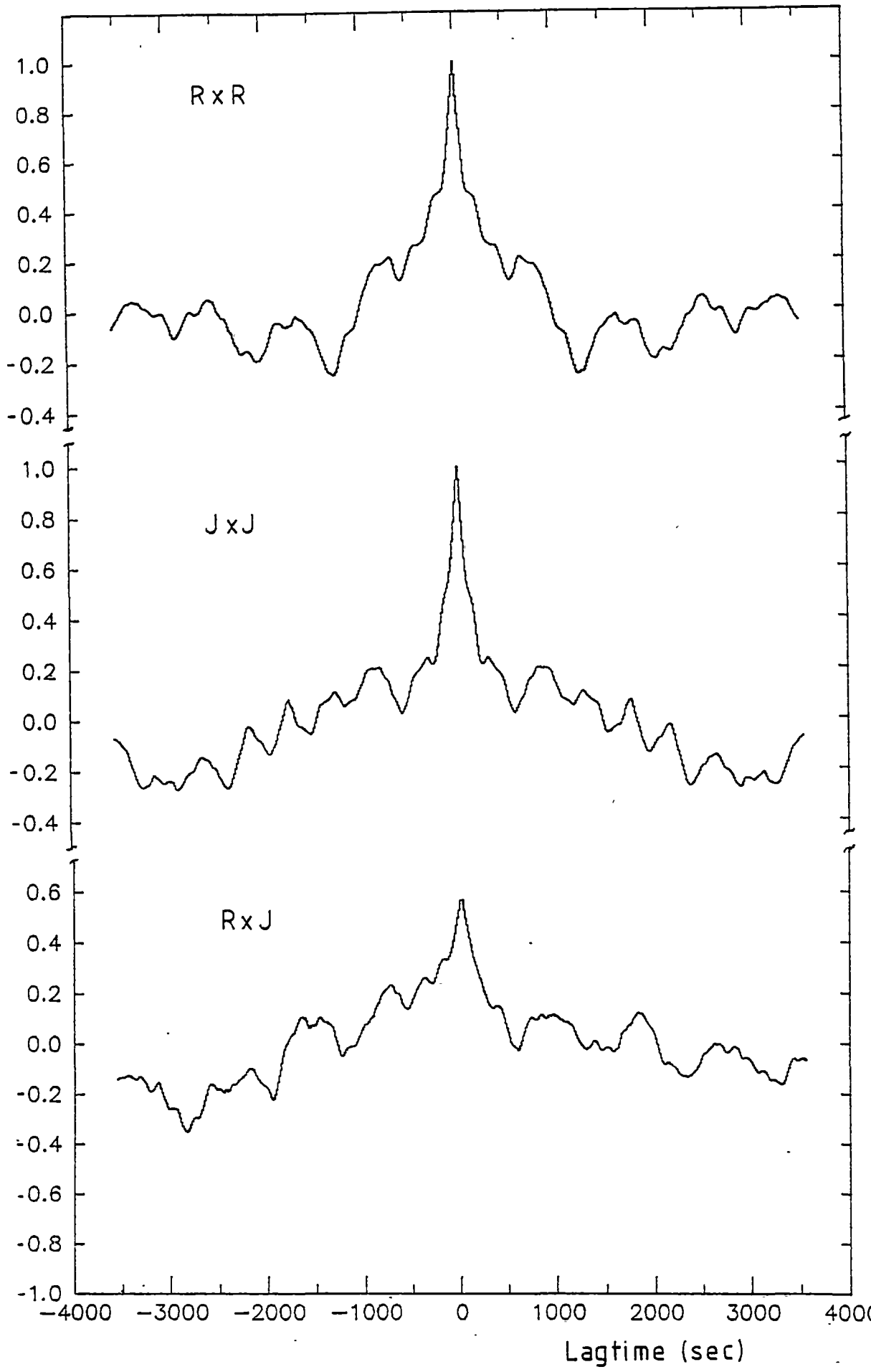

Figure 6.27 Correlation plots of R and J of V1223 Sgr from 1982 June 7.

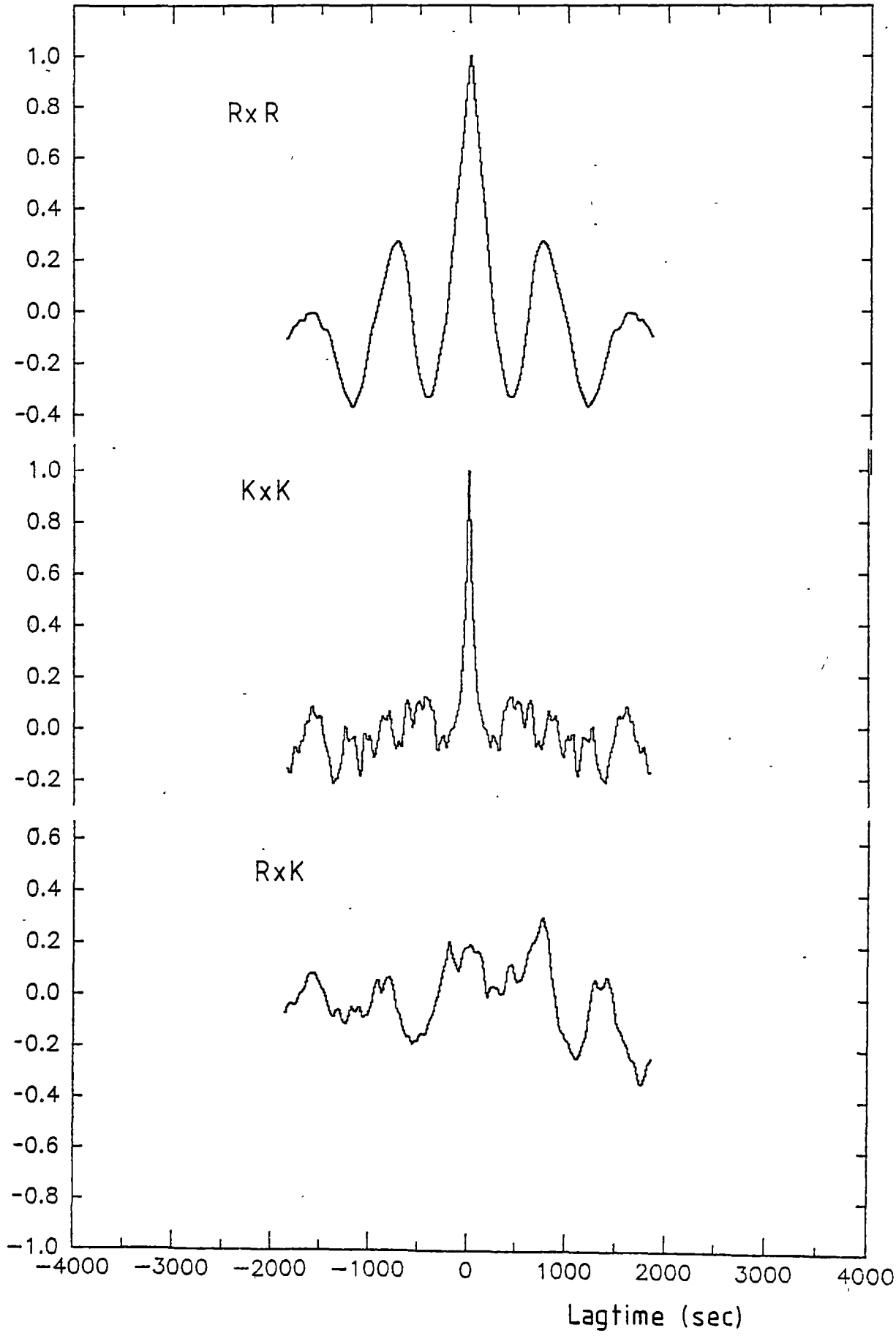

Figure 6.28 Correlation plots of R and K of V1223 Sgr from 1982 June 7.

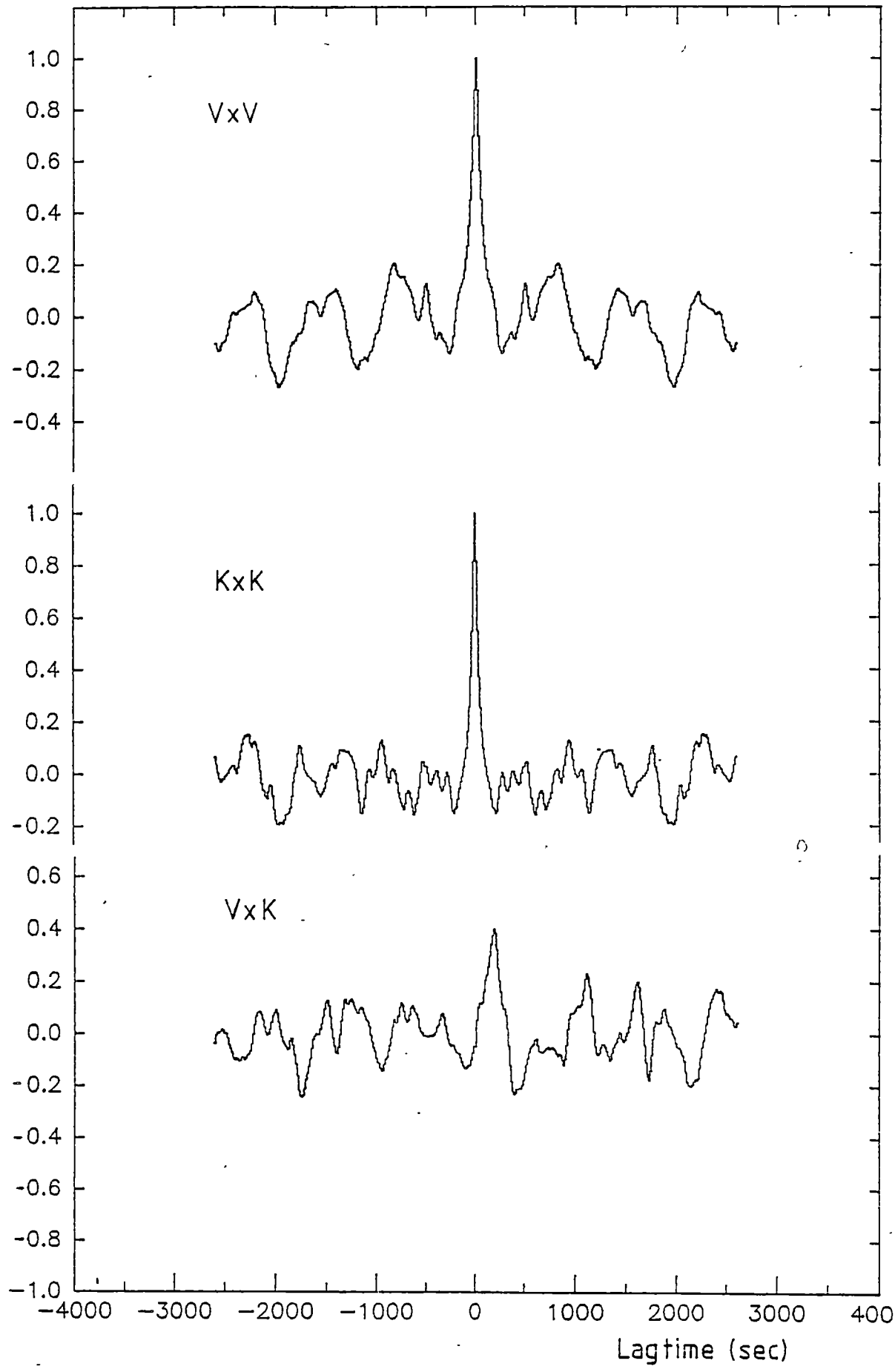

Figure 6.29 Correlation plots of V and K of V1223 Sgr from 1982 June 8.

i.e. the optical emission occurs before the IR. The significance of the feature was confirmed by testing random data with errors similar to the observed data. The maximum power from the cross correlation was ~0.15 well below the observed power of the 190 sec peak of 0.41. The standard deviation of this test data was 0.05.

6.2.2 Polarimetry

Modulation in circular polarization is expected at the rotation period of the white dwarf. Figure 6.30 is the circular polarization of the 4 pass bands folded at one of the proposed white dwarf rotation periods of 745 sec assuming the 794 sec period arises from the hot spot/companion. It is plotted twice for clarity. There is no obvious modulation in V, R and J. K appears to be modulated but the errors are large. Upper limits to polarization and time average means are listed in Table 6.11.

TABLE 6.11

Upper limits of polarization from V1223 Sgr 1982 June

Pass Band	Upper limit to circular polarization (%)	mean (%)
V	± 3	-0.48 ± 0.62
R	± 1	0.03 ± 0.13
J	+ 1, -2	-0.36 ± 0.20
K	± 10	1.14 ± 1.26

Similarly, Figure 6.31 is folded at the period of 794 sec. Other periods do not show any modulation with comparable upper limits.

6.2.3 Spectroscopy

Figure 6.32 is the sum of the 67 spectra taken on 1982 June 11. Superimposed on a blue continuum, there are strong lines of H_β, H_γ, H_δ and HeII λ4686. Unfortunately, the wavelengths covered just missed

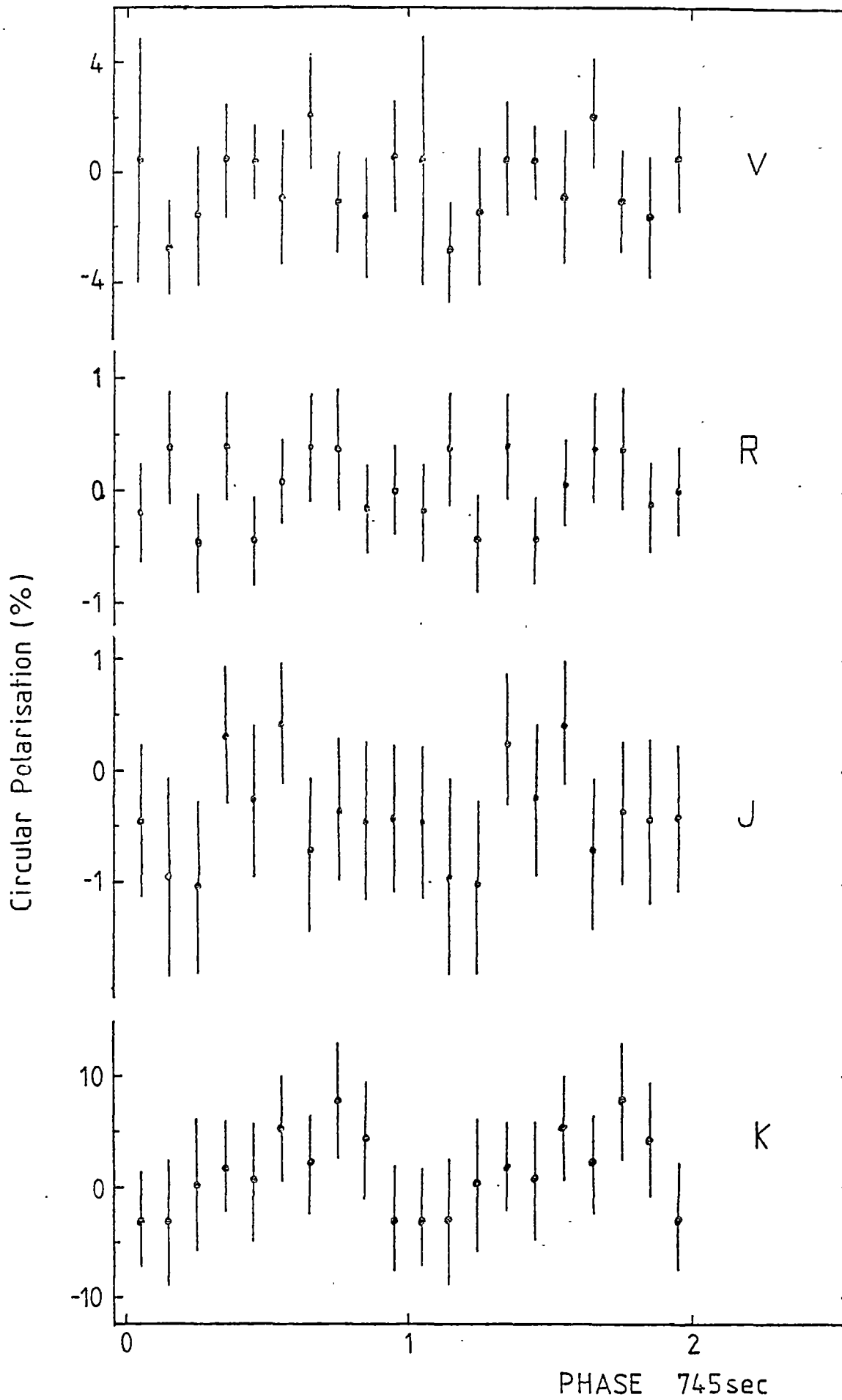

Figure 6.30 Circular polarization curves for 4 photometric bands folded at the period of 745 sec. Phase zero is at HJD 2445127.5048. Error bars are one sigma.

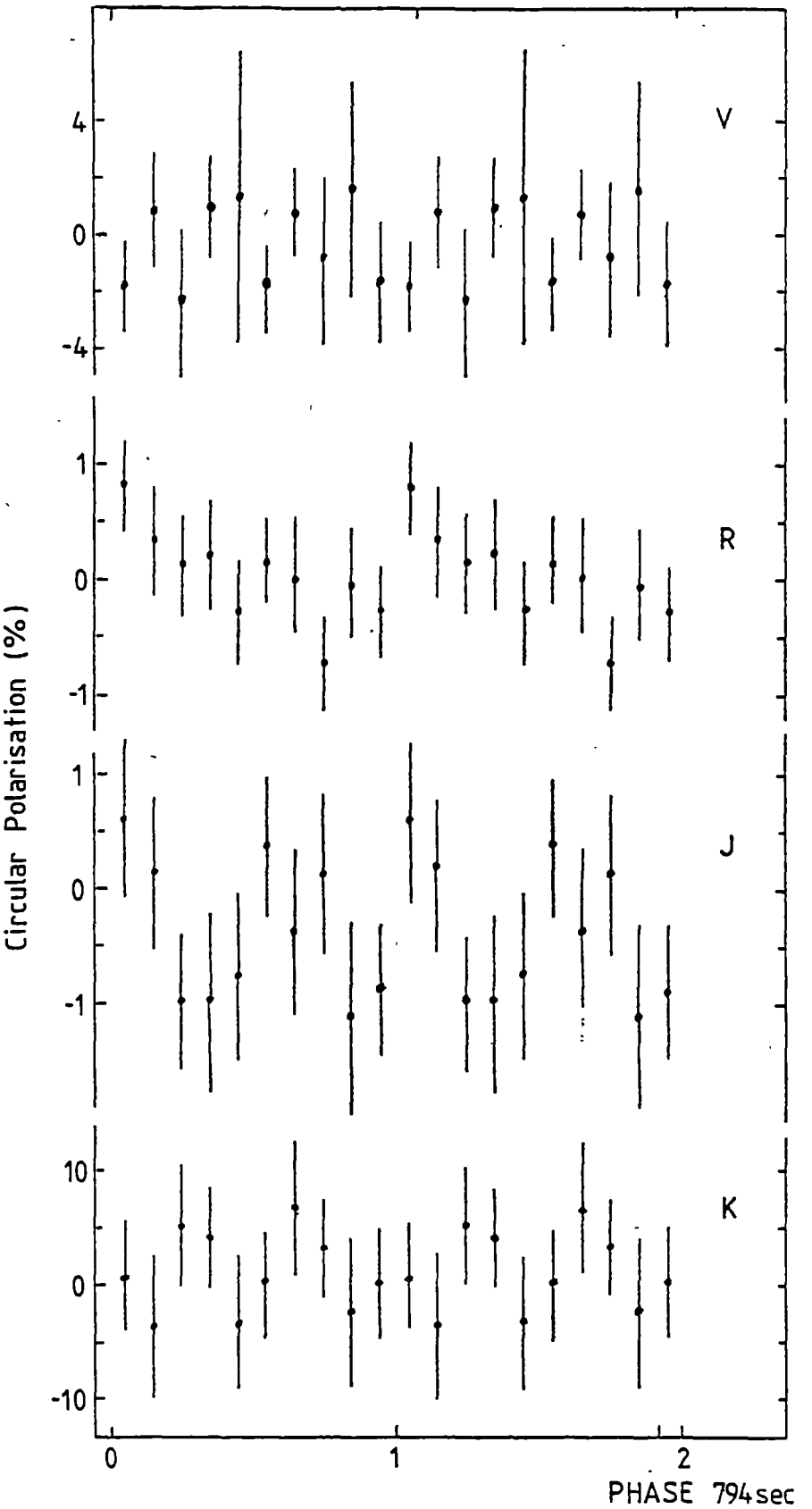

Figure 6.31 Circular polarization curves for 4 photometric bands folded at the period of 794 sec. Phase zero is at HJD 2445127.5048. Error bars are one sigma.

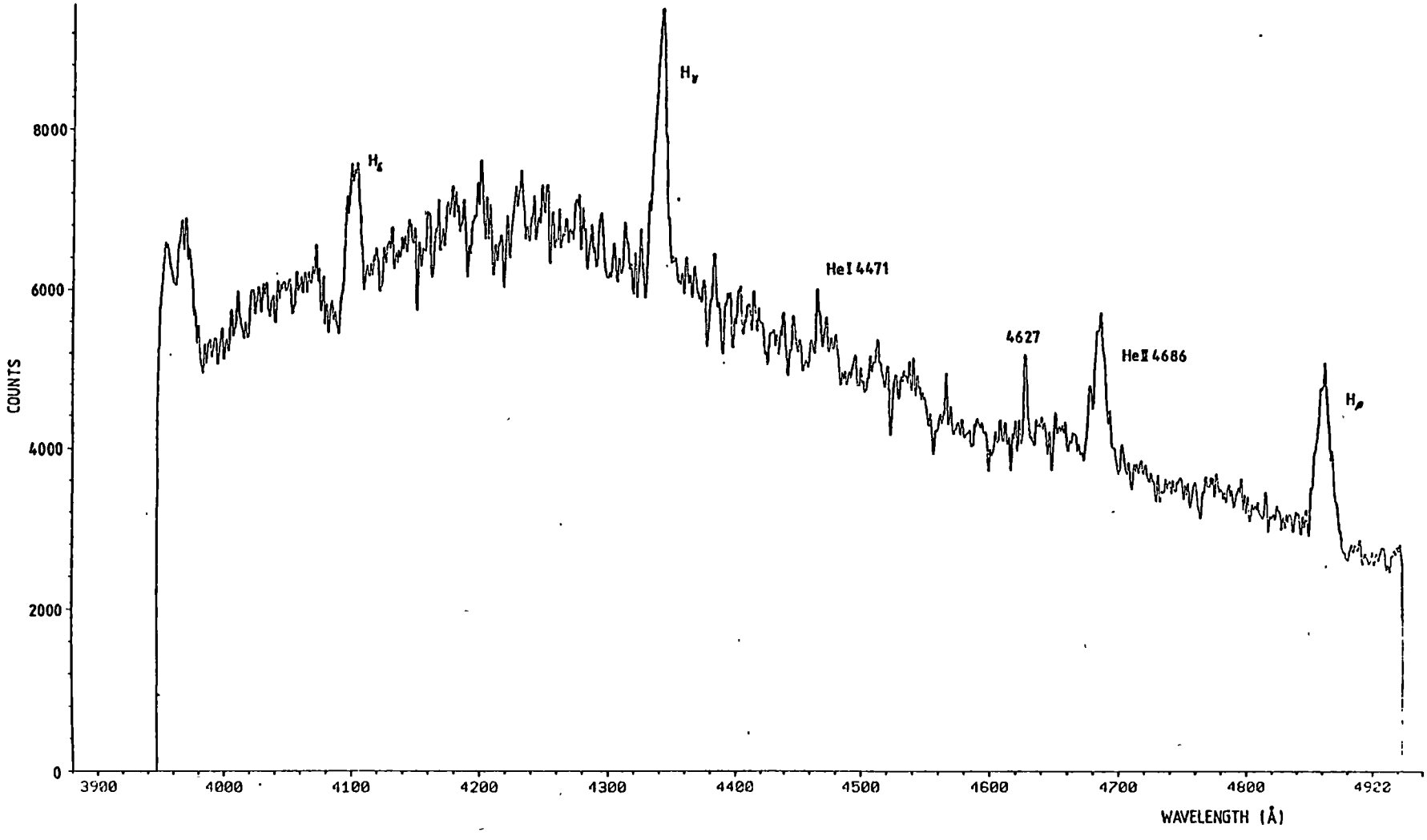

Figure 6.32 IPCS spectrum of V1223 Sgr observed on 1982 June 11 1732 UT to 1939 UT. The shape of the spectrum reflects the instrumental response. Dwell time is 5300 sec.

the H_ϵ line so we cannot comment satisfactorily on the shape of that line. Two weak lines are apparent, HeI λ4471 and a narrow line at 4627Å. Possible identifications are FeII λ4627.9 or the CIII/NIII blend at 4630Å. We favour the FeII identification for two reasons. First it is only 0.9Å from our estimate and within the resolution limits of the spectrum (~0.8Å) and second Steiner et al. (1981) suggest, from low resolution spectra, that FeII λ5150 is present. We find no evidence of the blend CIII/NIII λ4640 seen by Steiner et al. A puzzling feature is the broad deep absorption feature blueward of the H_δ line. It is shown in more detail in Figure 6.33 and is present in all spectra. It does not appear to be an artifact of the data reduction. If the pixels in the spectrograph shifted in wavelength between flat fielding and the actual observations then small sharp spikes would be expected in the spectrum and not a broad feature. The small sharp features, in absorption or emission may be as a result of such a shift.

The deepest minimum of the absorption feature corresponds to a velocity of -850 km sec^{-1}. The equivalent width (EW) and full width of half maximum (FWHM) of all lines are listed in Table 6.12.

To determine any orbital parameters, the spectra have been summed into 5 scans with dwell times ~26 min. The evolution of all lines are shown in Figures 6.34 to 6.38. The start-end times of the integrated spectra and the corresponding orbital phases are listed in Table 6.13.

TABLE 6.12

EW and FWHM at all lines of V1223 Sgr
1982 June 11

Line	EW (Å)	FWHM (Å)
H_β	9.62	14.1
HeII λ4686	5.55	11.3
FeII λ4627	0.78	2.8
HeI λ4471	1.16	~14
H_γ	5.61	9.9
H_δ emission	2.40	11.3
absorption	1.15	12.7

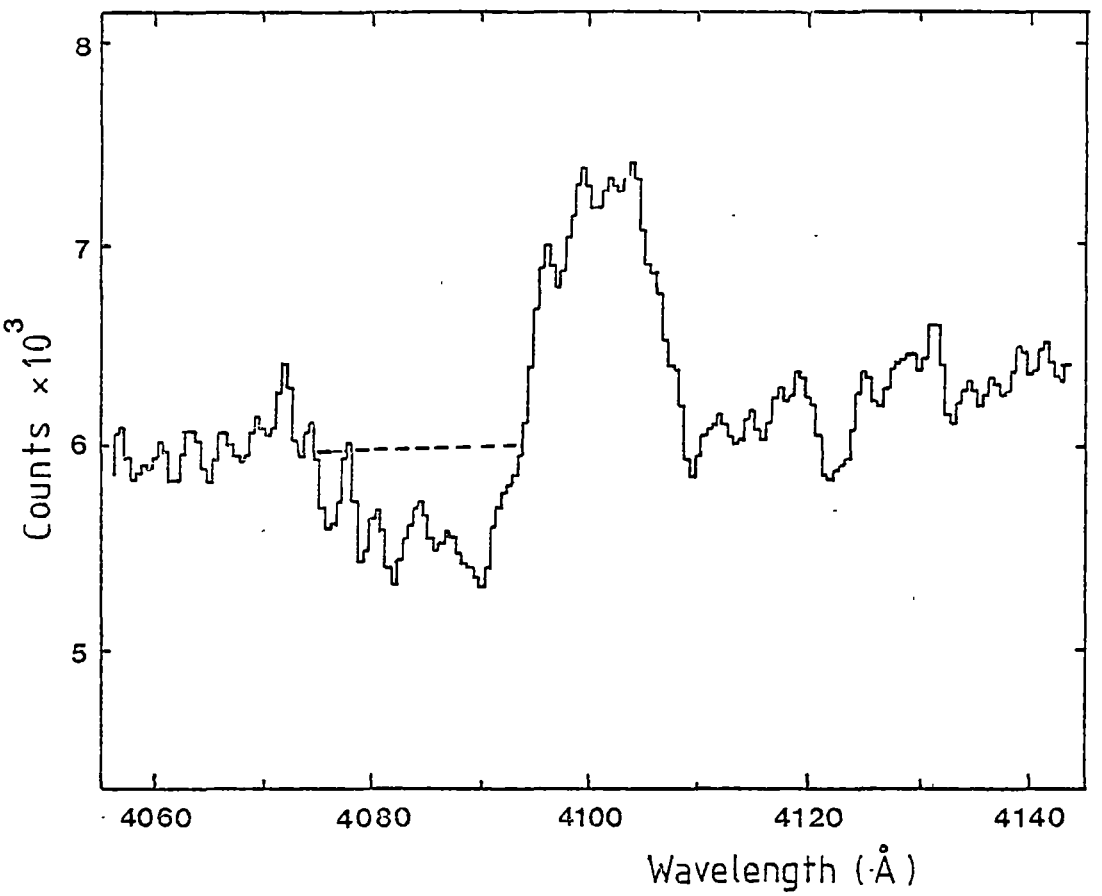

Figure 6.33 H_{δ} line profile of V1223 Sgr. Dashed line is the continuum.

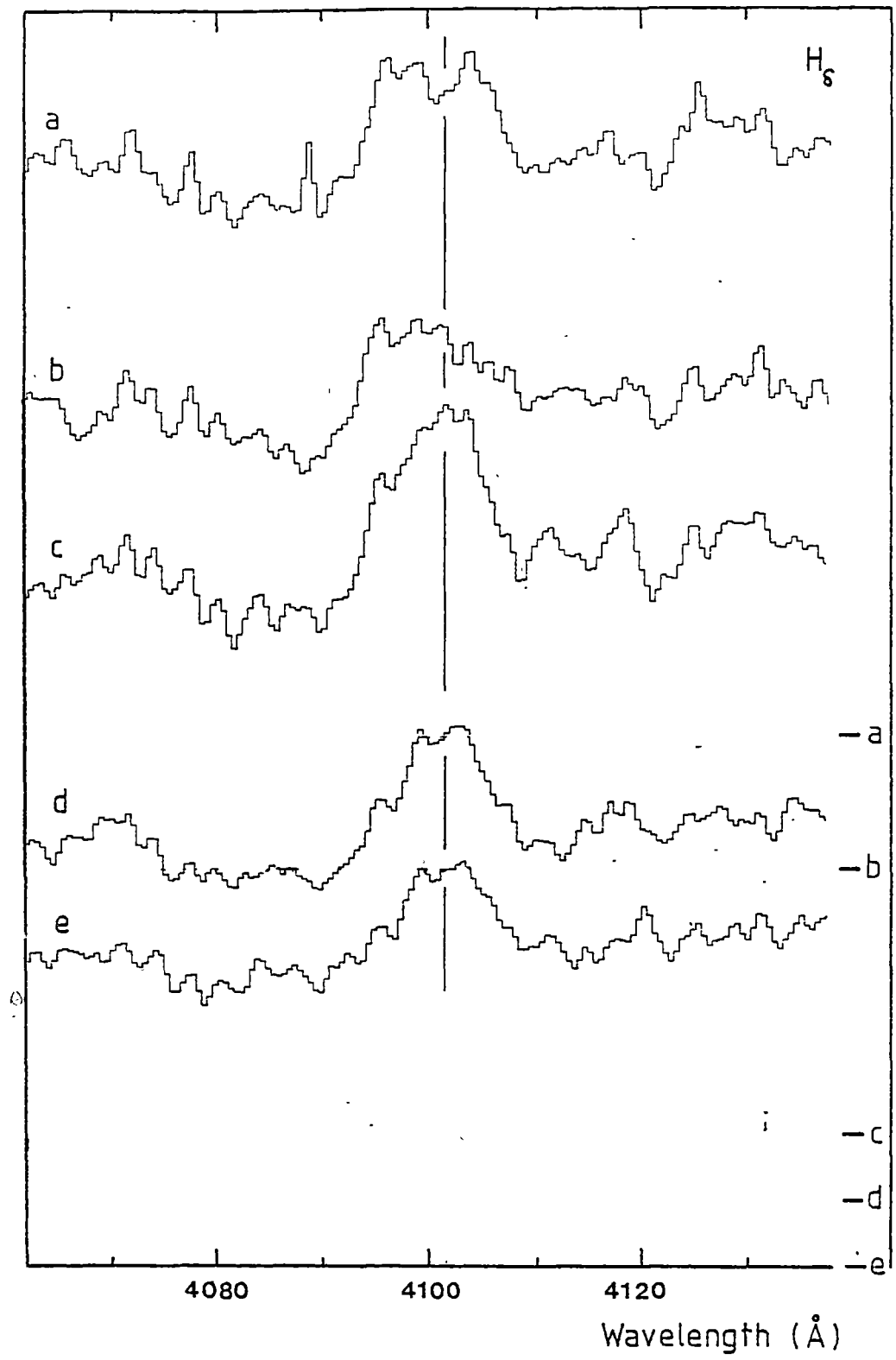

Figure 6.34 H_δ line profiles as a function of time from top (a) to bottom (e). Dwell time per spectrum is 26 min. Zero levels are marked on right. Vertical line is rest wavelength.

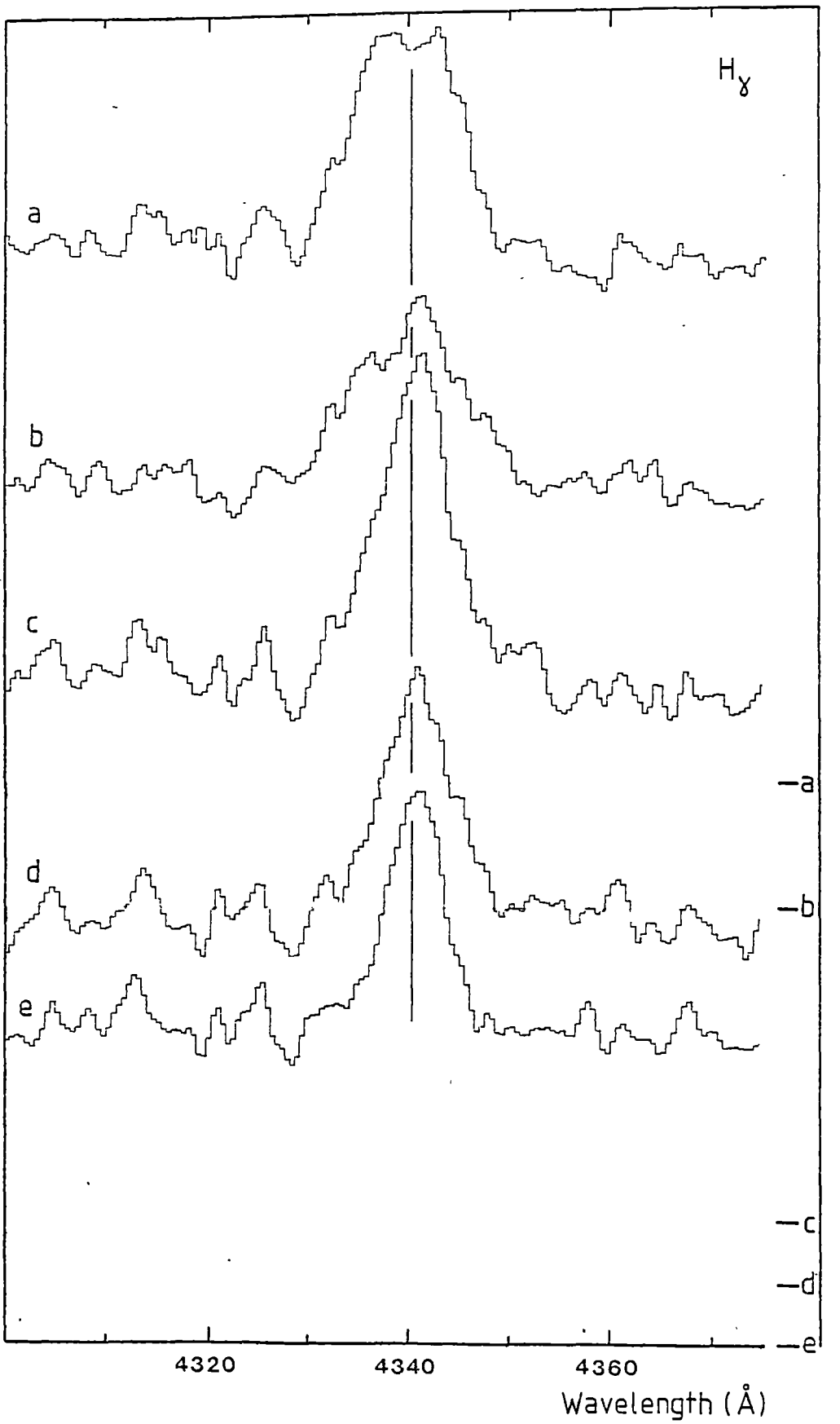

Figure 6.35 H_γ line profiles as a function of time from top (a) to bottom (e). Dwell time per spectrum is 26 min. Zero levels are marked on right. Vertical line is rest wavelength.

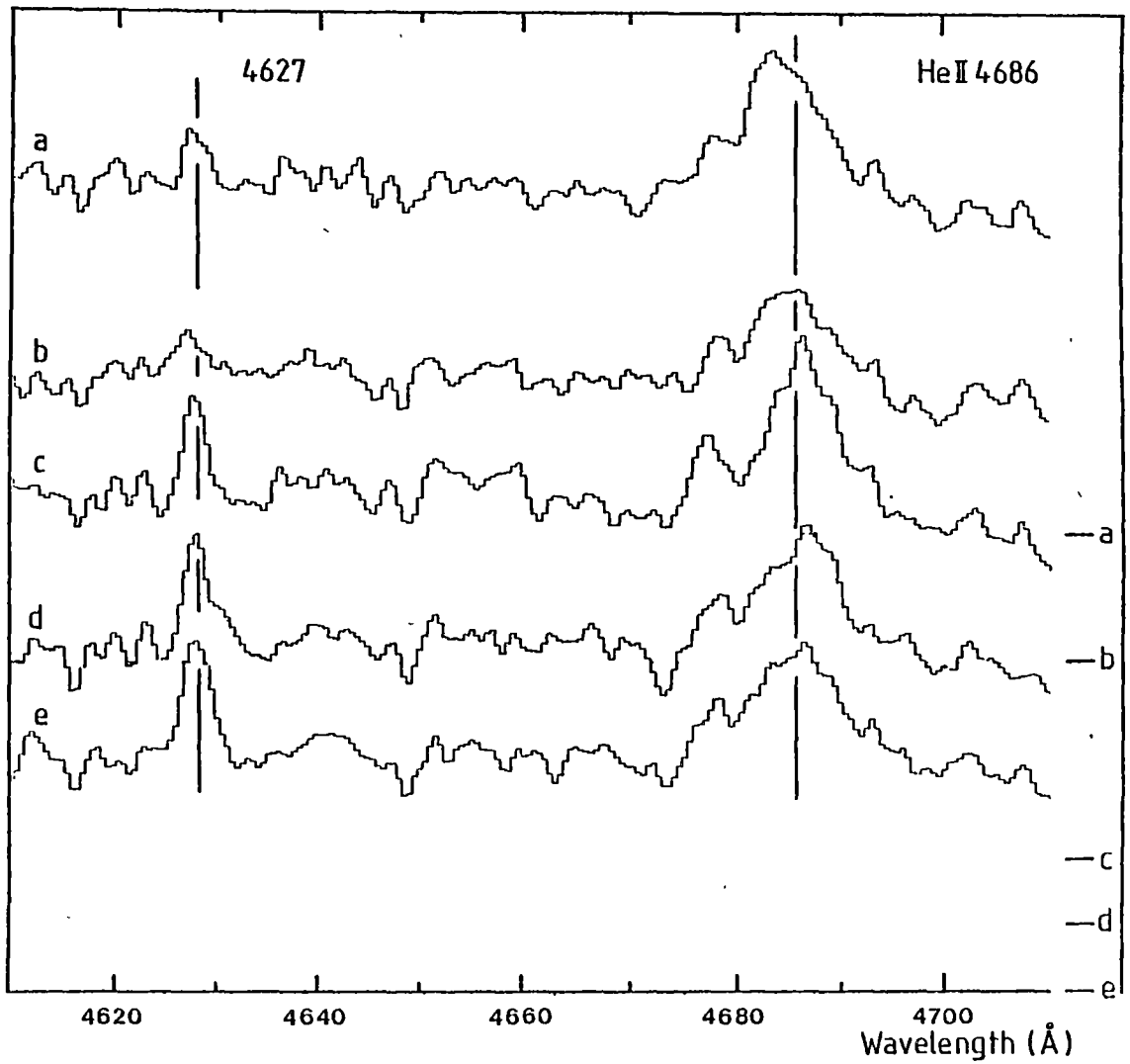

Figure 6.36 HeII λ4686 and FeII λ4627 line profiles as a function of time from top (a) to bottom (e). Dwell time per spectrum is 26 min. Zero levels are marked on right. Vertical lines are rest wavelengths.

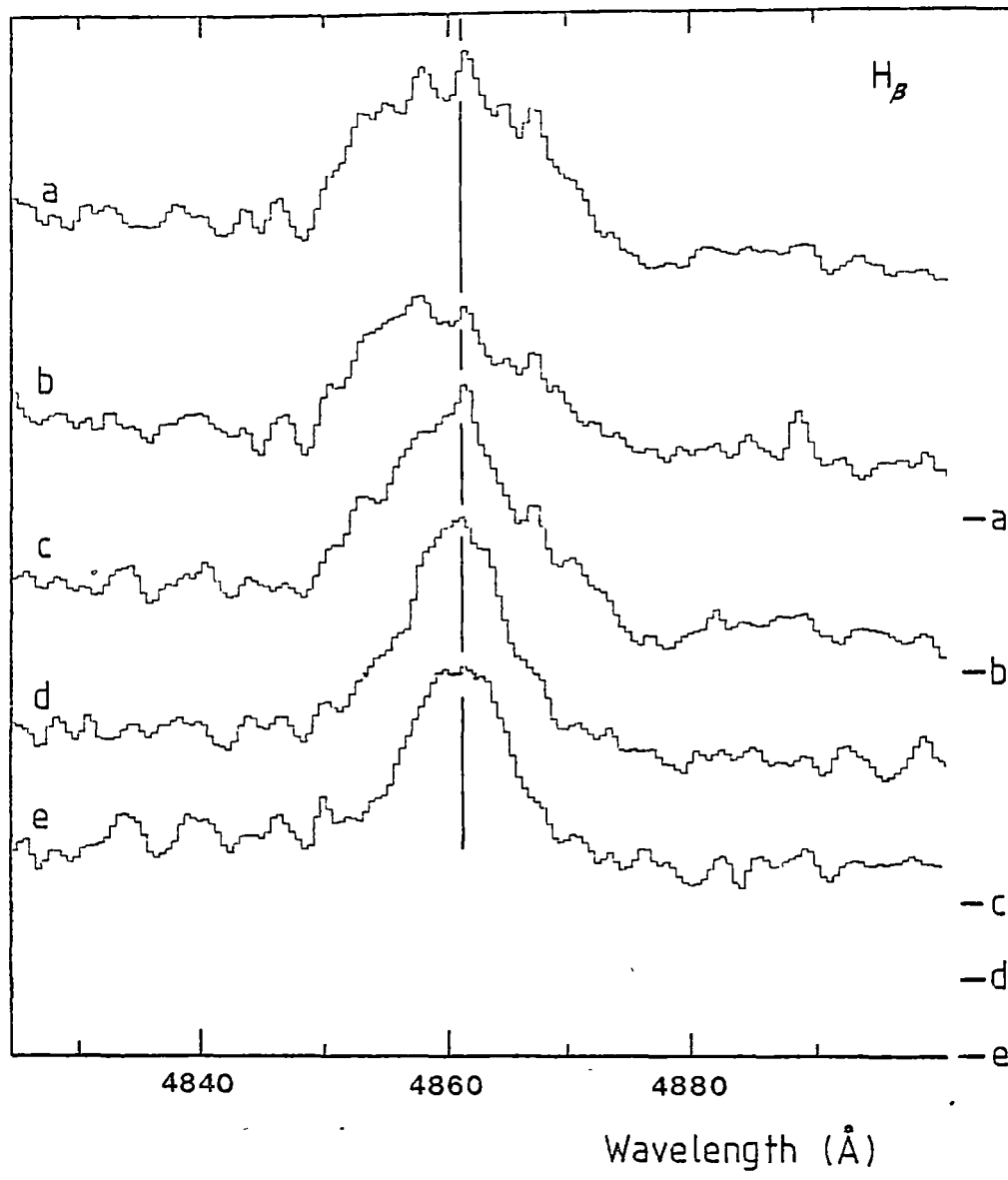

Figure 6.37 H_β line profiles as a function of time from top (a) to bottom (e). Dwell time per spectrum is 26 min. Zero levels are marked on right. Vertical line is rest wavelength.

TABLE 6.13

Start-end times and orbital phases of spectra from V1223 Sgr

Spectrum	Start-end time 1982 June 11		ϕ
A	1732 UT	to 1758 UT	0.65-0.78
B	1758	1824	0.78-0.91
C	1824	1850	0.91-0.04
D	1850	1917	0.04-0.17
E	1917	1940	0.17-0.29

On each diagram, the zero level for each spectrum is indicated on the right of each spectrum. The intensity of spectrum A should be multiplied by 0.73 to correctly scale with other spectra. The rest wavelength of each line is indicated by the vertical line. The EW, FWHM and continuum near the lines for spectra A to E are plotted in Figure 6.38. The continuum was at maximum at 1832 UT corresponding to phase 0.95 ± 0.05 of the orbital period (equation 6.2). The H lines are broad and double peaked in spectra A and B but narrow considerably for the last three spectra (Figure 6.38b) indicating that either the blue component has disappeared or the two components have merged. The HeII λ4686 line does not follow the behaviour of the H lines. It remains broad and a distinct component at 4678 Å is present in each spectrum. The absorption feature next to H_δ (Figure 6.34) appears in all spectra. The EW of the H lines reached a minimum at 1810 UT (Figure 6.38c). After 1840 UT , the EW stayed constant. The EW of FeII λ4627 increased steadily from 0.38 Å at 1745 UT to 2.1 Å at 1930 UT.

Blue shifted sharp components are also seen in H2215-086 (Shafter and Targan, 1982) but the sharp components of H2252-035 are red shifted (Wickramsinghe et al., 1982). From phase zero, the blue peaks of the H lines have disappeared apart from the H_δ peaks. The blue peak of HeII λ4686 at -500 km sec^{-1} persists in all spectra.

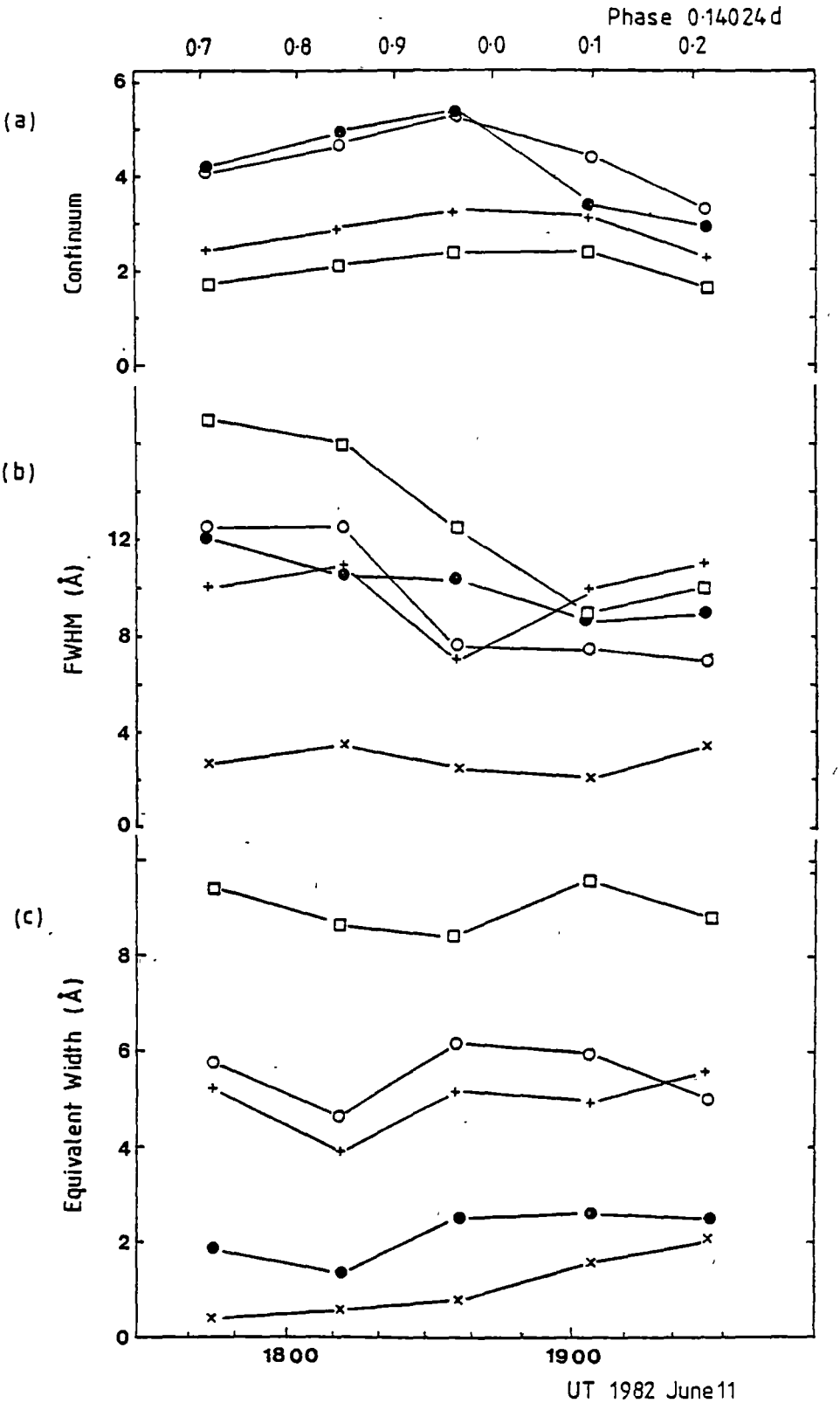

Figure 6.38 Data from IPCS spectra of V1223 Sgr on 1982 June 11.
(a) continuum flux (arbitrary units) near indicated lines.
(b) FWHM for all lines
(c) EW
Symbols are H_δ ●, H_γ o, HeII λ4686 +, FeII λ4627 x and H_β □.

Since there exist several components in the emission lines, the radial velocities were determined by three methods, the moment centre, the base of the profile and the sharp emission peaks. The method using the base radial velocities at 20% of the height of the line was inconclusive since the scatter was large and the lines were not consistent with each other. Both H_β and HeII λ4686 are difficult to measure since the HeII λ4686 has strong secondary emission peaks and H_β is very assymmetric. H_δ is confused by the blue absorption feature. Both H_γ and FeII λ4627 gave mutually consistent results and were compatable with the moment centres of all the lines. The rms scatter of the moment centre method was ~25 km sec^{-1} considerably less than for the other methods and suggests that this is the best estimate of the radial velocity of the system. The broad line emission from the disc dominates the line strengths.

The broad HeII λ4686 yielded similar velocities to the H lines. From the study of the origin of emission lines from discs, Williams and Ferguson (1982) find that the HeI and H lines are generally from the outer edges of accretion discs whilst HeII is from a more confined area of the disc. One possibility is the ionized outer skin of the upper and lower surfaces of the disc with the ionizing X-rays originating from the white dwarf. Our results are consistent with this possibility and not from any hot spot since the radial velocity fits are the same suggesting a common centre of emission.

Unfortunately, only half a period was observed with the consequent problem of determining which features are related to orbital effects. Figure 6.39 is the radial velocity plot of spectra A to E. Open symbols are measured from the centre of moment whilst filled symbols are the sharp components. The dashed line is the best fit radial velocity curve of the moment centre measurements assuming a circular orbit of 0.14024^d. The derived orbital parameters are listed in Table 6.14.

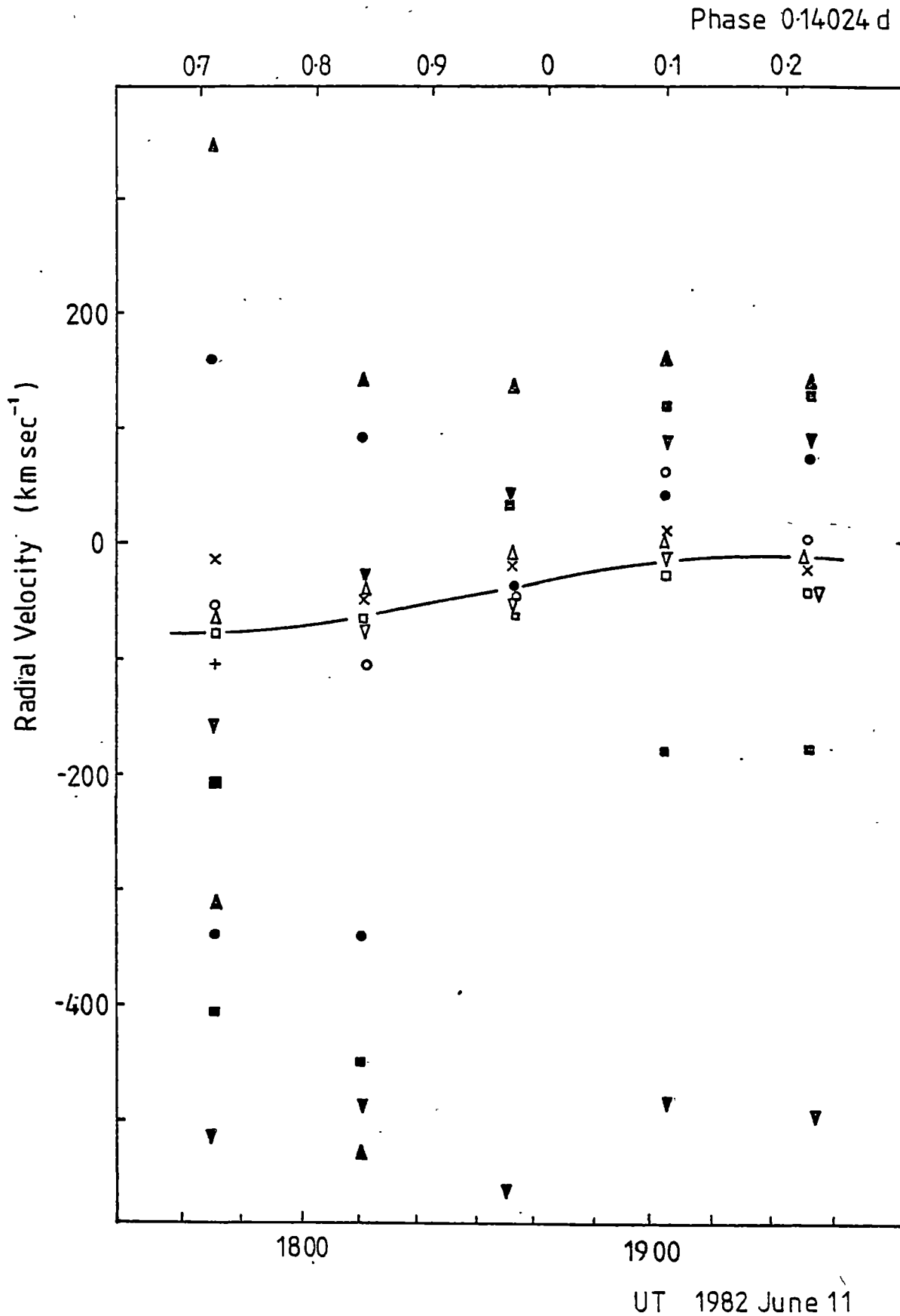

Figure 6.39 Radial velocities of V1223 Sgr on 1982 June 11. Filled symbols are peaks H_δ ■, H_γ ▲, HeII λ4686 ▼, and H_β ●. Open symbols are moment centres H_δ □, H_γ Δ, FeII λ4627 x, HeII λ4686 ∇ and H_β o. Solid line is best fit radial velocity curve.

TABLE 6.14

Orbital parameters of V1223 Sgr

semi-amplitude	33 ± 8 km sec^{-1}
phase of inferior conjunction	0.92 ± 0.07
systemic velocity	-47 ± 8 km sec^{-1}
mass function	(5.0 ± 3.8) x $10^{-4} M_{\odot}$
a sini	(6.2 ± 1.6) x 10^{9} cm

To detect any effects due to the 794 sec periods, the individual spectra have been added into 10 phase bins. The equivalent widths of all the emission lines are shown in Figure 6.40. The only significant modulations occur in H_{β} and H_{γ}, the others are essentially constant. The dip centred at phase 0.4 implies that the H_{β} and H_{γ} lines vary considerably more than the continuum. HeII λ4686 in H2252-035 varies at the 859 sec beating period (Wickramsinghe et al. 1982) yet in V1223 Sgr no significant changes are seen. Folding the spectra at twice the pulsation period, i.e. 1588 sec revealed no periodic changes in EW or FWHM.

Line profile changes are evident in the phased spectra but there were no common components in the H lines, perhaps indicating that the orbital effects discussed previously are dominant. Comparison of observations over two orbital cycles would be required to detect any consistent variations associated with periods other than the orbital period.

6.3 VY Sculptoris

X-ray Observations

The Einstein Observatory observed VY Scl on day 349, 1979, for 1540 seconds using the Image Proportional Counter (IPC) and the Monitor Proportional Counter (MPC). Figure 6.41 is the combined IPC and MPC spectrum. Error bars are one sigma and upper limits are 2σ. The spectral shape cannot be uniquely defined. However, the best fit

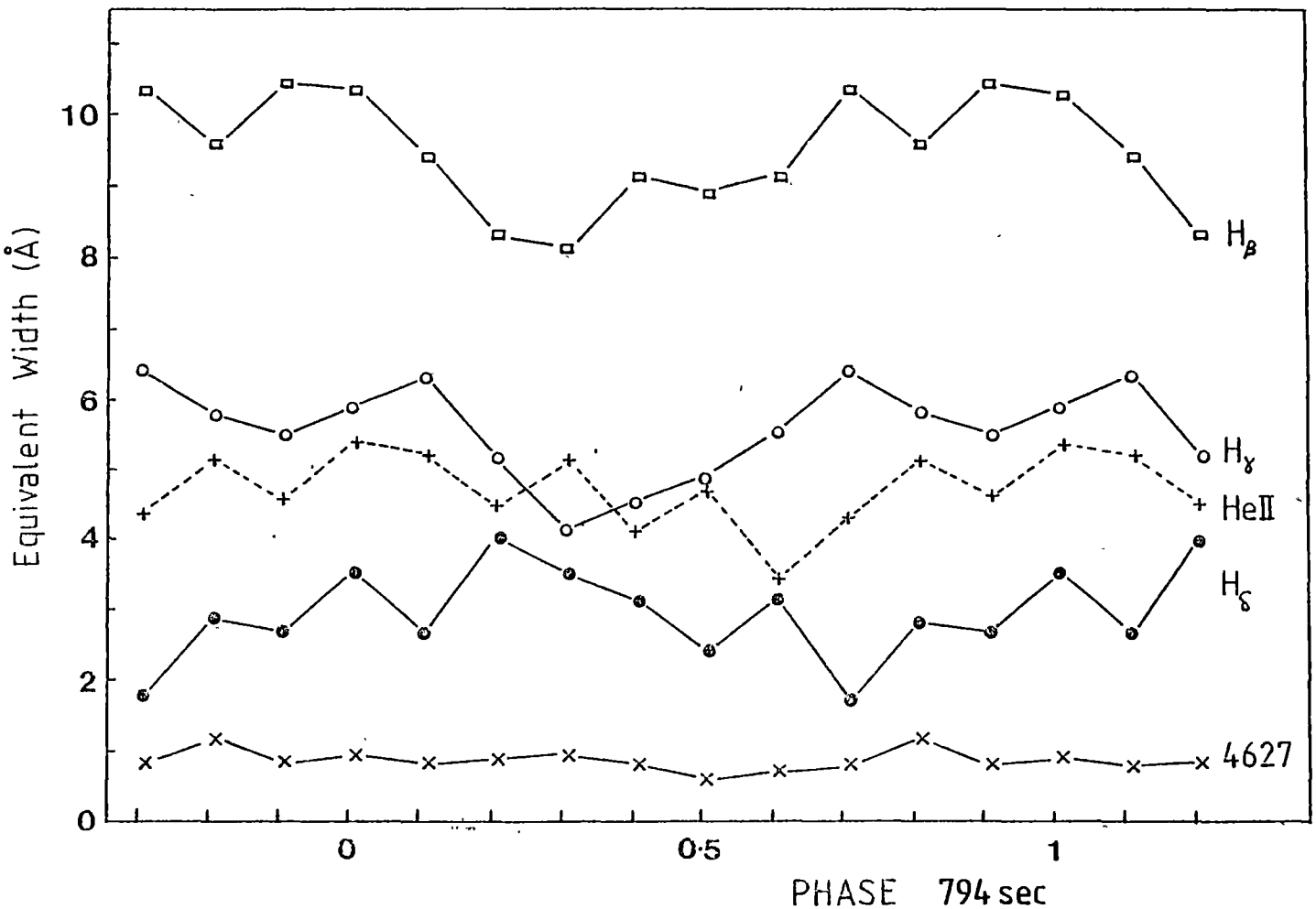

Figure 6.40 EW of all emission lines as a function of phase of the 794 sec period. Symbols as in Figure 6.38. Phase zero corresponds to maximum light (HJD 2445132.2386)

thermal bremsstrahlung has a temperature kT = 1.23 ± 0.35 keV with a log hydrogen column density of $20.6^{+0.4}_{-0.6}$ cm^{-2}. This spectrum is shown as the solid line on Figure 6.41. The IPC data allow for a temperature of ~4 keV, but the MPC data constrains the spectrum to be soft. Total IPC luminosity is 2.9×10^{-12} erg $cm^{-2} sec^{-1}$ (0.2-4.5 keV) or 6.7×10^{30} $(D/100)^2$ erg sec^{-1}, where D is the distance in pc. The X-ray to optical luminosity is ~0.6 if it was in its normal bright state at the time of observation. This is the expected value for accretion onto a white dwarf and is typical of the results of cataclysmic variables studied by Córdova et al. (1981a,b).

The IPC light curve and hardness ratio is shown in Figure 6.42. The background level is indicated by the dashed line. The hardness ratio of the spectrum is defined by counts (1.15-4.5 keV) divided by counts (0.15-1.15 keV). This ratio was selected since, on average, there are approximately the same number of counts in each bin and each ratio yields the best signal to noise ratio. Córdova et al. (1981a) have defined the IPC spectral hardness ratio to be counts above 0.55 keV divided by those below 0.55 keV. This ratio for VY Scl is 3.4 ± 0.6, a typical value for cataclysmic variables (Córdova et al., 1981a; Becker, 1981). The mean IPC count rate is 0.123 ± .01 counts sec^{-1}. The peaks in the light curve have a spacing of 500 - 600 sec; the same timescale of flares seen by Burrell and Mould (1973). If they are of a common origin, the X-ray to optical flux is ~1, assuming a 1000Å bandpass in blue light from Burrell and Mould's observation. They did not specify the bandwidth of their data. A similar ratio has been seen from 2A0526-328 for the 700 sec quasi-periodic oscillations. The spectrum during the middle of the observation appears harder, but there is no distinct correlation between spectral hardness and intensity as seen in 2A0526-328 (Figure 6.13).

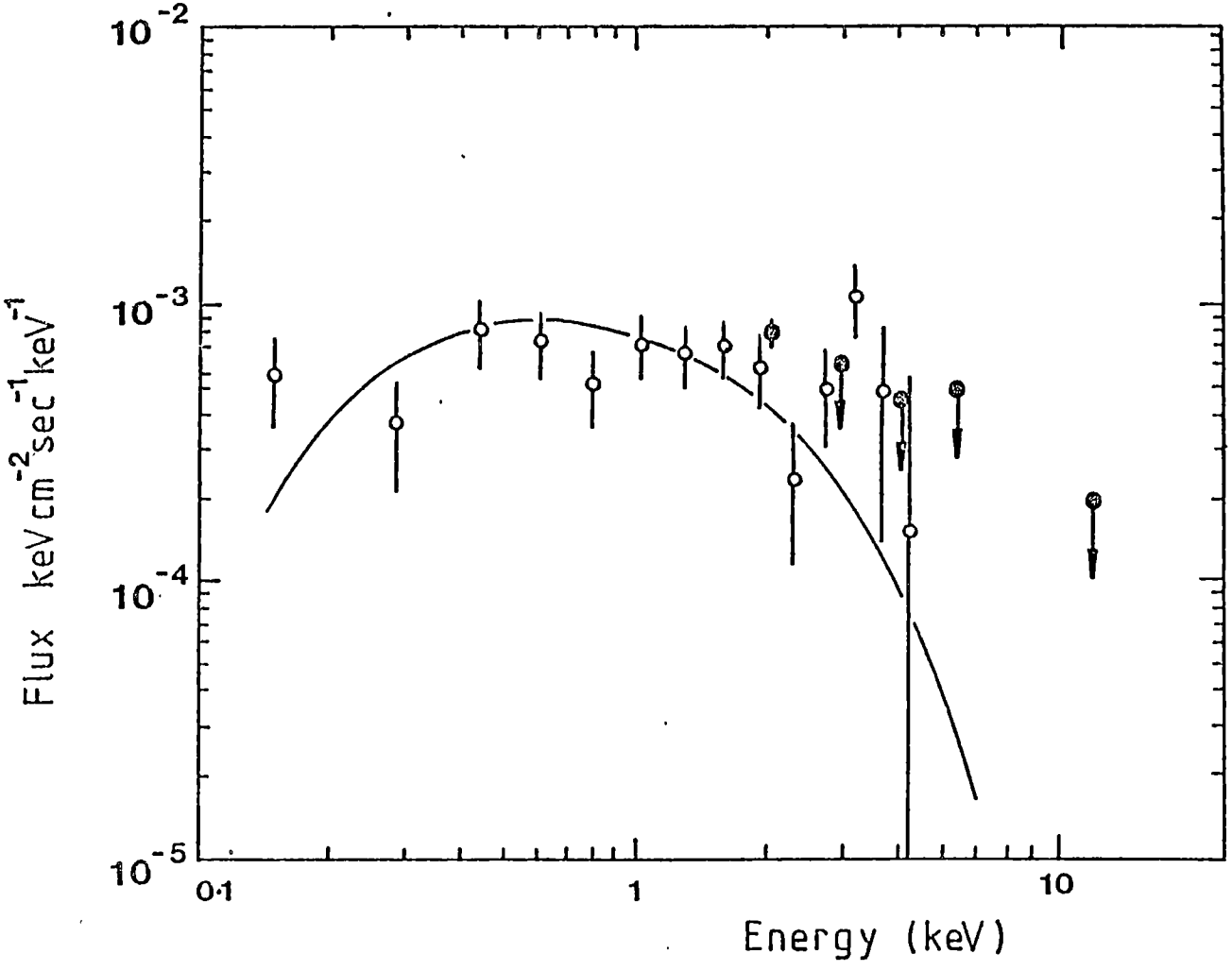

Figure 6.41 The X-ray spectrum of VY Scl. Open circles are from the IPC and filled circles from the MPC. Upper limits are 2σ. Line is best fit thermal bremsstrahlung (kT = 1.23 keV, $n_H = 4 \times 10^{20}$ cm^{-2}).

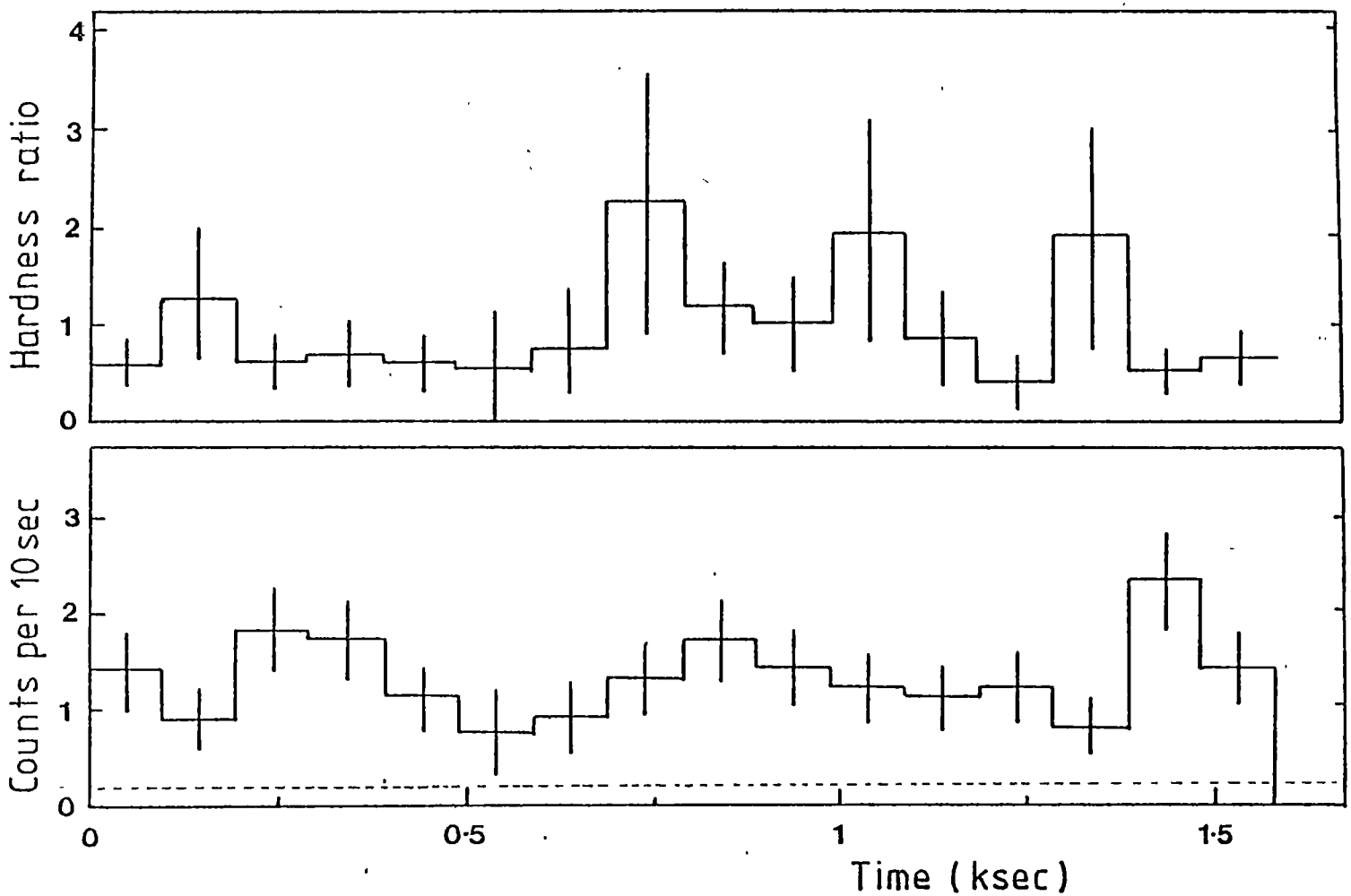

Figure 6.42 IPC Light curve and hardness ratio of VY Scl. Start of observation is JD 2444222.6389. Dashed line is background level.

CHAPTER 7

MODELS OF INTERMEDIATE POLARS

In this chapter, a discussion of possible models of the intermediate polars 2A0526-328 and Vl223 Sgr and the nova-like object VY Scl are presented. An alternative model of 2A0526-328 to the model of Hutchings et al. (1981) (hereafter HCCTC) is developed and its observational consequences outlined. Vl223 Sgr is compared with other intermediate polars in Section 7.2. In section 7.3 models of synthetic light curves are compared with available data. Section 7.4 contains a brief discussion on VY Sculptoris.

7.1 2A0526-328

To explain the three periods in the system, HCCTC have proposed that the white dwarf is in non-synchronous rotation about its companion. The spectroscopic period of 5.4864^{h} is the orbital period and the photometric period of 5.1914^{h} is the rotation period of the white dwarf. The beat period of 4.024^{d} is the rotation period of the white dwarf as seen by its companion. They suggest that the 4-day photometric variation is driven by X-ray heating by a beam from the white dwarf perhaps originating from the accretion column.

Independently, we found the spectroscopic period differed from the photometric period (Hill, 1980) with two possible values of 4.65 ± 0.05^{h} and the 24 hour alias 5.58 ± 0.05^{h}, and had developed a model different from HCCTC. The white dwarf with an oblique magnetic axis rotates at the spectroscopic period, more accurately determined by HCCTC, of 5.48^{h}. Line emission occurs in the upper part of the accretion column at the region of the disc where the white dwarf field can disrupt the Keplerian motion and channel the disc material down the field lines. Hard X-rays are generated closer to the poles at the point where a standing shock occurs. Photometric maxima occur when the magnetic axis is aligned towards the companion and some form of X-ray heating occurs either on the surface of the companion or in the region between the stars where there should be substantially more accreting matter. A disc can form in this

object but the inner radius is quite large (~1 $R_\odot$) as discussed later. Since the disc has a large inner radius it is more appropriate to call it an accretion ring, but both terms will be used. The 4-day period is the orbital period of the system and the orbit is retrograde. Figure 7.1 is a schematic of both models. The white dwarf is drawn over scale for clarity. In further discussion, this model will be referred to as the 4 day model.

An immediate difficulty is the formation of a system with a retrograde orbit. Normally the white dwarf will gain angular momentum in the same direction as the orbit from the accreting matter. We do not address this question in any detail except that the study of the evolution of such systems will be required. A possibility is capture of the white dwarf and would lead to a spin down of the white dwarf. In HCCTC's model, the white dwarf should spin up. The time scale of detection of a period change is expected to be several years.

Similar beating behaviour has been observed in two other objects; the X-ray cataclysmic variable H2252-035 (Griffiths et al., 1980; Patterson and Price, 1981) and the X-ray pulsar 4U1626-67. In H2252-035, the white dwarf rotates at the X-ray period of 805.4 sec whilst optical pulsations with a period of 858.7 sec are caused by the reprocessing of the X-rays on the surface of the secondary (Patterson and Garcia, 1980). The derived orbital period is the same as the observed period of 3.59^h (Williams and Johns, 1980). The 7.7 sec pulsar 4U1626-67 has been found to have a side lobe frequency that is 0.3% lower in frequency than the main optical pulse and yields an orbital period of 2500 sec (Middleditch et al., 1981). Both H2252-035 and 4U1626-67 have prograde orbits.

In all three systems, only one source of X-rays near or on the degenerate object is assumed. In the case of H2252-035 and 4U1626-67, the pulsation period is well known and must be related to the degenerate's oblique magnetic axis. It would be expected that such a region would

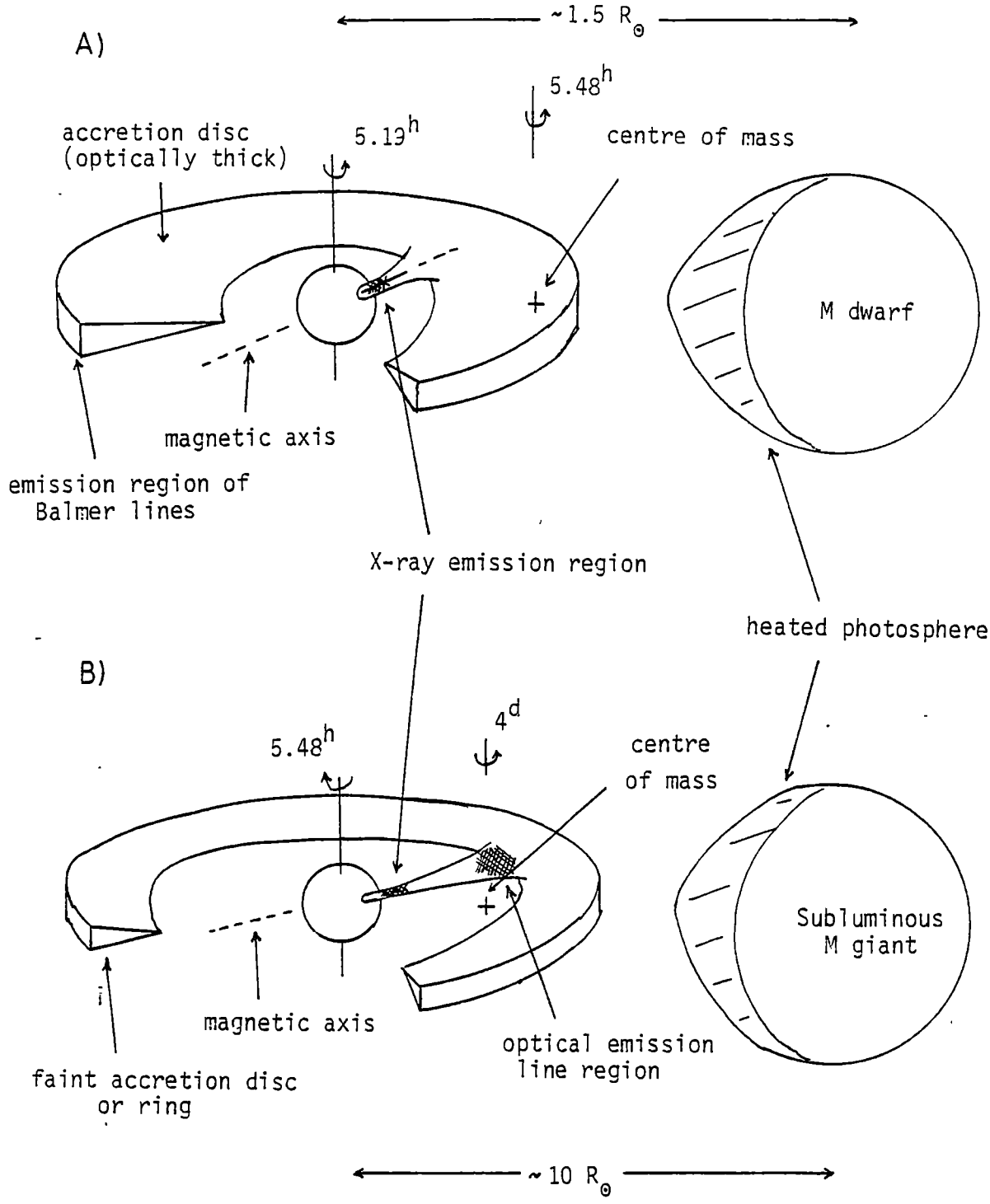

Figure 7.1 Schematic of HCCTC's model (A) and the 4-day model (B). The white dwarf is drawn oversize.

occur over both magnetic poles and provide approximately equal contributions to the optical heating pulsations.

Only one pole must be active in H2252-035 since the beat between the X-ray and optical reprocessing periods is the orbital period (equation 6.4). If the X-ray period were half the rotation period then half the reprocessing period would be 920.1 sec not the observed 858.7 sec period. A displacement of the dipole towards one pole, as proposed by Priedhorsky and Krzeminski (1978) for AM Her, could reduce the emission from one polar column. An asymmetric dipole field also means that one pole is closer to the rotation axis than the other. This would reduce the apparent modulation from that pole and make the system appear to have a single pole. It is possible also that the inclination angle is small and that the radiation from the more distant pole is eclipsed or suppressed by the degenerate and/or disc. This is possibly the case for 4U1626-67 where the orbit inclination is estimated to be $18^{+18}_{-7}{}^{\circ}$ (Middleditch et al., 1981). No eclipses have been seen from H2252-035 (Patterson and Price, 1981) and an upper limit of $\sim 60^{\circ}$ can be set for the inclination angle. Wickramsinghe et al. (1982) estimate the inclination angle to be $\sim 30^{\circ}$. A single beaming model has been invoked to explain eclipse-related phase shifts in the rapid oscillations of the variables DQ Her and UX Uma (Petterson, 1980). However, the inclination angles that best describe the data are 89° and 75° respectively, indicating that systems with high inclination angles still obscure one magnetic hot spot. The nova-like variable AE Aquarii has 33 sec pulsations in its X-ray light curve (Patterson et al., 1980) whilst in the optical 16.5 sec and 33 sec oscillations are detected (Jablonski, 1981). The 16.5 sec pulsations arise because the two poles contribute to the optical emission. However, the light curve indicates that one pole dominates the observed flux. We conclude that a single or dominant emission line region is possible and is consistent with other well-studied systems.

The velocity of the emission line region about the white dwarf is 116 km sec^{-1}, the K velocity of the base of the H lines (HCCTC). An estimate of the white dwarf magnetic field required to corotate the optical emission region will be discussed later. The mass ratio q can be estimated from the contribution of the orbital radial velocity to the radial velocity curves. The radial velocity data for both H and He lines were demodulated from the spectroscopic period of 5.48^h using the orbital solutions of HCCTC, and the residuals were plotted as a function of the 4.042^d phase. There was no detectable modulation and we obtain an upper limit to the orbital velocity of ~25 km sec^{-1}, which implies $q \leq 0.2$. HCCTC noted a variation of 75 ± 28 km sec^{-1} in V_o for HeII λ4686 as a function of the 4-day period. This would imply $q \sim 0.6$, but it seems more likely that the effect is not orbital.

The mass of the companion is $\leq 0.2\ M_\odot$ if we assume a white dwarf mass of $1\ M_\odot$, the mean mass value for white dwarfs in cataclysmic variables (Warner, 1976b). For accretion to occur via Roche lobe overflow, the companion must have a radius of ~2.8 $R_\odot$ compared with the zero age main sequence (ZAMS) radius for a $0.2\ M_\odot$ star of $0.3\ R_\odot$ (Allen, 1973). ZAMS stars will not fill the Roche lobe for this system if the mass is $<5\ M_\odot$. A similar dilemma was present with the old nova GK Per which has a period of 1.9^d (Bianchini et al., 1981) and the companion would have substantially under-filled its Roche lobe if it were a ZAMS star. However, observations by Gallagher and Oinas (1974) found the spectral type of the companion to be K2 IV, indicating the companion had evolved. Whyte and Eggleton (1980) have discussed the evolution of cataclysmic binaries and have demonstrated that GK Per could have evolved to its present state in a nuclear evolution dominated system. They present equations for the equilibrium radius and luminosity of ZAMS stars and correction terms to allow for various degrees of nuclear evolution denoted by the parameter n. n is essentially the ratio of He to H produced by hydrogen burning. Figure 7.2 gives the radii (a)

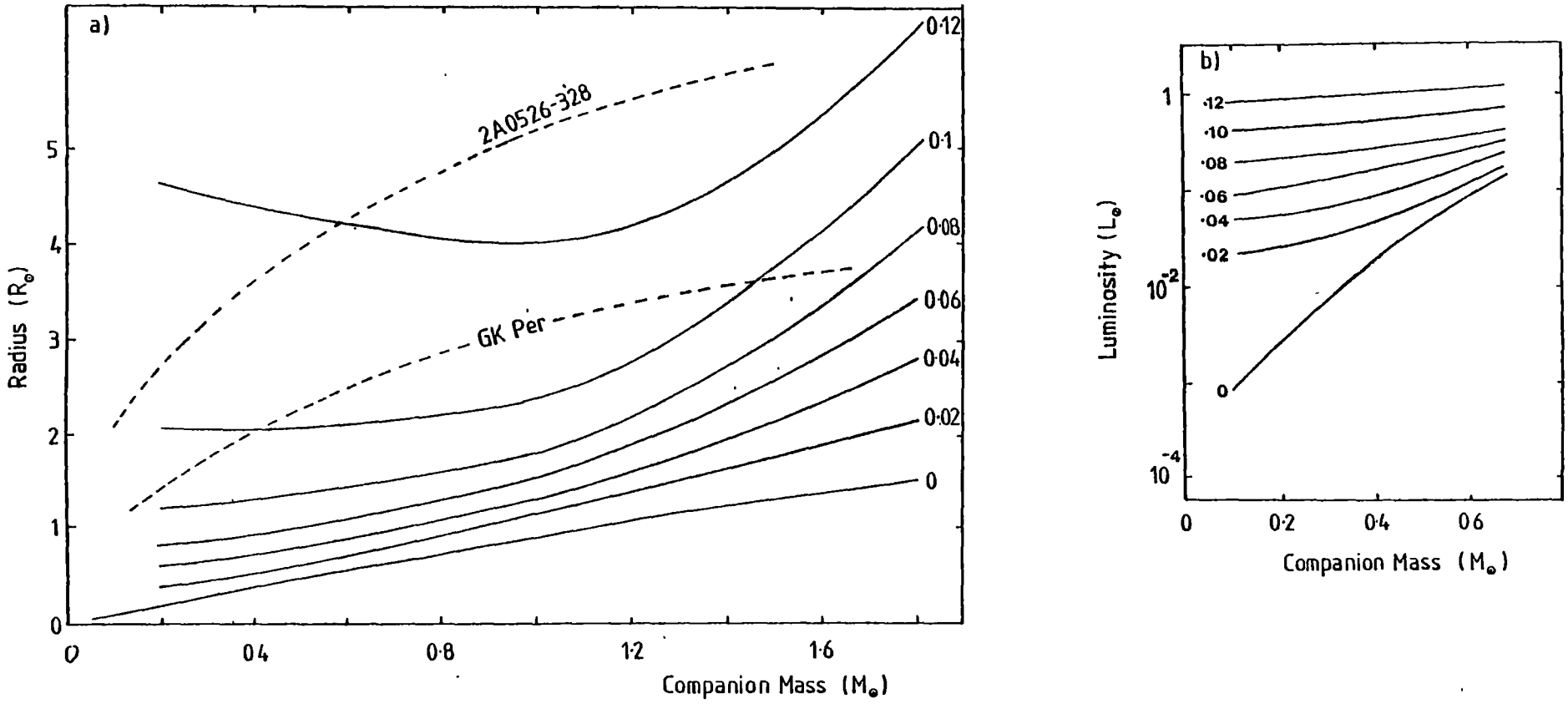

Figure 7.2 Radius (a) amd Luminosity (b) for various degrees of nuclear evolution (0 to 0.12) as a function of companion mass. For ZAMS stars, n=0. The dashed lines are the Roche lobes for 2A0526-328 and GK Per, assuming a white dwarf mass of 1 $M_\odot$.

and luminosity (b) of evolved ZAMS stars from those equations for various n. n = 0 is ZAMS star. Also plotted is the Roche lobe radius for a 4.024^{d} orbit assuming a 1 $M_{\odot}$ white dwarf and for comparison, the line for GK Per. A more complete description of the nature of secondaries possible is outlined in section 7.1.7 where the equations for the Roche lobe are presented. We restrict the following discussion to q = 0.2.

For a companion mass M_R = 0.2 $M_{\odot}$, the variation of n from 0.08 to 0.12 allows the radius of the star to vary from 1.2 to ~4 $R_{\odot}$, whilst the luminosity L_R varies from 0.2 to 0.9 $L_{\odot}$. The luminosity L_R, for a given $n \geq 0.08$, is remarkably insensitive to the mass and, by adopting $n \simeq 0.1$, a lower limit to the distance can be set by estimating an upper limit on the spectral contribution of the companion. We estimate an upper limit of ~15% contribution to the spectra of the 1980 February 10 and 11 observations yielding m_b (companion) $\geq$ 15.8. For n = 0.1, $L_R \sim 0.5\ L_{\odot}$ with a stellar radius of 2.8 $R_{\odot}$ yields an effective temperature of 3000 K and a bolometric correction of ~2.7 (Allen, 1973). The lower limit to the distance is then ~300 pc. The distance must be less than ~1 kpc since the interstellar extinction from the 2200 Å absorption feature in the UV spectrum is low ($A_V \simeq 0.2$, $E(B-V) \simeq 0.06$) (Mouchet, 1982).

Assuming a mean local density of 0.6 atoms cm^{-3}, the distance is ~240 pc. This is subject to considerable error since Klare et al. (1982) comment that the open cluster NGC752 has an interstellar extinction of E(B-V) = 0.03 yet its distance is 380 pc. 2A0526-328 could be ~800 pc distant from its observed reddening.

7.1.1 Estimates of B and $\dot{M}$

The lack of observed eclipses by Motch (1981) and by us leads to an upper limit for the inclination angle. For a companion mass of 0.2 $M_{\odot}$ (and $R \sim 2.8\ R_{\odot}$) $i \leq 70^{\circ}$. Using the K velocity of the emission region and the rotation of the white dwarf, we estimate the orbit radius of

the emission line region to be ~0.42/sin i $R_\odot$. If we associate this radius with the region where the angular velocity of the plasma is reduced from the Keplerian value to the corotational value by the magnetic field then this radius r_0 is

$$r_0 = 3.7 \times 10^{-4} B_6^{\frac{4}{7}} \left(\frac{R_*}{10^9}\right)^{\frac{12}{7}} \left(\frac{M_*}{M_\odot}\right)^{-\frac{1}{7}} \dot{M}^{-\frac{2}{7}} R_\odot \qquad (7.1)$$

where B_6 is the magnetic field in units of 10^6 gauss, R_* is the radius of the white dwarf, M_* its mass, and $\dot{M}$ is the accretion rate in $M_\odot$ yr^{-1} (Fabbiano et al., 1981 and references therein). For a white dwarf of 1 $M_\odot$, $R_* = 5 \times 10^8$cm, and we have

$$B_6 = 1.7 \times 10^6 \sin i^{-7/4} \dot{M}^{\frac{1}{2}} \qquad (7.2)$$

For $i \leq 70^\circ$, and an upper limit of ~10^7 gauss from Tapia's 0.5% linear and circular polarization measurements (see Charles et al., 1979) we obtain $\dot{M} < 10^{-11} M_\odot$ yr^{-1}. This is consistent with the results of Whyte and Eggleton (1980) who estimate $\dot{M} < 5 \times 10^{-11} M_\odot$ yr^{-1} for cataclysmic variables at the end of nuclear-dominated evolution. An accretion rate of $10^{-11} M_\odot$ yr^{-1} has been suggested for the low state of SS Cyg (Fabbiano et al., 1981) and if we adopt this as a lower limit for accretion rates, a field of ~6×10^6 gauss is required. This is comparable to the field estimate for SS Cyg of ~2×10^6 gauss (Fabbiano et al., 1981) where linear polarization from 0 to 0.4% has been seen (Szkody et al., 1980).

Another estimate of B is obtained from the condition that the accretion flow be sub-Alfvénic. If the flow exceeds the Alfvén velocity it becomes unstable. From Tuohy et al. (1981), the radius R_A above which the flow is super-Alfvénic is

$$R_A = 5.2 \left(\frac{f}{10^{-2}}\right)^{\frac{2}{5}} \left(\frac{M_*}{M_\odot}\right)^{\frac{1}{5}} \left(\frac{R_*}{10^9}\right)^{\frac{8}{5}} B_6^{\frac{4}{5}} \left(\frac{L}{10^{34}}\right)^{-\frac{2}{5}} R_\odot \qquad (7.3)$$

where L is the luminosity in erg sec^{-1} and f the fractional area of the white dwarf that the accreting matter is falling upon. Setting $R_A = 0.5\ R_\odot$ and assuming a 1 $M_\odot$ white dwarf, we have

$$(L/f)^{-\frac{2}{5}} B_6^{\frac{4}{5}} = 1.52 \times 10^{-14}$$

R_A should in fact be greater than $0.5\ R_\odot$ to disrupt material from Keplerian flow to radial inflow and form the line emission region so, we have

$$B_6 \geq 5.3 \times 10^{-18} (L/f)^{\frac{1}{2}}$$

In the discussion on the X-ray data in Section 7.1.3 we have the condition $B_6 \geq 2.4 \times 10^{-14} (L/f)^{\frac{2}{5}}$ for cyclotron dominated emission from the accretion column. If this condition is not met, the soft X-ray flux would exceed the hard X-ray flux, (e.g., Imamura and Durisen, 1982) contrary to observations. Both conditions are essentially the same for fields between 10^5 and 10^7 gauss.

A second characteristic radius is the corotation radius where the velocity of corotation is equal to the Keplerian velocity. For a period of 5.4864^h, the corotation radius R_C is

$$R_C = 1.56\ M_*^{\frac{1}{3}}\ R_\odot \qquad (7.4)$$

If $R_A \simeq R_C$ then $i \simeq 16^\circ$. If $i > 16^\circ$ then $R_C > R_A$ and material is trapped by the field and can accrete. In H2252-035 and V1223 Sgr, the corotation radius is considerably larger than the inner radius of the accretion disc estimated from the steady state disc models (Mouchet, 1982).

It is therefore possible to obtain magnetic field strengths that are consistent with the lack of optical polarization, provided $\dot{M}$ is low ($\sim 10^{-11} M_\odot\ yr^{-1}$). Observations of polarization at infrared wavelengths could test the value of B.

7.1.2 Line Splitting

Line splitting was observed during 1979 February 21 (Figure 6.3) and on a few occasions with the 1980 February 10 data.

Several possible mechanisms giving rise to time-dependent line splitting are discussed below.

(a) Accretion Disc

If the source of optical emission is an accretion disc, then one observes a double line (Huang, 1972) modulated at the orbital period. Superimposed on this may be a line originating from the accretion disc hot spot. The combination of the three might produce one large unresolved line with a radial velocity of the total emission region surrounding the condensed object. Perhaps twice during the orbit, eclipses of the hot spot, first by the condensed object and then by the companion, would remove the hot spot line to produce the observed double line. This double line would be expected when the radial velocity was near zero, contrary to observations. More significantly, this model fails to explain the modulation of the width and intensity of the lines. (Figure 6.4d). The 1980 February data did not show any correlation between phase and the width of the lines.

(b) Accretion Columns

For two accretion columns to be resolved, then the direction of accretion must be in the line of sight. Every rotation will provide two opportunities for the columns to be observed. This model provides a natural explanation for the FWHM modulation (Figure 6.4d) and for the two periods of line splitting occurring with a separation of approximately half the expected rotation period of 5.5^{h}. Observations of the AM Her object CW1103+254 (Bailey et al., 1982) show the existence of two accretion columns with velocity separations of ~600 km sec^{-1}. In 2A0526-328, the velocity difference between the two peaks is ~350 km sec^{-1} suggesting radial velocities in the accretion column of ~200 km sec^{-1}.

For i ~ 30°, this represents typical infall velocities onto a 1 $M_\odot$ white dwarf.

(c) Absorption by Cold Gas

A model has been constructed for the 0.51^d binary V Sge in which the H absorption reversals seen for 90% of its orbit are due to cold foreground gas that has been ejected by one of the components of the system (Herbig et al., 1965).

It is possible that line splitting in our data was caused by absorption in such a gas cloud. The period 1979 February 21 1044-1212 UT when no splitting was observed would correspond to that portion of the orbit for which the cold gas was not obscuring the emission region. This model gives a simple explanation for the narrowness of the dip at the central wavelength of the emission lines. It does not explain the modulation of the line width.

(d) Zeeman Splitting

If the line splitting is due to the Zeeman effect, the field strength is about 3×10^5 gauss. The emission lines originate in the accretion columns and when the line of sight is parallel to the polar field lines, that is, about 1979 February 21, 1020 and 1240 UT (Figure 6.3), Zeeman splitting is observed. One quarter of an orbital period later at about 1130 UT the line of sight is perpendicular to the field lines and the Zeeman triplet is observed. This is not resolved in our observations and, since the central component is twice as strong as the wing lines, appears narrower than when the line of sight is parallel to the field. While this model is in qualitative agreement with our observations, modelling indicates difficulties in explaining the narrowness of the dip at the central wavelength of the emission lines and in the rather rapid transition from narrow single lines to broader split lines.

Of the 4 models discussed, the accretion column model explains the data adequately but we cannot exclude the others.

7.1.3 X-Ray

7.1.3.1 X-ray Spectrum

The temperature (19.7 ± 8.8 keV) of the thermal bremsstrahlung spectrum of 2A0526-328 is comparable with values for AM Her of 18 keV (Staubert et al., 1978), SS Cyg of ~20 keV (Fabbiano et al., 1981), U Gem of 5 ± 3 keV (Swank et al., 1978), EX Hydrae of 4.5 keV (Córdova and Riegler, 1979), 4U1849-31 of ≥8 keV (Steiner et al., 1981), 1E0643.0-1648 of ~10 keV (Chlebowski et al., 1981), H2252-035 of ≥8 keV (Patterson and Garcia, 1980), and 2A0311-227 of 18 keV (White, 1981). The hardness ratio for the ~20 cataclysmic variables observed by Córdova et al. (1981a) and Becker (1981) suggest that hard spectra (kT > 10 keV) are common. It is remarkable that the temperature of the hard X-ray emission is the same for most of these systems even though there is thought to be an order of magnitude difference between the magnetic fields of the polars and the SS Cyg class of X-ray emitting cataclysmics and the DQ Her class. The large X-ray cut-off for 2A0526-328 of 3.5 ± 0.2 keV implies a hydrogen column density of $1.2 \times 10^{22} cm^{-2}$, which if interstellar in origin implies a distance ≈1 kpc. It is more likely that a significant proportion is circumstellar, possibly due to accreting material around the X-ray source. Alternatively, the high column density may be an artifact of characterising a complex spectrum with a simple model.

The most probable means of producing hard (>2 keV) X-rays is the model of radial inflow by Fabian et al. (1976). The magnetic field of the white dwarf is able to disrupt the inner region of the accretion disc or ring, leading to radial inflow along the field lines onto the white dwarf surface. A stand-off shock is formed above the poles, heating the accreting gas to X-ray temperatures (~60 keV). Magnetic fields $\geq 10^5$ gauss are considered necessary for the production of X-rays via this mechanism, although if the field is too high for a given accretion rate,

the shocked material cools by self-absorbed cyclotron radiation rather than bremsstrahlung, and no X-rays are produced. Similarly, if the accretion rate is too high, the hard X-rays will be degraded by Compton scattering to soft X-rays. The model allows a maximum accretion rate of $\sim 3 \times 10^{-8}$ $M_\odot$ yr^{-1}, which is slightly dependent on the magnetic field strength of the white dwarf. The estimated accretion rate and field strength allow for hard X-ray emission from 2A0526-328.

The electron density of the X-ray emission region can be estimated from the emissivity for thermal bremsstrahlung which is

$$\frac{dP_B}{dVd\nu} = 6.8 \times 10^{-38} T^{-\frac{1}{2}} e^{-E/kT} N_e N_Z Z^2 g_B(T,E) \text{erg cm}^{-3}\text{sec}^{-1}\text{Hz}^{-1} \qquad (7.5)$$

where Z is the atomic number of the ion species, N_Z the ion number density, N_e the electron density, T the temperature and $g_B(T,E)$ the gaunt factor. For $E \sim kT$, $g_B(T,E) \simeq (E/kT)^{-0.4}$. Using the observed values of kT = 20 keV, the luminosity and assuming a hydrogen plasma, the emission measure is

$$N_e^2 V \simeq 3.3 \times 10^{54} \left(\frac{D}{100}\right)^2 \text{cm}^{-3} \qquad (7.6)$$

where D is the distance in parsecs. For comparison the emission measure for AM Her as estimated from its X-ray flux (Tuohy et al., 1978) is an order of magnitude larger. Since the X-ray region is contained in a volume with diameter ≤ 0.5 $R_\odot$, we require $n_e > 10^{12}\text{cm}^{-3}$. Wada et al. (1980) have made numerical calculations of the cyclotron (optical) and free-free (X-ray) emission of accretion columns for various magnetic field strengths (B) and accretion rates ($\dot{M}$). They have used a white dwarf mass of 1 $M_\odot$ and radius 1×10^9cm, but the results are not strongly dependent on the white dwarf parameters. For $B = 6 \times 10^6$ gauss and $\dot{M} = 5 \times 10^{-11} M_\odot\ yr^{-1}$ (Wada et al., Case I), the model predicts $L_x = 1.5 \times 10^{32}$erg sec^{-1} and $L_{opt} = 8 \times 10^{31}$ erg sec^{-1}. If $\dot{M}$ is

increased to 2 x $10^{-10} M_\odot$ yr^{-1} (Case II) then L_x = 4 x 10^{32} erg sec^{-1} and L_{opt} = 6 x 10^{31}erg sec. Between these two accretion rates, it is possible to obtain luminosities consistent with the observed fluxes. The source of unpolarized optical emission possibly arises from the blackbody emission from the X-ray heated white dwarf surface. Imamura and Durisen (1982) and Kylafis and Lamb (1982) have published detailed spectral and X-ray light curves of white dwarfs under a wide variety of conditions, but with B < 6 x 10^6 $(L_f/10^{36}\text{erg/s})^{2/5}$ gauss where L_f = L/f is the effective luminosity. L is the actual luminosity and f the fraction of the white dwarf onto which the matter accretes. In this regime bremsstrahlung cooling is more important than cyclotron cooling. Wada et al. (1980) only considered B > 6 x 10^6 $(L_f/10^{36}\text{erg/s})^{2/5}$ gauss, or cyclotron dominated cases. Imamura and Durisen (1982) and Kylafis and Lamb (1982) predict a large soft X-ray flux L_s comparable or larger than the hard flux L_h in all cases studied. The source of the soft X-ray flux is blackbody radiation from heating of the white dwarf surface from intercepted bremsstrahlung and cyclotron radiation.

The absence of a dominant far UV/soft X-ray component in the spectrum of 2A0526-328 is more compatible with cyclotron dominated models (e.g. Lamb and Masters, 1979; Kylafis and Lamb, 1979). For 2A0526-328, L_s/L_h = 0.5 implying that B ≥ 6 x 10^6 $(L_f/10^{36}\text{erg/s})^{2/5}$ gauss. For B ≤ 6 x 10^6 gauss, $L_f \leq 10^{36}$erg sec^{-1}. With $L_h + L_s = 1.5 \times 10^{32}(D/100)$ erg sec^{-1}, $f \geq 1.5 \times 10^{-4}(D/100)^2$, indicating that a sizable portion of the white dwarf surface is undergoing accretion. Estimates of f for AM Her are comparable and range from 9 x 10^{-4} to 9 x 10^{-2} (Tuohy et al., 1981). It should be noted that the nature of the soft X-ray components in cataclysmic variables upon which these conclusions rest are not fully understood. X-ray observations of AM Her whilst in an optical low state suggest that the soft X-ray flux is not from reprocessed bremsstrahlung (Fabbiano, 1982) nor do nuclear burning models adequately explain the data. (Kylafis and Lamb, 1982).

7.1.3.2 X-ray Heating

We believe X-ray heating of the companion and/or the accreting matter between the two stars gives rise to the photometric maxima. From the observed hard X-ray flux $L_x = 1.2 \times 10^{32}(D/100)$ erg sec^{-1}, the separation $a = 10.1\ R_\odot$ and the radius of the companion $R = 2.8\ R_\odot$, we estimate the expected optical flux L_{opt} from the heated photosphere of the companion using the equation (Margon et al., 1977).

$$L_{opt} = \frac{1}{4} \rho_x \left(\frac{R}{a}\right)^2 L_x \frac{2}{3\pi}(\sin \alpha + (\pi-\alpha)\cos \alpha) \qquad (7.7)$$

where ρ_x is the X-ray pulsed fraction and α the angle between the X-ray source, the companion and the observer. Inserting the above results and letting $\alpha = 0$, we have

$$L_{opt} = 2 \times 10^{30}(D/100)^2 \rho_x \text{ erg sec}^{-1} .$$

The observed optical modulation is 0.27 mag (Motch, 1981) or $\sim 1.8 \times 10^{31}(D/100)^2$ erg sec^{-1}. This is a factor 9 too high, but the estimates of X-ray flux are from different epochs from the photometric results. The difference can be reduced by a factor of 3 by using the Ariel V flux estimate. If there is any anisotropy of the X-rays, the difference can be reduced further, or if a portion of the reprocessed light is from the accreting matter. A similar problem exists for the HCCTC model.

Motch (1981) ruled out X-ray heating of the secondary because the system reddened as it brightened instead of becoming blue like, for example, 4U2129+47 (Thorstensen et al., 1979). It is possible, however, that X-ray heating may lead to reddening if the companion is relatively cool (M5 or later) and makes only a minor contribution to the optical luminosity at minimum light. A rise in the companion's temperature of 1.2 to 1.5 times gives rise to a change in the system's B and V magnitude of -0.3 and -0.4 respectively, or B-V from 0.1 to 0.2. This small change in B-V could be easily masked by the 0.1 mag colour fluctuations

seen by Motch (1981). There will be little change in U magnitude, so the observed change in U-B could be due to heated material between the two stars. Furthermore, the only known optical modulation amplitudes are at U,B and V which covers a relatively narrow spectral band. UV modulation has been detected in the 5.48^{h} spectroscopic period but none at the other periods (Mouchet, 1982). Figure 7.3 is the spectrum of the pulsation fluxes of 2A0526-328. For comparison the line of best fit of the 794 sec pulsation spectrum in V1223 Sgr (Figure 6.23) is shown. It is displaced downward by a factor of 10 in order not to confuse the 2A0526-328 data. It can be seen that the results from 2A0526-328 are not inconsistent with the data from other intermediate polars. Obviously observations at R and I and the infrared are necessary. Finally it should be noted that reprocessing effects are not simple as shown in observations

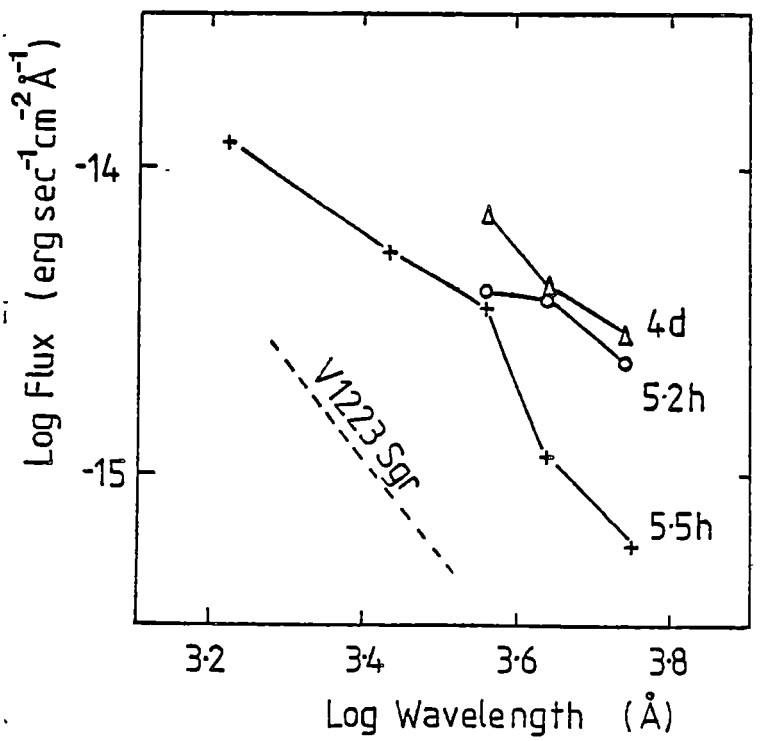

Figure 7.3 Pulsation fluxes of 2A0526-328. UV data from Mouchet (1982) and optical from Motch (1981). Dashed line is the optical 794 sec pulsation flux from V1223 Sgr for comparision and displaced down by a factor of 10 for clarity.

of AM Her. Photometry of AM Her when it was in a bright state by Szkody and Brownlee (1977) showed that it became bluer on brightening whilst observations by Priedhorsky and Krzeminski (1978) showed the converse when the system was about 0.7 mag fainter. In a system where little or no disc is expected to exist, as in the 4^d model of 2A0526-328, it is not valid to equate brightening with heating from the companion alone. A combination of heating from accreting matter and the companion is more probable. Only when the disc thickness exceeds ~20% of its outer radius will the companion be obscured by the disc, from the source of the X-ray flux near the white dwarf.

7.1.3.3 X-ray Variability

Variability on a timescale of ~700 seconds has been observed in the 1.1-21.0 keV X-ray band with a modulation of ~50% (Figure 6.13). This corresponds to flux variations of $7 \times 10^{30}(D/100)^2$erg sec^{-1}, which can be compared with the optical flickering of 0.15 mag in B or $\sim 5 \times 10^{30}(D/100)^2$erg sec^{-1} if the flickering occurs equally strongly at all optical wavelengths. Patterson, Williams and Hiltner (1981) observed quasi periodic pulsations (QPO) of ~360 second in X-ray from 2A0311-227 and noted similar behaviour in all other published photometry. They outlined five possible sources: (1) pulsations of the white dwarf, (2) pulsations of the companion, (3) pulsations of the accretion disc, (4) instability in the accretion column, and (5) a relaxation oscillation in the accretion rate. Source (1) is unlikely due to the low coherence seen in 2A0311-227. Observations of U Gem indicate that QPO do not originate in the companion or mass transfer stream excluding source (2). It is difficult to understand how instabilities in the accretion column (4) could be quasi-periodic. Pulsations of the accretion disc (3) is the most natural explanation for QPO seen in dwarf novae during outburst. However to produce oscillations of the order of minutes requires a source

at large disc radii and therefore not related to the X-ray pulsations. Source (5) is the most promising candidate. Matter not fully ionised in the accretion column absorbs soft X-rays and is prevented from accreting. The X-ray flux will then turn on and off on a time-scale of the free-fall time from the accretion disc. In the case of 2A0526-328, the hardness ratio and luminosity of the X-ray flux is anti-correlated suggesting absorption at X-ray turn on from accreting material. As the accreting material is forced away, the spectrum is fainter from the lower accretion rate but harder. A freefall time of 700 sec onto a 1 $M_{\odot}$ white dwarf corresponds to a height of 2.9 x 10^{10}cm (0.41 $R_{\odot}$). The centripetal acceleration, due to corotation, is negligible compared to the gravitational acceleration below a height of ~7 x 10^{10}cm. It is perhaps significant that the freefall height is very similar to the emission line region height.

7.1.4 UV Spectrum

The P Cygni profiles in the UV spectrum reported by Coe and Wickramasinghe (1981) indicate the existence of a stellar wind. The spectroscopic phase of this observation was 0.54-0.81, and the 4-day photometric phase 0.09-0.11 (HCCTC). Córdova and Mason (1982) found P Cygni profiles from the dwarf nova TW Vir during an optical outburst. Comparison with other cataclysmic variables suggests P Cygni profiles are seen from systems of relatively high luminosities (>10 $L_{\odot}$) and low inclination angles, and deduce that the high velocity wind emanates from above and below the accretion disc. The wind is accelerated to escape velocity via radiation pressure. P Cygni profiles are not seen in the UV spectrum of AM Her (Tanzi et al., 1980) which suggests that the dim accretion disc is not sufficiently luminous to radiatively accelerate the stellar wind since the accretion disc is dim. Hence in the 4-day orbital model the stellar wind may be emanating from the Lagrangian point L3 since the 4-day photometric maximum (ϕ = 0.0) should

occur when the white dwarf is near inferior conjuction. In the HCCTC model, the source of the P Cygni profiles is the accretion disc. The detection of P Cygni profiles will be phase-independent for the HCCTC model and possibly modulated at the orbital period for the 4-day model if the emission from L3 is correct.

7.1.5 UV and Optical Continuum

The optical continuum of 2A0526-328 follows roughly $F_\nu \alpha \nu^{0.4}$, which is consistent with a spectrum from an optically thick accretion disc (Pringle and Rees, 1972). This conclusion is supported by IUE observations by Coe and Wickramasinghe (1981) which show $F_\nu \alpha \nu^{0.3}$ in the UV. A blackbody fit to the UV continuum yields a temperature of 2.3×10^4K making it comparable with the disc systems SS Cyg and EX Hya. However, fitting the UV data with the standard optically thick disc model (see Bath et al., 1980) by Mouchet (1982) yielded unacceptably high accretion rates and disc luminosities. A distance of 3.5 kpc is inferred from the fit which is an order of magnitude too large.

Our model proposes the source of the continuum is the accretion columns as in the AM Her types. These sources show a great diversity in the UV spectral shape. For example, the UV spectrum of AM Her during the X-ray eclipse is $F_\nu \alpha \nu^{-1}$ whilst at X-ray maximum it is $F_\nu \alpha \nu^{2.1}$ (Raymond et al., 1979). Jameson et al. (1982) discuss UV observations of the nova-like object TT Ari and reject the hot spot model for the source of the continuum because the optical, UV and X-radiation all vary in the same manner. They suggest a similar model to HCCTC's and suggest that the dominant optical UV flux is from an accretion column with a blackbody temperature of ~3×10^5K. The continua in both TT Ari and 2A0526-328 are remarkably similar. In the long wavelength UV, the spectral index α (from $F_\nu \alpha \nu^\alpha$) is 0.81 and 0.51 for TT Ari and 2A0526-328 respectively, whilst in the optical both objects can be fitted with $\alpha = 0.3$. Jameson et al. (1982) suggests the source of the UV and optical

to be the base of the accretion column in TT Ari and similar behaviour may exist in 2A0526-328.

Since the magnetic fields are expected to be smaller than in the AM Her types, circular polarization is expected to peak in the IR. A sensitive observation would be required since the polarized flux will be heavily diluted by unpolarized radiation from the companion and ring. In the 4-day model the polarization should be modulated at the spectroscopic period of 5.48^h whilst the HCCTC model predicts modulation at the photometric period of 5.19^h.

7.1.6 Disc Emission

The effective temperature of a steady state accretion disc at a distance R from the white dwarf is (Bath et al., 1980)

$$T_e(R) = \frac{3GM_*\dot{M}}{8\pi\sigma R^3}\left(1 - \sqrt{\frac{R_{IN}}{R}}\right)^{\frac{1}{4}} \qquad (7.8)$$

where R_{IN} is the inner radius of the disc, M_* the white dwarf mass and $\dot{M}$ the accretion rate. In solar units

$$T_e(R) = 4.1 \times 10^5 \frac{\dot{M}M_*}{R^3}\left(1 - \sqrt{\frac{R_{IN}}{R}}\right)^{\frac{1}{4}}$$

The disc luminosity L_D is

$$L_D = \tfrac{1}{2} GM\dot{M}/R_{IN} \qquad (7.9)$$

If the inclination angle of 2A0526-328 is $<70^\circ$ (from the condition that no eclipses occur) the line emission region defines the smallest R and $R_{IN} < R$ then $R \geq 0.45\ R_\odot$. This implies an effective temperature of

$$T_* \leq 7.3 \times 10^5\ \dot{M}^{\frac{1}{4}}$$

Varying $\dot{M}$ from 10^{-8} to $10^{-11} M_\odot yr^{-1}$, varies T_* from 10^4K to 1600K. At the expected low accretion rates ($<10^{-10} M_\odot yr^{-1}$), the disc spectrum peaks at ~12,000 Å, which corresponds to the IR J band. The corresponding luminosity from equation 7.9 is $L_D \approx 1.4 \times 10^{31}$ erg sec^{-1} or $\sim 20 \left(\frac{100}{D}\right)^2$ %

of the observed optical flux. At distances in excess of ~150 pc the IR flux is dominated by the secondary with a luminosity of ~1 $L_\odot$ (see section 7.1) and not by the accretion disc.

7.1.7 The Secondary

From the method of Bailey (1981), an estimate of the K magnitude of the secondary can be made. The input parameters of the method are the distance D, the Roche Lobe radius R_L and the V-K colour of the secondary. The surface brightness parameter S_K is a measure of the K unit area brightness of a star and for stellar types later than ones for which V-K ≈ 0, depends only on V-K and not on the luminosity class. The values of S_K from Bailey (1981) are

$$\begin{aligned} S_K &= 2.56 + 0.508\ (V-K) \quad V-K < 3.5 \\ &= 4.26 + 0.058\ (V-K) \quad 3.5 < V-K < 6.5 \end{aligned} \tag{7.10}$$

and

$$K = S_K - 5 + 5 \log D - 5 \log R_L \ . \tag{7.11}$$

Since V-K is unknown, a free variable X was defined to be the % contribution at B of the secondary to the total flux observed. A program was written to determine the range of the secondary K magnitude that could be expected from both the 4 day orbit model and HCCTC's model.

Let M_R and M_* be the companion and white dwarf masses respectively then the mass ratio is $q = M_R/M_*$. The Roche Lobe R_L is

$$\begin{aligned} R_L/a &= (0.38 + 0.20 \log q) \quad 0.5 < q < 20 \\ &= 0.46\{q/(1+q)\}^{1/3} \quad 0 < q < 0.5 \end{aligned} \tag{7.12}$$

where $a^3(R_\odot) = 0.1213\ \frac{M_R+M_*}{M_\odot}\ P^2(hr)$ is the cube of the orbital separation. For particular values of q, a value of the nuclear evolution parameter n can be calculated by equating R_L to the radius of the evolved companion using the equations of Whyte and Eggleton (1980) and hence a corresponding secondary luminosity L_R. From the blackbody equation $L_R = 4\pi R_L^2 \sigma T_e^4$ where σ is the Stefan Boltzmann constant, an effective secondary temperature T_e

is derived. By using the tables of Allen (1973) and Johnston (1966), a corresponding balometric correction BC and colour V-K is estimated. From the known B magnitude and estimated secondary contribution X, the distance is derived. The secondary magnitude follows from equations 7.10 and 7.11.

Figure 7.4 gives K magnitudes for various values of q, M_* and X for both models. (a) for the 4 day orbit model and (b) for HCCTC's model. (Also marked on each curve are the distances in units of 100 pc.) The range of K magnitude for the 4 day orbital model is from ~10.5 to 13 whilst for HCCTC's model, it is from ~12.5 to 15.5. In the 4 day model, as q decreases from 0.2 to 0.05, the K magnitude increases by ~1.2 mag. In this regime, nuclear evolution is important. For low q, R_L and M_R are smaller and a hotter smaller companion is required. Consequently V-K is smaller implying fainter K emission from the companion. In HCCTC's model, as q increases from 0.4 to 0.8, the K magnitude increases by ~2.5 mag. The reason is that at large q (>0.4) n = 0 and T_e > 4000K and the secondary spectrum peaks in the optical. The secondary is required to be faint and hence the K emission is small. As q increases, T_e increases and the K magnitude must increase. Below $q < 0.3$, $n \neq 0$ and the K magnitude must increase as outlined in the 4 day model.

The distance estimates marked on Figure 7.4 for the 4 day model are larger than for the HCCTC model. For a source distance of 500 pc, the 4 day model requires $X \geq 0.1$ for q between 0.05 and 0.2. The HCCTC model is not as severely constrained only requiring $q \leq 0.6$.

The 4 day model predicts the dominant IR flux to be from the secondary since it is expected that disc emission is faint. The IR flux from the HCCTC model is expected to be dominated by the disc and the flux at K from the system should be considerably more than the predictions of Figure 7.4(b). It is feasible for the K emission of the disc in HCCTC's model to be comparable to the K flux predicted for the 4 day model, and

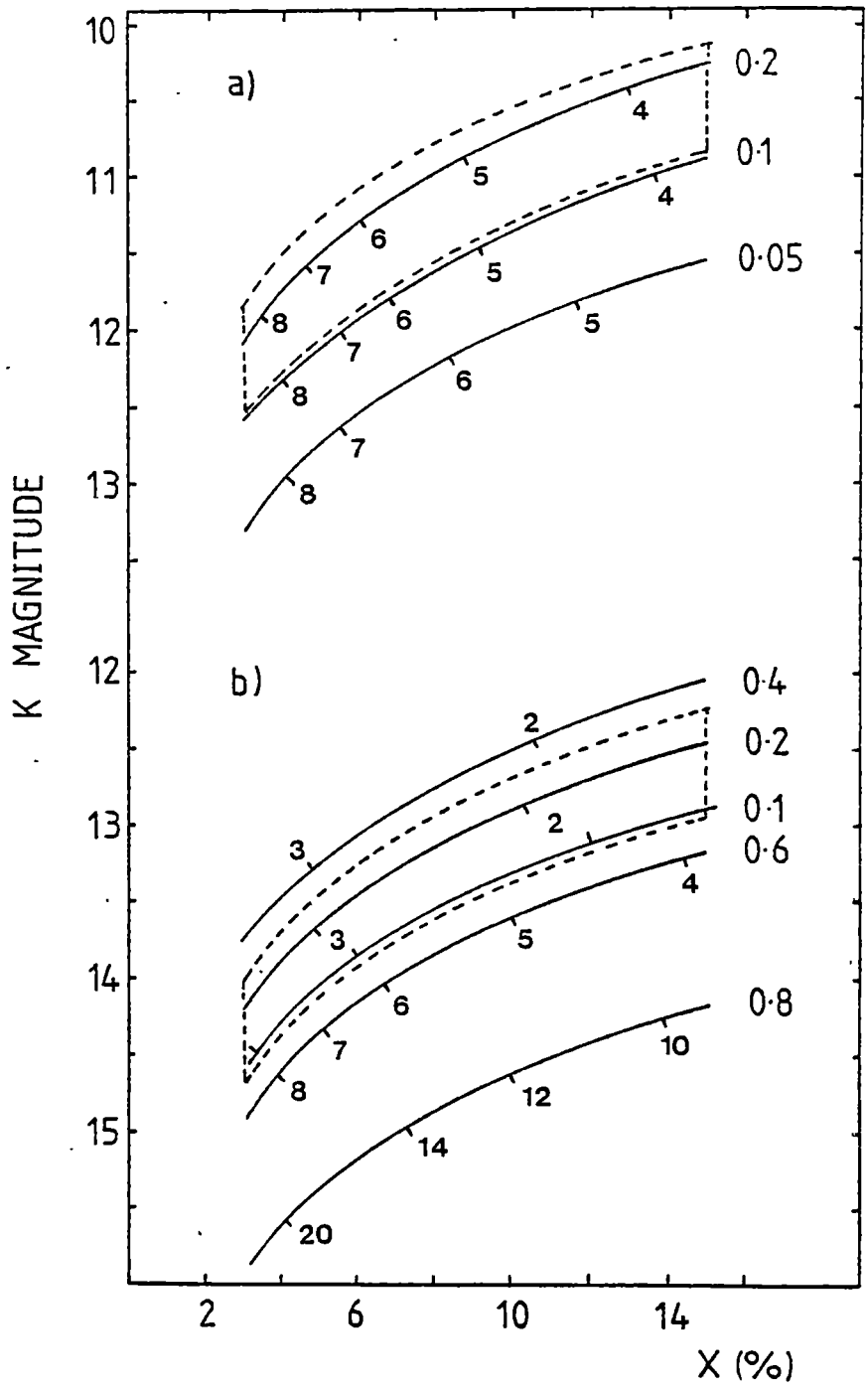

Figure 7.4 Estimated K magnitudes for both models (a) 4^d orbital and (b) HCCTC with varying secondary B contribution X. Solid lines are for $M_* = 1\ M_\odot$ and varying q as indicated on right of each line. The dashed lines are for q=0.2 and are for $M_* = 1.4\ M_\odot$ (upper line) and $M_* = 0.5\ M_\odot$ (lower line). Also marked on each curve is the distance in units of 100 pc.

light curve analysis may be the only way to test either model.

It is possible to estimate the modulation of the secondary K flux from the heating modulation observed at B. No infrared measurements of 2A0526-328 have been reported in the literature so the true modulation at K is not yet known. Since the contribution of the secondary to the heating is not known, it is left as a free parameter C where C is the fractional contribution of the secondary to the heating of the system at the photometric bandpass B. The estimated variation in K magnitude is shown in Figure 7.5 for C = 100%. The modulation at K from heating effects for C < 100% is less and Figure 7.5 represents the maximum value expected. Until the observed variation is known, all that may be said is for observed variations greater than 0.6 mag, the HCCTC model (Figure 7.5b) seems valid for X ≤ 6% and q ~ 0.2 to 0.6 whilst in the 4 day model (Figure 7.5a) only for q ≤ 0.05 do we predict a large K variation. The assumption we have made is that there are no other sources at K modulated with the heating period. For C < 100%, we would require some modulation from other components in the system. The most likely possibility is the accretion disc. It is feasible that the total change in K magnitude due to disc and companion is larger than the values shown in Figure 7.5.

7.1.8 Conclusions

The observations reported in section 6.1 confirm the suggestion of the different photometric and spectroscopic periods reported by HCCTC. We have proposed a model in which a white dwarf with an oblique magnetic axis and a rotation period of 5.48^{h} revolves in a retrograde orbit of 4 days. A problem with this model is the requirement of a retrograde orbit. Angular momentum from the companion would normally ensure the rotation of the white dwarf is in the prograde direction. The evolution of the system would need to be studied to see if a retrograde orbit is possible.

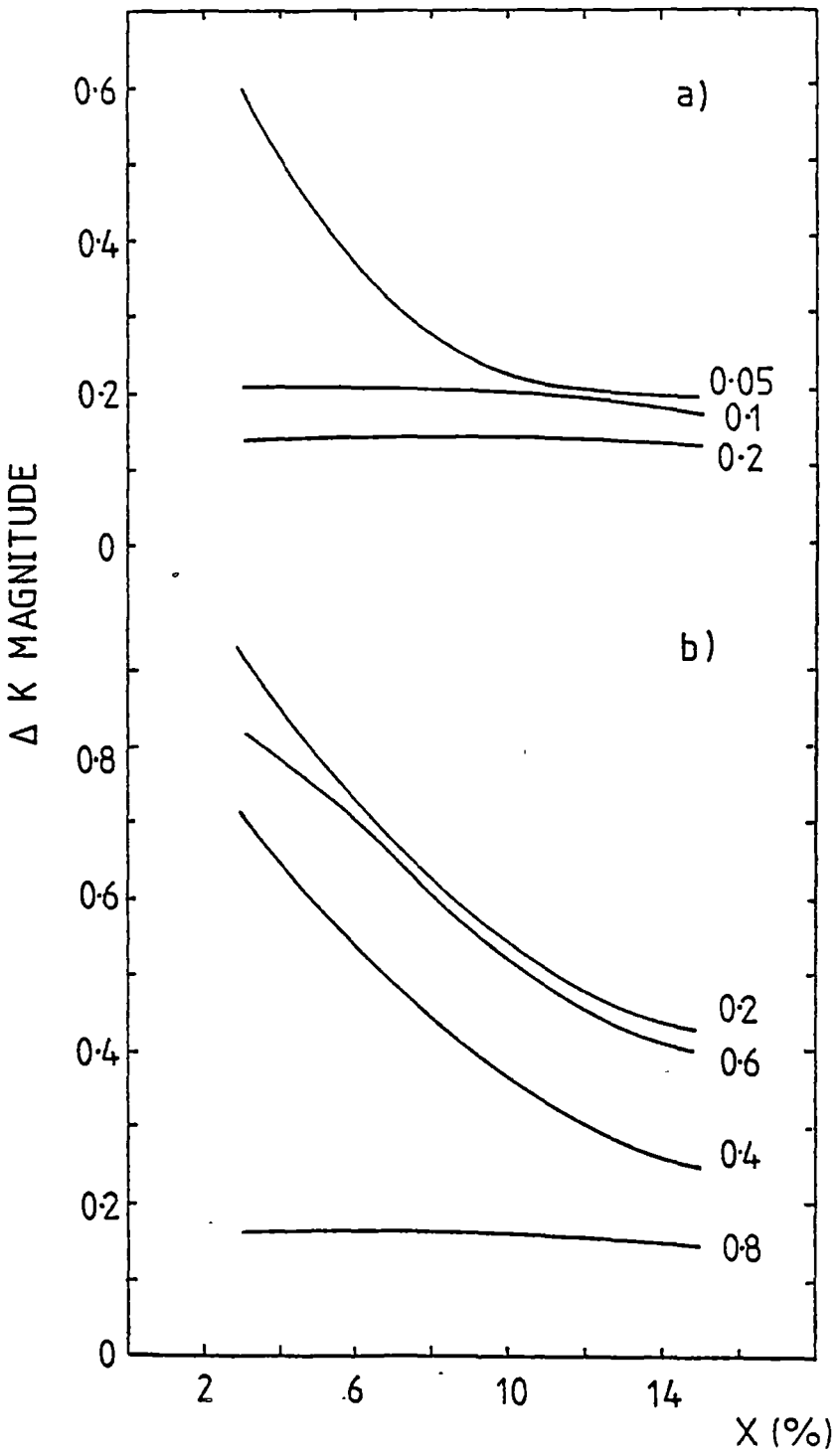

Figure 7.5 Estimated K magnitude variation assuming all the observed modulation at B is due to heating of the secondary. Models are (a) 4^d orbital and (b) HCCTC. X is contribution of the secondary at B. Mass of white dwarf is 1 $M_\odot$ and q is indicated on right of each line.

To ensure Roche lobe overflow and hence power the X-ray emission, the companion must have evolved from the main sequence to become a subluminous giant. The red companion should be readily detectable, between 11 and 13th mag at K and IR photometry and near infrared spectroscopy are needed to distinguish between our model and HCCTC's. Our upper limit on the contribution of the companion at optical wavelengths yields a minimum distance of ~300 pc and the absence of interstellar features in the spectrum gives an upper limit of ~1 kpc.

The X-ray flux is comparable with that of the brightest cataclysmic variables.

The hard X-ray spectrum can be characterised by a temperature kT = 19.7 ± 8.8 keV, very similar to that for AM Her. However, there is no evidence for the strong soft X-ray and far UV component present in the spectrum of AM Her, 2A0311-227, and SS Cyg. If this component is produced by nuclear burning of accreted matter, it is possible that 2A0526-328 is in an extended quiescent period for nuclear burning (Weast et al., 1980). Quasi-periodic flickering on a time scale ~700 sec is observed at both X-ray and optical wavelengths. The X-ray flickering probably originates as part of the accretion process and generates the optical flickering by heating the accretion column. The inverse relationship between the X-ray intensity and the hardness ratio suggests the source of the X-ray flickering is the accretion column. If we equate the 700 sec timescale to the freefall time of material being accreted onto the white dwarf, then the corresponding height above a 1 $M_\odot$ white dwarf is 2.9 x 10^{10} cm; the same height at which the optical emission line source is predicted to be. Observations of correlated variations in both X-ray and optical bands would be required to test this model.

The white dwarf magnetic field is expected to be of the order of 10^6 gauss for accretion rates $<10^{-10} M_\odot\ yr^{-1}$. X-ray and polarization measurements will distinguish our model and that proposed by HCCTC.

The HCCTC model predicts an X-ray and a polarimetric period equal to the 5.19^{h} photometric period, whilst our model predicts it to be equal to the spectroscopic period of 5.48^{h}.

7.2 V1223 Sgr

7.2.1 Source of the optical pulsations

The source of the optical pulsations from V1223 Sgr is not yet established. There are two proposed models of intermediate polars with respect to the source of the optical pulsations.

The first model (Model A) by Patterson and Price (1981) associates the dominant optical pulsations with X-ray heating of the secondary by the rotating white dwarf. Reinterpretation by Hassall et al. (1981) of the H2252-035 data of Patterson and Price (1981) suggest the pulsations arise from the hotspot which is located on the line between the stars. With the aid of further spectroscopic data, Wickramsinghe et al. (1982) argue for a combination of both. The source of the pulsations is the beating between the white dwarf rotation period and the orbital period. In H2252-035, the 805 sec pulsations are seen in X-ray and sometimes in the optical and must correspond to the rotation period of the white dwarf. Since the orbital period is 3.59 hrs, the expected beat period is 859 sec, for a prograde orbit. This is in fact the dominant optical period.

The second model (Model B) is the model proposed for the suspected intermediate polar EX Hya (Warner, 1982). Most of the optical flux is generated in the inner disc and is modulated by the influence of the oblique magnetic axis of the white dwarf at its rotation period. In the case of EX Hya, the 67 min rotation period is seen in the 33.5 min period splitting of the optical emission lines and 67 min modulation of the optical and X-ray light curves whilst the orbital period of 98.3 min is derived from radial velocity measurements and the presence of eclipses. A similar model has been proposed for H2215-086 by Patterson (see Warner, 1982). Both large amplitude 20.9 min and low amplitude 22.9 min optical oscillations are present (Warner, 1982). The large amplitude signal is from direct X-ray heating of the inner regions of the disc (Model B) and the low amplitude signal is from the secondary.

If the large amplitude period is from the secondary (Model A), then a retrograde orbit is required.

Since only two and not three photometric periods are well established in V1223 Sgr, either model A or B may be valid. Extensive photometry at ESO has failed to reveal any beat periods (A.B. Giles, 1982, private communication).

Folding the AAT and Mt. Canopus data at twice the 13.2 min period revealed no significant differences between odd and even pulses suggesting only one visible pole or two equal poles separated in phase by 180°. Searching for other periodic components in the light curves using the method of Lomb (1976) indicated the existence of periods expected from either model. In model A we predict a white dwarf period of 745 sec for a single beam model or 702 sec for a twin pole model. The 745 sec period is marked in Figure 6.21 whilst the 702 sec period is not evident indicating that only one pole is active. However, the two periods are in phase at maximum light and not at minimum light as expected from the Patterson and Price (1981) model.

From model B, equation 6.3 predicts that a beating period of 1828 sec should be present for a twin pole model. This period (and its 2nd harmonic) are present in both the R and J data (Figure 6.21). There is no evidence of the expected period of 850 sec if only one pole is active. The lack of modulation of circular polarization or X-ray flux at any of the proposed periods does not exclude either model.

The disc parameters for V1223 Sgr are similar to those of EX Hya. The steady state accretion disc model satisfactorily fits the UV to IR data of V1223 Sgr (Mouchet, 1982). It requires a disc inner radius $R_1 \sim 5 \times 10^8$cm and an accretion rate $\dot{M} \simeq 5.8 \times 10^{-10} M_{\odot} yr^{-1}$. The parameters for EX Hya are such that $\dot{M} = 1.3 \times 10^{-9} (M_*/M_{\odot})^{-1} (R_1/10^9 cm)^3 M_{\odot} yr^{-1}$ (Bath et al., 1980) and the ratio of outer disc radius R_0 to inner disc radius R_1 is $R_0/R_1 \geq 50$. Since the orbital period of

EX Hya is half the period of V1223 Sgr, then R_1 for EX Hya must be comparable to the radius of the white dwarf to accommodate R_0 inside the Roche Lobe of the white dwarf. This implies $\dot{M} \sim 1.3 \times 10^{-9} M_\odot yr^{-1}$ which is less than for V1223 Sgr. In EX Hya, the disc is thick enough to be the dominant source of the optical pulsations and to block any reprocessing from the secondary. If the disc viscosity is low and $\dot{M}$ high then matter entering the disc at the inner Lagrangian point cannot be transported immediately to the inner regions of the disc. Consequently, the density and pressure must rise in the outer disc and the vertical height of the disc will increase to compensate. If the height to radius ratio of the disc exceeds ~0.2, then the companion is hidden from the white dwarf by the disc. A similar phenomenon is possible for V1223 Sgr on the basis of nearly similar disc parameters. The disc parameters for H2252-035 (Mouchet, 1982) are similar to those for both EX Hya and V1223 Sgr yet the dominant optical pulsations are from the secondary/hot spot suggesting a thin disc. The disc viscosity of H2252-035 must be higher than EX Hya for reasons as yet unknown.

A difficulty with this model is the explanation of the orbital light curve of V1223 Sgr. The optical light curve of EX Hya is dominated by the 67 min white dwarf period with little evidence of the 98 min orbital period, apart from the eclipses (Vogt et al., 1980; Warner and McGraw, 1981). The inclination angle of EX Hya is $\simeq 75^\circ$ and any orbital modulation from the secondary should be apparent if it is heated by UV or X-rays from the disc and white dwarf. In the case of V1223 Sgr, i is small (see section 7.2.3) yet the orbital modulation is ~0.3 mag. If i is not too small, then the companion may eclipse the outer edges of the disc. This would lead to a light curve that is essentially flat when the disc is near inferior conjunction and produce a wide (up to 0.5 phase) sinusoidal dip when the disc is at superior conjunction. A small contribution of heating from the secondary when it is at

superior conjunction may modify the light curve to a sine shape as seen in the R light curve (Figure 6.15).

In any model, there exists the problem of the system being reddest before minimum light (Figure 6.17). If the hot spot is actually located on the leading edge of the accretion disc then the companion can obscure the hot spot before the secondary reaches inferior conjunction. If the hot spot is a major contributor of the optical continuum emission, then it is possible for the system to be reddest before minimum light. Since the changes in magnitude and colour index are smooth and not abrupt then the hot spot must be extended over a large area of the disc and not confined to a small area.

7.2.2 Spectra

7.2.2.1 Continuum

The broad absorption feature near H_δ is unusual (Figure 6.23) and is not seen in any other published spectrum of cataclysmic variables. It is very similar to a P Cygni profile with an outflow velocity of ~800 km sec^{-1}. No other H line had this feature although H_ϵ appeared unusual. Unfortunately, the spectra were only acquired from 3945 Å to 4900 Å and it is impossible to deduce the true shape of the H_ϵ line. It is possible that the feature is not in absorption but that the continuum between 4020 Å and 4080 Å is in emission. However, this is unlikely considering the shape of the continuum between these limits.

7.2.2.2 Radial Velocities

Patterson and Price (1981) suggested the secondary as the source of the emission lines since superior conjunction of the line emitting region measured at the base of the emission line occurs at maximum light. The UV/X-ray flux from the white dwarf/disc heat the secondary to provide the enhanced total continuum. This does not explain the broad nature of the emission lines, which are not to be expected from the atmosphere of a relatively cool late dwarf. Wickramsinghe et al. (1982) find evidence

of a hot spot in H2252-035 and associate the red shifted sharp emission lines with the hot spot and the blue shifted peaks with the white dwarf. A combination of the two produces an emission line that appears to mimic the behaviour seen by Patterson and Price (1981).

As mentioned in section 6.2, blue peaks are seen in V1223 Sgr similar to H2215-086. We do not see the red peaks seen in H2252-035. From the phasing of the velocity components Wickramsinghe et al. (1982) estimate that the hot spot in H2252-035 lies between the secondary and white dwarf on the centres of mass line. If we associate the blue peaks before phase 0.9 and the merged red peaks after orbital phase 0.9 (Figure 6.39) with the hot spot, then the phase of inferior conjunction is ~0.9 indicating that the hot spot lies on the leading edge of the accretion disc or near the centres of mass line but not on the trailing side of the disc. The hot spot is on the trailing edge of the disc in all other cataclysmic variables for which its position has been determined.

The source of the HeII λ4686 emission line is not clear. The peak emission does not follow the behaviour of any other emission peaks. However the moment centre radial velocities are indistinguishable from those of the H lines suggesting a common origin. In DQ Her, Chanan et al. (1978) find the HeII λ4686 arises from the inner edge of the accretion disc due to beaming of UV or X radiation from the white dwarf. A similar phenomenon may be occuring in V1223 Sgr since the disc appears to be thick. Unfortunately, the HeII λ4686 line in EX Hya is broad and too weak (Cowley, Hutchings and Crampton, 1981) to test this hypothesis. Studies of other cataclysmic variables, however, indicate that the hot spot is the source of HeII λ4686 and Wickramsinghe et al. (1982) find the hot spot is the most likely source in H2252-035. If the emission peaks of HeII λ4686 are indeed from a hot spot, then inferior conjunction is at phase ~0.9 and a similar problem arises in relation to the location of the hot spot. Another possibility is that the source is the low density

outer skin of the accretion disc. Extreme UV or X-rays from the region near the white dwarf may photoionize the disc and create a chromosphere (Williams and Ferguson, 1982). Since this may occur at larger disc radii than in the DQ Her model, the emission lines will not be double as is seen in Figure 6.36. The data tend to support the chromosphere model but we cannot exclude the inner disc region model.

7.2.3 Inclination Angle

There are several clues that suggest the inclination angle of V1223 Sgr is small. (1) The mass function $f = 5.0 \pm 3.8 \times 10^{-4} M_\odot$ indicates a low mass companion ($<0.15\ M_\odot$) unless $i < 30^\circ$. Figure 7.6 shows i versus secondary mass M_R for various white dwarf masses M_*. (2) The UV to IR data can be well fitted by an accretion disc model. The parameters derived by Mouchet (1982) are; inner radius of disc $R_1 = 5 \times 10^8$cm, outer radius $R_0 = 4.1 \times 10^{10}$cm, accretion rate $\dot{M} = 5.8 \times 10^{-9} M_\odot yr^{-1}$ and distance $D = 625/\sqrt{\cos i}$ pc. For low i ($<40^\circ$) the inferred distance is close to the value of 600 ± 60 pc derived from interstellar extinction (Bonnet-Bidaud et al., 1982). (3) The separation of the companion and white dwarf $a \sin i = 6.2 \pm 2.0 \times 10^9$cm will only exceed R_0 for $i \leq 9^\circ$. Conclusions (2) and (3) may require modification due to the pressure of the degenerate magnetic field since the field can modify the disc temperature distribution (Mouchet, 1982). (4) Any periodic modulation of X-rays expected from the two models is less than 20%. An Einstein IPC light curve appears in the preprint of Steiner et al. (1981) but not in the published version. If the angle between the rotation axis and magnetic field axis is η, then for high i, the X-ray modulation should be large unless η is small. At low i, η can be high since we are essentially looking pole on and little X-ray or direct optical modulation from the white dwarf is expected. η cannot be too small or the observed optical modulation would not be seen. This argument is difficult to quantify and would require the

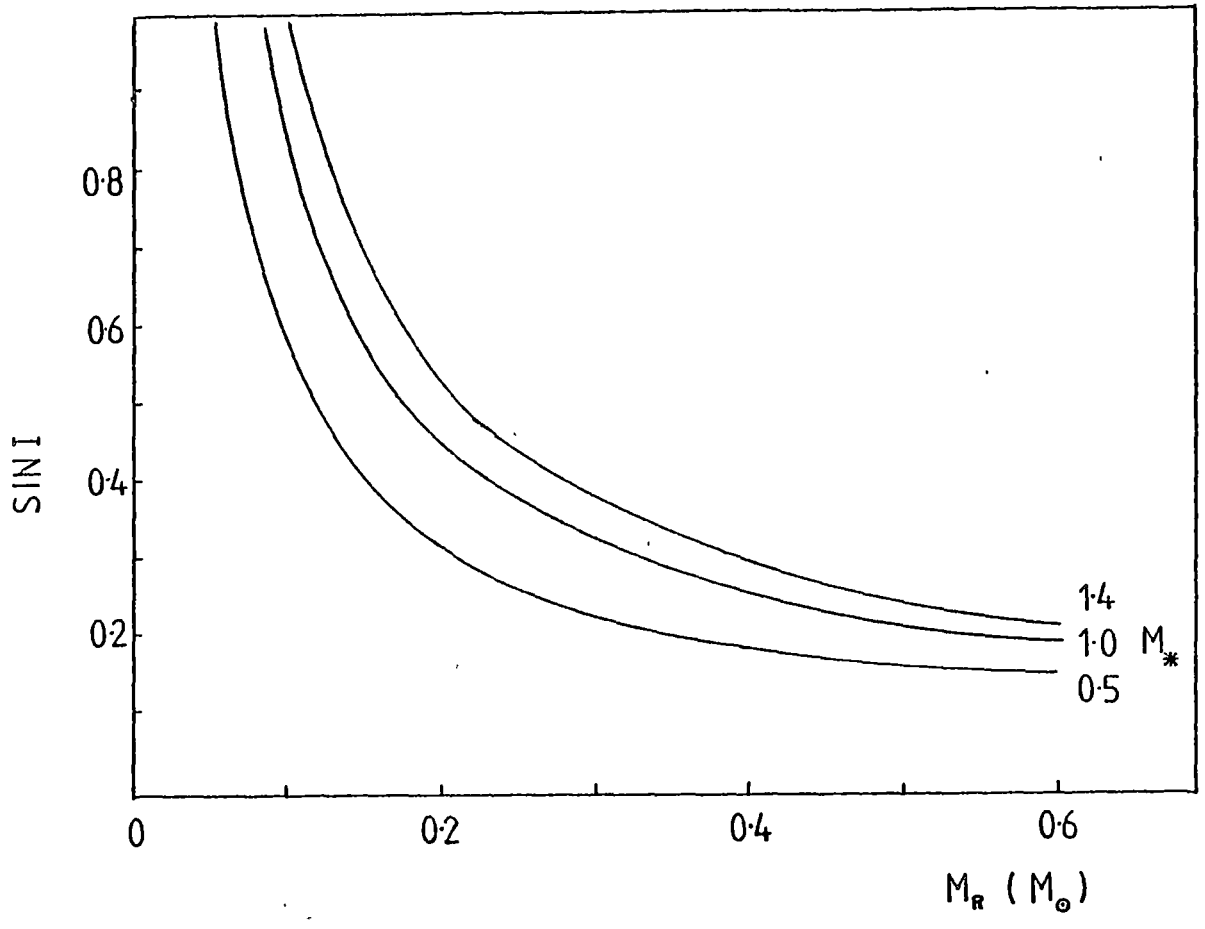

Figure 7.6 Relationship between companion mass (M_R), white dwarf mass (M_*) and inclination angle for V1223 Sgr.

development of detailed models of the system. (5) There are possible P Cygni profiles in the UV (Bonnet-Bidaud et al., 1982). Córdova and Mason (1982) have claimed evidence for mass loss from P Cyg profiles of cataclysmic variables with high luminosities ($>10L_\odot$) and low inclination angles. The mass loss rate is $\sim 10^{-11} M_\odot yr^{-1}$ or 10^{-2} to 10^{-3} of the expected mass accretion rate. They expect the wind region to be of conical shape centred on the rotation axis of the disc. The wind is driven by radiation pressure from the inner disc where the radiation pressure may exceed the gravitational force. A similar phenomenon is possible in V1223 Sgr since its disc luminosity is $12L_\odot$ if its distance is 600 pc. Point (5) places only a weak constraint on i.

A lower limit to i can be derived from the upper limit of the secondary luminosity at K. The K magnitude of the system is ~12.51 so an upper limit on the secondary magnitude is ~13.2 if no more than 50% of the flux is due to the secondary. By choosing an arbitary i and white dwarf mass, the companion mass and orbital separation follow from the mass function. The Roche Lobe radius is derived from equation 7.12 and hence the nuclear evolution parameter n such that the secondary fills its Roche Lobe. The secondary luminosity follows and its effective black-body temperature. The expected colour V-K of the secondary yields the surface brightness parameter S_K (equation 7.10). Assuming a distance of 600 pc, the K magnitude of the secondary follows from equation 7.11. At low i, n must be large for the secondary to fill its Roche Lobe. Consequently, the luminosity is large and hence also the flux at K. The calculations are not strongly dependent on the white dwarf mass. Using the above procedure, we find $i \geq 16^\circ$ corresponding to $M_R \leq 0.4\ M_\odot$. If all the K flux is from the secondary, then $i \geq 14^\circ$.

The FWZI of the broadest line is ~1100 km sec^{-1}. If we associate this with the Keplarian velocity of the inner edge of the disc then

$$R_1 = 1.1 \times 10^{10} \sin^2 i (M_*/M_\odot) \text{ cm} .$$

For $R_1 \geq 5 \times 10^8$cm, $i \geq 12^\circ$. Combining all the data suggests i is between 16° and 30°.

7.2.4 431 sec Pulsations

The period of the 431 sec oscillation seen at J but not R (Figure 6.21) is remarkably similar to the coherent period of 431 sec seen in the dwarf nova VW Hyi by Warner and Brickhill (1978). They offer two suggestions on the origins of the oscillations. (1) Oscillations of the disc and (2) Hot spots in Keplerian motion on the edge of the accretion disc. Van Horn, Wesemael and Winget (1980) have analytically studied the non-radial pulsations of optically thick discs generated by as yet unknown excitations and find that the peak luminosity of the pulsations corresponds to the disc radius $\frac{9}{4} R_1$ where R_1 is the inner radius of the disc. The Keplerian radius of the oscillation R_{osc} is then

$$R_{osc} = [GM_*(T_{osc}/2\pi)^2]^{\frac{1}{3}}$$

where T_{osc} is the observed periodicity. Since the period of oscillation is dependent on the radius, the power spectrum of the pulsations is broad. For V1223 Sgr, $R_{osc} = 3.7 \times 10^9$cm for $M_* = 1\ M_\odot$. The corresponding effective temperature of the disc is

$$T_e(R) = 4.1 \times 10^5 \left(\frac{\dot{M}M_*}{(R/R_\odot)^3} \right)^{\frac{1}{4}} K \quad .$$

From the UV data, $\dot{M} = 5.8 \times 10^{-9} M_\odot yr^{-1}$ implying $T_e(R_{osc}) = 32000$ K and for the low accretion limit of $10^{-11} M_\odot yr^{-1}$, $T_e(R_{osc}) = 6500$ K. The upper limit temperature of a blackbody yielding the observed fluxes is 4000 K and the low limit to the radius of the blackbody emission is $5.9 \times 10^9 (D/100)$ cm where D is the distance in pc. The temperature and area are too low and high respectively for a disc interpretation. If the emission region is multi-temperature then it must be dominated by temperatures less than 4000 K.

If the oscillations are from hot spots moving in a Keplerian manner then their radius is 7.2×10^9cm. This is neither on the outer or inner edge of the disc according to the disc parameters from Mouchet (1982). A similar problem exists regarding the temperature and required area of the emission region.

The area and low temperature are consistent with the source being the secondary. For $i \geq 16^\circ$, the Roche Lobe of the secondary is $< 8 \times 10^{10}$cm and effective temperature $\approx$3600K (see section 7.2.3). At a distance of 600 pc, the blackbody emission radius is $>3.6 \times 10^{10}$cm. If the entire pulsation is from radial changes in the secondary, then the radius of the secondary must change by at least 7%. This large change makes it unlikely to be the source of the pulsations. However if it is the source, then any small radial pulsation in the secondary will dramatically modify the accretion rate through the inner Lagrangian point. Its effect on the disc luminosity will depend on the time the disc requires to redistribute the inflowing material. The timescale of transfer of mass from the outer disc to the inner region, with a disc viscosity α is

$$t \simeq \alpha^{-1}(R/H)^2(R^3/GM_*)^{\frac{1}{2}}$$

where H is the disc thickness at radius R (Bath and Pringle, 1981). For $R = 10^{10}$cm, $H/R = 0.2$ and $M_* = 1\ M_\odot$ then $t \simeq \alpha^{-1}2500$. If $t \simeq 400$ sec, then $\alpha \simeq 10$. Bath and Pringle (1981) suggest $\alpha \simeq 1$ for dwarf novae and if a thick disc exists in V1223 Sgr then $\alpha << 1$. We conclude that the timescale of disc reaction to any radial changes in the secondary is much longer than the observed pulsations.

7.2.5 The VxK Cross Correlation

The lag of 190 ± 10 sec between V and K (Figure 6.29) is the largest yet seen in cataclysmic variables. Szkody and Margon (1980) found U filter data preceded V filter data by ~8 sec in AM Her and suggested ionizing radiation was responsible and not mass motions because the lagtime

was too short. This model can be eliminated from V1223 Sgr since the required distance is considerably larger than the separation of the components. Velocity streaming in accretion flows would require distances greater than ~2 x 10^9cm for velocities greater than 100 km sec^{-1}. Since a sin i = 6.2 x 10^9cm, it is easy to accommodate only low velocity flows (<100 km sec^{-1}). The problem is the location of the source of the initial optical perturbation and the consequent IR source. Since the width of the correlation at the lagtime of 190 sec is narrow, the separation of the two sources must be relatively stable over the time span of the observation (1.5 hr). It is possible that the optical (V) fluctuations are from the region where the Keplerian flow in the inner accretion disc is disturbed by the magnetic field and forced to flow via an accretion column to a shock region where the X-rays are produced. Below this point the accreting gas will produce cyclotron radiation peaking in the IR since the field strengths are expected to be lower than the ~2 x 10^7 gauss field of AM Her type objects. In the AM Her objects, the cyclotron radiation is at optical wavelengths. If the motion from the disc is freefall, then for a 1 $M_\odot$ white dwarf, the height of the optical emission region is 1.2 x 10^{10}cm. This height may be lower if the X-ray shock for cooling the accreting material by bremsstrahlung delays the propagation of the material. Stockman and Sargent (1979) have computed the infall velocities, onto a 1 $M_\odot$ white dwarf, of hot gas radiating most of its energy by bremsstrahlung. For a cross sectional accretion rate $\dot{M}/f > 10^{-7} M_\odot yr^{-1}$, where f is the fraction of the white dwarf onto which accretion occurs, the infall velocity is comparable to the freefall velocity. Since $\dot{M} \simeq 6 \times 10^{-9} M_\odot yr^{-1}$ from the disc spectrum, then for f = 1, the minimum height for the optical perturbation is ~3 x 10^9cm. To obtain heights less than this, f would be greater than 1 or $\dot{M}$ is too large. For a maximum freefall height of 1.2 x 10^{10}cm, f ~ 0.03 implying accretion onto a small area of the white dwarf. In between these two

limits, a wide range of f is permitted from this model.

7.2.6 Conclusions

The R band photometric light curve is consistent with the ephemeris of Warner (1983, private communication) and confirms the 0.14 day photometric period. The V and K light curves do not show any significant modulation at this timescale , however they only cover 0.4 of the 0.14 day period. Extended light curves are required to measure any orbital modulation at the long wavelengths, especially in the infrared.

Several periods near the dominant 794 sec period first seen by Steiner et al. (1981), are present in the R band data. From the beating relationship between the orbital period and the 794 sec pulsation, several periods are predicted dependent on the source of the 794 sec pulsation. If this is from reprocessed X-rays on the inner edge of the accretion disc (Model B) then either 850 sec or 1828 sec period should be present for a single pole or double pole beaming model. The detection of a 1828 sec period (and its 2nd harmonic) possibly indicates a double pole model. If the 794 sec pulsation arises from the secondary (Model A) then either 745 sec or 1404 sec pulsations should be present for respective single pole or double pole beaming. The presence of the 745 sec period suggests a single pole model. The relative phasing of the 794 sec and 745 sec periods exclude a model similar to H2252-035. Neither of the two models A or B can be rejected as yet. Further photometry is required to detect any beat periodicities.

A 431 sec pulsation seen at J but not R is probably from pulsations of the secondary since the maximum allowable blackbody temperature is 4000 K. It is not consistent with disc pulsations due to the low temperature. The size of the emission region, assuming a blackbody origin, requires the change in radius of the secondary to be excessively large at ~7%.

The correlation plots reveal zero lagtime correlated changes between R and J and R and K but not between V and K. The 190 ± 10 sec lagtime between V and K bands is remarkable. A feasible origin is the accretion column with the V fluctuations occuring in the turbulent region where Keplerian flow is disturbed by the magnetic field of the white dwarf and the corresponding K fluctuations occuring near the white dwarf at the base of the accretion columns.

No circular polarization was detected at any of the expected white dwarf spin periods. Upper limits to modulated polarization are ±3% at V, ±1% at R, +1,-2% at J and ±10% at K.

Spectroscopy revealed several unusual properties. A feature near H_δ is similar to a P Cygni profile with a mean outflow velocity of ~850 km sec^{-1}. No similar features are present near the other Balmer lines. The H lines are broad (FWZI ~ 1100 km sec^{-1}) and change dramatically in shape on a timescale of 0.5 hour. The line profiles are consistent with an S wave behaviour but requires the location of the hot spot to be on the leading edge of the disc at odds with all previous determinations of the position of the hot spots in cataclysmic variables. The small mass function of $5 \times 10^{-4} M_\odot$ determined from the moment centres of both the H lines and HeII λ4686 implies a low inclination angle ($i < 30^\circ$) if reasonable secondary masses are required. Since the contribution of the secondary is not apparent from the photometric fluxes nor the light curves, a low limit to i is 14° provided the secondary fills its Roche Lobe and follows the evolution equations of Whyte and Eggleton (1980) and using the V-K versus surface brightness of M dwarfs from Bailey (1981). Further interpretation of the radial velocities and emission line profiles is hampered by the lack of data covering a full orbital cycle.

7.3 Synthetic Light Curves of Intermediate Polars

7.3.1 Model

In order to distinguish between HCCTC's model and the model outlined in section 7.1, synthetic light curves of 2A0526-328 have been generated using the formalism of Motch and Pakull (1981). The reprocessed light, due to X-ray heating of the companions atmosphere can be described by

$$[b_{0\lambda} + b_{1\lambda}(\phi)][1 + \beta_\lambda(t)] \tag{7.13}$$

where ϕ is the orbital phase. The term $b_{0\lambda} + b_{1\lambda}(\phi)$ is the orbital modulation from the X-ray heating, partially modulated by the heating period $[1 + \beta_\lambda(t)]$ where $|\beta_\lambda|$ can vary between 0 and 1. The direct white dwarf modulation can be written as $a_\lambda(1+\alpha_\lambda(t))$ where $|\alpha_\lambda|$ is between 0 and 1. The total flux is thus

$$F_\lambda = [b_{0\lambda} + b_{1\lambda}(\phi)][1 + \beta_\lambda(t)] + a_\lambda(1 + \alpha_\lambda(t)) + c_\lambda \tag{7.14}$$

where c_λ is the unmodulated contribution from the system. Equation (7.14) can be rewritten as

$$F_\lambda = b_{1\lambda}(\phi)[1 + \beta_\lambda(t)] + b_{0\lambda}\beta_\lambda(t) + a_\lambda\alpha_\lambda(t) + d_\lambda \tag{7.15}$$

where $d = c_\lambda + a_\lambda + b_{0\lambda}$ represents all unmodulated fluxes. The terms $b_{1\lambda}$, $b_{0\lambda}\beta_\lambda$ and $a_\lambda\alpha_\lambda$ are directly measured from the respective observed orbital, heating and white dwarf modulations.

Since β_λ cannot be measured directly, the parameter $b_{0\lambda}$ is a free variable subject to the condition that $\beta_\lambda < 1$, i.e. $b_{0\lambda}$ is greater than the observed heating modulation. Two other assumptions are required. The first is that the three modulations can be represented by sine functions and second that the white dwarf modulation has opposite phase to the heating modulation at maximum orbital light. The first assumption is supported by the sinusoidal appearance of the pulsation profiles from H2252-035 (Motch and Pakull, 1981). The second assumption is shown in the observations of H2252-035 (Motch and Pakull, 1981) and occurs when the white dwarf is at inferior conjunction. From the meshing of the three

periods of 2A0526-328 from HCCTC's ephemeris, a similar phenomenon cannot be excluded.

Other models for the DQ Her stars have been developed to account for the eclipse related phase shifts and amplitude changes of the fast coherent oscillations. Petterson (1980) explained the effects seen in DQ Her and UX UMa, by the reflection of radiation off an accretion disc from a source near or on the rapidly spinning white dwarf. The markedly different behaviour of the two essentially similar objects is simply explained by a slightly smaller inclination angle in UX UMa. Both require eclipses by the companion to induce the observed effects and the phase shifts occur over only 20% of the orbit centred at the eclipse. Since no eclipses have been seen in the intermediate polars, the model is not suitable for our purposes. The model used in this study does not depend on the geometry of the system and has the least number of assumptions.

7.3.2 2A0526-328

The basic data (for various filters) from the light curves of 2A0526-328 are listed in Table 7.1 for both models. Amplitudes are in peak to peak magnitudes from Motch (1981).

TABLE 7.1

Light curve amplitudes for 2A0526-328 at various photometric pass bands

	4^d orbital model				HCCTC model			
	period	U	B	V	period	U	B	V
orbital	$4^d.024$	0.33	0.33	0.33	$5^h.4864$	0.15	0.07	0.06
heating	$5^h.1905$	0.22	0.27	0.27	$4^d.024$	0.33	0.33	0.33
white dwarf rotation	$5^h.4864$	0.15	0.07	0.06	$5^h.1905$	0.22	0.27	0.27

Motch did not detect any modulation in B and V at the spectroscopic period ($5^h.4864$) from re-analysis of his 1979 November UBV data. However, he quotes modulation in U, U-B and B-V of 0.15, 0.08 and 0.05 mag

respectively. From this, the B and V modulation is 0.07 and 0.06 mag respectively. It is possible that ~~the intrinsic scatter of the observations~~ flickering have masked this modulation. For the model, we have used the calculated modulations for the colour changes listed in Table 7.1, but note that they are possibly quite close to the intrinsic scatter, and may in fact be upper limits.

The first effect to be noted is the difference in U and B light curves (Figure 7.7) for $b_{0\lambda} > 100$. Since $\beta_\lambda < 0.01$, the light curves are essentially a linear sum of the 3 periods and are the same for both models. Note the relative shift in the peaks of U and B at maximum light. As the spectroscopic modulation is small at B, the B light curve is composed of only two signals, the short and the long photometric periods. This implies that the spacing between the beat period maxima is approximately constant. On the other hand spectroscopic modulation at U is comparable to the magnitude of the modulation at the short photometric period. This causes a shift in minima since at minimum light they are in phase but at maximum they are not. To illustrate this behaviour, the phases of the maxima and minima for the two light curves in Figure 7.7 are plotted in Figure 7.8. The data are from Table 6.5, from the IUE FES data of Mouchet et al. (1981) and from Motch (1981). The data in Figure 7.8 are from various wavelengths. Motch's data and the MSSSO data are from Johnson B band whilst the others are white light data. Motch has used an arbitary phase to fold his data. From his figure 3(a), mean maximum light occurs at phase 0.87 whereas in HCCTC it is defined to be zero. To convert the phases of minimum and maximum to the correct phase, 0.13 has been added to the phases measured on Motch's figure 1(b) and (c). The predicted phase from the model has been arbitarily shifted up or down with respect to the phase of the 5.2 hour modulation to achieve the best fit to the data since this only depends on how the minima and maxima are defined.

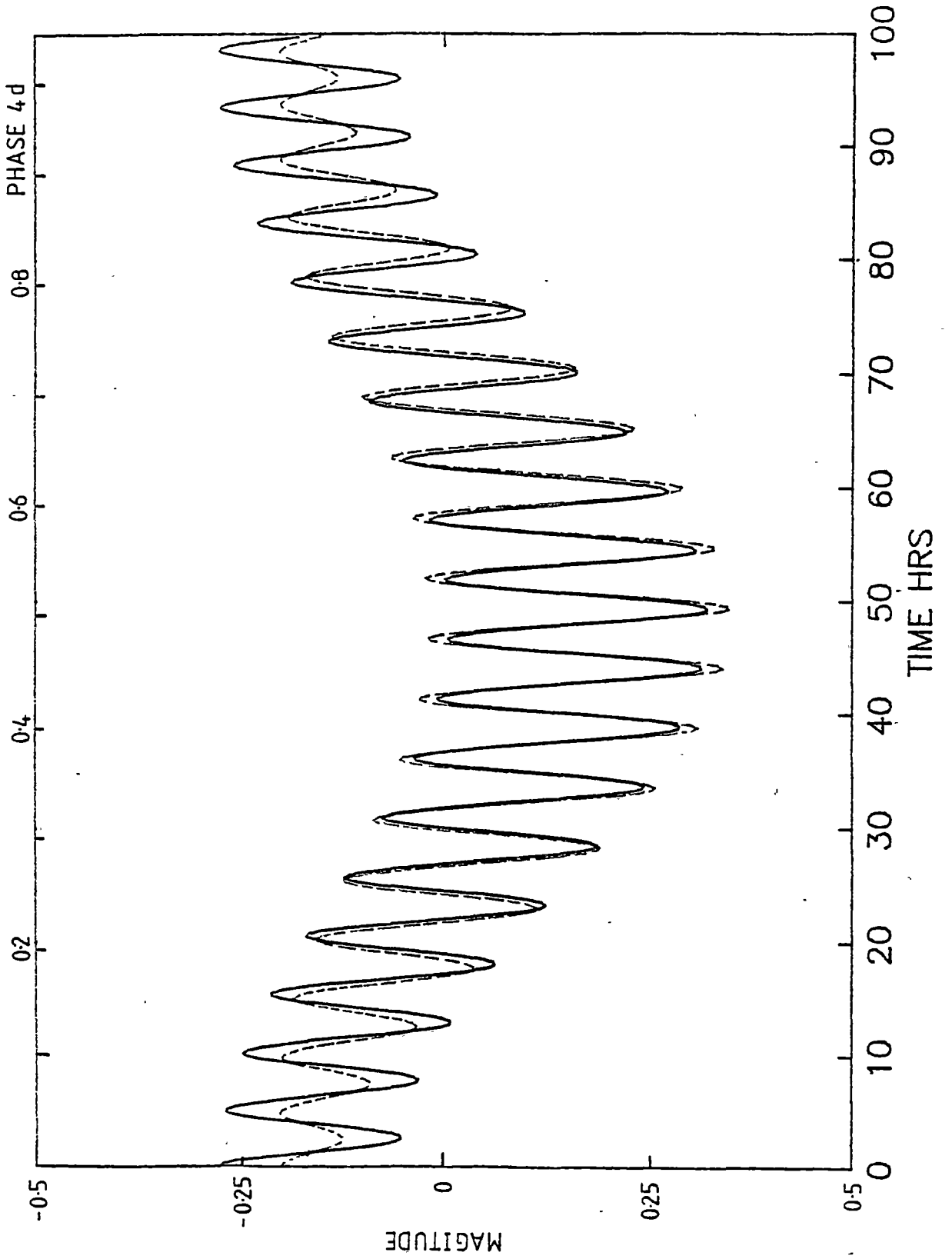

Figure 7.7 Theoretical light curve of 2A0526-328 for $b_{o\lambda}>100$. U band is dashed line and B band is solid line.

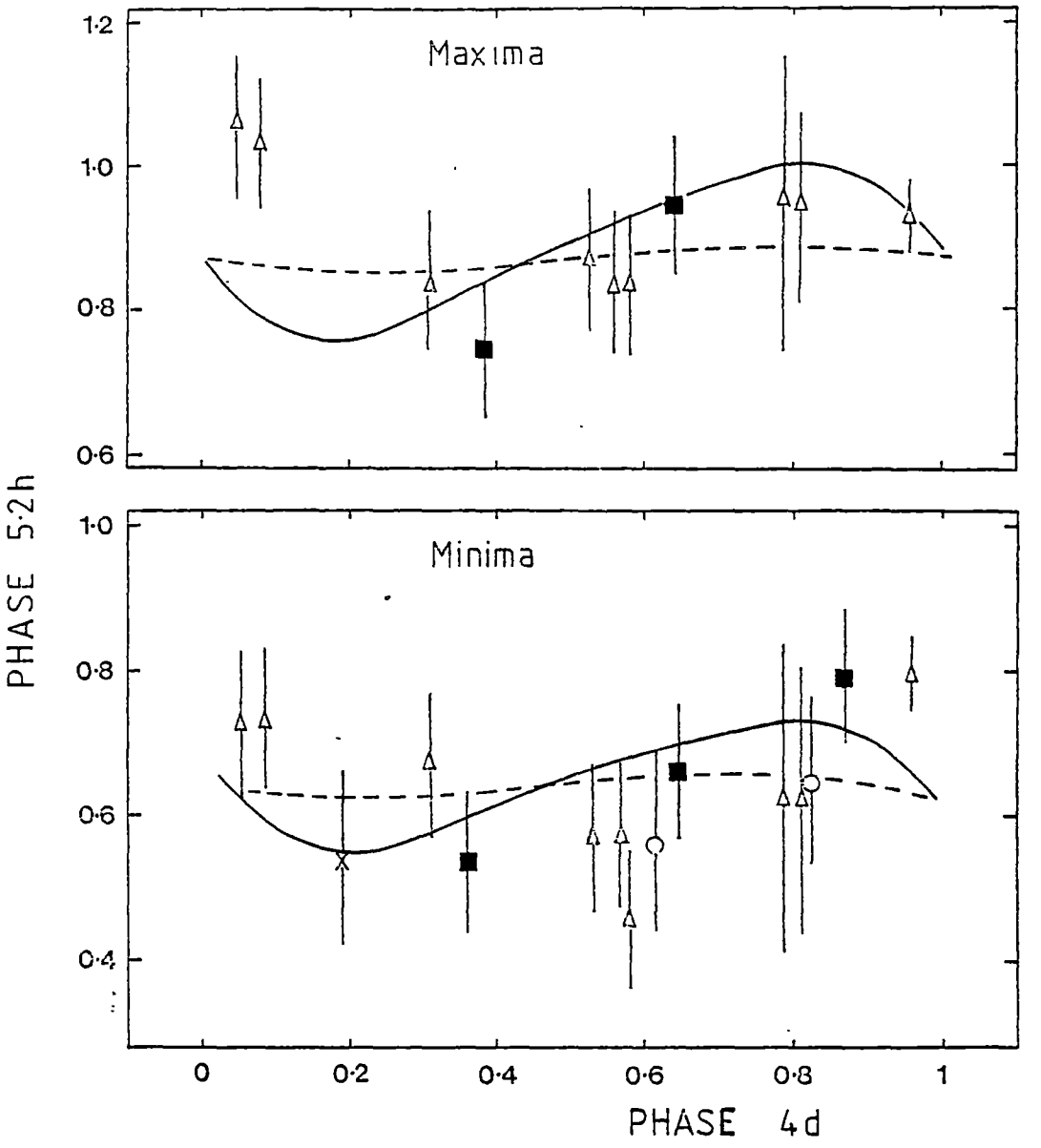

Figure 7.8 Observed minima and maxima photometric phases versus 4 day photometric phase. Data from: filled squares 1979 Nov Siding Spring, triangle Motch (1981), cross IUE FES (Mouchet et al 1981) and open circle 1981 Nov Mt. Stromlo. Solid line is predicted U minima and maxima for $b_{o\lambda}>100$. Dashed line is for B.

Motch (1981) defined minima to be when the light curve suddenly rose whereas our minima are the true minima of the computed light curves.

The predicted U curve for the maximum satisfactorily fits all except the first two data points. The model correctly predicts the advancing $5^h.2$ phase as the 4^d phase increases between 0.2 and 0.8. The fit for the minima is not so good. As previously stated, the B curves are much flatter than the U curves. Since the model predicts a wavelength dependence on the timing of the maxima and minima, more photometric observations should cover as wide a wavelength as possible with emphasis on U or UV wavelengths where the phase shifts are predicted to be the greatest.

The model also predicts a second effect. The modulation amplitude at maximum light (phase $4^d = 0$) is different than at minimum and is dependent on $b_{0\lambda}$. Light curves using U data for different $b_{0\lambda}$ are shown in Figure 7.9 for the 4^d orbital model and in Figure 7.10 for HCCTC's model. For both models, as $b_{0\lambda}$ decreases until $\beta_\lambda = 1$, the amplitude at phase zero generally increases whilst at phase 0.5 the amplitude of the 5.2 hour period decreases. The dependence of the ratio of modulation at maximum light to the modulation at minimum light (A_λ) is shown in Figure 7.11. Also shown is the ratio for B band light curves. The data for V is similar to B. The behaviour for each model is remarkably different. As expected, for $b_{0\lambda} \geq 10$ the models yield the same ratio but at $b_{0\lambda} < 3$ the results diverge.

Given an observed A_λ, it is possible to predict a corresponding $b_{0\lambda}$. In the case of 2A0526-328, Motch (1981) did not detect any amplitude change in B and V between maximum and minimum light. If the error in the amplitude measurement is ~0.05 mag then $A_\lambda = 1.0 \pm 0.25$. No colour changes in U-B are seen in the 4^d cycle, so a similar amplitude ratio in U is necessary. In the case of the B and V curves on Figure 7.11 it predicts $b_{0\lambda} > 1$ for the 4^d orbital model whilst HCCTC's model,

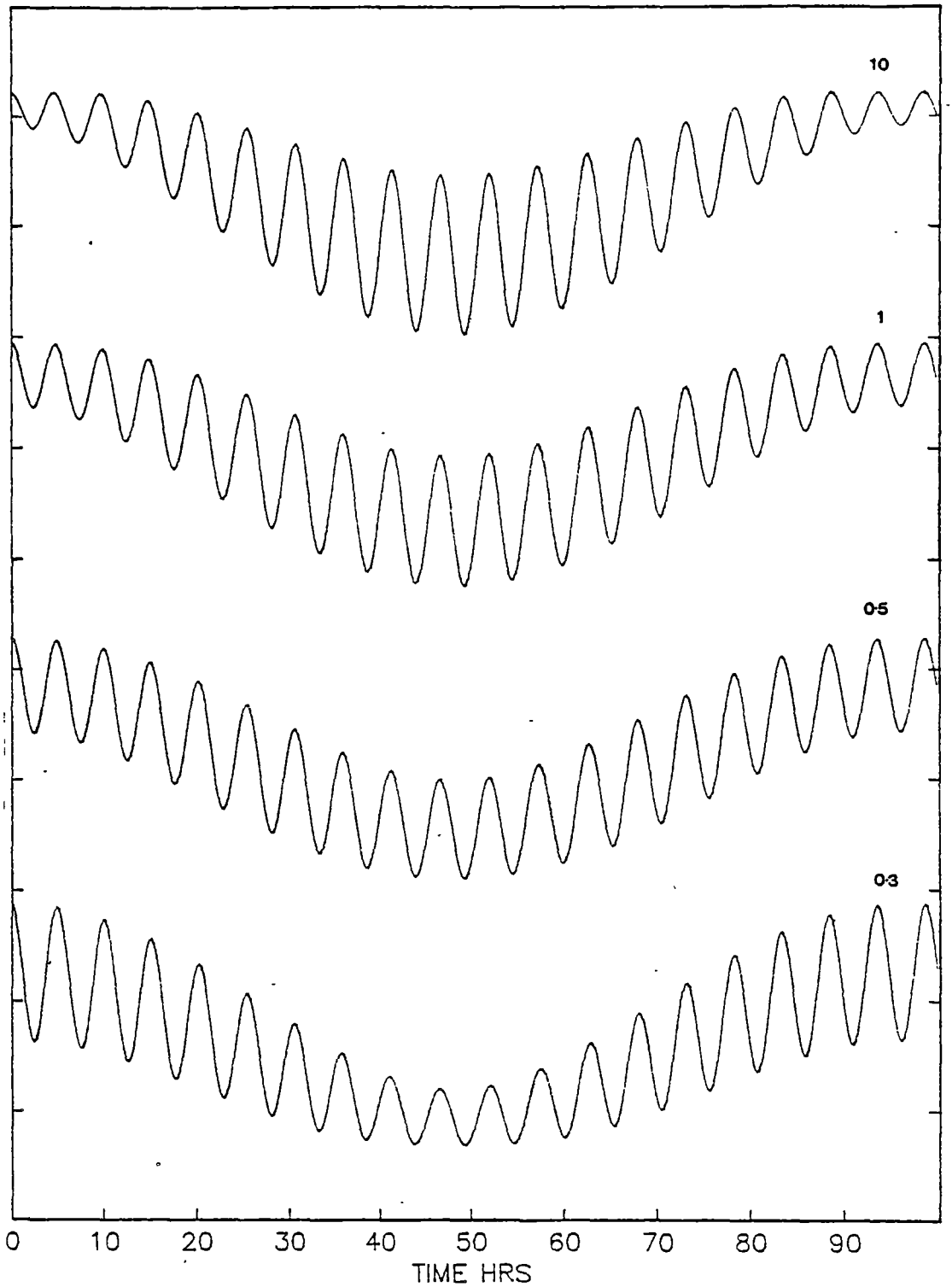

Figure 7.9 Theoretical light curves of 2A0526-328, for $b_{o\lambda}$ from 0.3 to 10 from the 4 day orbital model. Vertical scale marks are 0.25 mag.

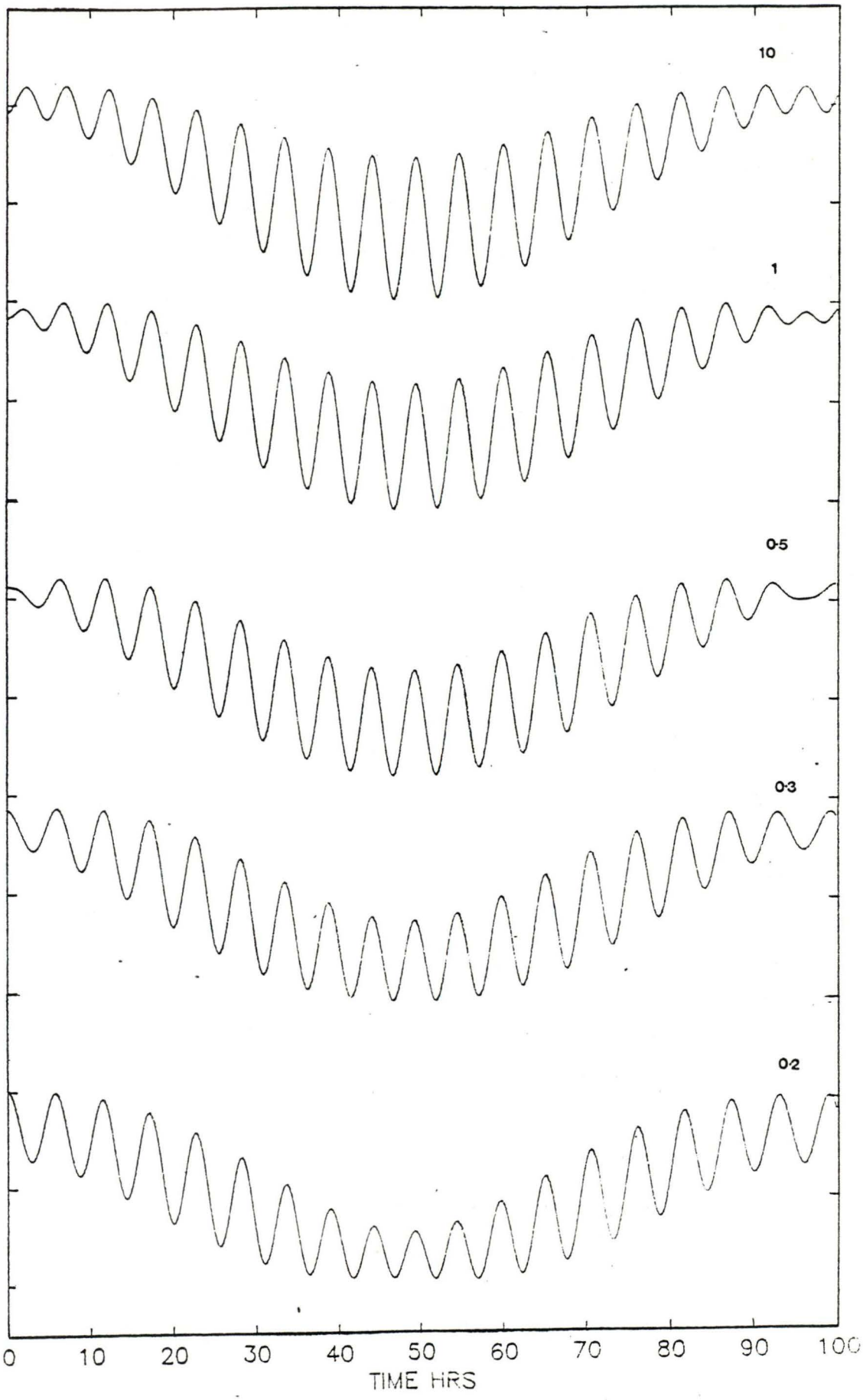

Figure 7.10 Theoretical light curves of 2A0526-328, for $b_{o\lambda}$ from 0.2 to 10 from the HCCTC model. Vertical scale marks are 0.25 mag.

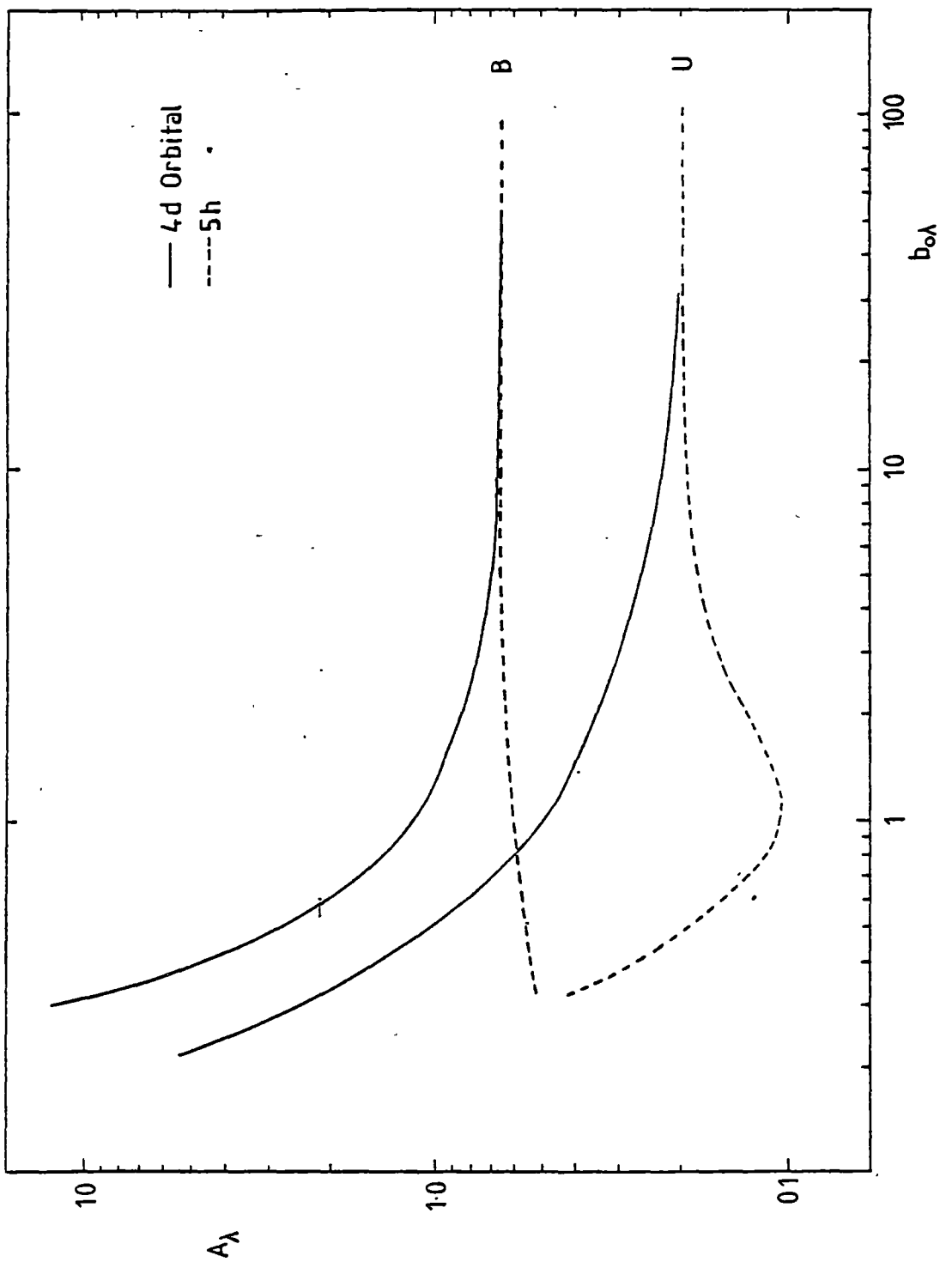

Figure 7.11 Predicted modulation of 5.2 hour period as a function of $b_{o\lambda}$. A_λ is the ratio of modulation at maximum light to modulation at minimum light. Solid line is 4 day model and dashed line is HCCTC model for U and B data.

requires $b_{0\lambda} > 0.4$. The constraints on $b_{0\lambda}$ at U are much smaller. For the 4^d orbital model, $b_{0\lambda}$ lies between 0.42 and 0.65 but for HCCTC's model no value of $b_{0\lambda}$ lies within the observed value of A_λ. The closest value of $A_\lambda = 0.5$ is when $\beta_\lambda = 1$, i.e. $b_{0\lambda} = 0.33$.

By determining $b_{0\lambda}$ at various wavelengths, it is possible to determine the spectral form of the unmodulated heating. In the case of 2A0526-328, and the 4^d model, $b_{0\lambda}$ is larger at longer wavelengths which is consistent with the 5.2^h pulsed heating spectrum flattening at wavelengths less than 4000 Å as is evident in Figure 7.3. Further data at near infrared and infrared wavelengths are required to test this. More maxima and minima are required to remove any effects from brightness variations not associated with the orbital and rotational effects. For example, Motch (1981) detected a small dip just before minima on 1980 January 5 which cannot be satisfactorily explained. The advantage of further photometric studies of 2A0526-328 (and TT Ari which has a comparable period (Jameson et al., 1982)) versus the other intermediate polars is that the modulations at the three periods are much larger and flickering effects should not confuse the analysis. A disadvantage is that long sets of photometry are required over timescales of days rather than hours.

The same light curve synthesis can be applied to the other intermediate polars where sufficient data are available.

7.3.3 Vl223 Sgr

Estimates of $b_{0\lambda}$ can be derived for Vl223 Sgr from the photometric observations discussed in section 6.2. Only two bands (R and J) can be used since the V and K light curves do not cover an orbital cycle. The data for Vl223 Sgr is given in Table 7.2. It is assumed that the 794 sec period is the heating period and only one pole is optically active.

TABLE 7.2

Peak to peak magnitudes of the pulsations from V1223 Sgr

	period (min)	R	J
orbital	201.9	0.27	0.17
heating	13.24	0.053	0.024
white dwarf rotation	12.42	0.018	<0.012

Folding R data at minimum light and maximum light yields $A_R = 1.78 \pm 0.3$ and for J, $A_J = \sim 1.0$. Estimated values of $b_{0\lambda}$ are 0.41 ± 0.05 and 0.32 ± 0.05 respectively. Further data at UBV will be required to determine the spectrum of the heating.

In all the available photometry of V1223 Sgr, there is phase jitter of the dominant optical pulsations about the expected epoch. This is also seen in H2215-086 (Figures 2 and 3 of Shafter and Targan, 1982) 3A0729+103 (Figure 4 of Warner, 1982). In the case of V1223 Sgr, it appears uncorrelated with the orbital period whereas in 2A0526-328, there is a distinct correlation between the two photometric periods. (See Figure 7.8). Since flickering has a timescale of minutes, then in the case of the objects with pulsations <15 minutes the flickering may mask or distort any orbit dependent phase shifts of the pulsations. Only in 2A0526-328 and TT Ari are the periods long enough to overcome this effect.

7.3.4 H2252-035

Motch and Pakull (1981) could not directly interpret the average energy spectrum observed in H2252-035 due to the unknown contributions of the average heating $b_{0\lambda}$ and the average of the pulsed light at the X-ray period (a_λ). Applying the model to the Walraven band data on H2252-035 and noting that there was a possible weakening of 0.006 mag in the amplitude of the reprocessed light at maximum light, A_λ can be

determined and consequently $b_{0\lambda}$. They are listed in Table 7.3. The white light data are from Hassall et al. (1981) and they estimate an upper limit to the white light amplitude of the reprocessed light of 35% which is consistent with the Walraven data. A determination of $b_{0\lambda}$ at white light would not assist in estimating the spectrum. As can be seen, $b_{0\lambda}$ increases at longer wavelengths. Data at R, I and infrared are needed for comparison with V1223 Sgr data.

TABLE 7.3

band pass	W	U	L	B	V	white
central λ (Å)	3255	3633	3838	4325	5467	-
A_λ	0.9	0.89	0.87	0.85	0.84	1.15-0.85
$b_{0\lambda}$ (mag) (±0.02)	0.16	0.16	0.17	0.19	0.27	

7.3.5 Conclusions

Due to a lack of photometric data covering a wide spectral range, it is difficult to compare the orbital heating spectra of the three intermediate polars discussed. Studies of H2252-035 and 2A0526-328 at near infrared and infrared wavelengths are required and at wavelengths less than 5000Å for V1223 Sgr. The other intermediate polars H2215-086 and 3A0729+103 have stronger pulsations (up to 40%) than H2252-035 and V1223 Sgr and are obvious candidates for a similar light curve analysis.

On the nature of 2A0526-328, the synthetic light curves suggest that the 4 day orbital model is valid since the HCCTC model does not predict the observed photometric behaviour. It is possible, in the 4 day model, to obtain $b_{0\lambda}$ such that the ratio of modulation at maximum light to the modulation at minimum light A_λ fits the observed

ratios of $A_B = A_V = 1.0 \pm 0.25$. The maximum value of A_λ from the HCCTC model is only 0.5 at U and 0.7 at B. However, other sources of light may confuse the simple model that has been used. Partial eclipses of the reprocessed light due to the accretion disc or the companion at inferior conjunction may affect the modulation. Further data are required at all phases of the 4 day period and at other wavelength bands for detailed modelling of the interaction of the three light sources. More timing of maxima and minima will assist in understanding the phase related changes in the light curve first noted by Motch (1981).

7.4 VY Sculptoris

The H emission lines of VY Scl are narrow (Burrell and Mould, 1973) (FWZI = 800 km sec^{-1}) compared with other cataclysmic variables. If this represents the Keplerian velocity of the inner disc at the surface of the white dwarf, then the inclination angle must be less than 15° for white dwarf masses from 0.2 to 1.4 $M_{\odot}$. If there is a white dwarf magnetic field that can disrupt the inner edge of the accretion disc, then larger inclination angles are allowed. No eclipses have been reported corroborating the view that the system is pole-on. This may explain why VY Scl has a small, low energy X-ray cut-off of ~1 keV. Since we are looking at the source of the X-ray emission directly, there would be little if any absorption from any disc material. Correlating inclination angle versus low energy cutoff for other systems may reveal this phenomenon and give clues to the structure of the disc.

A similar phenomenon is noted in the galactic bulge sources. Milgrom (1978) commented on the lack of X-ray or optical eclipses. He explained it by postulating the existence of a thick accretion disc. At high inclination angles, when eclipses should be seen, the disc is thick enough to extinguish any X-ray emission from reaching the observer. At low i, the disc is not obscuring the X-ray emission region but no eclipses can occur. The X-ray emission and eclipses are mutually exclusive properties. Only in the bulge sources Sco X-1 and 4U1626-67 (Middleditch et al., 1981) have orbital periods been determined.

If the X-ray cutoff is due entirely to interstellar extinction, then the distance is $\sim 230^{+300}_{-170}$ pc implying an X-ray flux between 2.4×10^{30} and 1.9×10^{32} erg sec^{-1}. We assume an interstellar hydrogen density of 0.6 atom cm^{-3}.

At quiescence, VY Scl is at ~18 mag (Warner, 1980b) possibly indicating that there is very little contribution from the red companion. This suggests a small orbital period because the Roche lobe radius of the

secondary must be small. The long term photometric behaviour is very similar to that of the nova-like object MV Lyr which has a period of 0.134^{d} (Robinson et al., 1981). We predict that VY Scl has a comparable orbital period. Warner (1982) suggests VY Scl to be an intermediate polar. The presence of X-rays strengthens this idea because of the increased probability of a white dwarf magnetic field.

CHAPTER 8

Optical Observations of Unidentified X-ray Sources

As part of a collaborative program with F. Seward (Smithsonian Centre for Astrophysics) and P. Hill (Anglo Australian Observatory and St. Andrews University), spectroscopic observations have been conducted at the Anglo-Australian Telescope (AAT), in an attempt to identify optical counterparts of Einstein and HEAO-1 objects. Observations were conducted on 1979 February 16-17, June 3-4, 1980 February 10 and July 4. All observations used the RGO spectrograph and Image Photon Counting System (IPCS). Grating 250B, mounted blaze to collimator, with 250 lines/mm was used to obtain low resolution spectra (~6Å) from 3400 Å to 7400 Å at a dispersion of 156Å/mm. To calibrate the IPCS response, we observed the standard L970-30 (Oke, 1974). This is valid only for 1979 February 16-17 and 1980 February 10 spectra. Spectra were classified using the IPCS count rate curves of A to M stars from Krug, Morton and Tritton (1980) and the strengths of absorption lines.

Table 8.1 lists, in order of Right Ascension, all stars observed giving date and dwell times. Positions are either from the AAT pointing position (±3") (AAT) or astrometry from Schmidt plates (plate) using the UK Schmidt Unit measuring machine. On 1982 June 10, we did infrared mapping of the X-ray pulsar 4U1510-59 to search for candidates using the Infrared Photo-Spectrometer (IRPS).

A brief discussion on each object follows.

A0538-66

We attempted to identify the optical counterpart of the 16.6^{d} X-ray transient A0538-66 using the finding chart of Johnston et al. (1979). We acquired spectra from stars 20, 14, B and from the bright star 35" N.W. from Star B. Subsequent observations by the HEAO-1 MC experiment (Johnston, Griffiths and Ward, 1980) refined the error box

Table 8.1 Position, date and dwell times of candidate stars.

Source	detector	X-ray position (1950)	error radius (')	STAR	Optical position 1950	source	DATE	dwell sec	spectral type
A0538-66				14	05 35 46.4 -66 52 10		1979 Feb 16	700	B
				20	05 35 54.4 -66 52 32		"	850	B
				B	05 35 42.1 -66 52 32		"	1000	B
					05 35 38.2 -66 52 10		"	500	B
H0544-665	HEAO-1	05 44 11.5 -66 35 24	120"	1	05 44 16.3 -66 34 57	AAT	1979 Feb 16	750	Be
				23	05 44 19.1 -66 34 35		"	350	A or F
				24	05 44 17.6 -66 34 22		"	550	late F
E0832-44	IPC	08 32 57.8 -44 38 51	120"	6	08 33 3.9 -44 38 20	AAT	1979 Feb 16	1000	late G
				11	08 33 1.2 -44 39 40		"	1000	M
				8	08 33 8.3 -44 38 11		"	600	G
				17	08 32 54.8 -44 39 55		Feb 17	1000	F
				15	08 32 57.3 -44 41 02			1000	G
E1344-60	IPC	13 44 07.3 -60 22 59	60"	1	13 44 5.32 -60 22 32.0	plate	1979 June 4	573	M
	HRI	13 44 09.5 -60 22 09	10"	2	13 44 6.90 -60 22 52.7	"	"	500	F or G
				3	13 44 13.73 -60 22 56.3	"	"	530	F
				4	13 44 13.73 -60 22 56.3	"	"	530	F
				5	13 44 0.44 -60 22 27.6	"	"	1800	F6-G
				6	13 44 10.09 -60 22 09.0	"	"		G
2S1417-624	SAS-3	14 17 26.2 - 62 28 14	30"	1	14 17 29.5 -62 28 15	AAT	1979 Feb 16	1100	late G
				6	14 17 24.8 -62 27 56		"	500	late G
				13	14 17 26.6 -62 27 20		"	620	F
				14	14 17 20.0 -62 27 59		1979 Feb 17	900	G
				15	14 17 33.8 -62 27 55		Feb 16	630	A
				16	14 17 20.6 -62 28 21		Feb 17	250	red
4U1510-59	HRI	15 09 59.5 -58 56 57	5"	1	15 09 58.71 -58 56 38.1	plate	1980 Feb 10	1600	06.5
				2	15 09 58.50 -58 57 29.7	"	July 4	857	late A
				3	15 10 0.75 -58 57 16.5	"	July 4	503	-
				4	15 10 01.50 -58 56 46.6	"	July 4	329	-
				LSSJ319	15 09 44.5 -59 00 37	AAT	1979 Feb 16		WC9
E1630-47	HRI	16 30 20.5 -47 17 18	5"	E	16 30 21.6 -47 17 19	AAT	1979 June 5	1670	G
E1631-64	HRI	16 31 47.5 -64 28 53	5"	1	16 31 45.9 -64 28 30.4	plate	1979 June 4	1500	G
				2	16 31 48.9 -64 28 52.4		"		-
				3	16 31 48.1 -64 29 11.0		1980 Feb 10	418	-
A1710-34	SAS-3	17 11 1.3 -33 59 32	40"	2	17 11 2.1 -33 58 51	AAT	1979 June 3	1500	G
				3	17 11 3.2 -33 59 07		"	2000	too noisy
				4	17 11 5.0 -33 59 12		"	900	G ?
				11	17 10 58.0 -33 59 09		"	2000	too noisy

to 25 arc sec radius which excludes the four stars observed. They suggested STAR Q on the basis of historical variability from archive plates. Pakull and Parmar (1981) showed from optical studies that Star Q is in the LMC making it one of the most luminous stellar objects known (L_X ~8 x 10^{38} erg sec^{-1}, 2-17 keV). The star shows spectral changes from O type to Be. The Be phase and X-ray flares occur when the compact object accretes material at periastron in its $16^d.6$ eccentric orbit. Einstein observations, whilst the object was in outburst, show pulsations with a period of 69.2126 msec, making it the fastest X-ray pulsar in a binary system (Skinner et al., 1982). Estimates of the stellar separation of the components (~39 $R_\odot$) and the radius of the companion (~40 $R_\odot$) suggest that the neutron star may actually become immersed in the envelope of the companion star.

HO544-655

During scanning observations of the LMC using the HEAO-1 modulation collimator, Johnston, Bradt and Doxsey (1979) discovered a faint source, HO544-655, with a flux of 1.8 mJy (1.5-13.5 keV). It was not detected in the Einstein survey of the LMC by Long, Helfand and Grabelsky (1981) implying an X-ray variability > 500. We observed stars 1, 23 and 24 using the designation of stars from the finding chart of Johnston, Bradt and Doxsey. Stars 23 and 24 have spectral type A or F but star 1, the brightest in the error circle, is a Be star. The spectrum is shown in Figure 8.1. It has emission at H_α and the Balmer continuum and possibly filled in H_β. The UV excess is not unusual since at least 60% of Be stars have such behaviour (Mendoza, 1982).

Thorstensen and Charles (1980) found the star slightly variable and a further study by van der Klis et al. (1983) showed star 1 to have photometric behaviour typical of Be stars. The absolute visual magnitude is M_V ~ -3.5 ± 0.3 if it is situated in the LMC. The optical flux, from

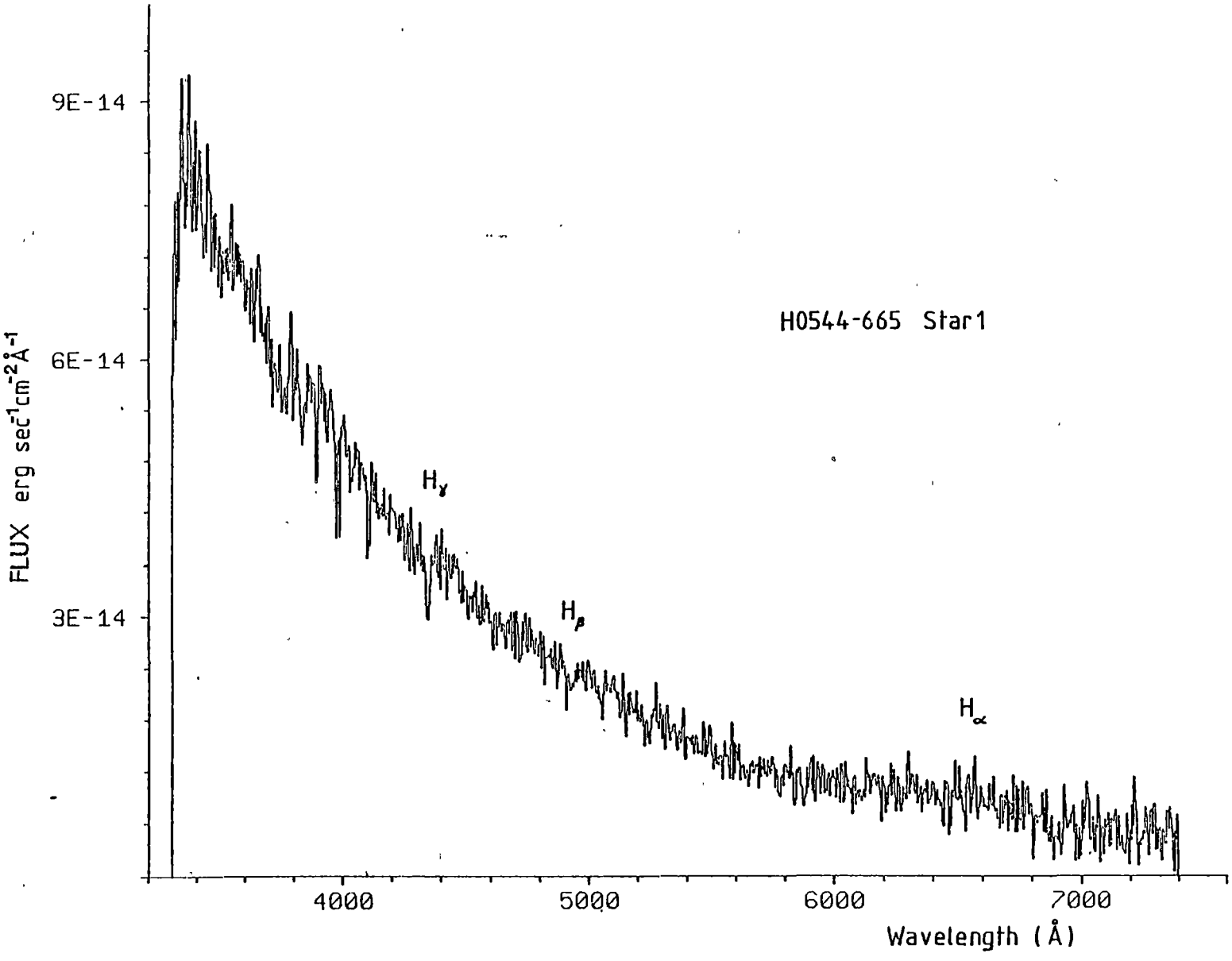

Figure 8.1 IPCS spectrum of Star 1 H0544-665

our data, is 5.3 x 10^{-13} erg $cm^{-2}sec^{-1}$ (3400-7200Å) or 3.7 x 10^{35} erg sec^{-1} at a distance of 55 kpc. An error of 30% can be assumed because the spectrum is from a narrow slit measurement. The respective X-ray fluxes from the HEAO-1 and Einstein observations are 1.8 x 10^{37} erg sec^{-1} (1.5-13.5 keV) and <3.5 x 10^{34} erg sec^{-1} (0.15-4.5 keV). The X-ray to optical flux ratios are 49 and 0.1 respectively on the assumption that the optical flux did not change. The range of X-ray to optical fluxes from Be stars in X-ray binaries range from 6 x 10^{-6} to 3 (de Loore et al., 1982), whereas for isolated Be stars $L_x \simeq 10^{33}$erg sec^{-1} (Peters, 1982). This suggests that this star, if it is the candidate, is binary and perhaps similar to AO538-66. Further X-ray and concurrent optical observations are desirable.

EO832-44

This object was found during one of the first IPC observations, and consequently has a large error circle (radius ≃120"). Figure 8.2 is the finding chart from a IIIaF plate (passband 6300-7200Å). Five stars were observed, numbers 6, 8, 11, 15 and 17 and none appeared abnormal.

E1344-60

Both IPC and HRI positions are available for this source and are shown in Figure 8.3 superimposed on an SRC-J plate (passband 3950-5900Å). Positions of stars 1 to 6 were measured from the same plate. Star 6 is a possible candidate although its spectrum appears to be a normal G type. Grindlay (1981) found G star candidates for 4U1744-26, 4U1813-14 and 4U1916-05. Further observations are required to check for any variability in this star or test the nature of the two faint stars in the HRI error circle. Star 5 shows weak H_α emission but is well outside the HRI error circle.

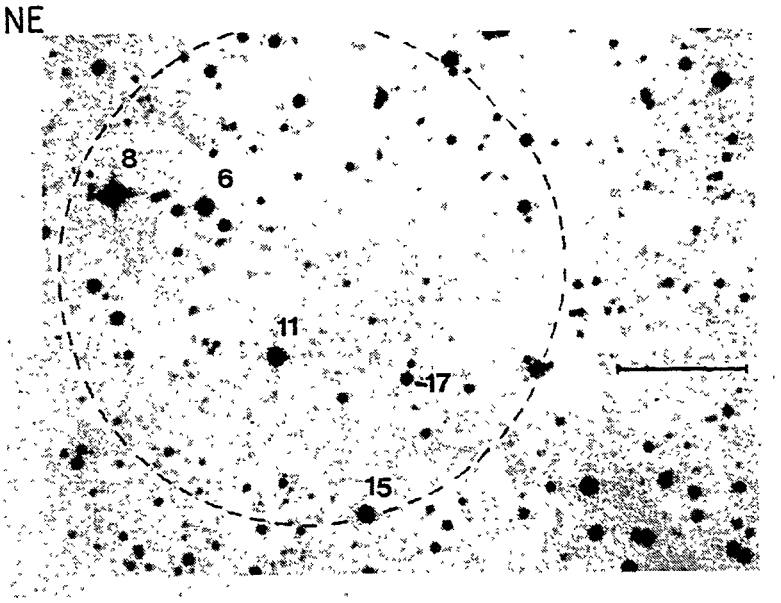

Figure 8.2 Finding chart of E0832-44 from IIIaF plate. Bar is 1 arcmin long.

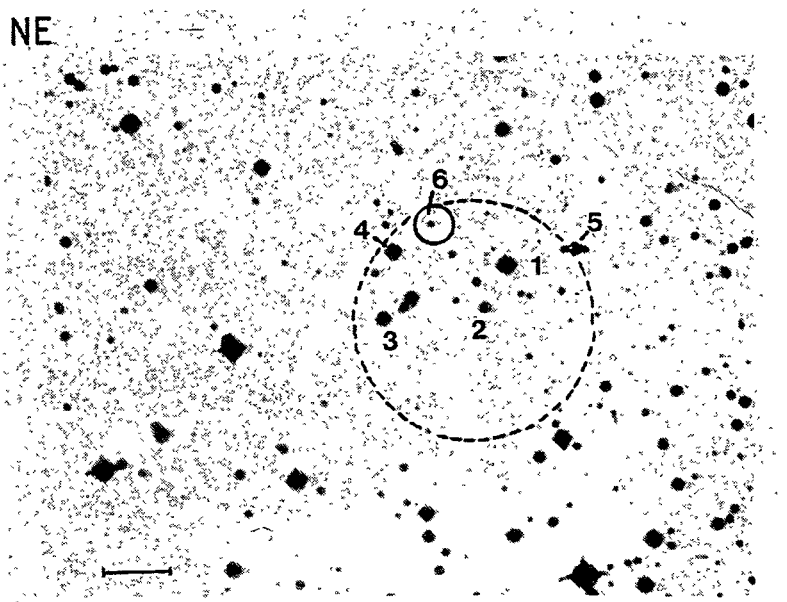

Figure 8.3 Finding chart of E1344-60 from SRC-J plate. Large dashed circle is IPC error box and small circle HRI position. Scale is indicated by bar 30 arcsec long.

2S1417-624

During 1978 July 25-30, SAS-3 observed the source 4U1416-62 and refined the error box to a circle of radius 30". A finding chart is in Apparao et al. (1980). Temporal analysis of the SAS-3 data by Kelley et al. (1981) showed a coherent 17.64 sec pulsation. The pulse profile is double peaked between 2-11 keV and is similar to the pulsars Vela X-1 and A0535+26. Pulse timing constrains possible orbital periods to > 15 days unless the mass function is very small ($< 10^{-2} M_{\odot}$).

In poor conditions, six stars were observed. Stars 1 and 6 are late G. The other stars are outside the error box and are not named by Apparao et al. (1980). They are:

(1) STAR 13 65" due north of error box centre type F

(2) STAR 14 35" due west of STAR 6 type G

(3) STAR 15 25" due east of STAR 2 type A

(4) STAR 16 20" south west of STAR 14 red

Star 8 has been proposed as the candidate by Grindlay (1981) because of strong and possibly variable H_{α} emission.

4U1510-59

Originally a Uhuru source, this object has recently been found to be an X-ray pulsar with a period of 0.15 seconds, and it is most likely associated with the surrounding supernova remnant MSH15-52 (Seward and Harnden, 1982). Attempts to identify the optical counterpart have been unsuccessful since no stellar object down to mag 21 exists in a ten arc sec radius about the position (Figure 8.4) (Seward et al., 1982). Radio pulsations subsequently reported by McCulloch, Hamilton and Ables (1982) and by Manchester, Tuohy and D'Amico (1982) confirm the large period derivative ($\dot{P}/P = 47$ μs Yr^{-1}) implying the object is not a member of a binary system and support the association of the pulsar with the SNR.

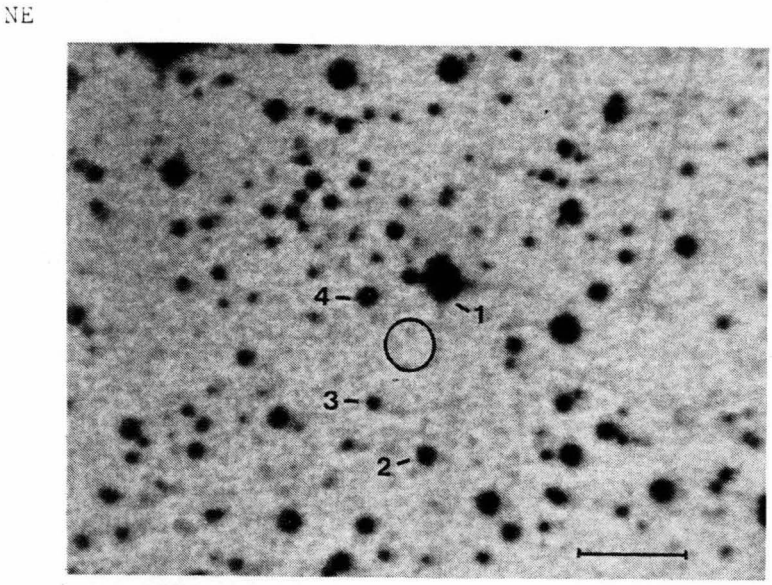

Figure 8.4 Finding chart of 4U1510-59 from SRC-J plate. Bar is 30 arcsec long and circle is HRI error box.

Before the X-ray source was known to be a pulsar, we searched for optical counterparts in July 1980. Star 1 (Figure 8.4) was identified as a heavily reddened O6.5III(f) star (A_V ~5.5) (Figure 8.5) corresponding to a distance of ~4 kpc. HeII λ4686 is present as a weak absorption line possibly partly filled in by emission. It initially appeared to be the most suitable candidate even though it is 18 arc sec from the centre of the HRI error box. OSO7 observations indicated the X-ray source was very hard (kT ~20 keV or α ~ 0.5) (Markert et al., 1979). This was confirmed by Ariel V observations of the Cir X-1 region (Chiappetti and Bell Burnell, 1982). The photon spectral index is ~1.6 between 2 and 10 keV. The association of an O star with a hard X-ray source possibly indicated a binary pulsar, e.g. Cen X-3.

Before the error box was refined by Einstein observations, a previous candidate was the Wolf-Rayet star LSS 3319 (WRA1297). At the

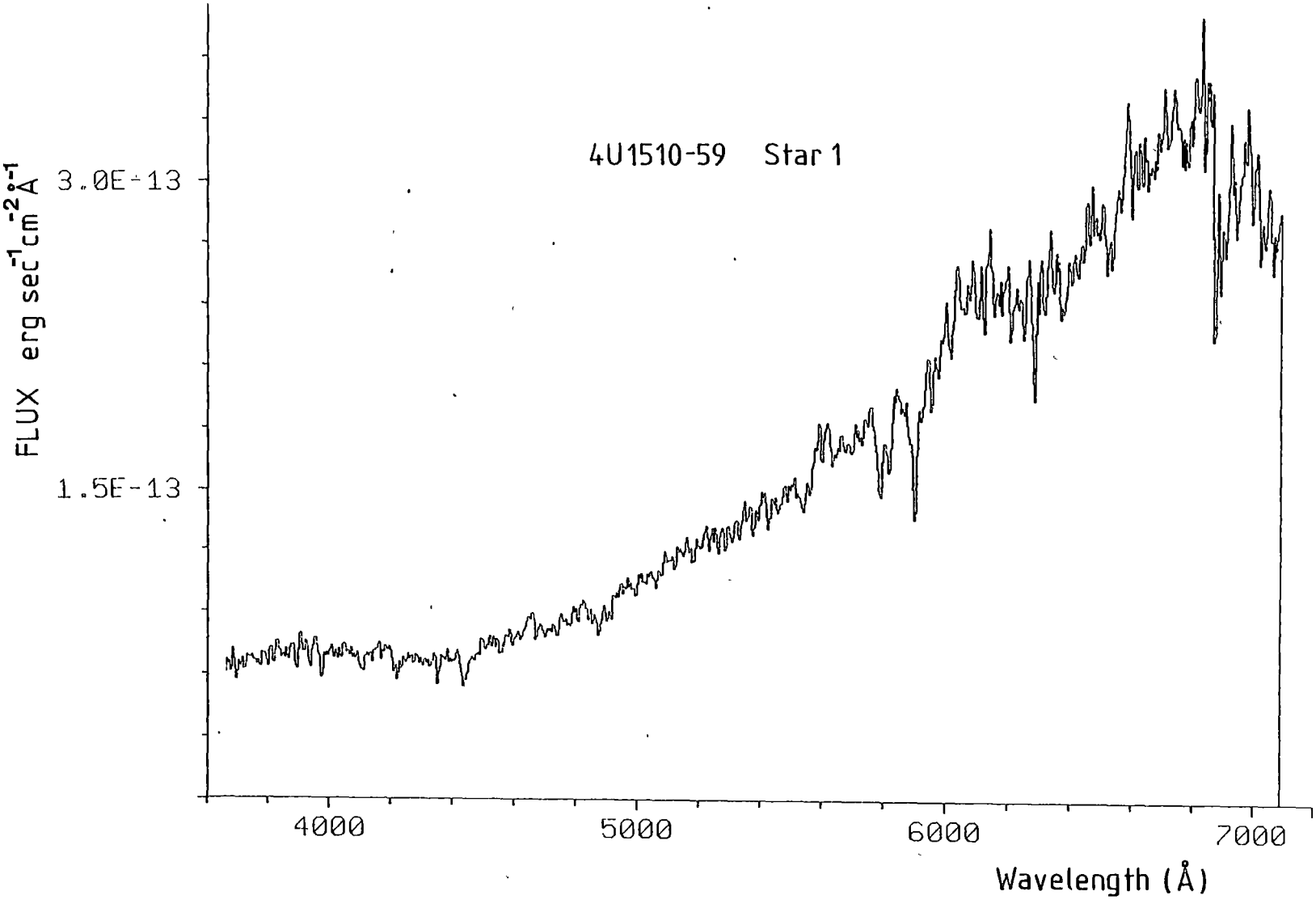

Figure 8.5 IPCS spectrum of Star 1 4U1510-59

request of P. Murdin, we obtained spectra of this star during 1979 February 16. It is classified as a WC 9 star and the spectrum is shown in Figure 8.6 with identification of the stronger emission lines. Further details and finding chart are in the galactic Wolf-Rayet survey of van der Hucht et al. (1981).

To search for the optical candidate of the pulsar and because of the large extinction, we mapped the region in infrared in the J and K bands in 1982 June, using the IRPS in a scanning mode. The dewar and amplifier are stable over a period of hours allowing D.C. operation, i.e. without sky chopping. The results are illustrated in Figure 8.7. Each map is 32 x 32 bins with each bin being 1 arc sec square. Six and eight scans were done for J and K respectively using an integration time of 100 m sec per bin per scan. The aperture was 2 arc sec. Immediately apparent are stars to the west and north of the error circle. There is one possible star in the error circle, it is 2 arc sec north of the centre. Table 8.2 gives J and K magnitudes of all confirmed images in Figure 8.7. These data are supplied by Dr. A. Giles. Upper limits for any other stars are J ~ 16.5 and K ~ 15.7. Astrometry of STAR 1 yields a position 2 arc seconds different from the AAT position originally derived from our observations and listed in Seward et al. (1982). The position of all field stars on the SRC-J and I plates and from the IR scan are shown in Figure 8.8. The dashed box is the IR map area, the circle the HRI position derived from the astrometric positions (error ± 0.8 arc sec), the small filled square Seward et al. (1982) HRI position, filled circles images on SRC-J plate, open circles from I plate and crosses from IR map. Stars 5, 6, 7, 8 and 10 are on the CCD image of Seward et al. (1982). There is some doubt as to which star, 12 or 13, is the CCD image.

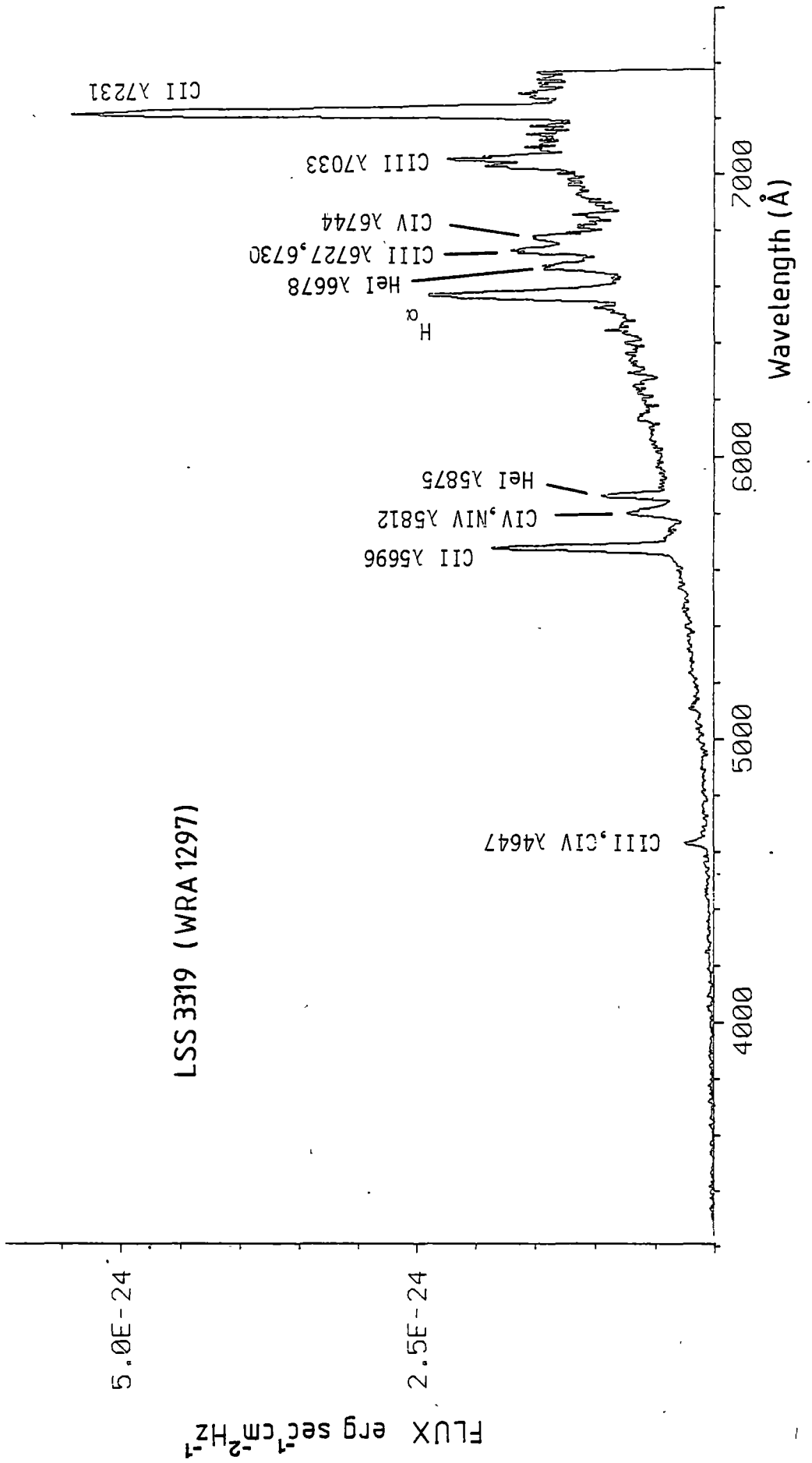

Figure 8.6 IPCS spectrum of Wolf-Rayet star LSS 3319

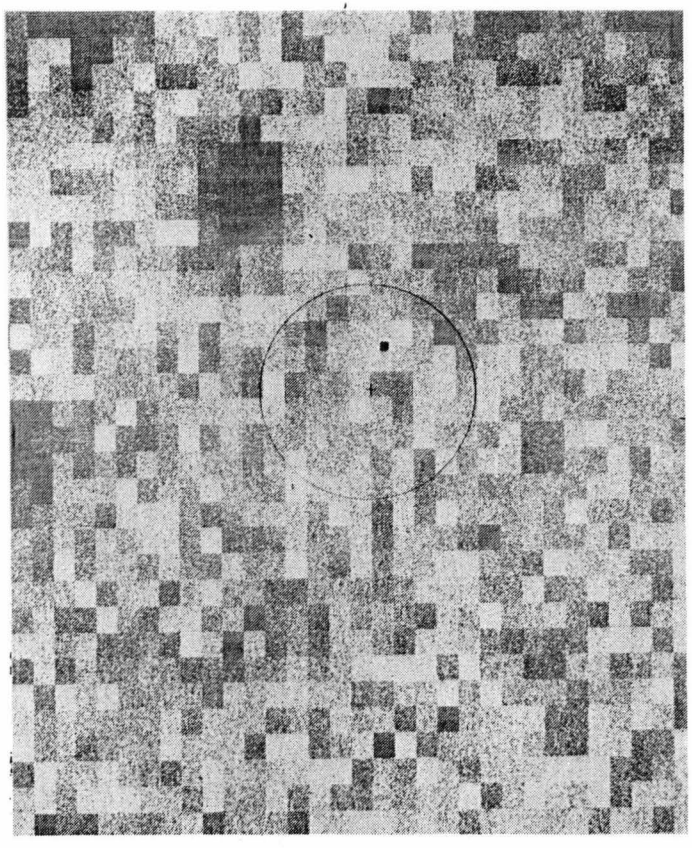

J

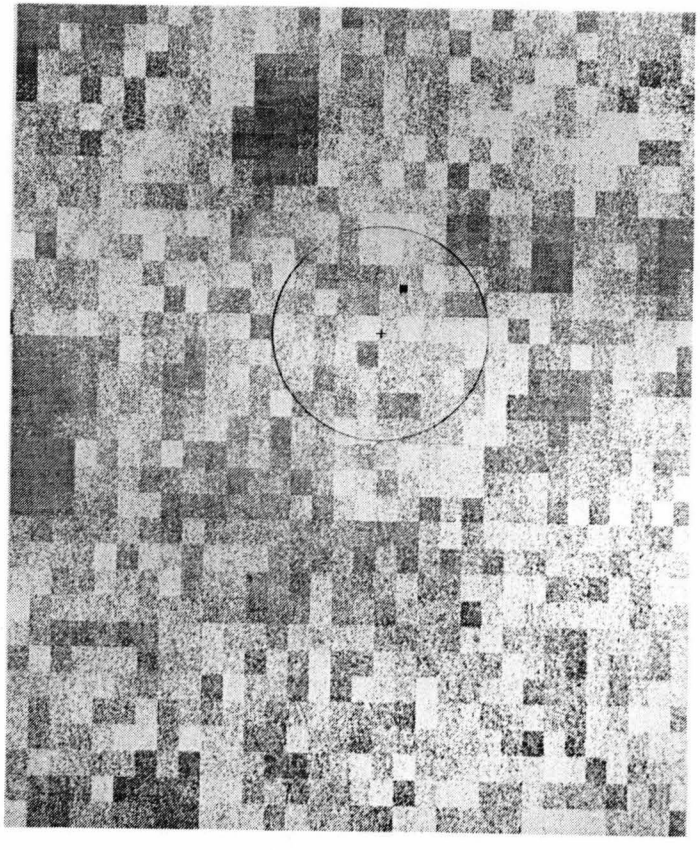

K

Figure 8.7 J and K maps of the field of 4U1510-59. Bins are 1 arcsec square. Circle is HRI error circle and square is HRI centre from Seward et al (1982)

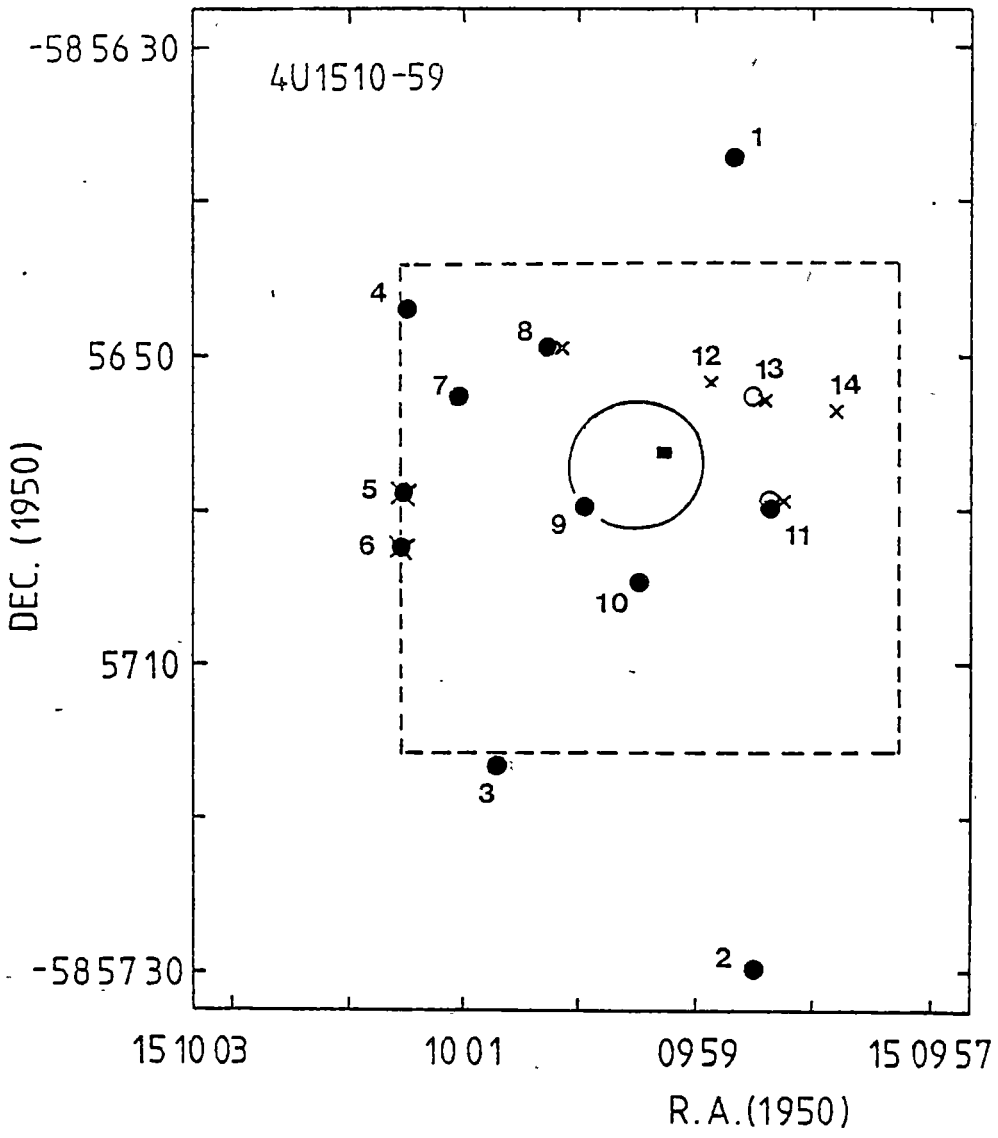

Figure 8.8 Positions of stars from SRC-J plate (filled circles) and I plate (open circles) and IR maps (crosses). Square is Seward et al (1982) HRI position. Large square is IR map area (Figure 8.7)

TABLE 8.2

Infrared magnitudes of stars in 4U1510-59 field

Star	J	K
4	15.5 ± 0.4	14.0 ± 0.2
5	15.5 ± 0.4	13.6 ± 0.2
6	16.0 ± 0.6	13.5 ± 0.15
8	13.3 ± 0.07	13.5 ± 0.12
11	16.0 ± 0.6	14.6 ± 0.3
12	15.9 ± 0.5	14.8 ± 0.3
13	16.0 ± 0.6	14.7 ± 0.3
14	15.8 ± 0.5	14.7 ± 0.3

E1630-47

This object has been previously detected by Uhuru, SAS-3 and the HEAO-1 scanning modulation collimator (MC) and a finding chart is in Reid et al. (1980). Five X-ray outbursts have been detected. The first four appear quasiperiodic with a spacing of 615 days whilst the last outburst was delayed (Jones et al., 1976; Kaluzienski and Holt, 1977). Figure 8.9 shows the HEAO-1 MC and Einstein HRI error regions. The candidate star proposed by Grindlay (1977) is ~90" from the HRI position. We observed star E on 1979 June 5. Its spectral type is G. Conditions were unfavourable to acquire spectra of the 2 faint stars in the HRI error circle.

E1631-64

The only apparent star in the HRI position (Figure 8.10) is a faint star on the southern edge of the error circle. Star 1 is the only star that could be satisfactorily classified - it is type G.

A1710-34 (2S1711-339)

The position of A1710-34 was refined to an 80 arc sec diameter error circle by SAS-3 RMC measurements (Greenhill et al., 1979a). Stars 2, 3, 4 and 11 from the finding chart of Greenhill et al. were observed in

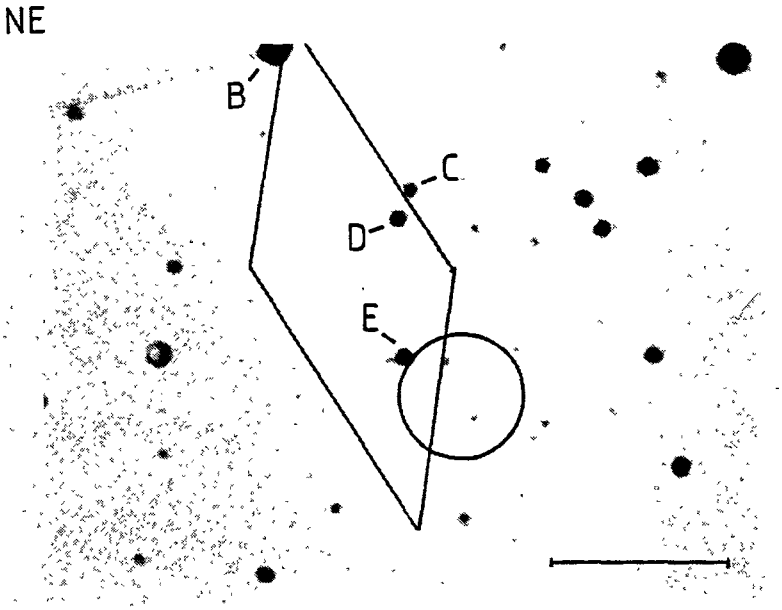

Figure 8.9 Finding chart of E1630-47 from SRC-J plate. Diamond is HEAO-1 MC box and circle is a 10 arcsec circle centered on the HRI position. Bar is 30 arcsec long.

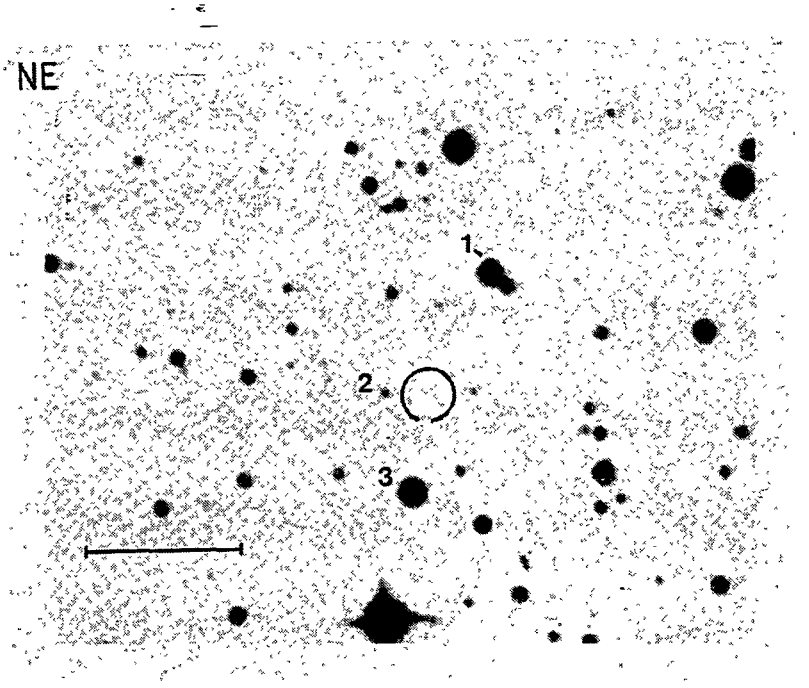

Figure 8.10 Finding chart of E1631-64 from SRC-J plate. Circle is 5'' error circle of HRI position. Bar is 30 arcsec long.

1979 June 3. The data from stars 3 and 11 were too noisy to permit spectral classification. Stars 2 and 4 appeared normal.

References

Adams, W.M. and Petrosian, V., 1974; Astrophys.J. 192, 199.

Allen, C.W., 1973; Astrophysical Quantities, 3rd ed., Athlone Press, London.

Apparao, K.M.V., Naranan, S., Kelley, R.L., and Bradt, H.V., 1980; Astron.Astrophys. 89, 249.

Ashton, S.C., 1980; Honours thesis, University of Tasmania.

Bailey, J., 1981; Mon.Not.R.astra.Soc. 197, 31.

Bailey, J. and Hough, J.H., 1982; Publs.astra.Soc.Pacif. 94, 618.

Bailey, J., Hanes, D., Watts, D.J., Giles, A.B., and Greenhill, J.G., 1982; IAU Circ. No. 3712.

Bambynek, W., Crasemann, B., Fink, R.W., Freund, H.-U., Mark. H., Swift, C.D., Price, R.E., and Rao, P.V., 1972; Rev.Mod.Phys. 44, 716.

Barton, J.R. and Allen, D.A., 1980; Publs.astra.Soc.Pacific 92, 368.

Bath, G.T. and Pringle, J.E., 1981; Mon.Not.R.astra.Soc. 194, 967.

Bath, G.T., Pringle, J.E., and Whelan, J.A.J., 1980; Mon.Not.R.astra. Soc. 190, 185.

Becker, R.H., 1981; Astrophys.J. 251, 626.

Becker, R.H. and Marshall, F.E., 1981; Astrophys.J.Lett. 244, L93.

Becker, R.H., Boldt, E.A., Holt, S.S., Pravdo, S.H., Rothschild, R.E., Serlemitsos,P.J., and Swank, J.H., 1976; Astrophys.J.Lett. 207, L167.

Belserene, E.P., 1981; Bull.A.A.S. 13, 524.

Bhatt, H.C., 1982; Astrophys. Space Sci. 81, 379.

Bianchini, A., Hamzaoglu, E., and Sabbadin, F., 1981; Astron.Astrophys. 99, 392.

Blades, J.C., 1980; 'A user's guide to the RGO spectrograph', Anglo-Australian Observatory.

Blissett, R.J. and Cruise, A.M., 1979; Mon.Not.R.astra.Soc. 186, 45.

Boley, F., Johns, M., and Maker, S., 1979; IAU Circ.No. 3324.

Boksenberg, A., 1972; ESO/CERN Conference on "Auxiliary Instrumentation for Large Telescopes" p.295, eds. S. Lausten and A. Reiz.

Bonnet-Bidaud, J.M., Mouchet, M., and Motch, C., 1982; Astron. Astrophy. 112, 355.

Brocklehurst, M., 1971; Mon.Not.R.astr.Soc. 153, 471.

Burrell, J.F. and Mould, J.R., 1973; Publs.astra.Soc.Pacif. 85, 627.

Carlson, L.A., Morgan, P.S., Cormack, R.H., Stefan, K., and Wilson, W.C., 1973; Texas Engr.Expt. Station Rpt.No. TAMRF-921-7307.

Chanan, G., Nelson, J., and Margon, B., 1978; Astrophys.J. 226, 963.

Chapline, G.Jr. and Stevens, J., 1973; Astrophys.J. 184, 1041.

Charles, P., Thorstensen, J., Bowyer, S., and Middleditch, J., 1979; Astrophys.J.Lett. 231 , L131.

Chiappetti, L. and Bell Burnell, S.J., 1982; Mon.Not.R.astra.Soc. 200, 1025.

Chiappetti, L., Tanzi, E.G., and Treves, A., 1980; Space Sci. Review 27, 3.

Chiappetti, L., Blissett, R.J., Branduardi-Raymont, G., Bell Burnell, S.J., Ives, J.C., Parmar, A.N., and Sanford, P.W., 1981; Mon.Not.R.astra.Soc. 197, 139.

Chlebowski, T., Halpern, J.P., and Steiner, J.E., 1981; Astrophys.J. Lett. 247, L35.

Crampton, D. and Cowley, A.P., 1977; Publs.astra.Soc.Pacif. 89, 374.

Coe, M.J., Engel, A.R., Evans, A.J., and Quenby, J.J., 1981; Astrophys. J. 243, 155.

Coe, M.J. and Wickramasinghe, D.T., 1981; Nature 290, 119.

Cooke, B.A., Ricketts, M.J., Maccacaro, T., Pye, J.P., Elvis, M., Watson, M.G., Griffiths, R.E., Pounds, K.A., McHardy, I., Maccagni, D., Seward, F.D., Page, C.G., and Turner, M.J.L., 1978; Mon.Not.R.astra. Soc. 182, 489.

Cooper, G., 1971; Phys.Rev. D 3, 2312.

Córdova, F.A., 1980; in IAU Coll.No. 53 (Rochester: University of Rochester), p.507.

Córdova, F.A. and Garmire, G.P., 1979; Nature 279, 782.

Córdova, F.A. and Riegler, G.R., 1979; Mon.Not.R.astr.Soc. 188, 103.

Córdova, F.A. and Mason, K.O., 1982; Astrophys.J. 260, 716.

Córdova, F.A., Mason, K.O., and Nelson, J.E., 1981a; Astrophys.J. 245, 609.

Córdova, F.A., Jensen, K.A. and Nugent, J.J., 1981b; Mon.Not.R.astra. Soc. 196, 1.

Cousins, A.W.J., 1973; Mem.R.astr.Soc. 77, 223.

Cowley, A.P. and Crampton, D., 1977; Astrophys.J.Lett. 212, L121

Cowley, A.P., Crampton, D., Hutchings, J.B., and Marlborough, J.M., 1975; Astrophys.J. 195, 413.

Cowley, A.P., Hutchings, J.B., and Crampton, D., 1981; Astrophys.J. 246, 489.

Davidsen, A., Malina, R., and Bowyer, S., 1976; Astrophys.J. 203, 448.

Davidsen, A., Malina, R., and Bowyer, S., 1977; Astrophys.J. 211, 866.

Delvaille, J.P., Geller, M.J., and Schnopper, H.W., 1978; Astrophys.J. Lett. 226, L69.

Dennis, B.R., Beall, J.H., Cutler, E.P., Crannell, C.J., Dolan, J.F., Frost, K.J., and Orwig, L.E., 1980a; Astrophys.J.Lett. 236, L49.

Dennis, B.R., Cutler, E.P., Becker, R.H., Dolan, J.F., Crannell, C.J., Frost, K.J., Orwig, L.E., and White, N.E., 1980b; Bull.A.A.S. 12, 513.

Dolan, J.F., 1972; Astrophys. and Space Sci. 17, 472.

Doty, J.P. et al. (1978) presented at the HEAO/AAS meeting, San Diego 1978,

Doty, J.P., Hoffman, J.A., and Lewin, W.H.G., 1981; Astrophys.J. 243, 257.

Dower, R.G., Griffiths, R.E., Bradt, H.V., Doxsey, R.E., and Johnston, M.D., 1980; Astrophys.J. 235, 355.

Doxsey, R.E., Apparao, K.M.V., Bradt, H.V., Dower, R.G., and Jernigan, J.G., 1977; Nature 270, 586.

Duldig, M.L., 1981; Ph.D. thesis, University of Tasmania.

Duldig, M.L., Emery , M.W., Fenton, A.G., Fenton, K.B., Greenhill, J.G., and Thomas, R.M., 1977; Proc.Astron.Soc.Aust. 3, 117.

Duldig, M.L., Greenhill, J.G., Thomas, R.M., Haynes, R.F., Simons, L.W., and Murdin, P.G., 1979; Mon.Not.R.astra.Soc. 187, 567.

Elvis, M., Maccacaro, T., Wilson, A.S., Ward, M.J., Penston, M.V., Fosbury, R.A.E., and Perola, G.C., 1978; Mon.Not.R.astra.Soc. 183, 129.

Evans, R.D., 1955; "Atomic Nucleus", McGraw Hill.

Fabbiano, G., 1982; Astrophys.J. 262, 709.

Fabbiano, G., Hartmann, L., Raymond, J., Steiner, J., Branduardi-Raymont, G., and Matilsky, T., 1981; Astrophys.J. 243, 911.

Fabian, A.C., Pringle, J.E., and Rees, M.J., 1976; Mon.Not.R.astra. Soc. 175, 43.

Fabian, A.C., Guilbert, P.W., and Ross, R.R., 1982; Mon.Not.R.astra. Soc. 199, 1045.

Field, G.B. and Perrenod, S.C., 1977; Astrophys.J. 215, 717.

Forman, W., Jones, C., Cominsky, L., Julien, P., Murray, S., Peters, G., Tananbaum, H., and Giacconi, R., 1978; Astrophys.J.Suppl. 38, 357.

Gallagher, J.S. and Oinas, V., 1974; Publs.astra.Soc.Pacif. 86, 952.

Garmire, G.P., 1979; Adv. in Sp.Ex. 3, 111.

Giacconi, R., Branduardi, G., Briel, U., Epstein, A., Fabricant, D., Feigelson, E., Forman, W., Gorenstein, P., Grindlay, J., Gursky, H., Harnden, F.R.Jr., Henry, J.P., Jones, C., Kellogg, E., Koch, D., Murray, S., Schreier, E., Seward, F., Tananbaum, H., Topka, K., van Speybroeck, L., Holt, S.S., Becker, R.H., Boldt, E.A., Serlemitsos, P.J., Clark, G., Canizares, C., Markert, T., Novick, R., Helfand, D., and Long, K., 1979; Astrophys.J. 230, 540.

Glass, I.S., 1979; Mon.Not.R.astra.Soc. 187, 807.

Glass, I.S. and Feast, M.W., 1973; Nature Physical Science 245, 39.

Griffiths, R.E., Ward, M.J., Blades, J.C., Wilson, A.S., Chaisson, L., and Johnston, M.D., 1979; Astrophys.J.Lett. 232, L27.

Griffiths, R.E., Lamb, D.Q., Ward, M.J., Wilson, A.S., Charles, P.A., Thorstensen, J., McHardy, I.M., and Lawrence, A., 1980; Mon.Not.R. astr.Soc. 193, 25P.

Grindlay, J., 1977; IAU Circ.No. 3104.

Grindlay, J., 1981; IAU Circ.No. 3620

Grindlay, J.E., Steiner, J.E., Forman, W.R., Canizares, C.R., and McClintock, J.E., 1980; Astrophys.J.Lett. 239, L43.

Gorenstein, P., Gursky, H., and Garmire , G., 1968; Astrophys.J. 153, 885.

Greenhill, J.G., Thomas, R.M., Duldig, M.L., Jernigan, J.G., Murdin, P.G., and Haynes, R.F., 1979a; Nautre 279, 620.

Greenhill, J.G., Coe, M.J., Bell Burnell, S.J., Strong, K.T., and Carpenter, G.F., 1979b; Mon.Not.R.astra.Soc. 189, 563.

Greenhill, J.G., Fenton, A.G., Fenton, K.B., Thomas, R.M., Duldig, M.L., Emery, M.W., Cooke, D.J., Phillips, J., Watts, D.J., Hudson, R.M., and Middleton, E., 1979c; 16th Int.Cosmic Ray Conf., Kyoto 11, 8.

Greenhill, J.G., Duldig, M.L., Emery M.W., Fenton, A.G., Fenton, K.B., Thomas, R.M., and Watts, D.J., 1979d; Proc.Astron.Soc.Aust. 3, 349.

Guilbert, P.W. and Fabian, A.C., 1982; Nature 296, 226.

Guilbert, P.W., Fabian, A.C., and Ross, R.R., 1982; Mon.Not.R.astra. Soc. 199, 763.

Hassall, B.J.M., Pringle, J.E., Ward, M.J., Whelan, J.A.J., Mayo, S.K., Echevarria, J., Jones, D.H.P., Wallis, R.E., Allen, D.A., and Hyland, A.R., 1981; Mon.Not.R.astra.Soc. 197, 275.

Hawkins, F.J., Mason, K.O., and Sanford, P.W., 1973; Nature Phys.Sci. 241, 109.

Hayakawa, S., 1981; Space Sci.Rev. 29, 221.

Haymes, R.C., Walraven, G.D., Meegan, C.A., Hall, R.D., Djuth, F.T., and Shelton, D.H., 1975; Astrophys.J. 201, 593.

Hearn, D.R. and Marshall, F.J., 1979; Astrophys.J.Lett. 232, L21.

Helfand, D.J., 1981; in "X-ray Astronomy with the Einstein Observatory" ed. Giacconi, R., p39.

Herbig, G.H., Preston, G.W., Smak, J., and Paczynski, B., 1965; Astrophys.J. 141, 617.

Hill, P.W., 1980; IAU Circ.No. 3492.

Holm, A.V., Panek, R.J., and Schiffer III, F.H., 1982; Astrophys. J. Lett. 252, L35.

Holt, S.S., 1981; in "X-ray Astronomy with the Einstein Satellite" ed. R. Giacconi (D. Reidel, Dordrecht), p173.

Huang, S., 1972; Astrophys.J. 171, 549.

Hutchings, J.B., Crampton, D., Cowley, A.P., Thorstensen, J.R., and Charles, P.A., 1981; Astrophys.J. 249, 680. (HCCTC)

Imamura, J.N. and Durisen, R.H., 1982; Astrophys. J. 268, 291

Jablonski, F., 1981; IAU Information Bulletin on Variable Stars No. 1911.

Jameson, R.F., Sherrington, M.R., King, A.R., and Frank, J., 1982; Nature 300, 152.

Johnson, H.L., 1966; Ann.Rev.Astron.Astrophys. 4, 193.

Johnson, W.N. III, Harnden, F.R.Jr., and Haymes, R.C., 1972; Astrophys. J.Lett. 172, L1.

Johnston, M.D., Bradt, H.V., Doxsey, R.E., Griffiths, R.E., Schwartz, D.A., and Schwarz, J., 1979; Astrophys.J.Lett. 230, L11.

Johnston, M.D., Bradt, H.V. and Doxsey, R.E., 1979; Astrophys.J. 233, 514.

Johnston, M.D., Griffiths, R.E., and Ward, M.J., 1980; Nature 285, 26.

Jones, C., 1980; in "X-ray Astronomy" ed. Giaconni and Seti, p153.

Jones, C., Forman, W., Tananbaum, H., and Turner, M.J.L., 1976; Astrophys.J.Lett. 210, L9.

Kaluzienski, L.J., and Holt, S.S., 1977; IAU Circ.No. 3144.

Kelley, R.L., Apparao, K.M.V., Doxsey, R.E., Jernigan, J.G., Naranan, S., and Rappaport, S., 1981; Astrophys.J. 243, 251.

Kendziorra, E., Staubert, R., Reppin, C., Pietsch, W., Voges, W., and Trümper, J., 1980; Contribution to NATO Institute on Galactic X-ray Sources, Cape Sounion 1980 May-June.

King, A.R., Ricketts, M.J., and Warwick, R.S., 1978; Mon.Not.R. astra.Soc. 187, 77P.

Klare, G., Krautter, J., Wolf, B., Stahl, O., Vogt, N., Wargau, W., and Rahe, J., 1982; Astron.Astrophys. 113, 76.

Koo, J-W.C. and Haymes, R.C., 1980; Astrophys.J.Lett. 239, L57.

Krug, P.A., Morton, D.C., and Tritton, K.P., 1980; Mon.Not.R.astra.Soc. 190, 237.

Krzeminski, W. and Priedhorsky, W.C., 1978; Publs.astra.Soc.Pacif. 90, 434.

Kylafis, N.D. and Lamb, D.Q., 1979; Astrophys.J.Lett. 228, L105.

Kylafis, N.D. and Lamb, D.Q., 1982; Astrophys.J.Supp. 48, 239.

Lamb, D.Q., 1981; in "X-ray Astronomy in the 1980s" ed. S.S. Holt, p 37.

Lamb, D.Q. and Masters, A.R., 1979; Astrophys.J.Lett. 234, L117.

Lamb, P. and Sanford, P.W., 1979; Mon.Not.R.astra.Soc. 188, 555.

Lampton, M., Margon, B., and Bowyer, S., 1976; Astrophys.J. 208, 177.

Lang, K.R., 1974; "Astrophysical Formulae", Springer-Verlag, Berlin, p504-505.

Latham, D.W., Liebert, J., and Steiner, J.E., 1981; Astrophys.J. 246, 919.

Lee, See-Woo, 1976; Ph.D. thesis, Australian National University.

Leiter, D. and Boldt, E., 1982; Astrophys.J. 260, 1.

Lewin, W.H.G., Ricker, G.R., and McClintock, J.E., 1971; Astrophys. J.Lett. 169, L17.

Lewin, W.H.G. and Joss, P.C., 1981; Space Sci.Rev. 28, 3.

Liang, E.P.T., 1979; Astrophys.J.Lett. 231, L111.

Liebert, J., Stockman, H.S., Angel, J.R.P., Woolf, N.J., Hege, K., and Margon, B., 1978; Astrophys.J. 225, 201.

Linsky, J.L., 1981; in "X-ray Astronomy in the 1980s" ed. S.S. Holt, p13.

Lightman, A.P., 1982; Space Sci. Reviews 33, 335.

Lightman, A.P. and Rybicki, G.B., 1979; Astrophys.J.Lett. 229, L15.

Lomb, N.R., 1976; Astrophys. Space Sci. 39, 447.

Long, K.S., Helfand, D.J., and Grabelsky, D.A., 1981; Astrophys.J. 248, 925.

de Loore, C., Burger, M., van Dessel, E.L., and Mouchet, M., 1982; in IAU Symposium No. 98, 'Be Stars', ed. M. Jaschek and H. Groth, p347.

Makishima, K., Miyamoto, S., Oda, M., Ogawara, Y., Pelling, R.M., and Peterson, L.E., 1980; Bull.Inst. Space and Aeronaut.Sci.Univ. Tokoyo B (Japan), Vol. 16, no. 2B, p1033.

Manchester, R.N., Tuohy, I.R., and D'Amico, N., 1982; Astrophys.J.Lett. 262, L31.

Maraschi, L., Treves, A. and van den Heuvel, E.P.J.,1977; Astrophys.J. 216, 819.

Margon, B., Nelson, J., Chanan, G., Thorstensen, J.R., and Bowyer, S., 1977; Astrophys.J. 216, 811.

Markert, T.H., Winkler, P.F., Laird, F.N., Clark, G.W., Hearn, D.R., Sprott, G.F., Li, F.K., Bradt, H.V., Lewin, W.H.G., and Schnopper, H.W., 1979; Astrophys.J.Supp. 39, 573.

Marshall, F.E., Swank, J.H., Boldt, E.A., Holt, S.S., and Serlemitsos, P.J., 1979a; Astrophys.J.Lett. 230, L145.

Marshall, F.E., Boldt, E.A., Holt, S.S., Mushotzky, R.F., Pravdo, S.H., Rothschild, R.E., and Serlemitsos, P.J., 1979b; Astrophys.J.Supp. 40, 657.

Marshall, F.E., Boldt, E.A., Holt, S.S., Miller, R.B., Mushotzky, R.F., Rose, L.A., Rothschild, R.E., and Serlemitsos, P.J., 1980; Astrophys. J. 235, 4.

Marshall, N., Warwick, R.S., and Pounds, K.A., 1981; Mon.Not.R.astra. Soc. 194, 987.

Mason, K.O., Lampton, M., Charles, P.A., and Bowyer, S., 1978; Astrophys. J.Lett. 226, L129.

Mason, K.O., Kahn, S.M., and Bowyer, C.S., 1979; Nature 280, 568.

Matilsky, T., Shrader, C., and Tananbaum, H., 1982; Astrophys.J.Lett. 258, L1.

Matteson, J., 1978; Proc. 16th Aerospace Sciences Meeting, Huntsville, Alabama, Paper 78-35.

Maurer, G.S., Johnson, W.N., Kurfess, J.D., and Strickman, M.S., 1982; Astrophys.J. 254, 271.

Mayo, S.K., Wickramasinghe, D.T., and Whelan, J.A.J., 1980; Mon.Not. R.astra.Soc. 193, 793.

McCulloch, P.M., Hamilton, P.A., and Ables, J.G., 1982; IAU Circ.No. 3704.

Mendoza, E.E., 1982; in IAU Symposium No. 98 "Be Stars" ed. M. Jaschek and H. Groth, p3.

McHardy, I.M., Lawrence, A., Pye, J.P., and Pounds, K.A., 1981; Mon.Not. R.astra.Soc. 197, 893.

McHardy, I.M., Pye, J.P., Fairall, A.P., Warner, B., Allen, S., Cropper, M., and Ward, M.J., 1982; IAU Circ.No. 3687.

Middleditch, J., 1982; Astrophys.J.Lett. 257, L71.

Middleditch, J., Mason, K.O., Nelson, J.E., and White, N.E., 1981; Astrophys.J. 244, 1001.

Middleditch, J. and Córdova, F.A., 1982; Astrophys.J. 255, 585.

Milgrom, M., 1976; Astrophys.J. 208, 191.

Milgrom, M., 1978; Astron.Astrophys. 67, L25.

Motch, C., 1979; IAU Circ.No. 3427.

Motch, C., 1981; Astron.Astrophys. 100, 277.

Motch, C. and Pakull, M.W., 1981; Astron.Astrophys. 101, L9.

Motch, C., van Paradijs, J., Pedersen, H., Ilovaisky, S.A., and Chevalier, C., 1982; ESO preprint.

Mouchet, M., Bonnet-Bidaud, J.M., Ilovaisky, S.A., and Chevalier, C., 1981; Astron.Astrophys. 102, 31.

Mouchet, M., 1982; to appear, Proceedings of IAU Coll.no. 72, Haifa, August 1982.

Murdin, P., Jauncey, D.L., Haynes, R.F., Lerche, I., Nicolson, G.D., Holt, S.S., and Kaluzienski, L.J., 1980; Astron.Astrophys. 87, 292.

Mushotzky, R.F., Marshall, F.E., Boldt, E.A., Holt, S.S., and Serlemitsos, P.J., 1980; Astrophys.J. 235, 377.

Nolan, P.L., Gruber, D.E., Knight, F.K., Matteson, J.L., Rothschild, R.E., Marshall, F.E., Levine, A.M., and Primini, F.A., 1981; Nature 293, 275.

Oke, J.B., 1974; Astrophys.J.Suppl. 27, 21.

Oke, J.B. and Wade, R.A., 1982; Astron.J. 87, 670.

Pakull, M. and Parmar, A., 1981; Astron.Astrophys. 102, L1.

Parsignault, D.R. and Grindlay, J.E., 1978; Astrophys.J. 225, 970.

Patterson, J., 1981; Astrophys.J.Supp. 45, 517.

Patterson, J. and Garcia, M., 1980; IAU Circ.No. 3514.

Patterson, J., Branch, D., Chincarini, G., and Robinson, E.L., 1980; Astrophys.J.Lett. 240, L133.

Patterson, J. and Price, C., 1981; Astrophys.J.Lett. 243, L83.

Patterson, J., Williams, G., and Hiltner, W.A., 1981; Astrophys.J. 245, 618.

Payne-Gaposchkin, C., 1977; "Novae and related stars", ed. M. Friedjung, p3.

Peters, G.J., 1982; in IAU Symposium No. 98, 'Be Stars' ed. M. Jaschek and H. Groth, p353.

Petterson, J.A., 1980; Astrophys.J. 241, 247.

Piccinotti, G., Mushotzky, R.F., Boldt, E.A., Holt, S.S., Marshall, F.E., Serlemitsos, P.J., and Shafer, R.A., 1982; Astrophys.J. 253, 485.

Pravdo, S.H., 1979; in '(COSPAR) X-ray Astronomy', ed. W.A. Baity and L.E. Peterson, Pergamon Press, Oxford, p169.

Pravdo, S.H. and Bussard, R.W., 1981; Astrophys.J.Lett. 246, L115.

Pravdo, S.H., White, N.E., Boldt, E.A., Holt, S.S., Serlemitsos, P.J., Swank, J.H., Szymkowiak, A.E., Tuohy, I.R., and Garmire, G., 1979; Astrophys.J. 231, 912.

Priedhorsky, W.C. and Krzeminski, W., 1978; Astrophys.J. 219, 597.

Pringle, J. and Rees, M.J., 1972; Astron.Astrophys. 21, 1.

Rappaport, S. and Joss, P.C., 1977; Nature, 266, 683.

Rappaport, S. and Joss, P.C., 1981; in "X-ray Astronomy with the Einstein Satellite", ed. R. Giacconi, p123.

Rappaport, S. and van den Heuvel,E.P.J., 1981; "Be Stars", IAU Symposium No. 98, ed. M. Jasheck and H. Groth, p327.

Rappaport, S., Cash,W., Doxsey, R., McClintock, J., and Moore, G., 1974; Astrophys.J.Lett. 187, L5.

Raymond, J.C., Black, J.H., Davis, R.J., Dupree, A.K., Gursky, H., and Hartmann, L., 1979; Astrophys.J.Lett. 230, L95.

Reid, C.A., Johnston, M.D., Bradt, H.V., Doxsey, R.E., Griffiths, R.E., and Schwartz, D.A., 1980; Astron.J. 85, 1062.

Ricker, G.R., McClintock, J.E., Gerassimenko, M., and Lewin, W.H.G., 1973; Astrophys.J. 184, 237.

Ricker, G.R., Gerassimenko, M., McClintock, J.E., Ryckman, S.G., and Lewin, W.H.G., 1976; Astrophys.J. 207, 333.

Ricker, G.R., Clarke, G.W., Doxsey, R.E., Dower, R.G., Jernigan, J.G., Delvaille, J.P., MacAlpine, G.M., and Hjellming, R.M., 1978; Nature 271, 35.

Ricketts, M.J., 1983; Astron.Astrophys. 118, L3.

Ricketts, M.J., Hall, R., Page, C.G., Pounds, K.A., and Sims, M.R., 1981; Vistas in Astronomy 25, 71.

Ricketts, M.J., Hall, R., Page, C.G., Whitford, C.H., and Pounds, K.A., 1982; Mon.Not.R.astra.Soc. 201, 759.

Robinson, E.L., 1976; Ann.Rev.Astron.Astrophys. 14, 119.

Robinson, E.L., Barker, E.S., Cochran, A.L., Cochran, W.D., and Nather, R.E., 1981; Astrophys.J. 251, 611.

Rothschild, R., Boldt, E., Holt, S., Serlemitsos, P., Garmire, G., Agrawal, P., Riegler, G., Bowyer, S., and Lampton, M., 1979; Space Science Instrumentation 4, 265.

Rothschild, R.E., Gruber, D.E., Knight, F.K., Matteson, J.L., Nolan, P.L., Swank, J.H., Holt, S.S., Serlemitsos, P.J., Mason, K.O., and Tuohy, I.R., 1981; Astrophys.J. 250, 723.

Samini, J., Share, G.H., Wood, K., Yentis, D., Meekins, J., Evans, W.D., Shulman, S., Byram, E.T., Chubb, T.A., and Friedman, H., 1979; Nature 278, 434.

Schneider, D.P. and Young, P., 1980a; Astrophys.J. 238, 946.

Schneider, D.P. and Young, P., 1980b; Astrophys.J. 240, 871.

Schwartz, D.A., Bradt, H.V., Briel, U., Doxsey, R., Fabbiano, G., Griffiths, R.E., Johnston, M., and Margon, B., 1979; Astron.J. 84, 1560.

Seward, F.D. and Harnden, F.R.Jr., 1982; Astrophys.J.Lett. 256, L45.

Seward, F.D., Harnden, F.R.Jr., Murdin, P., and Clark, D.H., 1982; Center for Astrophysics preprint 1641. Astrophys. J. 267, 711

Shafter, A.W. and Targan, D.M., 1982; Astron.J. 87, 655.

Shaham, J., 1981; Vistas in Astronomy 25, 217.

Shapiro, S.L., Lightman, A.P. and Eardley, D.M., 1976; Astrophys.J. 204, 187.

Skinner, G.K., Bedford, D.K., Elsner, R.F., Leahy, D., Weisskopf, M.C., and Grindlay, J., 1982; Nature 297, 568.

Smak, J. and Stepién, K., 1975; Acta Astron. 25, 379.

Staubert, R., Kendziorra, E., Pietsch, W., Reppin, C., Trümper, J., and Voges, W., 1978; Astrophys.J.Lett. 225, L114.

Staubert, R., Kendziorra, E., Pietsch, W., Proctor, R.J., Reppin, C., Steinle, H., Trümper, J., and Voges, W., 1981; Space Sci.Rev. 30, 311.

Stein, J.A. and Lewin, W.H.G., 1967; J.Geophys.Res. 72, 383.

Steiner, J.E., Schwartz, D.A., Jablonski, F.J., Busko, I.C., Watson, M.G., Pye, J.P., and McHardy, I.M., 1981; Astrophys.J.Lett. 249, L21.

Stockman, H.S. and Sargent, T.A., 1979; Astrophys.J. 227, 197.

Stockman, H.S., Schmidt, G.D., Angel, J.R.P., Liebert, J., Tapia, S., and Beaver, E.A., 1977; Astrophys.J. 217, 815.

Stockman, H.S., Liebert, J., and Moore, R.L., 1982; Astrophys.J. in press.

Strickman, M.S., Johnson, W.N., and Kurfess, J.D., 1980; Astrophys.J. Lett. 240, L21.

Sulkanen, M.E., Wayne Brasure, L., and Patterson, J., 1981; Astrophys. J. 244, 579.

Swank, J., Lampton, M., Boldt, E., Holt, S., and Serlemitsos, P., 1977; Astrophys.J.Lett. 216, L71.

Swank, J.H., Boldt, E.A., Holt, S.S., Rothschild, R.E.,and Serlemitsos,P.J., 1978; Astrophys.J.Lett. 226, L133.

Szkody, P., 1981; Astrophys.J. 247, 577.

Szkody, P. and Brownlee, D.E., 1977; Astrophys.J.Lett. 212, L113.

Szkody, P. and Margon, B., 1980; Astrophys.J. 236, 862.

Szkody, P. and Mateo, M., 1982; IAU Circ.No. 3752.

Szkody, P., Michalsky, J., and Stokes, G., 1980; in IAU Coll.No. 53 (Rochester: University of Rochester), p498.

Tanaka, Y., 1983; IAU Circ.No. 3787.

Tanzi, E.G., Tarenghi, M., Treves, A., Howarth, I.D., Willis, A.J., and Wilson, R., 1980; Astron.Astrophys. 83, 270.

Taylor, B.G., Andresen, R.D., Peacock, A., and Zobl, R., 1981; Space Sci.Rev. 30, 479.

Tennant, A.F. and Mushotzky, R.F., 1983; Astrophys.J. 264, 92.

Tennant, A.F., Mushotzky, R.F., Boldt, E.A., and Swank, J.H., 1981; Astrophys.J. 251, 15.

Thollar, S., 1982; Honours thesis, University of Tasmania.

Thomas, R.M., Davison, P.J.N., Clancy, M.C., and Buselli, G., 1975; Mon.Not.R.astra.Soc. 170, 569.

Thomas, R.M., Duldig, M.L., and Greenhill, J.G., 1977; Nature 267, 332.

Thornstensen, J.R. and Charles, P.A., 1980; IAU Circ.No. 3449.

Thorstensen, J., Charles, P., Bowyer, S., Briel, U.G., Doxsey, R.E., Griffiths, R.E., and Schwartz, D.A., 1979; Astrophys.J.Lett. 233, L57.

Tonry, J. and Davis, M., 1979; Astron.J. 84, 1511.

Tuohy, I.R., Lamb, F.K., Garmire, G.P., and Mason, K.O., 1978; Astrophys.J.Lett. 226, L17.

Tuohy, I.R., Mason, K.O., Garmire, G.P., and Lamb, F.K., 1981; Astrophys. J. 245, 183.

Turner, M.J.L., Smith, A., and Zimmerman, H.U., 1981; Space Sci.Rev. 30, 513.

Urry, C.M., Mushotzky, R.F., Tennant, A.F., Boldt, E.A., and Holt, S.S., 1982; NASA TM 84937.

Van Horn, H.M., Wesemael, F., and Winget, D.E., 1980; Astrophys.J. 235, L143.

Van der Hucht, K.A., Conti, P.S., Lundström, I., and Stenholm, B., 1981; Space Sci. Review 28, 227.

van der Klis, M., van Paradijs, J., Charles, P.A., Thorstensen, J.R., Tuohy, I., and Elso, J., 1983; Mon.Not.R.astra.Soc. 203, 279.

van Paradijs, J., van den Heuvel, E.P.J., and Verbunt, F., 1980; IAU Circ.No. 3482, and priv. communication.

Van Speybroeck, L. and Bechtold, J., 1981; "X-ray Astronomy with the Einstein Satellite", ed. R. Giacconi, p153.

Voges, W., Pietsch, W., Reppin, C., Trümper, J., Kendziorra, E., and Staubert, R., 1982; Astrophys.J. 263, 803.

Vogt, N., Krzeminski, W., and Sterken, C., 1980; Astron.Astrophys. 85, 106.

Vogt, N., Geisse, H.S., and Rojas, S., 1981; Astron.Astrophys.Supp. 46, 7.

Wada, T., Shimizu, A., Suzuki, M., Kato, M., and Hoshi, R., 1980; Prog. Theoretical Phys. 64, 1986.

Wampler, E.J. and Morton, D.C., 1977; Vistas in Astronomy 21, 191.

Wang, Y.-M., 1981; Astron.Astrophys. 102, 36.

Wang, Y.-M. and Welter, G.L., 1981; Astron.Astrophys. 102, 97.

Warner, B., 1976a; Observatory 96, 49.

Warner, B., 1976b; IAU Symp. 73, ed. P.P. Eggleton, S. Milton and J. Whelan, p85.

Warner, B., 1980a; Mon.Not.R.astr.Soc. 190, 69P.

Warner, B., 1980b; IAU Circ.No. 3502.

Warner, B., 1982; to appear in proceedings of IAU Coll.No. 72, Haifa, August 1982.

Warner, B. and Robinson, E.L., 1972; Mon.Not.R.astra.Soc. 159, 101.

Warner, B. and van Citters, G.W., 1974; Observatory, 94, 116.

Warner, B. and Brickhill, A.J., 1978; Mon.Not.R.astra.Soc. 182, 777.

Warner, B. and McGraw, J.T., 1981; Mon.Not.R.astra.Soc. 196, 59P.

Warner, B., O'Donoghue, D., and Fairall, A.P., 1981; Mon.Not.R.astra. Soc. 196, 705.

Warren, D.M., 1980; Honours thesis, University of Tasmania.

Warwick, R.S., Marshall, N., Fraser, G.W., Watson, M.G., Lawrence, A., Page, C.G., Pounds, K.A., Ricketts, M.J., Sims, M.R., and Smith, A., 1981; Mon.Not.R.astra.Soc. 197, 865.

Waterworth, M.D., 1980; Proc.Astro.Soc.Aust. 4, 14.

Watson, M.G., Sherrington, M.R., and Jameson, R.F., 1978; Mon.Not.R. astra.Soc. 184, 79P.

Watts, D.J. and Thomas, R.M., 1979; Astrophys. and Space Sci. 64, 213.

Watts, D.J., Greenhill, J.G., and Thomas, R.M., 1980; Mon.Not.R. Astra.Soc. 191, 25P.

Watts, D.J., Greenhill, J.G., Hill, P.W., and Thomas, R.M., 1982; Mon.Not.R.astra.Soc. 200, 1039.

Weast, G.J., Durisen, R.H., Imamura, J.N., Kylafis, N.D., and Lamb, D.Q., 1980; in IAU Coll.No. 53 (Rochester: University of Rochester), p140.

White, N.E., 1981; Astrophys.J.Lett. 244, L85.

White, N.E. and Marshall, F.E., 1981; Astrophys.J.Lett. 249, L25.

White, N.E., Swank, J.H., and Holt, S.S., 1983; Astrophys.J. 270, 711

White, N.E., Mason, K.O., Huckle, H.E., Charles, P.A., and Sandford, P.W., 1976; Astrophys.J.Lett. 209, L119.

Whyte, C.A. and Eggleton, P.P., 1980; Mon.Not.R.astra.Soc. 190, 801.

Wickramsinghe, D.T., Stobie, R.S., and Bessell, M.S., 1982; Mon.Not.R. astra.Soc. 200, 605.

Williams, G. and Johns, M., 1980; IAU Circ.No. 3519.

Williams, R.E. and Ferguson, D.H., 1982; Astrophys.J. 257, 672.

Wilson, A.S. and Penston, M.V., 1979; Astrophys.J. 232, 389.

Worrall, D.M., Mushotzky, R.F., Boldt, E.A., Holt, S.S., and Serlemitsos, P.J., 1979; Astrophys.J. 232, 683.

Worrall, D.M., Boldt, E.A., Holt, S.S., and Serlemitsos, P.J., 1980; Astrophys.J. 240, 421.

Worrall, D.M., Knight, F.K., Nolan, P.L., Rothschild, R.E., Levine, A.M., Primini,F.A., and Lewin, W.H.G., 1981; Astrophys.J.Lett. 247, L31.

Postscript on V1223 Sgr

After completion of the thesis, a preprint was received (Warner, B. and Cropper, M., 1983 submitted to Mon.Not.R.astra Soc.) discussing the photometry of V1223 Sgr over two seasons. They detected the orbital period of 0.14 day, the rotation period of the white dwarf (794 sec) and occasionally the orbital sideband of 849.8 sec. The ephemerides are:

Orbital	HJD (max)	2444749.9866 + 0.140239 E
Rotation	HJD (max)	2444750.00404 + 0.009194215 E ±5
Sideband	HJD (max)	2444750.00350 + 0.00983588 E

where E is the cycle number. The 794 sec and 849 sec pulsations are in phase at maximum orbital light. Warner and Cropper interpret this as follows. The X-ray beam illuminates the accretion disc producing the 794 sec pulsations and a small fraction falls onto the source of the orbital sideband. This source is possibly the companion. Both are in phase when the secondary is at superior conjunction (maximum light). Since the disc will have a strong front back asymmetry for $i > 0$, the far side of the disc will be more visible to an observer. Both pulsations are from sources of reprocessed X-ray flux in relatively cool atmospheres. This is in contrast with H2252-035 where the source of the pulsations at the frequency of the rotation of the white dwarf (805 sec) is on or very near the surface of the white dwarf and follows a $F_\lambda \propto \lambda^{-4}$ law expected from the tail of a hot blackbody.

The proposed model for V1223 Sgr is similar to the Ex Hya model (Model B) in section 7.2.1 except some light illuminates the secondary. The difficulty of this model is to explain the large orbital modulation seen at R and J as mentioned in section 7.2.1.

The 850 sec pulsations were not detected with the AAT observations discussed in section 6.2.1. Upper limits to full amplitude pulsed flux after prewhitening with the 794 sec period are listed below.

These may be compared to pulsation fluxes at other periods listed in Table 6.10.

Passband	Flux (erg $sec^{-1} cm^{-2} \AA^{-1}$)
V	$< 3.2 \times 10^{-16}$
R	$< 1.5 \times 10^{-16}$
J	$< 5.6 \times 10^{-17}$
K	$< 1.8 \times 10^{-17}$

One possible reason for the nondetection of the 850 sec pulsations is the disc may have been completely obscuring the companion. This can occur if the accretion rate $\dot{M}$ is larger than normal and if the disc viscosity is small ($\alpha << 1$). The disc will expand in the Z direction because inward transport of matter is slowed due to low α. Correlating an inverse relationship between the system luminosity ($\propto \dot{M}$) and the amplitude of the 850 sec may answer this question.

Periods other than the 794 sec pulsations noted in Figure 6.21 are not related to the dynamics of the system and may represent random components of the light curve. All other conclusions on V1223 Sgr in section 7.2 remain unaffected.

List of Publications

"A Comparison of Spectral Reduction Methods in X-ray Astronomy", Watts, D.J. and Thomas, R.M. 1979, *Astrophys.Space Sci.* 64, 213.

"A Large Area Proportional Counter for Balloon-borne X-ray Astronomy", Greenhill, J.G., Fenton, A.G., Fenton, K.B., Thomas, R.M., Duldig, M.L., Emergy, M.W., Cooke, D.J., Phillips, J., Watts, D.J., Hudson, R.M., Middleton, E., and Salmon, G. 1979, *Proc. Cosmic Ray Conf. Kyoto Japan* Vol. 11, 8.

"Balloon Observations of Several Southern X-ray Sources", Greenhill, J.G., Duldig, M.L., Emergy, M.W., Fenton, A.G., Fenton, K.B., Thomas, R.M., and Watts, D.J. 1979, *Proc. A.S.A.* 3, 349.

"2A0526-328" *IAU Circ. No. 3334*, Thomas, R.M., Greenhill, J.G., and Watts, D.J. 1979.

"Emission Line Variability in the Optical Candidate for 2A0526-328", Watts, D.J., Greenhill, J.G., and Thomas, R.M. 1980, *Mon.Not.R.astra. Soc.* 191, 25P.

"2A0526-328" *IAU Circ. No. 3492*, Hill, P.W., Greenhill, J.G., and Watts, D.J. 1980.

"2A0526-328, an optical and X-ray study of a cataclysmic variable", Watts, D.J., Greenhill, J.G., Hill, P.W., and Thomas, R.M., 1982, *Mon.Not.R.astra.Soc.* 200, 1039.

"The UTIC hard X-ray Balloon-borne platform", Greenhill, J.G., Watts, D.J., Giles, A.B., Fenton, K.B., and Ashton, S.C., 1982, *Proc. A.S.A.* 4, 460.

"Enhanced X-ray emission above 50 keV in Sco X-1", Duldig, M.L., Greenhill, J.G., Watts, D.J., Thomas, R.M., and Fenton, K.B., 1983, Submitted to *Astrophys.Space Sci.*

"CW1103+254" *IAU Circ. No. 3712*, Bailey, J., Hanes, D., Watts, D.J., Giles, A.B., and Greenhill, J.G., 1982.

"H0139-68" *IAU Circ. No. 3720*, Bailey, J., Watts, D.J., Giles, A.B., and Greenhill, J.G., 1982.

"The AM Her type binary H1405-451", Bailey, J., Hough, J.H., Axon, D., Watts, D.J., and Giles, A.B., 1983, in preparation.

"On the Intermediate Polar V1223 Sgr", Watts, D.J., Giles, A.B., and Bailey, J., 1983, in preparation.

"Einstein observations of the nova-like object VY Scl", Hill, P.W., Watts, D.J., and Greenhill, J.G., 1983, in preparation.